

Azərbaycan Milli Elmlər Akademiyası  
Fizika-Riyaziyyat və Texnika Elmləri Bölməsi  
Fizika İnstitutu

---

2

# Fizika

Cild

XIV

2008

Bakı \* Elm

**PRODUCTION OF VERTICAL-ALIGNED CARBON NANOTUBES (VACNTS)  
WITH DIRECT CURRENT PLASMA ENHANCED CHEMICAL VAPOR DEPOSITION  
(DCPECVD)**

M. A. RAMAZANOV

*Baku State University, AZ-1148, Z. Halilov str., 23*

**K. ARBABI, MOJTAHED ZADEH LARIJANI M.**

*Agricultural, Medical & Industrial Research School (AMIRS), Karaj-Iran.*

In this investigation we could synthesis Carbon Nanotubes (CNT) with DCPECVD method for Vertical-Aligned CNT (VACNT). We have utilized a silicon sheet with 60 nm nickel layer as catalyst, C<sub>2</sub>H<sub>2</sub> gas and CNTs synthesized on it with about 2 μm height and 50 nm diameter. They are mix of single wall and multi wall CNTs. We changed some synthesis conditions for some problems and now we work to optimize new condition for CNT synthesis.

### Introduction

Carbon nanotubes were discovered in 1991 by means of transmission electron microscopy in the multiwalled form that consists of concentric shells of seamless cylinders of graphene (a layer of graphite). The quasi one-dimensional structure, large mechanical strength, and the conjugated electronic structure are among the most commonly mentioned properties of carbon nanotubes. Current and potential applications of carbon nanotubes include the probing tip in scanning tunneling microscopy (STM), artificial "muscle", units of electronic memory storage, to name just a few. The fascinating properties and potential uses have attracted much research interest in the carbon nanotubes.

The geometries, electronic properties and actuation of single-walled carbon nanotubes (SWNTs) obtained from high-level quantum mechanical calculations are presented in

this entry. The commonly used quantum mechanical methods are first reviewed, then the behaviors of small to medium SWNTs with different structures are discussed and comparison with experimental results is made when possible. The behaviors of different groups of SWNTs are attributed to their electronic band structures.

Shortly after the discovery of carbon nanotubes, the geometries and electronic band structures of these quasi one-dimensional extended systems were described in general terms. Idealized single-walled carbon nanotubes can be viewed as formed by rolling up a graphene sheet along the chiral vector (n,m), where n and m are numbers of the two lattice vectors (a<sub>1</sub> and a<sub>2</sub>) of graphene needed to construct the chiral vector. The translational vector is perpendicular to the chiral vector, thus parallel to the tube axis.

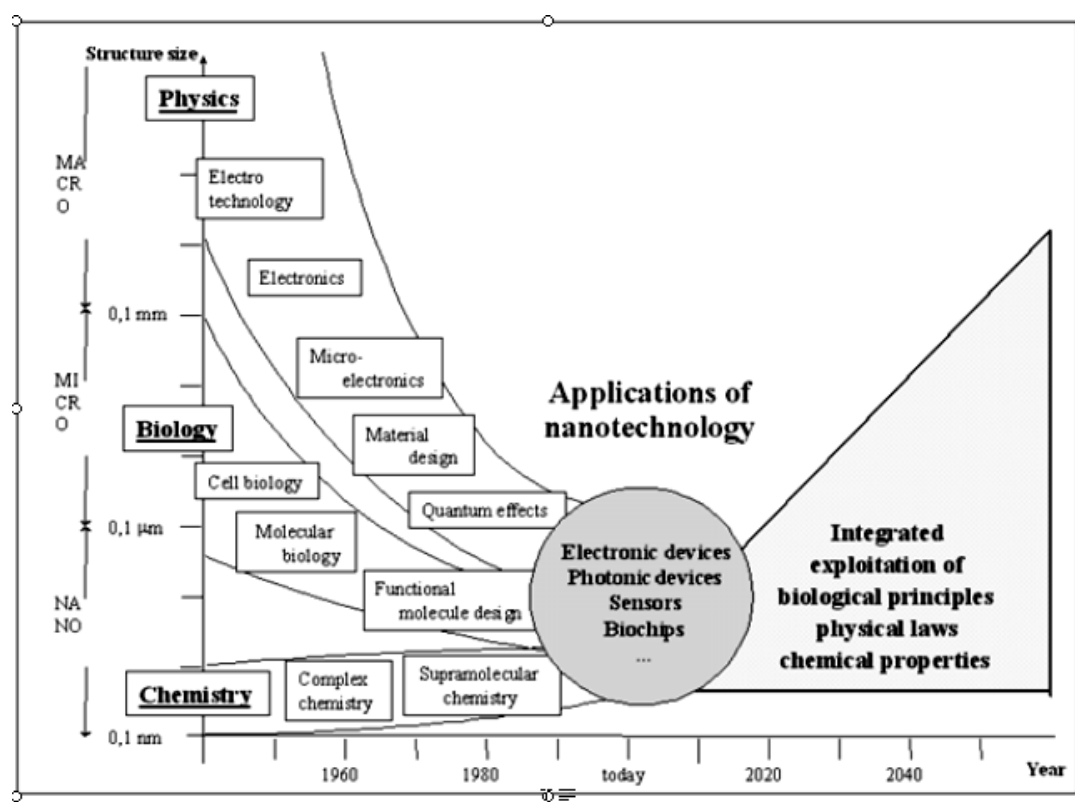


Fig.1. The convergence of the disciplines and multisector applications

Fig. 1 shows the chiral vector of a (5,3) chiral SWNT. Because of the two-dimensional symmetry of graphene,  $(n,m)$  is the same as  $(m,n)$ , therefore by convention  $n$  is larger than or equal to  $m$ . Depending on the values of  $n$  and  $m$ , SWNTs can be achiral or chiral:  $(n,n)$  armchair and  $(n,0)$  zigzag nanotubes are achiral, whereas general  $(n>m>0)$  nanotubes are chiral. For a detailed discussion of the general aspects of the geometrical and electronic structures of SWNTs, see other related entries in this encyclopedia. The characteristic behavior of SWNTs shows significant deviations from the behavior of graphene, mostly because the finite dimension perpendicular to the tube axis introduces quantization of the energy levels leading to subgroups of “metallic” and “semiconducting” tubes. The importance of the remainder of the  $(n-m)/3$  division has been discovered by applying a simple tight binding theory to the electronic structure of SWNTs. This simplification leads to results that we refer to as “ideal” in this entry. The remainder of  $(n-m)/3$  is related to the mapping of the highest occupied and lowest unoccupied levels of SWNTs to the energy levels of graphene that are closest to the Fermi energy, and this leads to the broad categories of “metallic” ( $n-m=3i$ ,  $i$  is an integer) and “semiconducting” ( $n-m=3i+1$  and  $3i+2$ ) SWNTs.

The observed SWNTs have diameters from a half to a few nanometers and lengths up to several micrometers, hence the name. In both graphite and nanotubes, the carbon atoms are in a  $sp^2$  hybridized form with one  $p$  atomic orbital perpendicular to the surface of graphene or the tube left to form the  $p$  molecular orbitals. Each carbon atom in graphite is  $sp^2$  hybridized and has three bonds connecting with its neighbors. These three bonds are symmetrically related and have identical length of  $1.42\text{ \AA}^\circ$  [1].

### **Carbon Nanotube (CNT) Growth Methods**

Some methods developed for growing of CNTs such as arc-discharge, laser ablation, and chemical vapor deposition (CVD) that have explained below [2].

#### **Arc-discharge Method**

The carbon arc discharge method is the most common and perhaps easiest way to produce CNTs, as it is rather simple. However, it is a technique that produces a complex mixture of components, and requires further purification - to separate the CNTs from the soot and the residual catalytic metals present in the crude product. This method creates CNTs through arc-vaporization of two carbon rods placed end to end, separated by approximately 1mm, in an enclosure that is usually filled with inert gas at low pressure. Recent investigations have shown that it is also possible to create CNTs with the arc method in liquid nitrogen. A direct current of 50 to 100A, driven by a potential difference of approximately 20 V, creates a high temperature discharge between the two electrodes. The discharge vaporizes the surface of one of the carbon electrodes, and forms a small rod-shaped deposit on the other electrode. Producing CNTs in high yield depends on the uniformity of the plasma arc, and the temperature of the deposit forming on the carbon electrode. [2]

#### **Laser Ablation Methods**

In 1996 CNTs were first synthesized using a dual-pulsed laser and achieved yields of >70wt% purity. Samples were

prepared by laser vaporization of graphite rods with a 50:50 catalyst mixture of Cobalt and Nickel at  $1200^\circ\text{C}$  in flowing argon, followed by heat treatment in a vacuum at  $1000^\circ\text{C}$  to remove the C<sub>60</sub> and other fullerenes. The initial laser vaporization pulse was followed by a second pulse, to vaporize the target more uniformly. The use of two successive laser pulses minimizes the amount of carbon deposited as soot. The second laser pulse breaks up the larger particles ablated by the first one, and feeds them into the growing nanotube structure. The material produced by this method appears as a mat of “ropes”, 10-20 nm in diameter and up to 100  $\mu\text{m}$  or more in length. Each rope is found to consist primarily of a bundle of single walled nanotubes, aligned along a common axis. By varying the growth temperature, the catalyst composition, and other process parameters, the average nanotube diameter and size distribution can be varied.

Arc-discharge and laser vaporization are currently the principal methods for obtaining small quantities of high quality CNTs. However, both methods suffer from drawbacks. The first is that both methods involve evaporating the carbon source, so it has been unclear how to scale up production to the industrial level using these approaches. The second issue relates to the fact that vaporization methods grow CNTs in highly tangled forms, mixed with unwanted forms of carbon and/or metal species. The CNTs thus produced are difficult to purify, manipulate, and assemble for building nanotube-device architectures for practical applications [2].

### **Chemical Vapor Deposition (CVD)**

Chemical vapor deposition of hydrocarbons over a metal catalyst is a classical method that has been used to produce various carbon materials such as carbon fibres and filaments for over twenty years. Large amounts of CNTs can be formed by catalytic CVD of acetylene over nickel, cobalt and iron catalysts supported on silica or zeolite. The carbon deposition activity seems to relate to the cobalt content of the catalyst, whereas the CNTs’ selectivity seems to be a function of the pH in catalyst preparation. Fullerenes and bundles of single walled nanotubes were also found among the multi walled nanotubes produced on the carbon/silica catalyst.

Some researchers are experimenting with the formation of CNTs from ethylene. Supported catalysts such as iron, cobalt, and nickel, containing either a single metal or a mixture of metals, seem to induce the growth of isolated single walled nanotubes or single walled nanotubes bundles in the ethylene atmosphere. CVD of carbon within the pores of a thin alumina template with or without a Nickel catalyst has been achieved. Ethylene was used with reaction temperatures of  $545^\circ\text{C}$  for Nickel-catalysed CVD, and  $900^\circ\text{C}$  for an uncatalysed process. The resultant carbon nanostructures have open ends, with no caps. Methane has also been used as a carbon source. In particular it has been used to obtain ‘nanotube chips’ containing isolated single walled nanotubes at controlled locations. High yields of single walled nanotubes have been obtained by catalytic decomposition of an H<sub>2</sub>/CH<sub>4</sub> mixture over well-dispersed metal particles such as Cobalt, Nickel, and Iron on magnesium oxide at  $1000^\circ\text{C}$ . The reduction produces very small transition metal particles at a temperature of usually  $>600^\circ\text{C}$ . The decomposition of CH<sub>4</sub> over the freshly formed nanoparticles prevents their

further growth, and thus results in a very high proportion of single walled nanotubes and fewer multi walled nanotubes [3].

### Methods and material

In this project for Carbon Nanotube (CNT) synthesis we have used DCPECVD method for Vertical-Aligned CNT (VACNT). We have utilized a silicon sheet of  $1 \times 1 \text{ cm}^2$  dimension which is coated with 60 nm nickel layer as catalyst. The silicon sheet placed on a heater into the chamber. The chamber is evacuated to base pressure  $1 \times 10^{-5}$  torr (Fig 1). The substrates are heated to  $700^\circ \text{C}$  on the hydrogen ambient at a pressure of 10 torr. The silicon and heater are as cathode and a grid with 2 cm diameter is settled just over the silicon as anode (Fig. 2). A DC discharge between cathode (sample) and the anode is initiated using a 1 kW supply. The anode–cathode distance is 6 mm. The difference potential is increased to about 300 V.

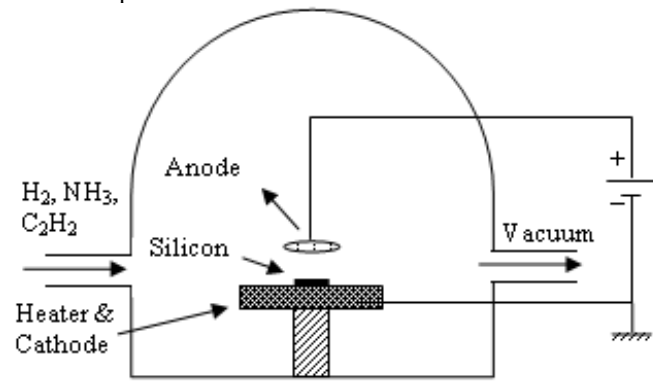


Fig .1. Schematic and picture of CNTs synthesis chamber

The growth of CNTs is performed in two steps. The first consist of formation of Ni islands by etching the surface by  $\text{NH}_3$  ions (100 sccm) and  $\text{H}_2$  ions (100 sccm) for 5 min (Fig 3). The second step is related to the growth of CNTs using  $\text{C}_2\text{H}_2$  ions (100 sccm),  $\text{H}_2$  (100 sccm) and  $\text{NH}_3$  (20 sccm) at a pressure of 10 torr for 20 min.

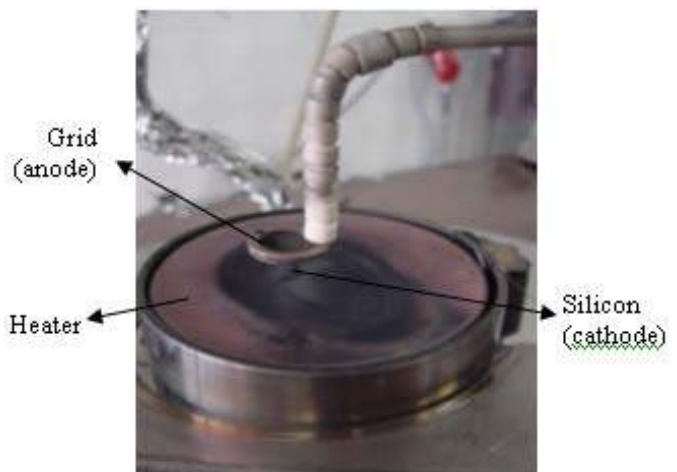


Fig. 2. Heater, silicon and grid

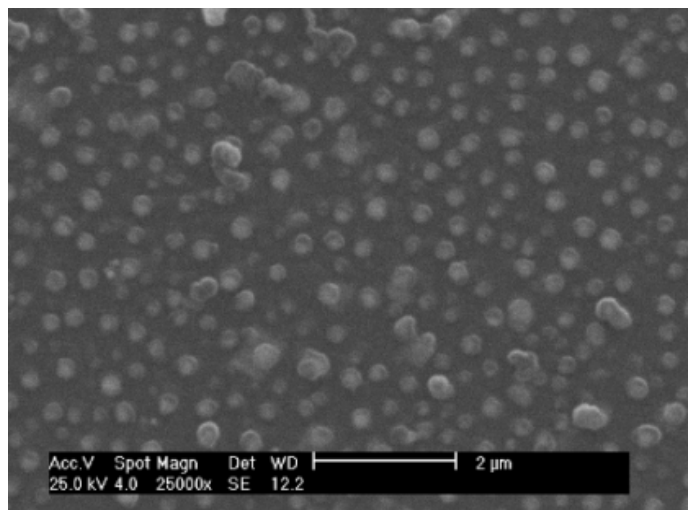


Fig. 3. Ni islands by etching the silicon surface

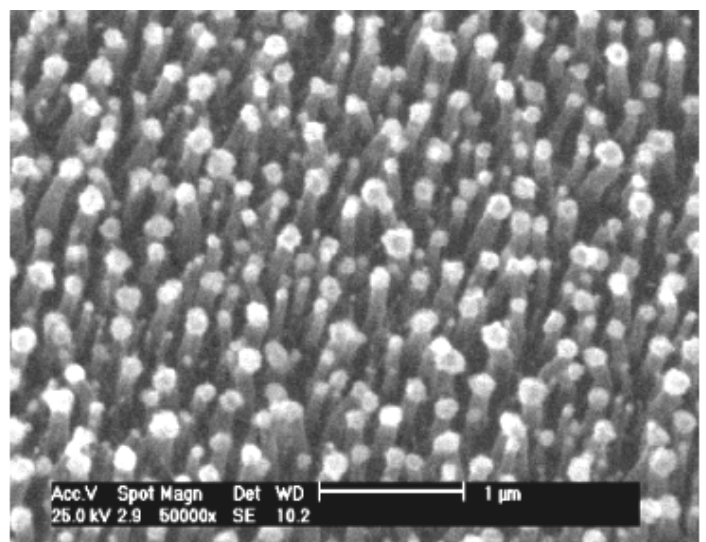


Fig. 4. Vertical and aligned CNTs that synthesized on silicon sheet

### Results

At the beginning, the vertical and aligned CNTs were synthesized using our apparatus (Fig.4). They have about 2  $\mu\text{m}$  height and 50 nm diameter. They are mix of single wall and multi wall CNTs. But a problem concerning the transfer

of heat to the chamber wall remains. Hence we were obligated to change heater insulator. To resolve this problem we have placed a cylindrical ceramic (alumina) around the heater. The heat transfer reduces but as a result of this change, we cannot synthesize the VACNTs. So for the moment we try to obtain the novels parameters to obtain the

VACNTs. Therefore for producing the CNTs we tried more and achieved to some results but they aren't enough. At the moment we could produced the CNTs but they aren't aligned and vertical (Fig. 5). In this interaction, many parameters must be controlled until reach to desired results.

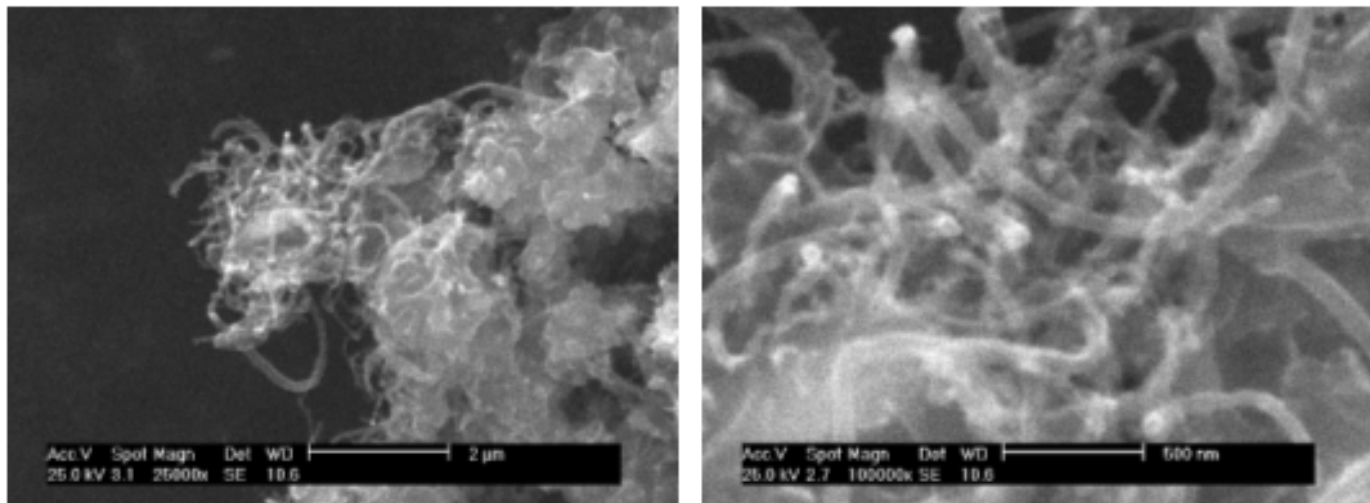


*Fig. 5. CNTs that They aren't vertical and aligned*

- 
- [1] *Guangyu Sun, Marc Nicklaus, Single-Walled Carbon Nanotubes: Geometries, Electronic Properties, and Actuation, National Cancer Institute, Frederick, Maryland, U.S.A., Miklos Kertesz, Georgetown University, Washington, District of Columbia, U.S.A., Dekker encyclopedia of nanoscience and nanotechnology, 2004.*
  - [2] *M. Wilson et al, Nanotechnology: Basic Science and Emerging Technologies, 2002.*
  - [3] *Pramod K. Sharma, Weifang Miao, Anit Giri, Srikanth Raghunathan, Nanomaterials: Manufacturing, Processing, and Applications, Nanomat, Inc., North Huntingdon, Pennsylvania, U.S.A., 2004.*

**M.A. Ramazanov, K. Arbabi, M. Mocahed Zade Larijani**

### **SABIT CƏRƏYAN PLAZMASINDA BUXARLANMA ÜSULU İLƏ NİZAMLI DÜZÜLÜŞLÜ KARBON NANOBORULARIN ALINMASI TEXNOLOGİYASI**

Məqalədə nizamlı şaquli düzülüşlü karbon nanoborularının alınma texnologiyasının nöticələri verilmişdir. Sintez zamanı silisium altlıq üzərində diametri Ø60nm olan aktiv xassəli Ni katalitik mərkəzlərdən istifadə olunmuşdur. Karbon nanoborularının alınması zamanı C<sub>2</sub>H<sub>2</sub> qazından istifadə edilmişdir. Diametri Ø50nm və uzunluğu 2mm karbon nanoboruları sintez olunmuşdur. Karbon nanoborularının alınma texnologiyasının optimallaşdırılması ilə əlaqədar tədqiqat işləri aparılmışdır.

**М.А. Рамазанов, К Арбаби, М. Можтахед Заде Ларижани**

### **ТЕХНОЛОГИЯ ПОЛУЧЕНИЯ УГЛЕРОДНЫХ НАНОТРУБОК В УСЛОВИЯХ ИСПАРЕНИЯ ПЛАЗМОЙ ПОСТОЯННОГО ТОКА**

В работе приведены результаты технологии получения вертикально упорядоченных углеродных нанотрубок. При синтезе использовали кремниевую подложку с активными каталитическими центрами из Ni с размером Ø60нм. Для получения нанотрубок использован газ C<sub>2</sub>H<sub>2</sub>. Синтезированы углеродные нанотрубки диаметром Ø50нм и длиной 2 мм. Проведены исследования по оптимизации технологии получения углеродных нанотрубок.

*Received: 08.04.08*

## LAZER ŞÜALARININ TƏSİRİ İLƏ ÇOX FOTONLU İONLAŞMA VAXTI MAYELƏRİN İSTİLİK TUTUMU

**Q.T. HƏSƏNOV, A.N. MƏMMƏDOVA**

*Azərbaycan Dövlət Neft Akademiyası*

*Bakı,, Az-370010, Azadlıq pr., 20.*

Lazer şüalarının mayelərlə qarşılıqlı təsiri zamanı üç fotonlu ionlaşma vaxtı istilik tutumu nəzəri tədqiq edilmişdir. Müəyyən edilmişdir ki, faza keçidi vaxtı mayelərin istilik tutumunun sıçrayışla dəyişməsi istilik tutumunun istilik şüalanmasının intensivliyindən kəskin asılılığı ilə izah oluna bilər.

Hal hazırda müxtəlif fiziki sahələrin maddə ilə qarşılıqlı təsirinə aid külli miqdarda nəzəri və təcrübi işlər vardır. Bu istiqamətdə lazer şüalarının mayelərlə qarşılıqlı təsirinin tədqiqinə aid işlər xüsusi yer tutur. Mayelərlə güclü lazer şüalarının qarşılıqlı təsiri zamanı müxtəlif fiziki proseslər baş verir. Lazer şüalarının qeyri-xətti udulma prosesi işıq enerjisinin istiliyə çevriləməsi nəticəsində mayelərin ionlaşması və buxarlanması ilə yanaşı gedir. Mayelərin ionlaşması ilə yanaşı ionların rekombinasiyası da baş verir. Güclü lazer şüalarının təsiri altında maye qızır və tarazlıqda olmayan hala keçir. Bütün istilik xassələri, o cümlədən istilik tutumu əsaslı dəyişir. Bu işdə lazer şüalarının təsiri altında üç fotonlu ionlaşmanın mayelərin istilik tutumuna təsiri tədqiq edilmişdir.

Yuxarıda deyilənləri nəzərə alaraq dairəvi en kəsiyinə malik olan boruda mayelərin qeyri izotermik axınına baxılmışdır, belə ki, boru istilik cəhətdən izolə edilmişdir və ətraf mühitə heç bir istilik mübadiləsi yoxdur. Maye boruya daxil olduqda lazer şüalarını udur və iki kəsikdə temperaturun zamanından asılılığı ölçülür. Bu asılılıq  $f_1(t)$  və  $f_2(t)$  ilə işarə olunur. Başlanğıc anda mayenin bütün nöqtələrində temperaturun eyni və sabit olduğu qəbul olmuşdur ( $T_0$ ). Mayelərdə üç fotonlu ionlaşma nəticəsində ionların konsentrasiyasının konveksiya və diffuziya yolu ilə kaustikadan çıxışını və rekombinasiyasının asılılığı aşağıdakı diferensial tənliklə təsvir edilir [1] :

$$N^*(s) = \left( \varphi^*(s) - \frac{\gamma I^3}{s \left( s + \frac{I}{\tau_o} \right)} \right) e^{\left( -\frac{s}{v} + \frac{I}{v\tau_o} \right)} + \frac{\gamma I^3}{s \left( s + \frac{I}{\tau_o} \right)} \quad (3)$$

Bir cins temperatur sahəsində mayedə temperaturun paylanması istilik keçirmənin diferensial tənliyi ilə təsvir edilir

$$c\rho \left( \frac{\partial T}{\partial t} + v \frac{\partial T}{\partial x} \right) = \lambda \frac{\partial^2 T}{\partial x^2} + \alpha IN + \sigma(E + vB)^2 \quad (4)$$

Burada  $\alpha$ - lazer şüalarının udulma əmsalıdır. Qalan işərələr ümumi qəbul olunmuş kəmiyyətlərdir.

Konveksiya yolu ilə istilik daşınmasının diffuziya hesabına olan daşınmadan xeyli böyük olduğunu nəzərə alsaq, yəni

$$c\rho v \frac{\partial T}{\partial x} \gg \lambda \frac{\partial^2 T}{\partial x^2}$$

$$\frac{\partial N}{\partial t} + v \frac{\partial N}{\partial x} = D \frac{\partial^2 N}{\partial x^2} + \gamma I^3 - \frac{N}{\tau_o} \quad (1)$$

harada ki,  $\gamma = \frac{a^2 \beta}{D}$ ,  $a$  - kaustikanın radiusu,  $\beta$  - üç fotonlu ionlaşma əmsalı,  $\tau_o$  - rekombinasiya müddəti,  $v$  - mayenin axının orta sürəti,  $I$  - lazer şüalanmasının intensivliyi,  $D$  - diffuziya əmsalıdır.

Mayelərdə ionların konsentrasiyasının dəyişməsi onların konveksiya hesabına kaustikadan çıxışı diffuz hesabına çıxışdan xeyli böyük olduğuna görə (1) tənliyi aşağıdakı şəklə düşür

$$\frac{\partial N}{\partial t} + v \frac{\partial N}{\partial x} = \gamma I^3 - \frac{N}{\tau_o} \quad (2)$$

Başlanğıc və sərhəd şərtləri aşağıdakı şəkildə verilir:

$$N(x,0) = 0 \quad N(0,t) = \varphi(t)$$

Bu məsələnin həlli üçün Laplas çevrilməsini tətbiq edirik. Surətdə (2) tənliyin aşağıdakı həlli vardır:

(4) tənliyi aşağıdakı şəkildə yazılar

$$c\rho \left( \frac{\partial T}{\partial t} + v \frac{\partial T}{\partial x} \right) = \alpha IN + \sigma(E + vB)^2 \quad . \quad (5)$$

Yuxarıdakı deyilənlərə əsaslanaraq (5) diferensial tənliyinin həlli üçün aşağıdakı başlanğıc və sərhəd şərtləri qəbul olunur:

$$T(x,0) = T_o = const$$

$$T(0,t) = f_1(t)$$

$$T(\ell,t) = f_2(t) \quad (6)$$

Beləliklə, lazer şüalarının və elektromaqnit sahəsinin mayələrin istilik tutumuna təsirinin təyini riyazi olaraq (6) başlangıç və sərhəd şərtləri daxilində (5) diferensial tənliyin həllinə gətirilir.

Bu məsələnin həlli üçün Laplas çevrilməsini tətbiq edir. Surətdə (5) tənliyi aşağıdakı şəkildədir

$$f_2^*(s) = f_1^*(s)e^{-al} + \left( \frac{\sigma(E+vB)^2}{c\rho vs} + \frac{T_o}{v} \right) \times \left( I - e^{-al} \right) \frac{v}{s} + \frac{\alpha\gamma}{c\rho} \frac{I^4}{s^2 \left( s + \frac{I}{\tau_o} \right)} \left( I - e^{-al} \right) - \frac{\alpha I \tau_o}{c\rho} \left( \varphi^*(s) - \frac{\gamma I^3}{s \left( s + \frac{I}{\tau_o} \right)} \right) \left( e^{-al} - I \right) e^{-al}, \quad (8)$$

harada  $a = \frac{s}{v}$ ,  $\alpha < 1$  və  $b < 1$  nəzərə alsaq,  $e^{-al}$  və  $e^{-bl}$  görə sıraya ayırib birinci iki hədlə kifayətlənsək (8) tənliyi aşağıdakı şəklə düşəcək.

$$f_2^*(s) - f_1^*(s) \left( I - \frac{s}{v} \ell \right) = \left( \frac{\sigma[E+vB]^2}{c\rho vs} + \frac{T_o}{v} \right) \ell + \frac{\alpha I \ell}{c\rho v} \left[ \varphi^*(s) \left( I - \frac{s}{v} \ell \right) + \frac{\gamma I^3 \ell}{v \left( s + \frac{I}{\tau_o} \right)} \right]$$

burada  $s = \frac{1}{t_o}$  olduğunu nəzərə alsaq, harada ki  $t_o$  relaksasiya müddətinin  $\frac{1}{4}$ -nə bərabər zamandır, onda istilik tutumunun təyini üçün aşağıdakı münasibəti alarıq:

$$f_2^*\left(\frac{1}{t_o}\right) - f_1^*\left(\frac{1}{t_o}\right) \left( I - \frac{\ell}{vt_o} \right) = \left( \frac{\sigma(E+vB)^2 t_o}{c\rho v} + \frac{T_o}{v} \ell \right) + \frac{\alpha I \ell}{c\rho v} \left[ \varphi^*\left(\frac{1}{t_o}\right) \left( I - \frac{\ell}{vt_o} \right) + \frac{\gamma I^3 \ell}{v \left( \frac{1}{t_o} + \frac{I}{\tau_o} \right)} \right]$$

$$T(t) = \frac{\alpha I^4 \gamma}{c\rho} \tau_o^2 \left( e^{-\frac{t}{\tau_o}} - 1 \right) + \frac{\sigma E^2}{c\rho} t + T_o$$

$t \leq t_o$  olduqda,  $T(t) = T^*$  onda istilik tutumu təyin etmək üçün alırıq:

$$c\rho = \frac{\tau_o (\sigma E^2 + \alpha I^4 \gamma \tau_o)}{T^* - T_o}$$

Bu düsturdan belə nəticə alınır ki, lazer şüalarının təsiri ilə faza keçidində mayələrin istilik tutumunun sıçraşıyla dəyişməsi, istilik tutumunun şüalanmanın intensivliyindən kəskin asılılığı ilə izah olunur.

$$N(t) = \gamma I^3 \tau_o \left( 1 - e^{-\frac{t}{\tau_o}} \right)$$

Temperaturun zamanından asılı olaraq dəyişməsi aşağıdakı şəklə düşür.

[1] Yu.K. Danileiko, T.P. Lebedeva, A.A. Manenkov, A.B. Sidorin. JETF, t. 74, vip.2, 1978, s.765-771. (Rusca)

**G.T. Gasanov, A.N. Mamedova**

**HEAT CAPACITY OF LIQUID AT MULTIQUANTUM IONIZATION UNDER THE INFLUENCE OF LASER RAYS**

Theoretically influence of laser rays on heat capacity of liquids at three-quantum ionization was studied. It was established that stepwise change of heat capacity of liquid at phase transition under influence of laser rays may be explained with significant dependence of heat capacity on the intensity of the heat radiation.

**Г.Т. Гасанов, А.Н. Мамедова**

**ТЕПЛОЕМКОСТЬ ЖИДКОСТИ ПРИ МНОГОФОТОННОЙ ИОНИЗАЦИИ ПОД ДЕЙСТВИЕМ ЛАЗЕРНЫХ ЛУЧЕЙ**

Теоретически исследовано влияние лазерных лучей на теплоемкость жидкостей при трехфотонной ионизации. Установлено, что скачкообразное изменение теплоемкости жидкости при фазовом переходе под действием лазерных лучей может быть объяснено существенной зависимостью теплоемкости от интенсивности теплового излучения.

*Received: 14.03.08*

## VAKUUMDA ÇÖKDÜRMƏ ÜSULU İLƏ ALINMIŞ $Yb_{1-x}Sm_x$ VƏ $As_2S_3$ NAZİK TƏBƏQƏLƏRİNİN QARŞILIQLI TƏSİRİ

**E.Ş. HACIYEV, A.İ. MƏDƏDZADƏ, C.İ. İSMAYILOV**

*Azərbaycan MEA H.M. Abdullayev adına Fizika İnstitutu,  
Bakı, AZ – 1143, H. Cavid pr.33*

Elektronların difraksiya metodu ilə  $Yb_{1-x}Sm_x$  ( $x=0,2$  at.%) və  $As_2S_3$  nazik təbəqələrinin qarşılıqlı təsiri tədqiq edilmişdir. Göstərilmişdir ki, nazik təbəqələrin qarşılıqlı təsiri nəticəsində  $Yb_{1-x}Sm_xAs_4S_7$  fazası ardıcıl buxarlanması 573 K, eyni anda buxarlanma zamanı 473 K temperaturda alınırlar.

Tərkibində nadir torpaq elementləri olan xalkoqenid şüsha əsaslı iki və üçqat birləşmələrin, yüksək həssaslıqlı foto və termoelementlər, lazer şüaların qəbul ediciləri və modulyatorları, qeyri-xətti optik çeviricilər və digər yarımkəcərici cihazların yaradılması üçün perspektivliyi haqda xarici və yerli mətbuatda geniş məlumat var.  $Ln - As - S$  ( $Ln - Sm, Yb$ ) sistemlərinin şüəvari yarımkəcərici birləşmələri akustooptik keyfiyyəti şərtləndirən əmsalların yüksək qiyməti ilə xarakterizə olunur və dalğa uzunluğunun  $\lambda=0,6-1,2$  mkm intervalında spektrin infraqırmızı oblastında şəffafdır. Yuxarıda qeyd olunan yarımkəcəricilərdən helium-neon lazer şüalarının idarə olunmasında akustooptik səs ötürüçüləri kimi istifadə olunur [1].

Təqdim olunan işdə  $Yb_{1-x}Sm_x$  ( $x=0,2$  at.%) –  $As_2S_3$  sisteminə daxil olan halogen tərkibli və nadir torpaq elementli komponentlərini yüksək vakuumda buxarlandıraraq alınmış nazik təbəqələrin yaranma şəraitləri, həmçinin müxtəlif strukturaya malik nazik təbəqələr arasında qarşılıqlı təsir nəticəsində əmələ gələn mümkün fazaların alınma xüsusiyyətləri və quruluşları tədqiq olunmuşdur.

Qalınlıqları 20 nm tərtibdə olan  $Yb_{1-x}Sm_x$  və  $As_2S_3$  nazik təbəqələri  $10^{-5}$  Pa yüksək vakuumda müxtəlif mənbələrdən termiki buxarlandırılaraq təzə kəsilmiş NaCl, KCl duzlarının səthləri üzərinə çökdürülməklə alınmışdır.  $As_2S_3$  nazik təbəqələrini almaq üçün istifadə olunan mənbə volframdan hazırlanmış spiralvari konus formali sobadan,  $Yb_{1-x}Sm_x$  nazik təbəqələrini almaq üçün isə volfram-reniyum xəlitəsindən hazırlanmış kvaziqapalı sobadan ibarətdir. Otaq temperaturunda yerləşən altlıqlar üzərində yaranan nazik təbəqələrdən alınmış elektronogrammalar göstərmişdir ki,  $As_2S_3$  nazik təbəqələri amorf,  $Yb_{1-x}Sm_x$  təbəqələri isə polikristaldır.

Əvvəlcə  $As_2S_3$  və  $Yb_{1-x}Sm_x$  komponentlərini ardıcıl buxarlandırmışla alınan nazik təbəqələr arasında qarşılıqlı təsir tədqiq olunmuşdur. NaCl, KCl altlıqları üzərində alınmış nazik təbəqələrin bir-biri ilə qarşılıqlı təsiri nəticəsində yaranan mümkün fazaların mövcudluğunu aşkar etmək üçün üzərinə  $As_2S_3 + Yb_{1-x}Sm_x$  çökdürülmüş altlıqlar yüksək vakuumda otaq temperaturundan  $T=673$  K qədər qızdırılmış və hər 50 K temperaturda nümunələrdən elektronogrammlar alınmışdır. Sonraki qızdırma zamanı tərkibində kükürd kimi tez uçucu komponentin təbəqəni tərk etməsinin qarşısını almaq üçün  $As_2S_3$  birləşməsi əvvəl, onun üzərinə isə  $Yb_{1-x}Sm_x$  maddəsi çökdürülmüşdür. Buxarlanması dərhal sonra, alınmış ikiqat  $As_2S_3 + Yb_{1-x}Sm_x$  nazik təbəqəsindən çəkilmiş elektronogrammaların analizi göstərmişdir ki, təbəqələr arasında qarşılıqlı təsir baş vermir və heç bir yeni faza müşahidə olunmur, belə ki, təbəqə  $As_2S_3$ ,  $Yb_{1-x}Sm_x$  və  $Yb_2O_3$  – dən ibarətdir.  $As_2S_3 + Yb_{1-x}Sm_x + Yb_2O_3$  tərkibli nazik təbəqənin sonrakı qızdırılması nəticəsində  $As_2S_3$  və  $Yb_{1-x}Sm_x$  təbəqələri arasında reaksiya baş verir və altlıq temperaturunun  $T=573$  K-

də reaksiya nəticəsində  $Yb_{1-x}Sm_xAs_4S_7$  fazası alınır (şək.1, cədvəl 1). Nazik təbəqə şəklində ilk dəfə alınmış və rombik qəfəsde kristallaşan fazanın quruluş parametrləri aşağıdakılardan ibarətdir:  $a=0,724$ ;  $b=0,568$ ;  $c=1,025$  nm, fəza simmetriya qrupu Pmna. Temperaturun növbəti artırılması nümunələrdən alınan elektronogrammaların difraksiya mənzərəsinə dəyişmir, yəni nazik təbəqələrin quruluşu və tərkibi dəyişməz olaraq qalır.



*Şəkil 1.  $Yb_{1-x}Sm_xAs_4S_7$  polikristal fazasından alınmış elektronogramma.*

*Cədvəl 1.  
 $Yb_{1-x}Sm_xAs_4S_7$  polikristal fazasından alınmış  
elektronogrammanın hesablanması*

$$2L\lambda=7,05 \text{ mm} \cdot \text{nm}$$

Nö	Intensivlik	$d_{eksp.}$ (nm)	$d_{nəz.}$ (nm)	H k l
1	Orta güclü	0,3234	0,3157	1 1 1
2	Çox güclü	0,2990	0,2997*	
3	Orta	0,2820	0,2734	0 0 2
4	Orta	0,2189	0,2220	parafin
5	Çox çox güclü	0,1958	0,1933	0 2 2
6	Çox çox güclü	0,1812	0,1843*	
7	Çox zəif	0,1699	0,1649	1 1 3
8	Orta	0,1670	0,1670	2 3 0
9	Orta	0,1546	0,1572*	
10	Çox çox zəif	0,1353	0,1367	0 0 4
11	Orta	0,1248	0,1254	1 3 3
12	Çox çox zəif	0,1152	0,1116	2 2 4
13	Çox çox zəif	0,1076	0,1052	1 1 5
14	Çox çox zəif	0,1014	0,1052	3 3 3
15	Orta	0,0959	0,0966	0 4 4
16	Çox zəif	0,0871	0,0834	3 3 5
17	Çox zəif	0,0825	0,0789	4 4 4

\*  $Yb_2O_3$

Təqdim olunan işdə həmçinin  $As_2S_3$  və  $Yb_{1-x}Sm_x$  komponentlərinin eyni anda müxtəlif sobalardan otaq temperaturunda olan NaCl, KCl altlıqları üzərinə çökdürülməklə alınan nazik təbəqələr arasında qarşılıqlı nüfuzetmə nəticəsində baş-

## VAKUUMDA ÇÖKDÜRMƏ ÜSULU İLƏ ALINMIŞ Yb<sub>1-x</sub>Sm<sub>x</sub> VƏ As<sub>2</sub>S<sub>3</sub> NAZİK TƏBƏQƏLƏRİNİN QARŞILIQLI TƏSİRİ

verən fazaəmələgəlmə prosesləri öyrənilmişdir. Dərhal buxarlanmadan sonra alınan nazik təbəqələrin elektronoqrafik analizi bu təbəqələrdə heç bir üçqat birləşmənin yaranmadığını göstərmişdir. Altılıq temperaturunu 473 K qədər yüksəlt-dikdə Yb<sub>1-x</sub>Sm<sub>x</sub>As<sub>4</sub>S<sub>7</sub> fazası əmələ gəlir. Qeyd etmək lazımdır ki, altılıq temperaturunun bu qiymətində eyni anda buxarlan-dırma zamanı alınan kondensatın tərkibində Yb<sub>2</sub>O<sub>3</sub> oksidinə rast gəlinmir. Bu onunla izah olunur ki, fazaəmələgəlmə prosesi buxar fazasında və ya altlıqdə böyük sürətlə baş verir. Altılıq temperaturunu 673 K-nə qədər artırıqda nazik təbəqə-dən alınan elektronoqrammada müşahidə edilən difraksiya xəttləri göstərir ki, laylar yalnız Yb<sub>1-x</sub>Sm<sub>x</sub>As<sub>4</sub>S<sub>7</sub> fazasından

ibarətdir; Yb<sub>2</sub>O<sub>3</sub> oksidinə aid reflekslər elektronoqrammada yenə də müşahidə olunmur.

Beləliklə, Yb<sub>1-x</sub>Sm<sub>x</sub> və As<sub>2</sub>S<sub>3</sub> nazik təbəqələrinin qarşılıqlı təsiri nəticəsində Yb<sub>1-x</sub>Sm<sub>x</sub>As<sub>4</sub>S<sub>7</sub> kimyəvi tərkibli birləşmə alınır. Bu birləşmə ardıcıl buxarlanma zamanı altılıq temperaturunun  $T=573$  K-də alındığı halda, eyni zamanda buxarlanma vaxtı altılıq temperaturunun  $T=473$  K qiymətində yaranır. Qeyd etmək lazımdır ki, tərkibində nadir torpaq elementləri olan halogen şüə əsaslı sistemlərin digər nümayəndəsi olan Yb – As<sub>2</sub>S<sub>3</sub> sistemində təbəqələr arasında qarşılıqlı təsir öyrənilən zaman oxşar (YbAs<sub>4</sub>S<sub>7</sub>) kimyəvi tərkibli birləşmə ilkin yaranan faza olmuşdur [2].

- [1] А. с. № 1374695. Халькогенидные стекло. П.Г. Рустамов, Р.М. Сардарлы, Т.М. Ильясов, А.И. Мамедов, Я.Н. Шарифов. 1987.  
[2] E. H. Efendiyyev, E. Sh. Hajiyev, R. B. Shafizade. Investigation of amorphous phase formation and

crystallization conditions in As<sub>2</sub>S<sub>3</sub> – Yb system. Physics of multicomp. semicond. Booklet of the abstract satellite conf. of the XXX annual meeting of the Euro. High pres. res. group Azerb. Rep., Baku, October, 12-14, 1992, p. 53.

**E.Sh. Hajiyev, A.I. Madadzade, J.I. Ismailov**

### **INTERACTION OF Yb<sub>1-x</sub>Sm<sub>x</sub> AND As<sub>2</sub>S<sub>3</sub> THIN FILMS OBTAINED BY VACUUM DEPOSITION**

Investigation of Yb<sub>1-x</sub>Sm<sub>x</sub>(x=0,2 at.%) and As<sub>2</sub>S<sub>3</sub> thin films obtained by vacuum deposition has been investigated by electron diffraction method. It is shown that Yb<sub>1-x</sub>Sm<sub>x</sub>As<sub>4</sub>S<sub>7</sub> phase forms as a result of interaction of films at T=573 K in the case of consequent evaporation of components and at 473 K it forms in the case of their simultaneous evaporation.

**Э.Ш. Гаджиев, А.И. Мададзаде, Дж.И. Исмаилов**

### **ВЗАЙМОДЕЙСТВИЕ ПЛЕНОК Yb<sub>1-x</sub>Sm<sub>x</sub> И As<sub>2</sub>S<sub>3</sub>, ПОЛУЧЕННЫХ ВАКУУМНЫМ ОСАЖДЕНИЕМ**

Методом дифракции электронов исследована взаимодействия тонких пленок Yb<sub>1-x</sub>Sm<sub>x</sub>(x=0,2 at.%) и As<sub>2</sub>S<sub>3</sub>, полученных вакуумным осаждением. Показано, что в результате взаимодействия тонких пленок образуется фаза Yb<sub>1-x</sub>Sm<sub>x</sub>As<sub>4</sub>S<sub>7</sub> при температуре 573 К в случае последовательного испарения компонентов, при 473 К – в случае их одновременного испарения.

*Received: 14.04.08*

## AN ALTERNATIVE APPROACH TO USING ATOMIC-FORCE MICROSCOPY IN THE SURFACE STUDIES

**S.D. ALEKPEROV**

*G.M. Abdullayev Institute of Physics of National Academy of Sciences,  
AZ-1143, H. Javid ave. 33, Baku, Azerbaijan*

A new research “MD mode” regime based on the atom force microscopy was developed. “MD mode” regime allows exploring any nonconductive surfaces with complex topography and large differences of heights. Moreover, it allows excluding uncontrollable interaction of probe with sample, and artifacts caused by scanning process. The experimental results demonstrating the possibility to use atomic force microscopy with “MD mode” for the measurement of number properties of the surface are given.

### 1. Introduction

Atomic-force microscopy (AFM) is the powerful method for studying the nanocrystalline material surfaces [1, 2]. Continuous improvement of methods and instruments for AFM has led to the development of number of new procedures and techniques for the investigation of surfaces. However, some AFM operators have serious problems in experiment result interpretation. It is connected with artifacts arising during the surface investigation with the complex relief in atmospheric ambience, because materials with complex surfaces are difficult to investigate using conventional AFM modes [3-5].

“Contact mode” techniques have a high resolution, but can be applied only to very limited group of surfaces which must be rigid and smooth. One more weak point of “contact mode” in application to complex surfaces is that they roughness of the latter commonly leads to the catching of the probe during scanning so that the probe quits its moving operation over the surface.

“Tapping mode” is a rather good mode for scanning of the complex surfaces without abrasion and catching of the probe, but the resolution of “tapping mode” is commonly worse than that of “contact mode”.

“Non-contact mode” provides conditions for avoiding probe’s pollution, destruction, abrasion and catching. However, a probability of probe catching to the surface is rather high in studying of the complex surfaces by “non-contact mode”.

All above problems are solved by using so-called “MD mode” regime [6-8]. In this paper we demonstrate the possibilities of the “MD mode” regime and report the results of scanning various surfaces.

### 2. “MD mode” regime and experimental details

“MD mode” regime operates in the following manner. As usual, a chosen section of the surface is scanned by probe with some step. But the path the probe is going along in the vertical plane is very different from the probe trajectory in conventional AFM modes [9]. “MD mode” probe operation is shown in Fig.1. In the beginning the tip of the probe is high enough over the surface (Fig.1, (1)) so as to avoid any probe-surface interaction. Then, the tip starts moving from this position down to the surface and stops after the contact with the surface is reached (Fig.1, (2)). At this stage topographic measurements of the surface coordinate are carried out. As the measurements are performed in full contact with the

surface, their resolution is comparable with “contact mode” resolution. After the measurements are completed the tip is removed from the surface back to the starting position (Fig.1, (3)). At the end of a scanning step the tip is shifted in lateral direction to the next point, as shown in Fig.1, (4, 5). Note that no friction occurs during the lateral moving since no contact between the probe and the surface is taking place. Data is recorded only when the probe is moving in the normal-to-surface direction. As a whole, “MD mode” operation is free from the abrasion and catching of the probe by complex surfaces and is very similar to the operation of a sewing machine.

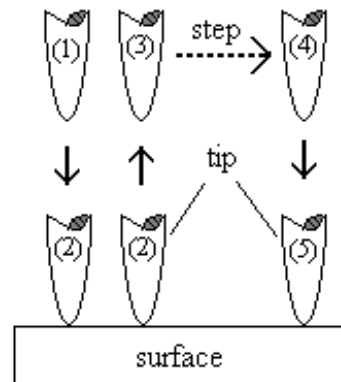


*Fig. 1. Path of probe movement at surface scanning by “MD mode” regime.*

In fact, the probe trajectory in moving to and back from the surface is more complicated than its schematic presentation in Fig.1 because this trajectory is described by force curve (Fig.2). In “MD mode” the basic information comes from the signal of the cantilever deviation along the normal to the scanning plane [10]. Recording the signal in the delivering of the probe to the surface and back to “no interaction” position gives a force curve –  $S(Z)$ , i.e. the magnitude of cantilever’s bending,  $S$ , as a function of the coordinate of the surface position,  $Z$ , that is always treated as known (Fig.2, (b)). Along with physical and chemical properties of the surface, the shape and parameters of the measured force curve are largely dependent of elastic properties of the cantilever (Fig.2, (a)), and geometric properties (size and shape) of the tip of the probe. Therefore, knowing the parameters of the last two, one can obtain not only complex topography but also adhesion force, thickness of adsorbed layer, and other important parameters of the surface [11, 12].

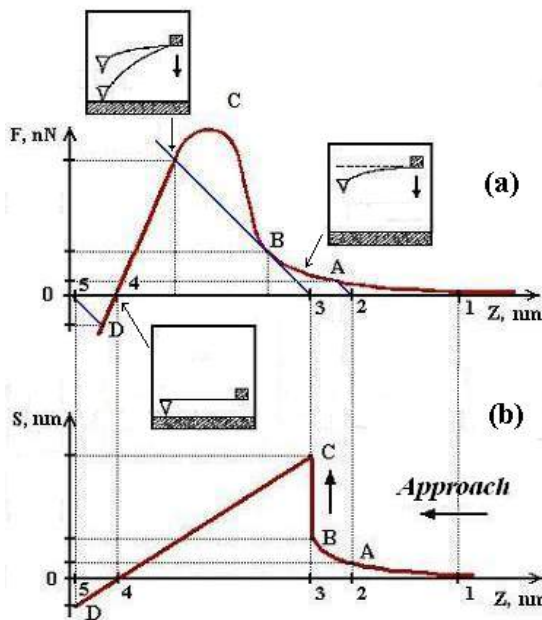


Fig. 2. The process of probe approach to the surface: dependence of Van-der-Waals interactions on the distance up  $F_s(Z)$  surface (a); force curve  $S(Z)$ , there has been shown cantilever positions with the probe on the coordinate of surface position (b).

By measuring the parameters of the  $S(Z)$  function, say, in an  $N \times N$  square of point on the surface under study, we can reconstruct the relief  $S_{tph}$ , a map of adsorbed layer distribution over the surface  $S_{adl}$ , a map of adhesion forces distribution over the surface  $S_{adf}$ , a map of the surface with the constant repulsion force  $F_{rpf}$  and a map of the surface with the constant force gradient  $F_{cfg}$ . If any other measurement "X" is made on the  $N \times N$  points, this would give an additional map of the surface  $S_x$  by the parameter "X". The property measured can be either the conductivity in the point "C" or the surface hardness as the slope of the function  $S(Z)$  in the region of repulsion ( $Z < 0$ ). The advantage of this regime is that it does not involve "dragging" of the tip along the surface. This "MD mode" regime also helps overcome the problem of the optical scheme drift because the "zero" of the optical system can be determined each time the tip is beyond the region of the surface force action. A disadvantage of this regime is a relatively long time of information acquisition which varies from 10 to 30 min for a  $128 \times 128$  frame. In addition, the regime of "MD mode" does not allow working with blunt ( $R > 20$  nm) tips.

### 3. Results and discussion

Below we present experimental results demonstrating the potentialities of the "MD mode" regime and the possibility to use AFM with "MD mode" for the measurement of number properties of the surface.

Fig. 3(a) shows the surface of an aluminium-oxide-based catalyst. The surface is characterized by a strongly developed relief, the difference in  $Z$  between the lowest and highest point positions corresponds to 30.5 nm. Fig. 3(b) displays the map of adhesion forces taken simultaneously with the relief. It is that the adhesion force radically varies within the frame

area. Apparently, the last fact is most likely to be a result of the influence of the capillary forces which are caused by the presence of the adsorbed layer on a porous surface of ceramic catalyst to give, in addition to adhesion forces, above strong variation ( $\Delta Z = 1.9$  nN) in adhesion force map.

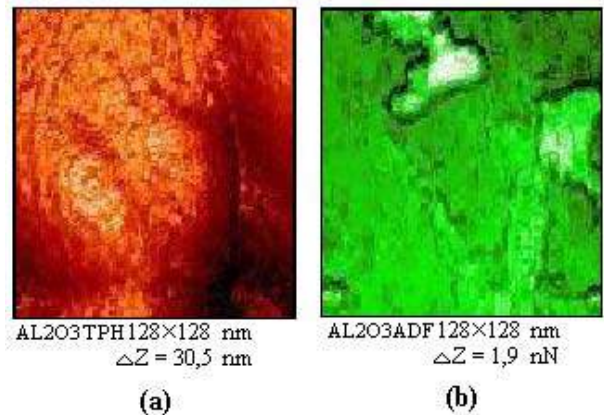


Fig. 3. Topographic image of a surface fragment of AL oxide-base ceramic catalyst  $S_{tph}$  (a); map of adhesion forces distribution over the  $AL_2O_3$  surface  $S_{adf}$  (b).

The potentialities of the "MD mode" regime in working with soft samples were tested on the surface of a  $2 \times 10^6$  nm mercury ball. Fig. 4(a) displays a picture of the mercury surface  $1000 \times 1000$  nm in size taken when the tip was

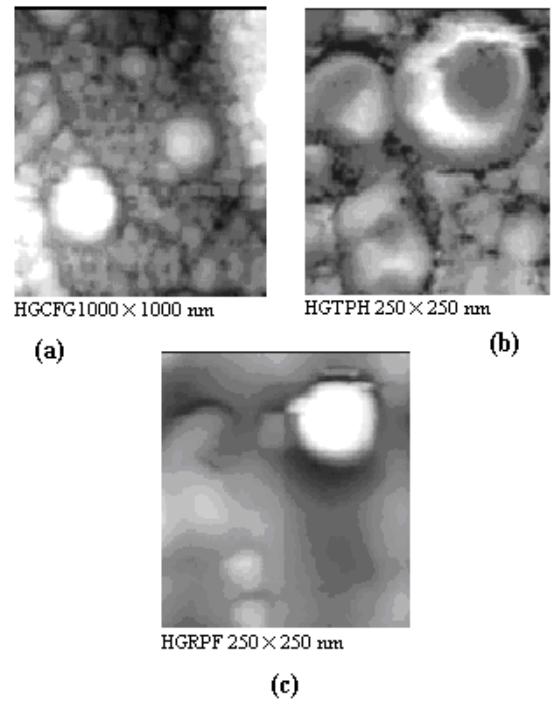


Fig. 4. Map of the surface with the constant force gradient  $F_{cfg}$  (a); topographic image of a surface of mercury droplet  $S_{tph}$  (b); map of the surface with the constant repulsion force  $F_{rpf}$  (c).

not in contact with the surface, that is, it was removed immediately after its jump towards the surface. Based on these results, we reconstructed the surface with the constant force gradient  $F_{cfg}$  ( $dF/dz = 4$  N/m). The data in Fig. 4(b) and Fig. 4(c) were obtained upon the repeated scanning of the lower left quadrant of the above surface. However, in this

case the tip was brought into contact with the surface with the repulsion force  $F_{\text{rpf}} \approx 10^{-9} \text{ N}$ . The relief of the surface  $S_{\text{tph}}$  is displayed in Fig. 4(b) and the map of the constant repulsion force  $F_{\text{rpf}}$  is displayed in Fig. 4(c). If these two pictures are superimposed, we obtain an exact copy of the lower left quadrant of the Fig. 4(a). This example demonstrates how radically the surface image obtained by the steady level of repulsion forces can differ from that obtained by the constant gradient.

Thus, “MD mode” regime of AFM is integrating in itself both the non-destructiveness of “tapping mode” and “non-

contact mode” and high resolution of “contact mode”. As shown in this work, “MD mode” regime, which allows simultaneous registration of a number of surface parameters, can be reliable applied to study surfaces with various physical-chemical characteristics.

The author acknowledges for possibility of work at the AFM provided by the probe microscopy laboratory collaborators of the Technology research and development Institute, Moscow, and Dr. S. Molchanov for valuable discussions.

- 
- [1] V. Bykov, V. Dremov, V. Losev, S. Saunin. Proceedings of all-Russian conference “Probe microscopy”, Nizhny Novgorod, 2000, 28 February-2 March, p. 298-302.
  - [2] G. Binning, H. Rohrer. Helv. Phys. Acta, 1982, v. 55, p. 726-731.
  - [3] P. Grutter, W. Zimmermann-Edling, D. Brodbeck. Appl. Phys. Lett., 1992, v. 60, p. 2741-2745.
  - [4] G.S. Batog, A.S. Baturin, V.S. Bormashov, E.P. She-shin. JTF, 2006, t. 76, v. 8, s. 123-128. (in Russian)
  - [5] S.A. Vinogradova, A.O. Golubok, N.A. Tarasov. Nauchnoye priborostroeniye, 1991, v. 1, p. 3-9.
  - [6] S.P. Molchanov, V.V. Dremov, A.P. Kirpichnikov. Patent № 2145055, 2000, Russia Federation.
  - [7] S.P. Molchanov, I.A. Chernova-Kharaeva, S.H. Abdullayeva, S.D. Alekperov. Proceedings of First International Scientific Seminar “Light in Nanosize Solids”, Baku, 2004, September 22 -28, p. 47-48.
  - [8] S.H. Abdullayeva, S.P. Molchanov, N.T. Mamedov, S.D. Alekperov. Physica Status Solidi (c), 2006, v. 3, n. 8, p. 2853-2857.
  - [9] S.P. Molchanov, I.A. Chernova-Kharaeva, S.H. Abdullayeva, S.D. Alekperov. Physica ANAS, 2005, v. XI, n.1-2, p. 56-58.
  - [10] S.P. Molchanov, I.A. Chernova-Kharaeva, S.H. Abdullayeva, S.D. Alekperov. Proceedings of First International Scientific Seminar “Light in Nanosize Solids”, Baku, 2004, September 22-28, p. 72-74.
  - [11] S.D. Alekperov. Transactions ANAS, 2007, v. XXVII, no. 2, p. 21-27.
  - [12] A.N. Petrukhin, A.A. Astafyev, P.N. Zolotavin. Khimicheskaya fizika, 2006, t. 25, № 9, s. 16-25. (in Russian)

#### S.C. Ələkbərov

#### ATOM-QÜVVƏ MİKROSKOPİYASI ƏSASINDA SƏTHİ TƏDQİQ ETMƏK ÜÇÜN ALTERNATİV ÜSUL

Atom-qüvvə mikroskopiyası üsuluna əsaslanan yeni “MD mode” tədqiqat rejimi işlənilmişdir. “MD mode” rejimi böyük dəyişkən yüksəkliyi və mürəkkəb relyefi olan qeyri-keçirici səthləri tədqiq etməyə imkan verir. Bu rejim, skaner prosesi əsnasında, zond ilə nümunə arasında yaranan bilən idarəolunmaz qarşılıqlı təsiri və artefaktları istisna edir. Atom-qüvvə mikroskopu vasitəsilə səthin bir sıra xüsusiyyətlərinin ölçülməsində “MD mode” rejimindən istifadənin imkanları experimental nəticələrdə nümayiş etdirilmişdir.

С.Д. Алекперов

#### АЛЬТЕРНАТИВНЫЙ ПОДХОД ПРИ ИССЛЕДОВАНИИ ПОВЕРХНОСТИ С ПОМОЩЬЮ АТОМНО-СИЛОВОГО МИКРОСКОПА

Разработан новый режим исследования поверхности “MD mode”, основанный на методе атомно-силовой микроскопии. Режим “MD mode” позволяет исследовать любые непроводящие поверхности со сложным рельефом и большими перепадами высот. При этом исключается неконтролируемое взаимодействие зонда с образцом и артефакты, вызываемые процессом сканирования. Приведены экспериментальные результаты, демонстрирующие возможность использования атомно-силового микроскопа с режимом “MD mode” для измерения ряда характеристик поверхности.

Received: 16.03.08

## NONLINEAR ABSORPTION AND SUSCEPTIBILITY OF THE FIFTH ORDER IN InSb AT THE WAVELENGTH OF 10.6 $\mu$ m

M.A. MUSAYEV

*The Azerbaijan State Oil Academy,  
Azadlıq ave. ,20, AZ-1010, Baku, Azerbaijan*

It is shown, that nonlinear absorption of laser radiation at the wavelength of 10.6  $\mu$ m in band-gap semiconductor InSb is caused by two-photon absorption and the constant of nonlinear absorption is measured in samples n-type with a different degree alloying. It is established, that the basic mechanism of nonlinearity responsible for reflection at degenerate four-wave mixing is caused by free electron generation at two-photon absorption. Growth of efficiency at four-wave mixing in band-gap semiconductors is limited to nonlinear absorption of interacting waves.

One of the major problems of applied nonlinear optics is search of materials with possible great values of nonlinear susceptibilities. In this respect semiconductors as have shown experiments, are one of the most perspective media [1]. Big nonlinearity of the last leaves that fact what exactly semiconductors with their rather small band gap  $E_g$  are characterized by low enough internal fields  $E_0 = \frac{mE_g^3}{e^2\hbar^2}$  determining bond forces of optical electron. Therefore, at all too high laser fields already should provide the big contribution to a susceptibility of electronic nonlinear polarization.

Studying of nonlinear susceptibilities is- the central question of nonlinear spectroscopy. The effects caused by a nonlinear susceptibility, underlie such methods of nonlinear spectroscopy as two-photon spectroscopy, spectroscopy of saturation, and also allow, will solve such important practical problem - as correction of phase distortions by a method of four-wave mixing [2,3].

For reception of high efficiency of reflection of radiation on length of a wave of the CO<sub>2</sub>-laser at four-wave mixing significant interest, represent band-gap semiconductors [2].

In the given work at temperature  $T=300$  K samples InSb of n-type with concentration donor impurity of  $\sim 10^{14}\text{-}10^{16}\text{cm}^{-3}$ , thickness  $\ell=0.5$  mm were investigated.

For all scopes of semiconductors, it is important to know a limit of their serviceability on intensity of laser radiation. A surface breakdown threshold of a material usually imposes this limit. Measurement of a threshold of breakdown on a surface of all samples investigated in our work has shown that this size lies in a range  $3\text{-}4\cdot10^7\text{Vt/cm}^2$ . As show measurements transmission of samples InSb, as against wide-gap semiconductors (for example, Ge) still at intensities of radiations are lower than a threshold of breakdown on a surface in them appreciable reduction transmission is observed (fig. 1).

This reduction transmission is convertible, is shown at intensity of radiation  $I \gtrsim 10^5\text{Vt/cm}^2$ , and caused by processes of nonlinear absorption of radiation in researched semiconductors. The compared sizes of quantum of radiation of the CO<sub>2</sub>-laser ( $\hbar\omega \approx 0.117$  eV) with InSb band gap ( $\sim 0.17$  eV at room temperature) allows to assume, that nonlinear absorption in them is caused by two-photon process. For definition from the data on transmission constants of absorption, we consider a problem about dependence transmission from intensity in view of linear and nonlinear absorption. In a stationary case change of intensity

at passage of light to semiconductors at presence of effects of two-photon absorption can be written down as follows

$$-dI = \alpha I(x)dx + \beta I^2(x)dx + \gamma I^3(x)dx \quad (1)$$

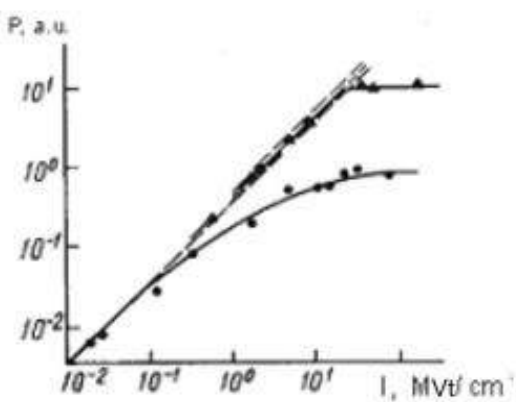


Fig. 1. Dependence of the past pulse power from intensity of a falling pulse. (Ge - triangles, InSb - dark points.)

Here  $\alpha$  is the linear optical absorption coefficient,  $\beta$  is the two-photon absorption coefficient,  $\gamma$  is the coefficient of absorption free hole, arising as a result of two-photon absorption.  $\gamma$  it is connected to the  $\beta$  following parity

$$\frac{\gamma}{\beta} = \frac{q\tau}{2\hbar\omega}, \quad (2)$$

where  $q$  is section of absorption free hole,  $\tau$  is time of a life of nonequilibrium carriers. In compounds of type A<sup>III</sup>B<sup>IV</sup> the section of absorption free hole appears so big [4] that already at moderate intensities laser radiation by the second member in the right part (1) it is possible to neglect. In this case, expression for transmission in view of two-photon absorption depending on intensity of falling radiation  $I_0$  becomes

$$T^{(2)} = (1 - r) \sqrt{\frac{\alpha e^{-2\alpha\ell}}{\alpha + \gamma I_0^2 (1 - e^{-2\alpha\ell})}}, \quad (3)$$

where  $r$  is coefficient of Fresnel reflection from a sample surface,  $\ell$  is sample length.

Comparison of results of experimental researches (fig. 2) with the data of calculation by formula (3) allows defining

sizes  $\gamma$  directly. In view of disorder of experimental data for InSb it is received  $\gamma = 500 \pm 200 \frac{\text{cm}^3}{\text{MVt}^2}$  also this value is constant for all samples.

The process of phase conjugation via four-wave mixing involves the incidence of three input waves ( $E_1, E_2, E_3$ ) onto a medium, with the nonlinear generation of an output field ( $E_4$ ) whose amplitude is proportional to the complex conjugate of one of the input fields (fig.3). The mechanism of occurrence of the inverted wave in such circuit most simply to explain, proceeding from holographic interpretation of optical phase conjugation [5]. Let on the nonlinear medium the any wave  $E_3(r)$  that is required to be turned and a pump wave  $E_1(r)$  from a constant on cross-section section amplitude falls. If waves  $E_1(r)$  and  $E_3(r)$  are coherent then they write down in nonlinear medium interference disturbance of dielectric permeability (hologram). If this hologram to illuminate from the opposite side with a pump wave  $E_2(r)$ , is exact a passer in relation to a pump wave  $E_1(r)$ , such, that  $E_2(r) = E_1^*(r)$  the hologram will restore the inverted wave

$$E_4(r) = \text{const} \cdot E_1(r) E_2(r) E_3^*(r) = \text{const} |E_1|^2 E_3^*(r) \quad (4)$$

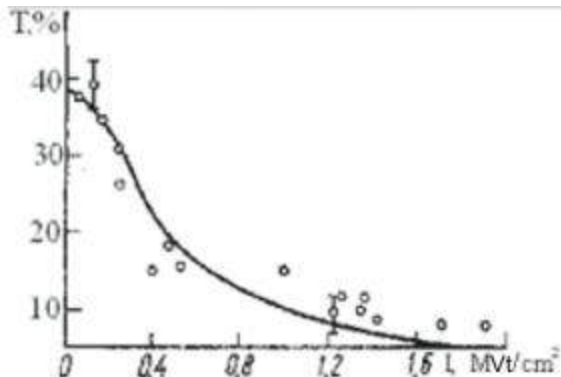


Fig. 2. Dependence transmission  $T$  from intensity falling radiations in InSb.

In the volumetric nonlinear medium record interference pictures waves  $E_2(r)$  and  $E_3(r)$  and reading by its wave  $E_1(r)$  from restoration of the same wave  $E_4(r)$  is possible. In the traditional experimental geometry, the second pump wave is created by reflection of the first by a flat mirror back.

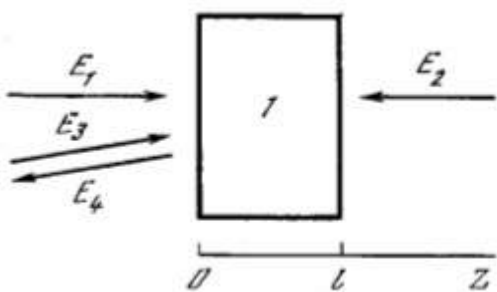


Fig. 3. Backward-going nonlinear optical phase conjugation via degenerated four-wave mixing

The measured dependence of efficiency of reflection at four-wave mixing from intensity of first pump wave  $R(I_l)$  is resulted on fig.4. Data processing in the field of  $I_l \approx 10 - 20 \text{ kVt/cm}^2$  on a method of the least squares has shown, that in logarithmic scale they are described by a straight line with an

inclination corresponding to dependence  $R \sim I_l^4$  with factor of correlation 0,85. At  $I_l > 20 \text{ kVt/cm}^2$  dependence  $R(I_l)$  starts to deviate already essentially dependence of kind  $R \sim I_l^4$  (dotted line). Such behavior of an experimental curve at degenerate four-wave mixing in InSb on 10,6  $\mu\text{m}$  at coherent probe and pump waves specifies that the effective nonlinear susceptibility responsible for phase conjugation, is caused by generation free electrons. As this process goes by two-photon absorption it is possible to draw a conclusion that in observable the dominating contribution is brought with a nonlinear susceptibility of the fifth order  $\chi^{(5)}$ . The continuous curve on fig.4 puts dependence  $R(I_l)$  in view of nonlinear absorption under the formula [6]

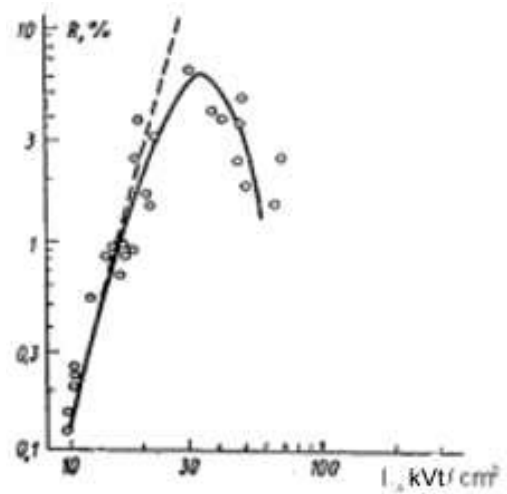


Fig. 4. Dependence of efficiency of reflection at four-wave mixing from intensity

$$R = \left[ (1-r)^3 \frac{2\pi\omega}{cn} \chi^{(5)} E_l^4 \frac{e^{-\alpha_n l} (1-e^{-\alpha_n l})}{\alpha_n} \right]^2, \quad (5)$$

where  $\alpha_n = \alpha + \gamma_3 I_{\sum}^2$ ,  $I_{\sum} = \sum_{i=1}^4 a_i |E_i|^2$ ;  $\omega$  is frequency of laser radiation;  $c$  is speed of light in vacuum;  $n = 3.95$  - a linear refractive index;  $\alpha = 5 \text{ cm}^{-1}$  and  $\gamma = 500 \pm 200 \frac{\text{cm}^3}{\text{MVt}^2}$  are coefficients of linear and nonlinear absorption in InSb;  $r$  is coefficient of Fresnel reflection from a surface of a sample;  $a_i$  are the factors which are taking into account the contribution of each interacting waves in nonlinear absorption.

In area intensities  $I_l$  from 10 up to 30 - 40  $\text{kVt/cm}^2$ , i.e. down to a maximum of dependence  $R(I_l)$ , the settlement curve well describes results of experiment. Substituting experimentally measured  $R$  and  $I_l$  at  $I_l < 40 \text{ kVt/cm}^2$  in the formula (5), we get a nonlinear susceptibility of the fifth order in InSb:  $\chi^{(5)} \approx 8 \cdot 10^{-8} \text{ esu}$ .

Proceeding from the assumption, that at  $I_l \leq 40 \text{ kVt/cm}^2$  the basic mechanism of the nonlinearity responsible for phase conjugation via four-wave mixing is caused by generation free electrons we shall estimate  $\chi^{(5)}$ . It is known [4], that at generation free electrons in semiconductors the nonlinear additive to dielectric permeability

$$\Delta\epsilon = -\frac{\omega_p^2}{\omega^2} = -\frac{4\pi^2 Ne^2}{m_{eh}^* \hbar \omega^2}, \quad (6)$$

Substituting (8) in (6) and defining connection  $\Delta\epsilon$  with  $\chi^{(5)}$  as  $\Delta\epsilon = 4\pi\chi^{(5)} \sum E_i E_j E_k E_\ell$  we get

$$\chi^{(5)} = -\frac{\eta\beta n^2 c^2 e^2 \tau}{64\pi^2 m_{eh}^* \hbar \omega^3} \quad (9)$$

where  $e$  is a charge of electron,  $N$  is concentration nonequilibrium free electrons in a zone of conductivity,  $m_{eh}^*$  - the reduced mass of electron-hole pair. Generally  $N$  it is defined by speeds of generation electron-hole pair (in our case as a result of two-quantum absorption), them recombination and diffusion:

$$\frac{\partial N}{\partial t} = \frac{\eta\beta I^2}{\hbar\omega} - \frac{N}{\tau} + D_a \frac{\partial^2 N}{\partial x^2}, \quad (7)$$

where  $\eta$  is quantum efficiency of generation electron-hole pair,  $\beta$  is the two-photon absorption coefficient,  $\tau$  is time of life electron-hole pair,  $D_a$  is coefficient of ambipolar diffusions. As in InSb at the contribution in  $R$  is given only with the rare lattice which is written down by passing waves, diffusion member in (7) can be neglected. Taking into account also, that in InSb at  $T=300$  K  $\approx 10^{-8}$  sec with [7], and duration of a laser pulse exceeds  $\sim 10^{-7}$  sec with, we get

$$N = \frac{\eta\beta I^2 \tau}{\hbar\omega} \quad (8)$$

Substituting in (9) known parameters InSb ( $\eta=0.5$ ,  $n=3.95$ ,  $m_{eh}^* \approx 0.012$  m,  $\beta \approx 5.5$  cm/MVt [6],  $\tau \approx 10^{-8}$  sec), we get  $\chi^{(5)} = 5 \cdot 10^{-8}$  esu, that will not bad be coordinated to experimentally measured value.

From results of researches of temperature dependence  $\tau$  in InSb [3,6] follows, that reduction  $T$  from  $\sim 300$  K up to 200 K in samples with concentration of impurity less allows to increase  $\tau$  than  $10^{15}$  cm $^{-3}$  up to  $(0.5-1) \cdot 10^{-6}$  sec with. Accordingly, taking into account, as  $\chi^{(5)} \sim \tau$  lowering temperature of a sample, it is possible to increase  $\chi^{(5)}$  on 1, 5 - 2 order.

Thus, direct experiments confirm, that the basic contribution to four-wave mixing in InSb on 10,6 μm is given with a nonlinear susceptibility of the fifth order, and  $\chi^{(5)}$  in InSb can be considerably increased.

- 
- [1] R.W. Boyd. Journal of modern optics, 1999, vol.46, №3, 367-378.  
 [2] V.I. Kovalev. Dispersive characteristics of a nonlinear response used for wave conjugation. Bulletin of the Russian Academy of Sciences. Physics. 1996, vol. 60, № 6, pp.908-920.  
 [3] A.V. Husakou., J. Herrmann. J.Opt.Soc.Am. B, 2002, v.19, №9, p.2171-2182.  
 [4] O. Madelung. The physics of semiconductor compounds of elements III and V groups. Moscow, Mir, 1967, p. 3-478 (in Russian).  
 [5] A. Yariv, D.M. Pepper Amplified reflection, phase conjugation, and oscillation in degenerate four-wave mixing. Opt. Lett., 1977, vol. 1, №1, p.16-18.  
 [6] N.G. Basov, V.I. Kovalev, M.A. Musaev, F.S. Faizullov. Nonlinear optical phase conjugation of radiation of a pulse CO<sub>2</sub>-laser.-Proceedings Lebedev Physical Institute, 1986, vol.172, p.116. (in Russian).  
 [7] Optical properties of semiconductors (semiconductor structure such as A<sup>III</sup>B<sup>V</sup>). Under edition. R. Uillardson and A.Bir Moscow, Mir, 1970, p. 3-488. (in Russian).

**M.A. Musayev**

## **InSb – DƏ İNFAQIRMIZI 10,6 μm DALĞA UZUNLUQ OBLASTINDA QEYRİ-XƏTTİ UDULMA VƏ BEŞİNCİ TƏRTİB QAVRAYICILIQ**

Dar qadağan zonalı yarımkərıcı InSb-da 10,6mkm dalğa uzunluğunda qeyri-xətti optik udulmanın ikifotonlu udulma nəticəsində baş verdiyi göstərilmiş və müxtəlif dərəcəli leqirə olunmuş n – tip nümunələrdə qeyri-xətti optik udulma sabiti ölçülmüşdür. Dörrdalğalı qarşılıqlı təsir prosesində qayıtmanın baş verməsinə səbəb olan əsas mexanizm ikifotonlu udulmada sərbəst elektronların generasiyasıdır. Bu prosesin effektivliyini məhdudlaşdırın əsas səbəb qeyri-xətti udulmadır.

**M.A. Musaev**

## **НЕЛИНЕЙНОЕ ПОГЛОЩЕНИЕ И ВОСПРИИМЧИВОСТЬ ПЯТОГО ПОРЯДКА В InSb В ИНФРАКРАСНОЙ ОБЛАСТИ ПРИ ДЛИНЕ ВОЛН 10,6μм**

Показано, что нелинейное поглощение на длине волны 10,6мкм в узкозонном полупроводнике InSb обусловлено двухфотонным поглощением и измерена константа нелинейного поглощения в образцах n-типа с разной степенью легирования. Установлено, что основной механизм нелинейности, ответственный за отражение при вырожденном четырехвольновом взаимодействии обусловлен генерацией свободных электронов при двухфотонном поглощении. Рост эффективности при четырехвольновом взаимодействии в узкозонных полупроводниках ограничивается нелинейным поглощением взаимодействующих волн.

Received: 10.04.08

## **$K_{1-x}Ag_xNO_3$ ( $x=0,025; 0,05; 0,1$ ) MONOKRİSTALLARINDA POLİMORF ÇEVİRİLMƏLƏR**

**E.V. NƏSİROV ,Y.Q. ƏSƏDOV**

*Azərbaycan MEA H.M. Abdullayev adına Fizika Institutu,  
AZ 1143, Bakı şəhəri, H.Cavid pr.33*

Təqdim olunan iş  $K_{1-x}Ag_xNO_3$  ( $x=0,025; 0,05; 0,1$ ) monokristallarında II $\leftrightarrow$ III polimorf çevrilmələri zamanı II və III-modifikasiya kristallarının böyümə morfologiyasının tədqiqinə həsr olunmuşdur. Modifikasiyalar arasında tarazlıq temperaturunu müəyyən edərək göstərilmişdir ki, baxılan halda polimorf çevrilmərdə kristal böyüməsi ana kristal daxilində yeni fazanın rüseyminin yaranması ilə baş verir.

Məlumdur ki,  $T>401K$  temperaturunda kalium nitratda  $D_{2h}^{15}$ -Pnma simmetriyalı rombik modifikasiya [1]  $D_{2d}^6$ -P3c simmetriyalı romboedrik modifikasiyaya çevrilir [2] və bu dəyişmə enantiatrop tiplidir. Kristal soyudulan zaman iki monotrop çevrilmə müşahidə edilir [3].  $\sim 397K$  temperaturda III modifikasiya  $C_{3v}^5$ -P3M simmetriyalı yeni modifikasiyaya, yalnız bundan sonra  $\sim 383K$  temperaturda bu modifikasiya da II- modifikasiyaya çevrilir. Müəyyən edilmişdir ki, baxılan nümunələrdə kristal böyüməsi Q.Folmerin təklif etdiyi iki ölçülü rüseyimli mexanizmlə baş verir [4-6]. Həmin kristallarda ilk dəfə olaraq II $\rightarrow$ III çevrilməsi zamanı ritmik böyümə müşahidə edilmişdir [7]. Sonradan kalium nitratda quruluş çevrilmərinin tədqiqi istiqamətində aparılan tədqiqat işləri daha da genişləndirilmişdir. Belə ki,  $KNO_3$ -da  $K^{1+}$  atomlarının  $Ag^{+1}$  atomları ilə qismən əvəz olunmasının polimorf çevrilmənin mexanizminə təsiri araşdırılmağa başlanmışdır [8]. Təqdim olunan iş həmin tədqiqat işlərinin davamı olub  $K_{1-x}Ag_xNO_3$  kristallarda polimorf çevrilmələrin mexanizminin tədqiqinə həsr olunmuşdur.

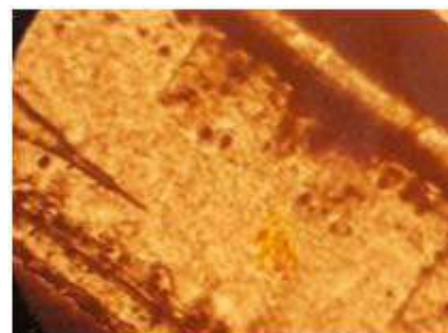
$K_{1-x}Ag_xNO_3$  ( $x=0,025: 0,05: 0,1$ ) birləşmələrinin suda məhlulundan otaq temperaturunda II modifikasiyanın mükəmməl üzlü, mikroskopik tədqiqat üçün yararlı olan təqribən  $1\times 0,5\times 10\text{ mm}$  ölçülü kristalları alınmışdır. Kristalların mükəmməlliyyini və təmizliyini təmin etmək məqsədilə istifadə olunan "XΥ" markalı gümüş nitrat və "UDA" markalı kalium nitrat çoxqat yenidən kristallaşma yolu ilə əlavə təmizləmişdir.

Alınmış müxtəlif xarici formalı kristallardan tədqiqat üçün müstəvi lövhə şəkilli və ya [001] kristalloqrafik istiqamətdə dərtlənmiş iynəvari kristallar seçilmişdir.

Əvvəlcə II və III fazanın tarazlıq temperaturu, ucları bilavasita nümunənin səthinə toxunan termocüt vasitəsilə  $+1^\circ C$  dəqiqliklə ölçülümiş və  $K_{0,975}Ag_{0,025}NO_3$ -ün II və III fazalarının tarazlıq temperaturu üçün  $T_0=383K$ ,  $K_{0,95}Ag_{0,05}NO_3$  üçün  $T_0=370K$ ,  $T_0=383K$ ,  $K_{0,90}Ag_{0,10}NO_3$  üçün isə  $T_0=368K$  alınmışdır.

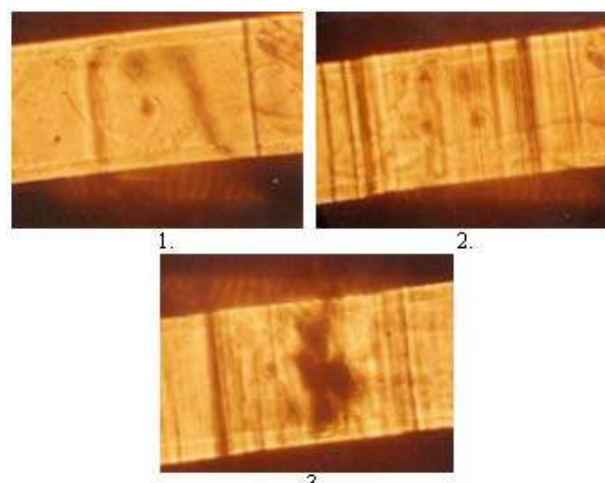
II və III fazaların tarazlıq temperaturu təyin edildikdən sonra II $\leftrightarrow$ III qarşılıqlı polimorf çevrilmə prosesində II və III modifikasiya kristallarının böyümə morfologiyası tədqiq edilmişdir.

1.  $K_{0,975}Ag_{0,025}NO_3$  kristalında II $\rightarrow$ III keçid həmişə  $T_K>T_0$  temperaturda baş verir. Burada  $T_K$ -çevrilmə temperaturu,  $T_0$ -tarazlıq temperaturudur.  $\Delta T=T_K-T_0$  temperaturlar fərqi, ədəbiyyatda [6] göstərildiyi kimi, ana kristalın keyfiyyətindən asılıdır və kalium nitrat üçün II $\leftrightarrow$ III qarşılıqlı çevrilmələri zamanı bu fərqli maksimal qiyməti  $\Delta T=5K$  olmuşdur. Bizim halda isə bu fərqli  $\Delta T=1K$  alınmışdır.



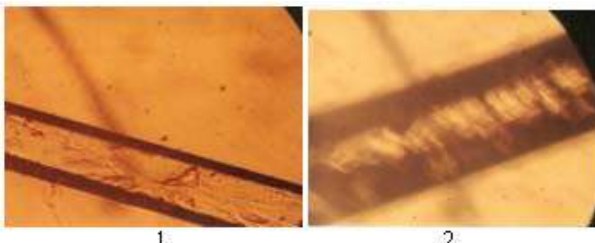
Şəkil 1. II kristal daxilində III modifikasiya kristalinin yaranması və böyüməsinin optik mikrofotoqrafiyası. Böyütmə  $90^\times$ .

III modifikasiyanın rüseyimi [100] kristalloqrafik istiqamətində çox tez böyür (Şəkil 1). Bu böyümə qurtardıqdan, yəni böyümə sərhəddi II modifikasiyanın digər üzünə çatdıqdan sonra, hər iki tərəfdən ana kristalin [001] istiqamətində böyüməsi davam edir. Bəzən yeni modifikasiyanın rüseyimi yalnız bir istiqamətdə böyür (Şəkil 2), lakin eks keçid hər iki tərəfdən baş verir. Bu hal, yeni modifikasiyanın rüseyimi iynəvari ana kristalin uclarından birində yaranarkən müşahidə edilir.



Şəkil 2.  $K_{0,975}Ag_{0,025}NO_3$ -da II $\rightarrow$ III polimorf çevrilmələri zamanı kristal böyüməsinin optik mikrofotoqrafiyası. Foto 1 II $\rightarrow$ III çevrilmə, foto 2 III modifikasiya, foto 3 III $\rightarrow$ II çevrilmə. Böyütmə  $90^\times$

Şəkil 2-dən göründüyü kimi, həm  $KNO_3$  həm də  $K_{0,975}Ag_{0,025}NO_3$ -da III $\rightarrow$ II keçidi ritmik xarakter daşıyır və III faza diskret lamellərlə böyür. Müəyyən III kristalin lamellərinin qalınlığı müxtəlif kristallarda müxtəlifdir.



Şəkil 3.  $K_{0.975}Ag_{0.025}NO_3$  kristallarında III -modifikasiyanın II→III çevrilmə zamanı ritmik böyüməsi. Foto 2 III-modifikasiya tam II→III çevrilmədən sonra. Böyütmə  $90^x$

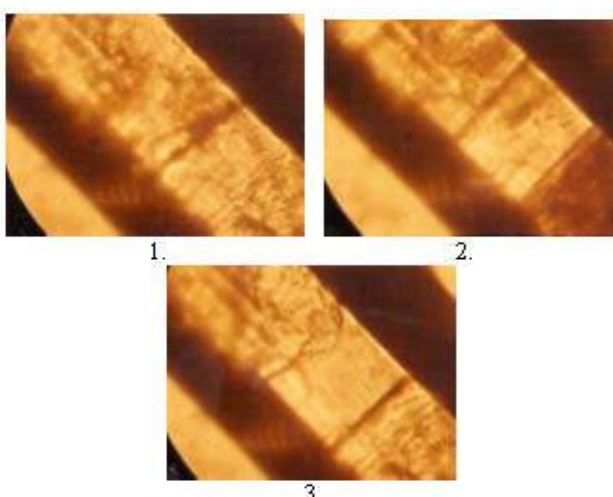
Şəkil 3-də  $K_{0.975}Ag_{0.025}NO_3$ -də tam II→III keçidindən sonra ölçüləri şəkil 2-dəkindən fərqli olan lamellər göstərilmişdir. Şəkil 3-də 1 və 2-ci şəkilləri müqayisə etdikdə, daxili gərginliklər hesabına ana kristalın genişləndiyi nəzərə çarpar.

$T_K=383K$  temperaturda III modifikasiya II modifikasiyaya çevrilir. II modifikasiyanın rüşeymləri, demək olar ki, çox tez yaranır və lamellər, nəzərə çarpmayan iz buraxaraq, yenidən II modifikasiyanın vahid monokristalına çevrilirlər.

Ədəbiyyatda [3] kalium nitratda II və III modifikasiyalar arasında 3-cü bir modifikasiyanın olduğu göstərilir. Bizim optik poliarizasiya mikroskopunda  $K_{0.975}Ag_{0.025}NO_3$  monokristallarında apardığımız tədqiqatlar zamanı II və III modifikasiyalar arasında I aralıq modifikasiya müşahidə edilməmişdir.

2.  $K_{0.95}Ag_{0.025}NO_3$  monokristalında II→III və III→II polimorf çevrilmə prosesləri öyrənilərkən müəyyən edilmişdir ki, bu keçidlər tarazlıq temperaturunda, yəni  $\Delta T \leq 1K$  temperaturda olduqca tez baş verir. Çox az hallarda kristalın mükəmməliyindən və keçidlərin sayından asılı olaraq  $\Delta T$  fərqi 2K-ə çatır.

$K_{0.95}Ag_{0.025}NO_3$ -də II↔III qarşılıqlı polimorf çevrilmələr adətən optik mikroskop altında görünən fazaların ayrılma sərhəddinin irəliləməsi şəklində olur. Bu çevrilmələr üzərində aparılan çoxsaylı müşahidələr göstərmışdır ki, II↔III keçidləri rüşeymin ana kristalda yaranması və onun fazaların düz-xətti ayrılma sərhəddi şəklində böyüməsi kimi baş verir. Bu rüşeymlər əsasən ana kristalın optik mikroskop altında görünən defektli yerlərində yaranırlar.

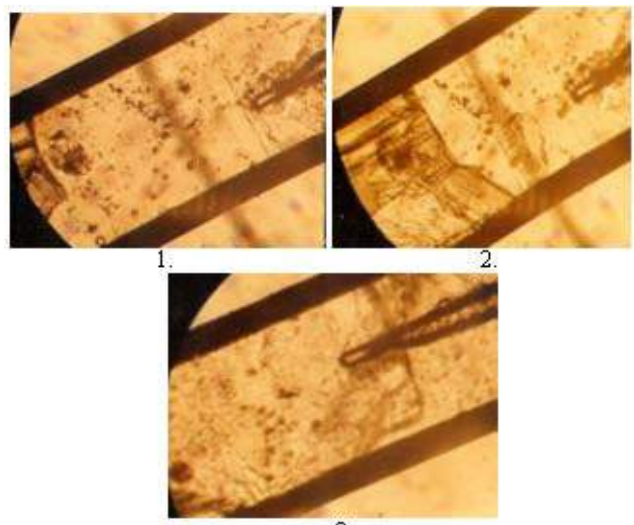


Şəkil 4.  $K_{0.95}Ag_{0.025}NO_3$  kristallarında II↔III çevrilməni əks etdirən optik mikrofotoqrafiyası foto 1, II↔III çevrilmə; foto 2, II→III çevrilmədən sonra III modifikasiya; foto 3, II→III çevrilmə. Böyütmə  $90^x$

Şəkil 4-də II↔III çevrilmə prosesi göstərmişdir. Şəkildən göründüyü kimi, II→III və III→II keçidlərinin vahid düz-xətti ayrılma sərhəddi var. Əks III→II keçidi də yubanmadan baş verir və bu kecid üçün  $\Delta T$  təxminən ~1K olur.

Aparılan təcrübələr göstərir ki, baxılan kristalda II və III modifikasiyalar arasındaki I aralıq modifikasiya yoxdur və II→III keçidi zamanı III modifikasiyanın ritmik böyüməsi müşahidə olunmur.

3. $K_{0.90}Ag_{0.1}NO_3$  monokristalında polimorf çevrilmə prosesləri öyrənilərkən müəyyən edilmişdir ki, bu kristallarda  $T_K>368K$  temperaturda II→III keçidi baş verir, yəni rombik modifikasiya romboedrik modifikasiyaya çevrilir. Yubanma temperaturu təqribən ~1K-dir.



Şəkil 5.  $K_{0.90}Ag_{0.1}NO_3$  kristallarında II→III çevrilməsinin optik mikrofotoqrafiyası, foto 1. II→III çevrilməsi, foto 2. III modifikasiya kristali, foto 3. III→II çevrilməsi. Böyütmə  $90^x$

Şəkil 5-də II→III çevrilmələri zamanı II və III modifikasiya kristallarının böyümə prosesi göstərilmişdir. III modifikasiyanın 1-ci rüşeymi ana kristalın sağ tərəfinin yuxarı küçündə yaranır. Şəkildə o, oxla göstərilmişdir. Fazaların ayrılma sərhəddi düz-xətti şəklini aldıqdan sonra ana kristalın sol tərəfində III modifikasiyanın qövsşəkilli 2-ci rüşeymi yaranır (şəkil 5, foto 1). Az müddətdən sonra bu rüşeym böyür və fazaların ayrılma sərhəddi sol tərəfdə düz-xətti şəklini alır. Sol tərəfdə fazaların ayrılma sərhəddi mikroskop altında aydın görünür, sağ tərəfdə isə yox. Nəhayət hər iki sərhədd təmasda olur. Görünür, nəticədə optik oxları müxtəlif istiqamətləri olan eyni strukturlu iki kristal alınmışdır. Müşahidə poliarizə olunmuş işıqda aparıldığından təmas sərhəddinin müxtəlif tərəflərində rənglərin müxtəlif olması bu nəticəyə gəlməyə imkan verir.

$T_K<368K$  temperaturda əks proses gedir və III→II çevrilməsinin vahid sərhəddi olur. III→II keçidi tam başa çatdıqdan sonra kristal öz əvvəlki rəngini alır, yəni vahid kristal alınır. Bu kristallarda da, əvvəlki iki kristalda olduğu kimi, II və III modifikasiya arasında I aralıq modifikasiya yoxdur, həmçinin  $K_{0.90}Ag_{0.1}NO_3$  monokristalında II→III kecid zamanı III modifikasiya kristallarının böyüməsinin ritmik xarakteri müşahidə edilməmişdir.

E.V. NƏSIROV, Y.Q. ƏSƏDOV

- [1] D.A.Edward. Z.Kristalloqr.,80,154,1931.
- [2] P.E. Tahvonen. Ann.Acad.Fennicae.Ser.A44,1947.
- [3] P.W. Bridjman. Prog.Amer.Acad.54,579,1916.
- [4] M.Volmer. Kinetik der phasen.Dresden und Leupziq,3,38,1939.
- [5] B.I. Насиров, Ю.Г. Асадов. Докл.Ан.Азерб, LVIII №1-2, 2002.
- [6] Ю.Г.Асадов, В.И.Насиров. Кристаллография, вып.6, т. 15,1204,1970.
- [7] Ю.Г.Асадов, В.И.Насиров. Докл.АН.Азерб,191 №4, 1970.
- [8] В.И.Насиров, Ф.Г.Магеррамова, Ю.Г.Асадов, Е.В.Насиров. Материалы Нац. Конф.по росту кристаллов( НКРК ) Москва, Стр 22,2006.

**E.V. Nasirov, Yu.G. Asadov**

**POLIMORPHIC TRANSFORMATION IN  $K_{1-x}Ag_xNO_3$  ( $x=0,025; 0,05; 0,1$ )  
SINGLE CRYSTALS**

Crystal growth morphology at II↔III polymorphic transformation was studied in  $K_{1-x}Ag_xNO_3$  by the optikal mikroskopy method. The equilibrium temperature for II and III phases are obtained. It is established that crystal growth at polymorphic transformation takes place at the formation and growth of the daughter modification nucleous of crystal in matrix crystal.

**Э.В. Насиров, Ю.Г. Асадов**

**ПОЛИМОРФНОЕ ПРЕВРАЩЕНИЕ В МОНОКРИСТАЛЛАХ  
 $K_{1-x}Ag_xNO_3$  (  $x=0,025; 0,05; 0,1$  )**

Методом оптической микроскопии была исследована морфология роста кристаллов при полиморфных превращениях II↔III в  $K_{1-x}Ag_xNO_3$ ( $x=0,025; 0,05; 0,1$ ). Определены температуры равновесия между модификациями. И установлено, что в данном случае рост кристаллов при полиморфном превращении происходит с образованием и ростом зародышей дочерней модификации в матричном кристалле.

*Received: 12.03.08*

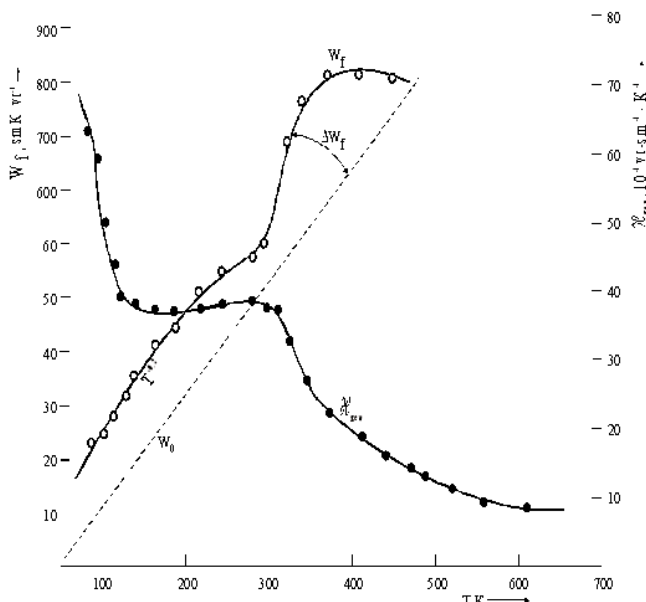
**(Fe<sub>3</sub>Sb<sub>2</sub>)<sub>0,98</sub>(Pb<sub>82,5</sub>Sb<sub>17,5</sub>)<sub>0,02</sub> KRİSTALINDA İSTİLİK KEÇİRİCİLİYİNİN XÜSUSİYYƏTLƏRİ**

**Ç.I. ƏBİLOV, M.F. AĞAYEVA**

*Azərbaycan Texniki Universiteti,  
Az-1073, Bakı, H. Cavid pr., 25*

Istiqamətləndirilən kristallaşdırma texnologiyası ilə (Fe<sub>3</sub>Sb<sub>2</sub>)<sub>0,98</sub>(Pb<sub>82,5</sub>Sb<sub>17,5</sub>)<sub>0,02</sub> tərkibli bərk məhlulun monokristalları yetişdirilərək, onlarda istilik keçiriciliyinin mexanizmi araşdırılmışdır. Göstərilmişdir ki, kristalda elektron və fonon səpilməsinin mürəkkəb təbiəti olmasının səbəbi, tərkibin çoxkomponentliliyi və kristallik quruluşdakı defektlərin mövcudluğudur. Kristalda elektron və fonon səpilməsinin elasti ki təbiəti olması aşkar edilmişdir.

Elektron cihazlarında və bəzi enerji çeviricilərində tətbiq ediləcək yeni tərkibli materialların axtarılması məqsədilə, tərəfimizdən Fe<sub>3</sub>Sb<sub>2</sub> - Pb<sub>82,5</sub>Sb<sub>17,5</sub> sistemi tədqiq edilmiş və Fe<sub>3</sub>Sb<sub>2</sub> əsasında bərk məhlul sahəsinin mövcudluğu aşkar edilmişdir [1]. Hazırkı məqalə (Fe<sub>3</sub>Sb<sub>2</sub>)<sub>0,98</sub>(Pb<sub>82,5</sub>Sb<sub>17,5</sub>)<sub>0,02</sub> tərkibli bərk məhlul monokristalinin istilik keçiriciliyinin və bəzi termomaqnit əmsallarının öyrənilməsinə həsr olunmuşdur. Göstərilən əmsalların ölçü metodikası [2]-də verilən üsullarla eynidir.

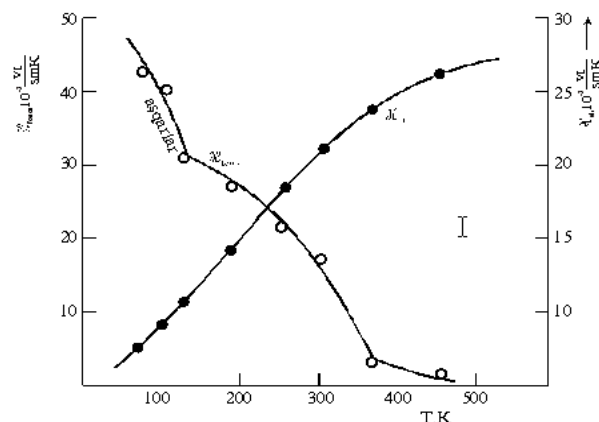


*Şəkil 1. (Fe<sub>3</sub>Sb<sub>2</sub>)<sub>0,98</sub>(Pb<sub>82,5</sub>Sb<sub>17,5</sub>)<sub>0,02</sub> kristalının ümumi istilik keçiriciliyinin  $\alpha_{iim}$  və fonon istilik müqavimətinin ( $W_f$ ) temperatur asılılığı.*

Kristalın elektrik xassələrinin tədqiqindən məlum olmuşdur ki, xüsusi elektrik keçiriciliyinin temperatur asılılığında yarımmetallik təbiətli geniş aşqar keçiriciliyi sahəsi vardır [3]. Təxminən 323 K-dən başlayaraq keçiriciliyin kəskin yüksəlməsi başlayır ki, bunun da səbəbi kristalda məxsusi keçiricilik sahəsinin başlanmasıdır. Bu sahədən hesablanan qadağan zolağının eninin qiyməti ~0,2 CV olmuşdur. Fe<sub>3</sub>Sb<sub>2</sub> əsasında aşkar edilən bərk məhlul kristallarının istilik xassələrinin tədqiqindən bir sıra maraqlı nəticələr əldə edilmişdir. Şəkil 1-də (Fe<sub>3</sub>Sb<sub>2</sub>)<sub>0,98</sub>(Pb<sub>82,5</sub>Sb<sub>17,5</sub>)<sub>0,02</sub> tərkibli kristalın ümumi istilik keçiriciliyi  $\alpha_{iim}$  və fonon istilik müqavimətinin ( $W_f$ ) temperatur asılıqları göstərilmişdir. Ümumi istilik keçiriciliyi bütün temperatur intervalında mənfi üstlü qanuna tabe ( $T^{0,2}$ ) olur ki, bu da kristalda istilik daşınmasının üçfononlu mexanizm üzrə baş verdiyini göstərir.

Fonon istilik müqavimətinin (Şəkil 1-də  $W_f$  əyrisi) temperatur asılılığından aşkar edilmişdir ki, ~320-350K-dən başlayaraq kristalda əlavə fonon istilik müqaviməti yaranır və nəticədə fonon səpilməsi, kristallik qəfəsəkəsi vakansiya tipli defektlərdən baş verir. Yaranan əlavə istilik müqavimətinin kəmiyyətcə qiymətini  $\Delta W_f = W_f - W_{iç,fonon}$  fərqi ilə dəyərləndirmək olar. Digər tərəfdən, yüksək temperaturlarda əlavə fonon istilik müqavimətinin yaranması, kristalda optiki-akustik mexanizminin də istiliyin daşınmasında rolü olduğunu göstərir. Əlavə fonon istilik müqavimətinin ~420K temperaturunda maksimuma çatması isə fonon səpilməsinə daxili elektromaqnit istilik mexanizminin təsirinin də olduğunu isitsna etmir. Videman-Frans qanunundan istifadə edərək, tədqiq olunan tərkibdə istilikkeçiriciliyinin elektronlara və fononlara görə olan payı hesablanmışdır. Şəkil 2-də (Fe<sub>3</sub>Sb<sub>2</sub>)<sub>0,98</sub>(Pb<sub>82,5</sub>Sb<sub>17,5</sub>)<sub>0,02</sub> tərkibli kristalın elektron və fononlara görə olan istilikkeçiriciliyinin temperatur asılıqları göstərilmişdir. Temperaturun yüksələməsi ilə elektronlara görə olan istilikkeçirmə artır, fonon istilik keçiriciliyi isə azalır.  $\alpha_{iim}$ -nin 80-200K intervalında azalmasının təbiəti fononların aşqar atomlarından, 250-400K intervalindəki azalması isə, kristallik quruluşun vakansiya tipli defektlərindən səpilməsinə uyğun gəlir.

Yükdaşıyıcılarının Holl yürüklüğünün temperatur [3] asılılığından məlum olmuşdur ki, yürüklüğün temperatur asılılığı  $T^{-0,9}$  qanunu üzrə dəyişir. Bu qanun, yükdaşıyıcılarının neytral aşqar atomlarından səpilməsini göstərir. Lakin asılılığın yüksək temperaturlardakı dəyişməsi, elektronların səpilməsinin akustik fononlardan baş verməsinin də olduğunu sübuta yetirir.



*Şəkil 2. (Fe<sub>3</sub>Sb<sub>2</sub>)<sub>0,98</sub>(Pb<sub>82,5</sub>Sb<sub>17,5</sub>)<sub>0,02</sub> tərkibli kristalda elektron və fonon istilikkeçiriciliyinin temperatur asılılığı.*

Məlumdur ki, kristalda elektron və fonon səpilməsinin elastiki və qeyri-elastiki təbiətli olmasını, uzununa termo-maqnit əmsalının ( $\varepsilon_y$ ) maqnit sahəsi gərginliyindən asılılığın-dan təyin etmək olur [4]. Ölçmələrimizdən aydın olmuşdur ki,  $\varepsilon_y \sim f\left(\frac{U_H H}{c}\right)$  asılılığında (burada,  $U_H$  - yükdaşıyıcılarının Holl yürüklüyü,  $H$ -maqnit sahəsi gərginliyi,  $c$ -isə işiq sürəti-

dir),  $\frac{U_H H}{c}$  nisbətinin qiyməti 0,1-0,2 arasında dəyişir. Bu səbəbdən fərz edilir ki, səpilmə elastiki təbiətlidir. Nümunənin maqnit müqavimətini  $\Delta p/p$  qiymətinin müsbət olması da bu fərziyyəni təsdiqləyir.

Bələliklə,  $(Fe_3Sb_2)_{0,98}(Pb_{82,5}Sb_{17,5})_{0,02}$  tərkibli kristalda istiliyin daşınmasının mürəkkəb mexanizm üzrə baş vermesi və fonon səpilməsinin elastiki təbiətli olması aşkar edilmişdir.

- 
- [1] C.I. Əbilov, M.F. Ağayeva  $(Fe_3Sv_2)_{1-x}(Pv_{82,5}Sv_{17,5})_x$  ərintilərinin fiziki-kimyəvi və bəzi elektrofiziki xassələri. Metallar fizikasının müasir problemlərinə dair Beynəlxalq elmi-praktiki konfransın materialları. Bakı 2007, «Elm», s 116-119.
  - [2] M.A. Kretova, E.S. Abilov, V.S. Zemskov. Vvedenie v metodiki eksperimenta (rezultatı i obsujdeniya) M, 2004, Nauka, 196 s.
  - [3] C.I. Əbilov, Ş.S. Ismayilov, M.F. Ağayeva  $(Fe_3Sv_2)_{0,58}(Pv_{82,5}Sv_{17,5})_{0,02}$  kristallarında elektron və fonon səpilməsinin xüsusiyyətləri. 24-cü Beynəlxalq fizika konfransı məruzələrinin tezisləri. Türkiyə, Malatya, 2007. Inoni Universitetinin mətbəəsi, s.326.
  - [4] S.A. Aliev, Dj.A. Baqirov, E.R. Iskenderov, E.I. Zulfiqarov, S.I. Safarova. O neupruqom xaraktere rasseyaniya elektronov v  $Pv_{1-x}Sn_xTe$ . Izv. AN SSSR, Neorqan. materialı. 1983, t.29, №3, s.499-502.

**Ch.I. Abilov, M.F. Agayeva**

### **FEATURES OF HEAT CONDUCTIVITY IN $(Fe_3Sb_2)_{0,98}(Pb_{82,5}Sb_{17,5})_{0,02}$ CRYSTALS**

In solid solution monocrystals of compound  $(Fe_3Sb_2)_{0,98}(Pb_{82,5}Sb_{17,5})_{0,02}$ , grown by directed cristallization technology, the mechanizm of heat condusivity has been elucidated. It has been shown, that the complexity of nature of phononic and electronic scattering in crystals deals with the complexity of compound and crystalline structure defektion. It has also been established, that scattering of phonons and electrons has the elastic nature.

**Ч.И. Абилов, М.Ф. Агаева**

### **ОСОБЕННОСТИ ТЕПЛОПРОВОДНОСТИ В КРИСТАЛЛАХ $(Fe_3Sb_2)_{0,98}(Pb_{82,5}Sb_{17,5})_{0,02}$**

В выращенных технологией направленной кристаллизации монокристаллах твердого раствора состава  $(Fe_3Sb_2)_{0,98}(Pb_{82,5}Sb_{17,5})_{0,02}$  выяснен механизм теплопроводности. Показано, что сложность характера фононного и электронного рассеяния связано со сложностью состава и дефектностью кристаллической структуры. Выявлено, что рассеяние фононов и электронов имеет упругий характер.

*Received: 19.03.08*

## THERMOELECTRIC EFFECTS IN QUANTUM WELL

**F.M. HASHIMZADE, Kh.A. HASANOV, B.H. MEHDIYEV**

*G.M. Abdullayev Institute of Physics of National Academy of Sciences,  
AZ-1143, H. Javid ave., 33, Baku, Azerbaijan*

In this paper we have calculated the thermomagnetic tensor components for the current density in a quantum well for any degree of degeneration. In our work, we are examined the diffusion component under the assumption that elastic scattering is dominated, and show that the magneto-thermo-e.m.f. is not determined by the entropy only, as is the case for three dimensions. Elastic electron scattering by acoustic phonons is considered. The magnetic field is directed across of confinement direction, i.e. it is located in the plane of a two-dimensional electron gas. When temperature gradient is along the direction of confinement, magneto-thermoelectric power has a nonmonotonic dependence on magnetic fields. For the magnetic fields less than 4 T magneto-thermoelectric power increase with the magnetic field, and decreased in higher magnetic field. The relative decrease magneto-thermoelectric power achieves 20% at the minimum, which is a significant change and can be easily detected in an experiment. When temperature gradient is along the direction of the free motion, magneto-thermoelectric power is monotonically increasing with magnetic field. For reference, are shown dependence of the non-dissipative magneto-thermoelectric power  $S/(e n)$  on magnetic field.

The theory of the quantum thermomagnetic effects in size-quantized systems was studied in [1-8]. In [1,2] the case of a strongly degenerate electronic gas was considered and a focus was placed on the oscillation phenomena. In [3] the thermopower in quantum well structures has been calculated, and the size dependence of thermopower in a quantum limit for different mechanisms of electronic scattering has been considered. The authors used the kinetic equation method and the density matrix approach. In the latter case, the scattering was entered into the equation of motion for the density matrix through the lifetime of a quantum state. In [4] the magneto-thermoelectric power of a two-dimensional electron gas (2DEG) was investigated in the regime of the quantum Hall effect at values of a magnetic field where thermopower is proportional to the entropy of the two-dimensional electron gas. In [5] the magneto-thermoelectric power of a two-dimensional electron gas has been investigated theoretically within the framework of the Boltzman kinetic equation for different mechanisms of electronic scattering taking into account phonon-drag contributions.

Hicks and Dresselhaus [6] predicted that the thermoelectric figure of merit for two-dimensional quantum wells and one-dimensional quantum wires should be substantially enhanced relative to the corresponding bulk materials. A theoretical study of this effect has been undertaken for a bismuth nanowire [7].

The theory of thermopower in quantum dots was developed in [8]. In this work it has been shown that there is an opportunity to create an appreciable temperature difference in a nanostructure and to measure the potential difference induced by this temperature gradient. The paper provides theoretical calculations of magnetothermoelectric power in quantum wells and quantum wires.

In this paper we have calculated the thermomagnetic tensor components for the current density in a quantum well for any degree of degeneration. It is common knowledge that the thermoelectric tensor has two contributions - diffusion and phonon drag, which are linearly additive ones. In our work, we are given an examination the diffusion component under the assumption that elastic scattering is dominated, and show that the magneto-thermo-e.m.f. is not determined by the entropy only, as is the case for three dimensions. Elastic electron scattering by acoustic phonons is considered. The magnetic field is directed across the confinement direction,

i.e. it is located in the plane of a two-dimensional electron gas. Thus, two cases for the relative arrangement of the current direction and the confinement direction are possible. In the case where the current is located in a plane of a two-dimensional electron gas it is sufficient to confine ourselves to the relaxation time approximation and to use the kinetic equation. In a case when the current is along the direction of confinement it is necessary to use the density matrix approach obtained in [9-11] for calculation of the diagonal conduction tensor components.

We consider a simple model for the quantum well, in which a two-dimensional electron gas is confined in the x-direction and a homogenous static magnetic field  $B$  parallel to the z-axis, with the vector-potential  $A(0, x, B, 0)$  in the Landau gauge. Then the one-particle Hamiltonian is given by

$$\hat{H} = \frac{\hat{p}_x^2}{2m^*} + \frac{1}{2m^*} \left( \hat{p}_y + \frac{e}{c} x B \right)^2 + \frac{\hat{p}_z^2}{2m^*} + U(x) \quad (1)$$

where  $p = (p_x, p_y, p_z)$  and  $m^*$ , respectively, are the momentum operator and the effective mass of a conduction electron.  $U(x)$  is the confining potential in the x-direction which is characterized by the parabolic potential:

$$U(x) = \frac{m^* \omega_0^2 x^2}{2} \quad (2)$$

The eigenvalues and eigenfunctions of the Schrodinger equation with Hamiltonian (1) are determined by the expressions

$$\varepsilon_\alpha = \left( \frac{1}{2} + N \right) \omega \hbar + \left( \frac{\omega_0}{\omega} \right) \frac{2 \hbar^2 k_y^2}{2m^*} + \frac{\hbar^2 k_z^2}{2m^*} \quad (3)$$

$$\phi_\alpha(x, y, z) = \frac{1}{2\pi} \varphi_N(x - x_\alpha) e^{i(k_y y + k_z z)} \quad (4)$$

where  $\omega = \sqrt{\omega_0^2 + \omega_c^2}$  is the "hybrid" frequency,  $\omega_c = \frac{eB}{m^* c}$  is the cyclotron frequency of electrons and  $N$  - is the oscillation quantum number. The expression

$$\varphi_N(x - x_\alpha) = \frac{1}{\sqrt[4]{\pi} \sqrt{R} \sqrt{2^N N!}} \exp\left(-\left(\frac{x - x_\alpha}{\sqrt{2R}}\right)^2\right) H_N\left(\frac{x - x_\alpha}{R}\right) \quad (5)$$

represents the wave function of a harmonic oscillator,  $x_\alpha = -\frac{\omega_c}{\omega} R^2 k_y$  - is the oscillator center, and  $R = \sqrt{\frac{\hbar}{m\omega}}$  - is the magnetic length,  $H_N(\xi)$  is the Hermite polynomial,  $\alpha = (N, k_y, k_z)$  is a set of quantum numbers that determine the electron states in a magnetic field.

For the magnetic field directed along the  $z$ -axis the current density components can be written in the form [12]

$$\begin{aligned} j_x &= \sigma_{xx} E_x + \sigma_{xy} E_y - \beta_{xx} \nabla_x T - \beta_{xy} \nabla_y T \\ j_y &= \sigma_{yx} E_x + \sigma_{yy} E_y - \beta_{yx} \nabla_x T - \beta_{yy} \nabla_y T \end{aligned} \quad (6)$$

where  $\sigma_{ik}$  and  $\beta_{ik}$  are the conduction tensor components,  $E_k$  is the components of the electric field and  $\nabla_k T$  is the temperature gradient.

From the conditions  $j_x = j_y = 0$ ,  $\nabla_k T = 0$  we obtain the thermoelectric power in a transverse magnetic field

$$\alpha_{yy} = \frac{E_y}{\nabla_y T} = \frac{\beta_{yy} \sigma_{xx} - \beta_{xy} \sigma_{yx}}{\sigma_{xx} \sigma_{yy} - \sigma_{xy} \sigma_{yx}} \quad (7)$$

Putting  $j_x = j_y = 0$ ,  $\nabla_y T = 0$  we obtain from Eqs. (6)

$$\alpha_{xx} = \frac{E_x}{\nabla_x T} = \frac{\beta_{xx} \sigma_{yy} - \beta_{yx} \sigma_{xy}}{\sigma_{xx} \sigma_{yy} - \sigma_{xy} \sigma_{yx}} \quad (8)$$

For the calculation of kinetic coefficients  $\alpha_{xx}$ ,  $\alpha_{yy}$  it is necessary to calculate both diagonal and non-diagonal

conduction tensor components  $\sigma_{ik}$  and  $\beta_{ik}$  [2,13].

Note that in bulk semiconductors  $\sigma_{yx} \gg \sigma_{xx}$ ,  $\beta_{yx} \gg \beta_{xx}$ ,  $\sigma_{xy} \gg \sigma_{yy}$  and  $\beta_{xy} \gg \beta_{yy}$ . It is related to the fact that a decrease in scattering potential results in the diagonal electric conductivity tensor components tending to zero, while the non-diagonal components stay finite[12]. In our case, as we will show later, it is not true.

The average value of the current density components carried by the electrons is defined by the expression

$$j_i = -e \text{Tr}(\hat{\rho} \hat{v}^{(i)}) = -e \sum_{\alpha\alpha'} \rho_{\alpha\alpha'} v_{\alpha'\alpha}^{(i)}, \quad i = (x, y, z) \quad (9)$$

where  $\hat{\rho}$  is the density matrix, and  $\hat{v}$  - is the velocity operator.

The matrix elements of the density matrix are evaluated from the solution of Liouville's equation

$$i\hbar \frac{\partial \hat{\rho}}{\partial t} = [H_t, \rho] \quad (10)$$

where  $\hat{H}_t$  is the total Hamiltonian of the system  $\hat{H}_t = \hat{H} + V + F$  which consists of the Hamiltonian (1), the scattering potential  $V$ , and the electron-electric field interaction  $F = e(\mathbf{E} \cdot \mathbf{r})$ .

The matrix elements of the components of the velocity operator in the representation (4) can be written as

$$\hat{v}_{\alpha\alpha'}^x = i\omega R \delta_{k_y, k_y'} \delta_{k_z, k_z'} \left( \delta_{N', N-1} \sqrt{\frac{N}{2}} - \delta_{N', N+1} \sqrt{\frac{N+1}{2}} \right) \quad (11)$$

$$\hat{v}_{\alpha\alpha'}^y = \omega_c R \delta_{k_y, k_y'} \delta_{k_z, k_z'} \left( \delta_{N', N+1} \sqrt{\frac{N+1}{2}} - \delta_{N', N-1} \sqrt{\frac{N}{2}} \right) + \frac{\omega_0^2 \hbar k_y}{m^* \omega^2} \delta_{\alpha, \alpha'} \quad (12)$$

Using Eqns. (11)- (12) in Eq.(9) and performing the summation over  $\alpha' = (N', k_y', k_z')$  we obtain the following expressions for the current density components:

$$j_x = -ie\omega R \sum_{\alpha} \left( \rho_{N-1, N} \sqrt{\frac{N}{2}} - \rho_{N+1, N} \sqrt{\frac{N}{2}} \right) \quad (13)$$

$$j_y = -e\omega_c R \sum_{\alpha} \left( \rho_{N+1, N} \sqrt{\frac{N+1}{2}} + \rho_{N-1, N} \sqrt{\frac{N}{2}} \right) - \frac{e\hbar}{m^*} \left( \frac{\omega_0}{\omega} \right)^2 \sum_{\alpha} k_y \rho_{\alpha, \alpha} \quad (14)$$

In a zero-order approximation with respect to the scattering potential  $V$  the matrix elements of the density matrix  $\rho_{\alpha, \alpha'}$  have the form

$$\rho_{\alpha', \alpha} = e(E_x x_{\alpha'\alpha} + E_y y_{\alpha'\alpha}) \frac{f_{\alpha'} - f_{\alpha}}{\epsilon_{\alpha'} - \epsilon_{\alpha}} \quad (15)$$

where  $x_{\alpha'\alpha}$  and  $y_{\alpha'\alpha}$  are the matrix elements of the x and y

coordinates, respectively. In Eq.(15)  $f_\alpha = f(\varepsilon_\alpha)$  is the equilibrium electron distribution function (Fermi- Dirac function)

$$f(\varepsilon_\alpha) = \left(1 + \exp\left(\frac{\varepsilon_\alpha - \zeta}{k_0 T}\right)\right)^{-1} \quad (16)$$

where  $\zeta$  is the chemical potential of the electrons, and  $k_0$  is the Boltzmann constant.

Substituting Eq.(15) into Eqs.(13)-(14) and calculating the matrix elements of the coordinates we obtain

$$j_y = \sigma_{yx} E_y, \sigma_{yx} = \frac{\omega_c e^2}{m^* \omega^2} \sum_\alpha f_\alpha = \frac{\omega_c e^2 n}{m^* \omega^2}, \quad (17)$$

$$j_x = 0$$

where  $\sum_\alpha f_\alpha = n$  is the areal density of the two-dimensional electron gas and

$$n = \frac{k_0 T m^*}{2\pi\hbar^2} \frac{\omega}{\omega_0} \sum_N \ln(1 + e^{\eta - x_N}) \quad (18)$$

where

$$\eta = \frac{\zeta}{k_0 T}, \quad x_N = \frac{\hbar\omega}{k_0 T} \left(N + \frac{1}{2}\right). \quad (19)$$

In the limit of strong magnetic fields,  $\omega_0 \ll \omega_c$ , or equivalently, in the bulk case, when  $\omega_0 \rightarrow 0$  the energy spectrum (3) equals that of an electron in a magnetic field. In this case the expression for  $\sigma_{yx}$  in (17) coincides with that for the non-diagonal component of the conductivity tensor of the bulk semiconductor material.

In order to find the explicit form of the non-diagonal component  $\beta_{xy}(B)$  we will take advantage of the Onsager reciprocal relation

$$\beta_{xy}(B) = \frac{1}{T} \gamma_{yx}(-B) \quad (20)$$

where  $\gamma_{ik}(B)$  is the coefficient in the formula of  $i$ -th heat flux density transported by the electrons  $W_i = \gamma_{ik} E_k$ .

In ref. [14] it was shown explicitly that in the presence of a magnetic field it is necessary to take into account the contribution to the current of electrons the edge current  $-c \nabla \times \mathbf{M}$  due to magnetization  $\mathbf{M}$ . In this case the coefficient  $\gamma_{yx}$  can be represented as

$$\gamma_{yx} = \gamma_{xy}^{(0)} - cM \quad (21)$$

where  $\gamma_{xy}^{(0)}$  is the coefficient in the heat flux density in the absence of scattering which defined by [12, 1]

$$W_y^0 = \frac{1}{2} \sum_{\alpha\alpha'} \rho_{\alpha'\alpha} v_{\alpha\alpha'}^y (\varepsilon_\alpha + \varepsilon_{\alpha'} - 2\zeta) \quad (22)$$

The magnetization  $M$  is defined by the relationship  $M = -\left(\frac{\partial \Omega}{\partial B}\right)_{T,\zeta}$ , where  $\Omega = -k_0 T \sum_\alpha \ln(1 + \exp(\frac{\zeta - \varepsilon_\alpha}{k_0 T}))$  is the Gibbs thermodynamic potential.

Substitution of the Eq.(15) into Eq.(22) yields the following expression for  $\gamma_{yx}^{(0)}$

$$\gamma_{yx}^{(0)} = -\frac{e\omega_c R^2}{\hbar\omega} \left( \bar{\varepsilon} - \zeta n + \sum_\alpha \hbar\omega \left(N + \frac{1}{2}\right) f_\alpha \right) \quad (23)$$

where  $\bar{\varepsilon} = \sum_\alpha \varepsilon_\alpha f_\alpha$  is the average energy of the system.

The magnetization can be written as

$$M = -\frac{\omega_c^2}{\omega^2} \frac{\Omega}{B} - \frac{1}{B} \frac{\omega_c^2}{\omega^2} \sum_\alpha \hbar\omega \left(N + \frac{1}{2}\right) f_\alpha \quad (24)$$

where

$$\Omega = -\left(k_0 T\right)^2 \frac{\omega}{\omega_0} \frac{m}{2\pi\hbar^2} \sum_N \int_{x_N}^{\infty} \ln(1 + \exp(\eta - x)) dx \quad (25)$$

is the thermodynamic potential per unit area.

Using (24) we obtain the following expression for  $\gamma_{yx}^{(0)}$  instead of Eq.(23):

$$\gamma_{yx}^{(0)} = -\frac{e\omega_c R^2}{\hbar\omega} \left( \bar{\varepsilon} - \zeta n - \frac{\omega^2}{\omega_c^2} MB - \Omega \right) \quad (26)$$

On the other hand, according to the definition of the thermodynamic potential

$$\Omega = \bar{\varepsilon} - \zeta n - TS \quad (27)$$

where  $S = -\left(\frac{\partial \Omega}{\partial T}\right)_{B,\zeta}$  is the entropy per unit area which has the following form:

$$S = \frac{mk_0^2 T}{2\pi\hbar^2} \frac{\omega}{\omega_0} \sum_N \left( (x_N - \eta) \ln(1 + e^{\eta - x_N}) - 2Li_2(-e^{\eta - x_N}) \right) \quad (28)$$

where  $Li_v(\xi)$  is the polylogarithmic function of order  $v$ .

Substituting (27) into (26) and using (21) we obtain

$$\gamma_{yx} = -\frac{e\omega_c}{m\omega^2} TS \quad (29)$$

Finally, for  $\beta_{xy}$  we obtain

$$\beta_{xy} = \frac{e\omega_c}{m\omega^2} S \quad (30)$$

Similar expression was obtained in Ref.[1] for a quantum wire.

For the strong magnetic field case,  $\omega_c \gg \omega_0$ , Eqn. (30) is

reduced to  $\beta_{xy}^{(bulk)} = cS/B$ , which was obtained in Ref.[14] for bulk specimens. At zero temperature, the transport coefficient  $\beta_{xy}$ , consequently, the entropy vanishes as required by the third law of thermodynamics.

For the calculation of the diagonal components of tensors  $\alpha_{xx}$  and  $\beta_{xx}$  when the electric field or the temperature gradient are perpendicular to the plane of two-dimensional electron gas we will make use of the expressions obtained in [9] and [12]:

$$\beta_{xx} = -\frac{e}{\Omega_0 T} \sum_{\alpha\alpha'} \left( -\frac{\partial f(\varepsilon_\alpha)}{\partial \varepsilon_\alpha} \right) \frac{(x_{\alpha'} - x_\alpha)^2}{2} (\varepsilon_\alpha - \zeta) W_{\alpha\alpha'} \quad (31)$$

$$\sigma_{xx} = \frac{e^2}{\Omega_0 T} \sum_{\alpha\alpha'} \left( -\frac{\partial f(\varepsilon_\alpha)}{\partial \varepsilon_\alpha} \right) \frac{(x_{\alpha'} - x_\alpha)^2}{2} W_{\alpha\alpha'} \quad (32)$$

where  $\Omega_0$  is the volume of the system,  $W_{\alpha\alpha'}$  is the electron transition probability from state  $\alpha = (N, k_y, k_z)$  to state  $\alpha' = (N', k'_y, k'_z)$  caused by the effect of the scattering

$$W_{\alpha\alpha'} = \sum_q w(q) |\langle \alpha | e^{iq_x x + iq_y y + iq_z z} | \alpha' \rangle|^2 \times \\ \times \left( N_q \delta_{k'_y, k_y + q_y} \delta_{k'_z, k_z + q_z} \delta(\varepsilon_{\alpha'} - \varepsilon_\alpha - \hbar\omega_q) + (N_q + 1) \delta_{k'_y, k_y - q_y} \delta_{k'_z, k_z - q_z} \delta(\varepsilon_{\alpha'} - \varepsilon_\alpha + \hbar\omega_q) \right) \quad (33)$$

where

$$w(q) = \frac{\pi E_1^2}{\rho s \Omega_0} q \quad (34)$$

Here  $s$  is the speed of sound,  $\rho$  is the density of the material,  $E_1$  is the constant of the acoustic phonon deformation potential,  $q$  is the phonon wave vector, and  $N_q = \left( \exp\left(\frac{\hbar\omega_q}{k_0 T}\right) - 1 \right)^{-1}$  is the occupation number (the Planck

Here  $L_n^m(\xi)$  is the associated Laguerre polynomial.

Further we will focus on the extreme situation, namely, the quantum limit in which the scattering of electrons is confined within the  $N = N' = 0$  level. For the quantum well in a magnetic field the quantum limit criterion is  $\hbar\omega > k_0 T$ .

Above 20 K the available acoustic phonon energies will be small compared to  $k_0 T$ . Since the electron scattering by the acoustic phonons is elastic, it is possible to neglect the

potential.

The scattering mechanism explicitly considered in the present paper is the acoustic phonon deformation potential (DPA scattering). Acoustic-phonon scattering via piezoelectric coupling could also be considered, but this will have a similar temperature and magnetic-field dependence to DPA scattering and so is not included separately. because will not qualitatively affect the results. Other scattering mechanisms, as the interface roughness mechanism, playes a negligible role in heterojunctions, because with the current crystal growth methods, high crystalline quality with atomically sharp resolution is easily achieved, that is interface are not especially rough. In addition, impurity scattering arising from background impurities in the quantum well or remote ionized donors it was to be expected, however in high magnetic fields the magnetic length will be much smaller than the scale of fluctuations due the remote impurities, so remote impurity scattering can be treated by the short-range point defect approach. In this case, the scattering from the point defects has the same functional form as for scattering from the DPA. Only, the temperature and electron concentration dependence will be different.

The transition probability due to the carrier scattering by acoustic phonons has the form

function) for phonons with frequency  $\omega_q = s q$ .

Using the wavefunctions from Eqn.(4), one can write the matrix elements of the electron - phonon interaction as

$$\langle \alpha | e^{i\mathbf{q}\cdot\mathbf{r}} | \alpha' \rangle = \left| J_{NN'}(q_x, q_y) \right|^2 \delta_{k'_y, k_y + q_y} \delta_{k'_z, k_z + q_z} \quad (35)$$

where

$$\left| J_{NN'}(q_x, q_y) \right|^2 = \frac{N!}{N'!} \exp \left( -\frac{R^2 \left( q_x^2 + q_y^2 \frac{\omega_c^2}{\omega^2} \right)}{2} \right) \left( \frac{R^2 \left( q_x^2 + q_y^2 \frac{\omega_c^2}{\omega^2} \right)}{2} \right)^{N'-N} \left( L_N^{N'-N} \left( \frac{R^2 \left( q_x^2 + q_y^2 \frac{\omega_c^2}{\omega^2} \right)}{2} \right) \right)^2 \quad (36)$$

phonon energy  $\hbar\omega_q$  in the arguments of the  $\delta$ -functions in (33). In addition, as  $\hbar\omega_q < k_0 T$ , therefore it is possible to expand the Plank function. Thus we obtain

$$2N_q + 1 \approx \frac{2k_0 T}{\hbar s q} \quad (37)$$

Taking Eq. (37) into account we can rewrite the expression for  $\sigma_{xx}$  in the form

**THERMOELECTRIC EFFECTS IN QUANTUM WELL**

$$\sigma_{xx} = \frac{e^2}{\Omega_0} \frac{w_0}{2} \left( \frac{\omega_c}{\omega} R^2 \right)^2 \sum_{q_x} \sum_{k_z, k_y, k'_y, k'_z} \left( -\frac{\partial f}{\partial \epsilon} \right) \left( k'_y - k_y \right)^2 e^{-\frac{R^2 \left( q_x^2 + \left( \frac{\omega_c}{\omega} \right)^2 (k'_y - k_y)^2 \right)}{2}} \times \\ \times \delta \left( \frac{\hbar^2 k_z'^2}{2m^*} + \left( \frac{\omega_0}{\omega} \right)^2 \frac{\hbar^2 k_y'^2}{2m^*} - \frac{\hbar^2 k_z^2}{2m^*} - \left( \frac{\omega_0}{\omega} \right)^2 \frac{\hbar^2 k_y^2}{2m^*} \right), \quad (38)$$

here

$$w_0 = \frac{4\pi TE_1^2 k_0}{s^2 \rho \Omega_0 \hbar} \quad (39)$$

Transforming the sum over  $q$ ,  $k_y$ ,  $k'_y$ ,  $k_z$  and  $k'_z$  in Eq.(38) into an integral form in a usual way we introduce new, deformed coordinates,

$$k'_y = \frac{\omega}{\omega_0} \tilde{k}'_y, \quad k_y = \frac{\omega}{\omega_0} \tilde{k}_y, \quad k'_z = \tilde{k}'_z, \quad k_z = \tilde{k}_z \quad (40)$$

Using the momentum conservation law  $\tilde{k}' = \tilde{k}$  and integrating over the angle between vectors  $\tilde{k}'$  and  $\tilde{k}$  we obtain:

$$\sigma_{xx} = \frac{1}{\tau_0} \frac{3e^2 n}{m^* \omega_0^2} \left( \frac{\omega_c}{\omega_0} \right)^2 \sqrt{\frac{\omega_0}{\omega}} \frac{1}{\ln(1+e^{\tilde{\eta}})} \int_0^\infty \left( -\frac{\partial f_0}{\partial x} \right) {}_2F_2 \left( \frac{5}{4}, \frac{7}{4}; \frac{3}{2}, 2; -8ax \right) dx. \quad (41)$$

Similarly, for  $\beta_{xx}$  we obtain

$$\beta_{xx} = -\frac{k_0}{e} \frac{1}{\tau_0} \frac{3e^2 n}{m^* \omega_0^2} \left( \frac{\omega_c}{\omega_0} \right)^2 \sqrt{\frac{\omega_0}{\omega}} \frac{1}{\ln(1+e^{\tilde{\eta}})} \int_0^\infty \left( -\frac{\partial f_0}{\partial x} \right) x(x-\tilde{\eta}) {}_2F_2 \left( \frac{5}{4}, \frac{7}{4}; \frac{3}{2}, 2; -8ax \right) dx \quad (42)$$

In Eqns.(41) and (42) the following notations were used

$$\tau_0 = \frac{\sqrt{2\pi} s^2 \rho \hbar^{7/2}}{m^{*3/2} E_1^2 k_0 T \sqrt{\omega_0}} \quad (43)$$

$$a = \frac{k_0 T \omega_c^2}{2 \omega \hbar \omega_0^2} \quad (44)$$

$$f_0 = (1 + \exp[x - \tilde{\eta}])^{-1}, \quad \tilde{\eta} = \eta - x_0 \quad (45)$$

and  ${}_2F_2(a_1, a_2; b_1, b_2; z)$  is the generalized hypergeometric function [15].

For the case of the electric field and the temperature gradient directed along the plane of two-dimensional electron gas, we use the solution of the kinetic equation to calculate the diagonal components of the tensors  $\alpha_{yy}$  and  $\beta_{yy}$ . These are given by

$$\sigma_{yy} = \frac{e^2}{\Omega_0} \sum_{\alpha} \left( -\frac{\partial f(\epsilon_{\alpha})}{\partial \epsilon_{\alpha}} \right) \tau_{\alpha} v_{k_y}^2 \quad (46)$$

$$\beta_{yy} = -\frac{e^2}{\Omega_0 T} \sum_{\alpha} \left( -\frac{\partial f(\epsilon_{\alpha})}{\partial \epsilon_{\alpha}} \right) (\epsilon_{\alpha} - \xi) \tau_{\alpha} v_{k_y}^2 \quad (47)$$

where

$$v_{k_y} = \frac{1}{\hbar} \partial_{k_y} \epsilon = \left( \frac{\omega_0}{\omega} \right) {}_2F_2 \left( \frac{1}{4}, \frac{3}{4}; \frac{1}{2}, 1; -\frac{4 \omega_c^2}{\omega \hbar \omega_0^2} \left( \epsilon - \frac{\hbar \omega}{2} \right) \right) \quad (48)$$

and  $\tau_{\alpha}$  is the relaxation time of electrons.

For the elastic scattering by acoustic phonons the relaxation time is given by a simple expression:

$$\frac{1}{\tau_{\alpha}} = \sum_{\alpha'} W_{\alpha \alpha'} \left( 1 - \frac{\mathbf{k}'}{\mathbf{k}} \right) \quad (49)$$

Taking into account expression (33) for the transition probability and proceeding the same was as above in the calculation of the transverse diagonal components of the transport coefficients, the following expression for  $\tau$  obtains in the quantum limit:

$$\tau = \tau_0 \left( \frac{\omega_0}{\omega} \right)^{3/2} \frac{1}{{}_2F_2 \left( \frac{1}{4}, \frac{3}{4}; \frac{1}{2}, 1; -\frac{4 \omega_c^2}{\omega \hbar \omega_0^2} \left( \epsilon - \frac{\hbar \omega}{2} \right) \right)} \quad (50)$$

Substitution of (49) into (46) and (47) and summation over  $\alpha$  yields

$$\sigma_{yy} = \frac{e^2 n}{m^* \ln(1+e^{\tilde{\eta}})} \tau_0 \left( \frac{\omega_0}{\omega} \right)^{7/2} \int_0^\infty \left( -\frac{\partial f_0}{\partial x} \right) \frac{1}{{}_2F_2 \left( \frac{1}{4}, \frac{3}{4}; \frac{1}{2}, 1; -8ax \right)} x dx \quad (51)$$

$$\beta_{yy} = -\frac{k_0}{e} \frac{e^2 n}{m^* \ln(1+e^{\tilde{\eta}})} \tau_0 \left( \frac{\omega_0}{\omega} \right)^{7/2} \int_0^\infty \left( -\frac{\partial f_0}{\partial x} \right) \frac{(x-\tilde{\eta})}{_2F_2(\frac{1}{4}, \frac{3}{4}; \frac{1}{2}, 1; -8ax)} x dx \quad (52)$$

Combining Eqs.(17), (30), (41), (42), (51) and (52) with Eqs. (7) and (8) and taking into account the symmetry of the conductivity tensor, we obtain the following expressions:

$$\alpha_{yy} = -\frac{1}{en} \frac{3k_0 n K_1 K_4 + S \ln^2(1+e^{\tilde{\eta}})}{3K_1 K_3 + \ln^2(1+e^{\tilde{\eta}})}, \quad (53)$$

$$\alpha_{xx} = -\frac{1}{en} \frac{3k_0 n K_2 K_3 + S \ln^2(1+e^{\tilde{\eta}})}{3K_1 K_3 + \ln^2(1+e^{\tilde{\eta}})}, \quad (54)$$

where

$$K_1 = \int_0^\infty \left( -\frac{\partial f_0}{\partial x} \right) {}_2F_2\left(\frac{5}{4}, \frac{7}{4}; \frac{3}{2}, 2; -8ax\right) x dx \quad (55)$$

$$K_2 = \int_0^\infty \left( -\frac{\partial f_0}{\partial x} \right) x (x-\tilde{\eta}) {}_2F_2\left(\frac{5}{4}, \frac{7}{4}; \frac{3}{2}, 2; -8ax\right) dx \quad (56)$$

$$K_3 = \int_0^\infty \left( -\frac{\partial f_0}{\partial x} \right) \frac{1}{_2F_2(\frac{1}{4}, \frac{3}{4}; \frac{1}{2}, 1; -8ax)} x dx \quad (57)$$

$$K_4 = \int_0^\infty \left( -\frac{\partial f_0}{\partial x} \right) \frac{(x-\tilde{\eta})}{_2F_2(\frac{1}{4}, \frac{3}{4}; \frac{1}{2}, 1; -8ax)} x dx \quad (58)$$

Eqs.(57)-(60) is applicable for any degree of degeneracy of two-dimensional electron gas.

For the degenerated electron gas, when  $\eta = \zeta/k_B T > 1$ , the expressions for the transport coefficients can be considerably simplified. In this case we replace  $\left( -\frac{\partial f(\varepsilon)}{\partial \varepsilon} \right)$  by the delta function  $\delta(\varepsilon - \zeta)$ . Then we obtain

$$n = \frac{m^* k_0 T}{2\pi \hbar^2} \frac{\omega}{\omega_0} \tilde{\eta}, \quad (59)$$

$$S^{(d)} = \frac{\pi m^* T k_0^2 \omega}{6 \hbar^2 \omega_0}, \quad (60)$$

$$\sigma_{yx}^{(d)} = \frac{\omega_c e^2 n}{m^* \omega^2}, \quad (61)$$

$$\beta_{yx}^{(d)} = -\frac{k_0}{e} \frac{\pi^2}{3\tilde{\eta}} \sigma_{yx}^{(d)} \quad (62)$$

$$\sigma_{xx}^{(d)} = \frac{1}{\tau_0} \frac{3e^2 n}{m \omega_0^2} \left( \frac{\omega_c}{\omega_0} \right)^2 \sqrt{\frac{\omega_0}{\omega}} {}_2F_2\left(\frac{5}{4}, \frac{7}{4}; \frac{3}{2}, 2; -8a\tilde{\eta}\right) \quad (63)$$

$$\beta_{xx}^{(d)} = -\frac{k_0}{e} \frac{\pi^2}{3\tilde{\eta}} \sigma_{xx}^{(d)} \left( 1 - \frac{35}{6} \frac{a\tilde{\eta}}{_2F_2(\frac{5}{4}, \frac{7}{4}; \frac{3}{2}, 2, -8a\tilde{\eta})} \right) \quad (64)$$

$$\sigma_{yy}^{(d)} = \frac{e^2 n}{m} \tau_0 \left( \frac{\omega_0}{\omega} \right)^{7/2} \frac{1}{_2F_2(\frac{1}{4}, \frac{3}{4}; \frac{1}{2}, 1; -8a\tilde{\eta})} \quad (65)$$

$$\beta_{yy}^{(d)} = -\frac{k_0}{e} \frac{\pi^2}{3\tilde{\eta}} \sigma_{yy}^{(d)} \left( 1 + \frac{3a\tilde{\eta}}{_2F_2(\frac{1}{4}, \frac{3}{4}; \frac{1}{2}, 1; -8a\tilde{\eta})} {}_2F_2\left(\frac{5}{4}, \frac{7}{4}; \frac{3}{2}, 2, -8a\tilde{\eta}\right) \right) \quad (66)$$

For the case of strongly degenerate electron gas the thermopower can be written as

$$\alpha_{yy} = -\frac{\pi^2 k_0}{e\tilde{\eta}} \frac{\Psi_1(1+3a\tilde{\eta}\Psi_1)+1}{(3\Psi_1+1)} \quad (67)$$

$$\alpha_{xx} = -\frac{\pi^2 k_0}{e\tilde{\eta}} \frac{\Psi_1(1-\frac{35}{6}a\tilde{\eta}\Psi_2)+\frac{1}{3}}{(3\Psi_1+1)} \quad (68)$$

where

$$\Psi_1 = \frac{{}_2F_2(\frac{5}{4}, \frac{7}{4}; \frac{3}{2}, 2, -8a\tilde{\eta})}{{}_2F_2(\frac{1}{4}, \frac{3}{4}; \frac{1}{2}, 1; -8a\tilde{\eta})} \quad (69)$$

$$\Psi_2 = \frac{{}_2F_2(\frac{9}{4}, \frac{11}{4}; \frac{5}{2}, 3; -8a\tilde{\eta})}{{}_2F_2(\frac{5}{4}, \frac{7}{4}; \frac{3}{2}, 2; -8a\tilde{\eta})} \quad (70)$$

In the case of strongly degenerate electron gas and weak fields,  $\tilde{\eta}$  depends on the magnetic field only weakly, and the observed changes in the transport coefficients are due to parameter  $a$

$$\alpha_{xx} = -\frac{k_0 \pi^2}{3(e\tilde{\eta})} + \frac{35k_0 \pi^2 a}{24e} \quad (71)$$

$$\alpha_{yy} = -\frac{k_0 \pi^2}{3(e\tilde{\eta})} - \frac{3(k_0 \pi^2)a}{4e} \quad (72)$$

one can see that  $\alpha_{xx}$  decreases by absolute value, whereas absolute value  $\alpha_{yy}$ , on the contrary, increases. Coefficients  $\alpha_{xx}$  and  $\alpha_{yy}$  are proportional to the temperature. In a strong magnetic field the situation is similar to the quantum limit for the bulk case.

We present a numerical calculations for the thermopower for GaAs/Al<sub>x</sub>Ga<sub>1-x</sub>As parabolic quantum well. We use the following set of physical parameters  $m^* = 0.066 m_0$ , where  $m_0$  is the free electron mass. The

parameter of the parabolic potential is  $\omega_0 = 1.4 \times 10^{13} \text{ s}^{-1}$ . The value of the deformation-potential constant is as  $E_l = 10 \text{ eV}$ . The density of the material and the speed of sound are taken as  $\rho = 5 \times 10^3 \text{ kg/m}^3$  and  $s = 5400 \text{ m/s}$ .

Notice that numerical calculations for the quantum limit criterion must be carried out when the Fermi level is between the first and second subbands  $\hbar\omega/2 \leq \zeta < 3\hbar\omega/2$ .

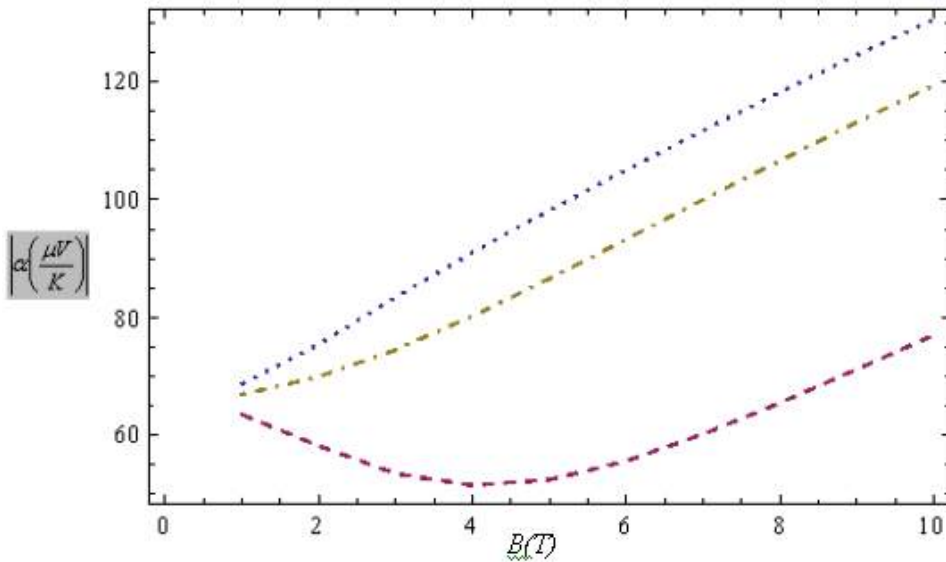


*Fig.1.* Absolute value transversal magneto-thermoelectric power of two-dimensional electron gas versus the magnetic field.  $T=20\text{K}$ ,  $n=10^{14} \text{ m}^{-2}$ ;  $\alpha_{yy}$  – dotted,  $\alpha_{xx}$  – dashed,  $S/(e n)$  – dotdashed.

The dependence of absolute value the magneto-thermoelectric power on magnetic field are shown in Fig.1 for  $T=20 \text{ K}$ ,  $n = 10^{14} \text{ m}^{-2}$ . When temperature gradient is along the direction of the confinement, magneto-thermoelectric power  $\alpha_{xx}$  has a nonmonotonic dependence on magnetic fields. For the magnetic fields less than  $4T\alpha_{xx}$  increase with the magnetic field, and decreased in higher magnetic field. As one can see from Fig. 1, the relative decrease  $\alpha_{xx}$  achieves

20% at the minimum, which is a significant change and can be easily detected in an experiment. When temperature gradient is along the direction of the free motion magneto-thermoelectric power  $\alpha_{yy}$  is monotonically increasing with magnetic field. For reference, in Fig.1 are shown dependence of the non-dissipative magneto-thermoelectric power  $S/(e n)$  on magnetic field [16].

- 
- [1] M.D. Blokh, Phys. Solid State 896, 1975. (in Russian).
  - [2] G.R. Aizin and V.A. Volkov, Zh. Eksp. Teor. Fiz., 1469, 1984. (in Russian).
  - [3] S.S. Kubakaddi, B.G. Mulimani and V.M. Jali, Phys. Stat. Sol. (b), 683, 1986.
  - [4] J.S. Davidson, E.D. Dahlberg, A.J. Valois and G.Y. Robinson, Phys. Rev. B, 2941, 1986.
  - [5] X. Zianni, P.N. Butcher and M.J. Kearney, Phys. Rev. B, 7520, 1994.
  - [6] L.D. Hicks and M.S. Dresselhaus, Phys. Rev. B, 12727, 1993.
  - [7] T. Koga, T.C. Harman, S.B. Kronin and M.S. Dresselhaus, Phys. Rev. B, 14286, 1999.
  - [8] C.W. Beenakker and A.A. Staring, Phys. Rev. B, 9667, 1992.
  - [9] E.N. Adams and T.D. Holstein, J. Phys. Chem. Sol., 254, 1959.
  - [10] P.S. Zyryanov and G.I. Guseva , Uspekhi Fizicheskikh Nauk , 565, 1968. [Sov. Phys. Usp., 538, 1969].
  - [11] A.I. Anselm and B.M. Askerov, Phys. Solid State, 31, 1967. (in Russian).
  - [12] B.M. Askerov, Electron Transport Phenomena in Semiconductors (World Scientific, Singapore, 1994).
  - [13] E.P. Sinyavskii and R.A. Khamidullin, Semiconductors, 924, 2002.
  - [14] Yu. N. Obraztsov, Fiz. Tverd. Tela (Leningrad), 414, 1964 [Sov. Phys.-Solid State, 331 (1964)].
  - [15] A.P. Prudnikov, Yu.A. Brychkov, and O.I. Marichev, Integrals and Series, Vol. More spesial Functions (Fizmatlit, Moscow, 2003).
  - [16] F.M. Gashimzade, A.M. Babaev and Kh.A. Gasanov, Semiconductors and Dielectrics, Vol.43, N10, pp.1850-1852, 2001.

**F.M. Haşımzadə, X.A. Həsənov, B.H. Mehdiyev**

### KVANT ÇUXURUNDA TERMOELEKTRİK EFFEKTİTLƏR

Bu məqalədə ixtiyari cırlaşma halında kvant çuxurunda cərəyan sıxlığının termomaqnit tensorunun komponentləri hesablanmışdır. Biz diffuziya komponentlərini elastiki səpilmə halında hesablayaraq göstərmişik ki, maqnit termoelektrik hərəkət qüvvəsi üçölçülü halda olduğu

kimi ancaq entropiya ilə təyin edilmir. Elektronların akustik fononlardan elastiki səpilməsinə baxılmışdır. Maqnit sahəsi ikiölçülü elektron qazının müstəvisi üzərində yerləşmişdir. Elektron qazı müstəvisinə normal istiqamətdə qradient temperaturu yaradıldıqda maqnit termo-ehq maqnit sahəsindən qeyri-monoton asılı olur. Maqnit sahəsi 4T-dən kiçik olduqda maqnit termoehq sahədən asılı olaraq artır, maqnit sahəsinin yuxarı qiymətlərində isə azalır. Minimum halda maqnit termoehq-nin nisbi azalması 20% təşkil edir və eksperimentdə asanlıqla aşkar edilə bilər. Temperatur qradienti sərbəst hərəkət istiqamətində yönəldikdə maqnit termoehq maqnit sahəsindən asılı olaraq artır. Müqayisə üçün qeyri-dissipativ maqnit termoehq-nin  $S/(en)$  maqnit sahəsindən asılılığı göstərilmişdir.

**Ф.М. Гашимзаде, Х.А. Гасанов, Б.Г. Мехдиев**

## **ТЕРМОЭЛЕКТРИЧЕСКИЕ ЭФФЕКТЫ В КВАНТОВОЙ ЯМЕ**

В данной статье мы рассчитали компоненты термомагнитного тензора для плотности тока в квантовой яме с произвольной степенью вырождения. В нашей работе мы проверили диффузионную компоненту в предположении доминирующей роли упругого рассеяния и показано, что магнетотермоэдс определяется не только энтропией, как в трехмерном случае. Рассмотрено упругое рассеяние электронов акустическими фононами. Магнитное поле расположено в плоскости двумерного электронного газа. Когда создается температурный градиент вдоль направления ограничения, магнетотермоэдс немонотонно зависит от магнитного поля. Для магнитного поля меньшего, чем 4T, магнетотермоэдс увеличивается с ростом магнитного поля, но уменьшается при высоких значениях магнитного поля. Относительное уменьшение магнетотермоэдс достигает 20% при минимуме, который является существенным изменением и может быть легко обнаружен при эксперименте. Когда температурный градиент направлен вдоль направления свободного движения, магнетотермоэдс монотонно растет с ростом магнитного поля. Для сравнения показана зависимость недиссилиативной магнетотермоэдс  $S/(en)$  от магнитного поля.

*Received: 18.03.08*

## SPECTROSCOPIC PROPERTIES OF NEODYMIUM IONS IN $\alpha$ -Gd<sub>2</sub>-S<sub>3</sub> SINGLE CRYSTALS

A.A. MAMEDOV

G.M. Abdullayev Institute of Physics of National Academy of Sciences,  
AZ-1143, Baku, H. Javid, 33

The radiation spectrum identification of Nd<sup>3+</sup> ions has been carried out in  $\alpha$ -Gd<sub>2</sub>-S<sub>3</sub> crystals on  ${}^4F_{3/2} \rightarrow {}^4I_{11/2}$  transition. The energy values of Stark sublevels are defined for each of Nd<sup>3+</sup> centers.

Nowadays Nd<sup>3+</sup> ions are the most distributive activators for solid-state lasers. The electron configuration of free thrice ionized neodymium atom is  $4f^3$ . The number of electrons is odd one and  $J$  values are half-integer ones. Each level of free Nd<sup>3+</sup> ion is degenerate one with  $2J+1$  degeneracy multiplicity. Each initially degenerated level, characterized by definite  $J$  value, splits on the series of sublevels (Stark components) under the influence of electric field, created by the ion surroundings in crystal lattice. Nd<sup>3+</sup> ions, being in crystal-basis, can be in the fields with different symmetry and intensity, moreover the number of such inequivalent positions (number of centers) can change in wide range. As a result each type of Nd<sup>3+</sup> optical center in the given crystal differs from other ones of the same crystal by the level scheme. The crystal optical properties in the given case present themselves the superposition of properties of separate center types. The given crystal disordered structure reveals in spectrums of absorption and luminescence Nd<sup>3+</sup> in the form of heterogeneous widening and splitting of its lines. The heterogeneous widening of Nd<sup>3+</sup> spectrums in several crystals is so big that it totally levels Stark splits of separate optical centers. The absence of information about structure of heterogeneously widened bands essentially makes difficult the analysis of processes taking place in excited activated medium.

The method of selective laser excitation allows us to carry out these gaps. It is based on constriction of heterogeneously widened luminescence lines at narrow-band selective excitation of separate centers.

$\alpha$ -Gd<sub>2</sub>S<sub>3</sub> crystal is the one from few semiconductors

allowing the introduction of high concentrations of Nd<sup>3+</sup> ions. This compound has orthorhombic structure in which Gd<sup>3+</sup> ions are in two equivalent positions [1]. The  $\alpha$ -Gd<sub>2</sub>S<sub>3</sub> structure is formed by Gd(1)S<sub>7</sub> and Gd(2)S<sub>8</sub> polyhedrons. The coordination polyhedron Gd(1)S<sub>7</sub> presents itself dual trigonal prism; Gd(2) is surrounded by seven sulfur atoms, forming distorted "monocapped" trigonal prism. The coordination number of sulfur atoms in  $\alpha$ -Gd<sub>2</sub>S<sub>3</sub> is equal to 5. Nd<sup>3+</sup> ions at introduction into crystal are also in inequivalent positions that reveals in their optical spectrums [2]. Thus, for example, the four well resolved peaks take place in absorption spectrum, corresponding to  ${}^4I_{9/2} \rightarrow {}^4F_{3/2}$  transition at  $T=4.2\text{K}$ , whereas  ${}^4F_{3/2}$  term should split only on two Stark components in the field of low symmetry. Thus, the task of thin structure identification of optical spectrums for which Nd<sup>3+</sup> ions, being in inequivalent positions are responsible arises. This task has been solved by us by the method of resonance selective laser excitation with the record of radiation spectrums with time resolution.

The convertible laser on LiF crystal is used in the capacity of resonance selective excitation. The duration of generation impulse is  $\sim 15$  nsec, and width of emission line is less than  $5\text{\AA}$ . The conversion region totally recovers the neodymium absorption spectrum  ${}^4I_{9/2} \rightarrow {}^4F_{3/2}$ . The spectrometer SDL-1 is used as spectral device. The luminescence signal coming from radiation sensor PEM-83 is given to strobe-integrator PAR-162 and recorded by logger. The duration of strobe impulse is  $\sim 0.5$  mcs, and delay time  $\tau=20$  mcs. The experiments are carried out at helium temperature.

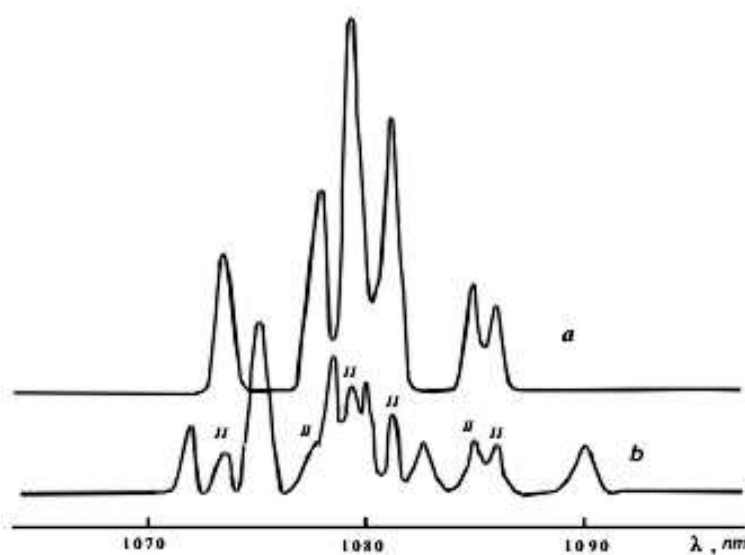


Fig.1. The luminescence spectrums  ${}^4F_{3/2} \rightarrow {}^4I_{9/2}$  of Nd<sup>3+</sup> ion in  $\alpha$ -Gd<sub>2</sub>S<sub>3</sub> at excitation in different absorption bands:  
a -  $\lambda_{excit}=900.4\text{nm}$ ; b -  $\lambda_{excit}=888.4\text{nm}$ . The delay time  $\tau=20\text{mcs}$ .

The  $^4F_{3/2} \rightarrow ^4I_{9/2}$  luminescence spectrums of Nd<sup>3+</sup> ion at excitation of each line in resonance absorption spectrum are identified in work [2]. The two types of centers are revealed and designated as center I and center II. The energy of low Stark component of  $^4F_{3/2}$  level in center I exceeds the one in center II. The schemes of Stark splitting of  $^4F_{3/2}$  and  $^4I_{9/2}$  Nd<sup>3+</sup> levels for each center have been constructed.

The scheme of Stark splitting of low laser level  $^4I_{11/2}$  has the special significance, i.e. the wave length generacy is defined especially by energy positions of Stark sublevels  $^4F_{3/2}$  and  $^4I_{11/2}$ . That's why luminescence spectrums  $^4F_{3/2} \rightarrow ^4I_{11/2}$  of neodymium ions have been investigated by us.

The luminescence spectrums  $^4F_{3/2} \rightarrow ^4I_{11/2}$  of Nd<sup>3+</sup> ion at excitation of each line in resonance absorption spectrum are presented on the fig.1. The six lines (fig.1,a) which one can

naturally identify as ones, related to one center, called center II in work [2], are observed in luminescence spectrum in the correspondence with theory in the case of line excitation, designated in absorption spectrum as lines II.

Using the given data, it isn't difficult to define the energy values, corresponding to Stark components of  $^4I_{11/2}$  Nd<sup>3+</sup> level for center II. These values are the following: 1800 cm<sup>-1</sup>; 1868 cm<sup>-1</sup>; 1880 cm<sup>-1</sup>; 1901 cm<sup>-1</sup>; 1928 cm<sup>-1</sup>; 1936 cm<sup>-1</sup>.

Such clear selection isn't observed at excitation of center I lines (fig.1,b). The lines of center II appear in luminescence center. Thus center II is excited at excitation in the absorption band of center I. Taking this into consideration, the energy values of corresponding Stark components of  $^4I_{11/2}$  Nd<sup>3+</sup> level for center I are defined. These values are: 1812 cm<sup>-1</sup>; 1840 cm<sup>-1</sup>; 1869 cm<sup>-1</sup>; 1881 cm<sup>-1</sup>; 1898 cm<sup>-1</sup>; 1960 cm<sup>-1</sup>.

- [1] Fizicheskiye svoystva khalkogenidov redkozemelnikh elementov. Pod.red. V.P. Juze. M. Nauka, 1973, 304s.  
(in Russian).

- [2] A.A. Mamedov, V.A. Smirnov, I.A. Shsherbakov. FTT, 1984, № 8, s.2405-2407.(in Russian).

### **A.Ә. Мәммәдов**

### **α-Gd<sub>2</sub>-S<sub>3</sub> MONOKRİSTALLARINDA NEODİM İONLARININ SPEKTROSKOPİK XASSƏLƏRİ**

α-Gd<sub>2</sub>-S<sub>3</sub> kristallarında  $^4F_{3/2} \rightarrow ^4I_{11/2}$  keçidində ionların şüalanma spektrleri identifikasiya edilmişdir. Hər bir Nd<sup>3+</sup> mərkəzi üçün stark səviyyələrinin enerjiləri müəyyən edilmişdir.

### **А.А. Мамедов**

### **СПЕКТРОСКОПИЧЕСКИЕ СВОЙСТВА ИОНОВ НЕОДИМА В МОНОКРИСТАЛЛАХ α-Gd<sub>2</sub>-S<sub>3</sub>**

В кристаллах α-Gd<sub>2</sub>-S<sub>3</sub> проведена идентификация спектров излучения ионов Nd<sup>3+</sup> на переходе  $^4F_{3/2} \rightarrow ^4I_{11/2}$ . Для каждого из центров Nd<sup>3+</sup> определены значения энергий штарковских подуровней.

*Received: 11.03.08*

## PHOTO- AND THERMO-LUMINESCENCE OF $\text{SrGa}_2\text{S}_4:\text{Eu}$ CRYSTALS

**B.G.TAGIYEV, S.A.ABUSHOV, O.B.TAGIYEV, F.A.KAZIMOVA**

*G.M. Abdullayev Institute of Physics of National Academy of Sciences,  
Baku AZ1143, Azerbaijan*

The photo-luminescence and thermo-luminescence (PhL and TL) of  $\text{SrGa}_2\text{S}_4$  crystals activated by  $\text{Eu}^{2+}$  in temperature interval 77÷320K have been investigated. It is seen that observable wide-band PhL in temperature interval 77–300K with maximum at 535 nm is connected with intracentral transitions  $4f^65d - 4f^7$  ( ${}^8\text{S}_{7/2}$ ) of  $\text{Eu}^{2+}$  ions and narrow-band TL is caused by discrete and quasicontinuously distributed electron traps with activation energies:  $E_c$ - 0,2 и  $E_c$ - ( 0,25- 0,53) eV in forbidden band.

### **Introduction.**

$\text{SrGa}_2\text{S}_4$ : Eu is related to tiogallate group with general formula  $\text{AB}_2\text{C}_4$  (A-Ca, Ba, Sr, Al; B - Ga, In; C- S, Se). The photo-luminescence (PhL) of doped and non-doped crystals of  $\text{AB}_2\text{C}_4$  type has been investigated in the works [1-4], and thermo-luminescence (TL) of these compounds excluding  $\text{CaGa}_2\text{S}_4$ ,  $\text{EuGa}_2\text{S}_4$  и  $\text{CaGa}_2\text{Se}_4$  compounds [5-7], hasn't been investigated. As these compounds are wide-band semiconductors, so trap levels in forbidden band should play the essential role in generation and recombination processes. TL investigation is the one of suitable method for definition of trap energy position directly participating in PhL and TL processes. In the given paper the results of PhL and TL investigations in  $\text{SrGa}_2\text{S}_4$ , activated by rare-earth ions  $\text{Eu}^{2+}$  (REI) are given.

### **Experiment technique.**

$\text{SrGa}_2\text{S}_4$ : Eu compound is synthesized from binary compounds  $\text{SrS}$ ,  $\text{Ga}_2\text{S}_3$  and  $\text{EuF}_3$ , taken in stoichiometric ratios in preliminary degasified quartz ampoules up to  $10^{-2}\text{Pa}$ . The concentration of  $\text{Eu}^{2+}$  is varied from 1 up to 7at.%. The powder mixture of the given compounds is endured in sulfur atmosphere at temperature 1230°C. TL is investigated on technique described in [6]. The samples are excited by mercury lamp light PRK-4 at temperature of liquid nitrogen. The sample temperature is defined with the help of differential thermocouple cuprum-constantan. PhL spectrums are investigated on spectrometer CDL-1. The continuous helium-cadmium laser ( $\lambda = 441,6\text{ nm}$ ) is used for excitation of PhL samples  $\text{SrGa}_2\text{S}_4$ : Eu.

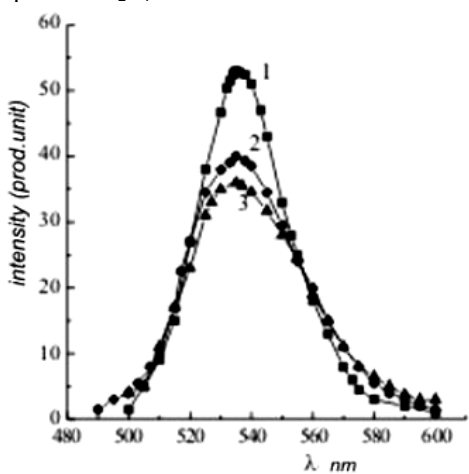


Fig.1. Photo-luminescence spectrum of  $\text{SrGa}_2\text{S}_4:\text{Eu}$  (5%) at temperatures: 1-140K, 2-230K, 3-286K.

PhL spectrums  $\text{SrGa}_2\text{S}_4$ :5%Eu at temperatures 120K, 230K and 286 K (curves 1, 2 and 3) are presented

on the fig.1. It is seen that they cover the spectral region 490-600 nm and their maximums correspond to wave length 535 nm, i.e. maximum energy position doesn't change and intensity decreases with temperature increase.

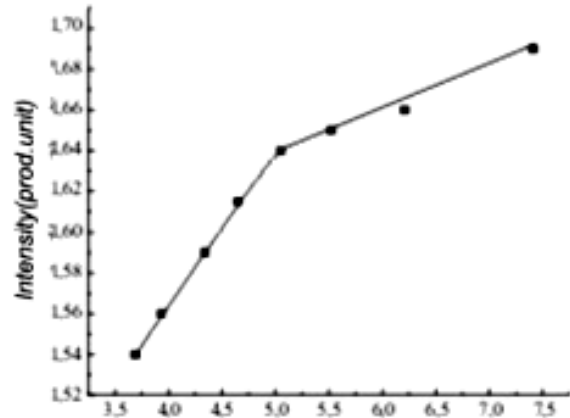


Fig.2. The dependence of photo-luminescence intensity of  $\text{SrGa}_2\text{S}_4:\text{Eu}$  (5%) crystals on temperature.

The temperature dependence of photo-luminescence band intensity with maximum 535 nm in  $\lg I \sim 10^3/T$  coordinates is presented on the fig.2. It is seen that intensity in temperature interval 80÷200K weakly depend on temperature, and later temperature increase leads to strong intensity decrease. The activation energy of photo-luminescence temperature quenching which is equal to 0,016 eV is defined on high-temperature inclination of this dependence.

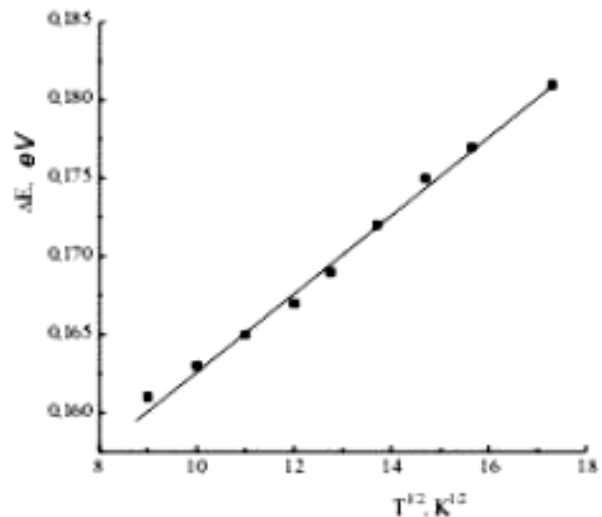


Fig.3. The dependence of PhL band half-width of  $\text{SrGa}_2\text{S}_4:\text{Eu}$  (5%) crystals.

The investigation of photo-luminescence spectrums, its temperature dependence of half-width and intensity of wide

band with maximum at 535 nm of  $\text{SrGa}_2\text{S}_4$ : Eu crystals, and also the dependence of this band intensity on activator content allows us to establish that this photo-luminescence band is connected with intracentral transitions  $4f^65d \rightarrow 4f^7(^8S_{3/2})$  of  $\text{Eu}^{2+}$  ion.

The temperature dependence of PhL band half-width with maximum at 535 nm in  $\Delta E$  and  $T^l$  coordinates<sup>2</sup> is presented on the fig.3. It is seen that this dependence has linear character. The temperature dependence of half-width is also calculated by formula [8]:

$$\Gamma(T) = \sqrt{8 \ln 2} \cdot h \nu \cdot \sqrt{s} \sqrt{\coth\left(\frac{h \nu}{2kT}\right)} \quad (1)$$

where  $s$  is Huang-Rice factor,  $h \nu$  is phonon energy,  $k$  is Boltzman constant. The taken values  $s$  and  $h \nu$  are equal to 12 and 35 meV correspondingly at  $\Gamma(T)$  calculation [9]. As it is seen from fig.3, the experimental points are on the calculated straight line. The linear dependence of half-width  $\Delta E = f(T)$  is connected with electron interaction in excited state with lattice high-frequency oscillations (optical phonons) [10, 11].

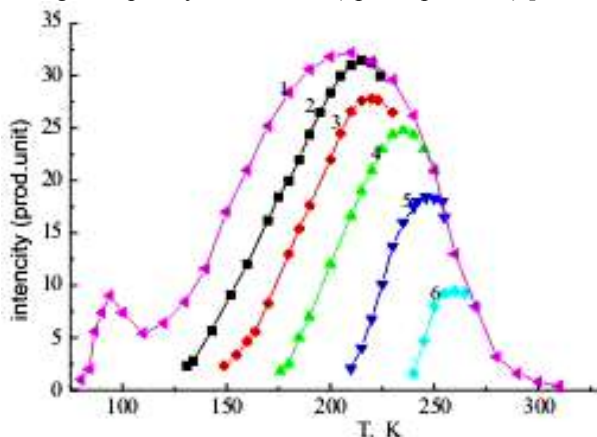


Fig.4. The thermo-luminescence spectrum of  $\text{SrGa}_2\text{S}_4$ : Eu crystal.

TL spectrum of  $\text{SrGa}_2\text{S}_4$ : 5%Eu crystals at heat rate 0,67K/c is presented on the fig.4 (curve 1). As it is seen it is wide-band one and covers the temperature interval 80÷320 K. The relative weak narrow peak with maximum at 95K( $\Delta T=20$ K) which collides with intensive wide band with maximum at 210 K is observed on this spectrum. The big half-width of TL wide band ( $\Delta T=108$  K), the complex

operation of its initial increase allows supposing that this band is connected with quasicontinuously distributed trap levels in forbidden band  $\text{SrGa}_2\text{S}_4$ : Eu crystals. The “thermal purification” of thermo-luminescence spectrum of investigated samples is carried out by us for confirmation of this supposition.

As it is seen from fig.4 (curves 2, 3, 4, 5, 6) the more 5 peaks with maximums at 216, 224, 235, 246 and 260 K are revealed after “thermal purification”. The trap depth of occurrence situated in interval 0,25-0,53 eV is defined on initial increase of these curves.

The results of thermo-luminescence measurements in investigated samples are theoretically analyzed on the model basis described in [9-13]. The wide maximums in thermo-luminescence spectrums are character for triple alkali- and rare-earth chalcogenides included in  $M^{2+}M_2^{3+}X_4$  group. For example, thermo-luminescence spectrum  $\text{CaGa}_2\text{S}_4$ :  $\text{Eu}^{3+}$  consists of wide residual structure with  $T_{max}$  in interval 130 K and peak half-width is 80K [5]. It is seen by method of “thermal purification” that TL spectrums  $\text{CaGa}_2\text{S}_4$ :  $\text{Eu}^{3+}$  are caused by electron traps quasicontinuously distributed in energy interval  $E_c$  is (0,1-0,3) eV.

The trap activation energy in  $\text{SrGa}_2\text{S}_4$ :  $\text{Eu}^2$  crystals is also defined by the method supposed in [14] on maximum temperatures of thermo-luminescence spectrum on formula:

$$E_a = AkT_m \quad (2)$$

where  $E_a$  is trap activation energy,  $A$  is constant,  $k$  is Boltzman constant. In work [15] firstly it is theoretically shown that  $A$  value in (2) is equal to 25. The further investigations [16] show that  $A$  can have values in interval 15-30 in the dependence on private factor, heat rate and kinetic order of relaxation process. A value is taken as equal one to 5 at calculation. The trap depth of occurrence calculated by formula (2) for  $\text{SrGa}_2\text{S}_4$ :  $\text{Eu}^{2+}$  is 0,2eV for low-temperature peak ( $T_m=95$ K) and 0,45eV for wide band( $T_m=210$  K) correspondingly.

Thus, the wide-band PhL which is caused by intracentral transitions  $4f^65d \rightarrow 4f^7(^8S_{7/2})$  of  $\text{Eu}^{2+}$  ions is observed in  $\text{SrGa}_2\text{S}_4$  activated by  $\text{Eu}^{2+}$  ions and low-temperature narrow-band and wide-band TL are connected with electron traps, discrete and quasicontinuously distributed in forbidden band  $\text{SrGa}_2\text{S}_4$ :  $\text{Eu}^{2+}$ . Their depth of occurrence  $E_c$  is 0,2eV and  $E_c$  is (0,25 – 0,53) eV correspondingly.

- 
- [1] M.R.Davalos, A.Garcia, C.Fonassier and P.Hagenmuller. Journal of Solid State Chemistry, 1989, 83, p.316-323
- [2] A.N. Georgobiani, B.G. Tagiyev, O.B. Tagiyev, B.M. Izzatov. Neorg. mat. 1995, t. 31, №1, s.19-22. (in Russian).
- [3] Ch. Barthou, P.Benalloul, B.Tagiye, O.B. Tagiyev, S.A.Abushov, F.Kazimova and A.N.Georgobiani. J.Phys.:Condens matter, 2004, 16, pp.8075-8084.
- [4] H. Najafov, A.Kato, H.Toyota, K.Twai, A.Bayramov, and S.Lida. J. Appl. Phys., 2002, part 1, 41(3A), p.1421.
- [5] A.N. Georgobiani, Yu.N. Emirov, A.N. Gruzincev, Ye. M. Zobov, B.G. Tagiyev, B.M.Izzatov, P. Benaloul, K.Bartou, I.Vang, Syu.Syun. Termoluminescenciya tiagallatov  $\text{CaGa}_2\text{S}_4$  s primeciyu Eu. Kratkiye soobshsheniya po fizike FIAN, 2001, №1, s.3-9. (in Russian).
- [6] A.N. Georgobiani, S.A. Abushov, F.A. Kazimova, B.G. Tagiyev, O.B. Tagiyev, P.Benalloul, K.Bartou. Neorg. mat. 2006, №4, s.1304-1307. (in Russian).
- [7] B.G. Tagiyev, S.A. Abushov, O.B. Tagiyev. Fizika, 2007,c.XIII, N4, c.203-205
- [8] B.Henderson, and G.Imbusch, Optikal spectroscopy of inorganic solids, Oxford: clarendon, 1989.
- [9] C.Charrier, C.barthou, P.Benalloul, J.M.Prigerio, J.Lumin. 111, 2005, 147.

## PHOTO- AND THERMO-LUMINESCENCE OF SrGa<sub>2</sub>S<sub>4</sub>:Eu CRYSTALS

- [10] Dorenbos P. J.Phys.:Condens. Matter, 2003,15, p.575-594.
- [11] Dorenbos P. J. luminescence. 2003, 104,p.239-260.
- [12] Ch.B. Lushshik. K teorii termoelektricheskogo visvechivaniya. DAN SSSR. 1995. t.104. s.64. (in Russian).
- [13] R.Chen. J.Appl.Phys., 1969; v.40, p. 570.
- [14] D.R. Rao. Phys.Stat. Solidi a; 1974, v.22, p. 337.
- [15] Yu.A. Gorokhovotskiy, G.A. Bordovskiy. Termoaktivacionnaya tokovaya spektroskopiya visokoomnikh poluprovodnikov i dielektrikov. M.: Nauka, 1991, 245 s. (in Russian).
- [16] A.Mentel. Phys.Status. Solidi A, 1992. v.130., p.169.
- [17] F.Urbach. Wein.Ber. Abt. 1930.B., 11a, N 139, p.353-360.
- [18] J.T Randall, Pros.Roy.Soc. A., 1945. v. 84.p. 366-389.
- [19] K.W.Boer,S.Oberlander. Ann.Phys.Soc.1948,N60, p.574-590.

**B.H. Tağıyev, S.A. Abuşov, O.B. Tağıyev, F.A. Kazimova**

### **SrGa<sub>2</sub>S<sub>4</sub>:Eu<sup>2+</sup> KRİSTALLARININ FOTO – VƏ TERMOLÜMİNESSENSİYASI**

Eu<sup>2+</sup> ionları ilə aktivləşdirilmiş SrGa<sub>2</sub>S<sub>4</sub> kristallarının fotoluminessensiyası və termoluminessensiyası (FL və TL) 77-320K temperatur oblastında tədqiq edilmişdir. Müəyyən edilmişdir ki, maksimumu 535 nm dalğa uzunlığında müşahidə edilən genişzolaqlı FL Eu<sup>2+</sup>ionlarının mərkəzdaxili  $4f^65d - 4f^7$ <sup>8</sup>S<sub>7/2</sub>) keçidləri ilə, maksimumları 95K və 210K olan darzolaqlı və genişzolaqlı TL isə aktivləşmə enerjiləri uyğun olaraq E<sub>c</sub>-0.2 və E<sub>c</sub>-(0.25-0.53)eV olan elektron tələləri ilə bağlıdır.

**Б.Г. Тагиев, С.А. Абушов, О.Б. Тагиев, Ф.А. Казымова**

### **ФОТО- И ТЕРМОЛЮМИНСЦЕНЦИЯ КРИСТАЛЛОВ SrGa<sub>2</sub>S<sub>4</sub>:Eu**

Исследованы фотолюминесценция и термолюминесценция (ФЛ и ТЛ) кристаллов SrGa<sub>2</sub>S<sub>4</sub>, активированных Eu<sup>2+</sup> в области температур 77÷320К. Показано, что наблюдаемая широкополосная ФЛ в области температур 77-300К с максимумом при 535 нм связана с внутрицентровыми 4f<sup>6</sup>5d – 4f<sup>7</sup> (<sup>8</sup>S<sub>7/2</sub>) переходами ионов Eu<sup>2+</sup>, а узкополосная и широкополосная ТЛ обусловлена соответственно дискретно и квазинепрерывно распределенными в запрещенной зоне электронными ловушками с энергиями активации: E<sub>c</sub>- 0,2 и E<sub>c</sub>-( 0,25- 0,53) эВ.

*Received: 15.04.08*

## METAL INTERLAYER NANO-PARTICLES IN BISMUTH TELLURIDE

F.K. ALESKEROV, S.Sh. KAGRAMANOV

*“Selen” scientific production association of Azerbaijan National Academy of Sciences*

*F. Agayev str., 14, Baku-1143, Azerbaijan*

M.A. RAMAZANOV

*Baku State University AZ-1148, Z. Khalilov str., 23*

The interlayer nano-aggregates, forming between  $T_e^{(1)} - T_e^{(1)}$  layers in  $\text{Bi}_2\text{Te}_3$  are the new class of fractal nano-objects. Their aggregation takes place at atom agglutination on the same mechanisms as the known solid-state fractal structures formed on free faces of crystal in unlimited volumes, have.

The analysis of nano-fragment fractality characters is carried out on the basis of AFM-images and X-ray-diffractometer photos in  $\text{Bi}_2\text{Te}_3\text{-metal}$  layered systems.

### Introduction

The article is dedicated to nano-particle formation problems in crystals of  $A_2^V B_3^{VI}$  type the Van der Waals bond of which is weak one. Indeed, the layered compound themselves are capable to “captivate” the guest molecules in the crystal growth process and also at intercalation. The class of intercalated compounds is practically unlimited on, i.e. there is big number of metals (especially easily-diffusing with small ion radii) which can be introduced in different layered crystals (graphite, GaSe, InSe,  $\text{Bi}_2\text{Se}_3$ ,  $\text{Bi}_2\text{Te}_3$ ,  $\text{Sb}_2\text{Te}_3$  and others). The combination of metal layers with semiconductor ones on microscopic level can lead to crystal obtaining with new electron properties. Such nano-objects with the position of high technology can be the subject of special investigations. The filling of nano-tubes by metals (Cu, Ni, Fe, Ag) with the goal of nano-wire obtaining covered by carbonic “wear” is mentioned in work [1].

The analysis shows that nano-chemistry produces the own nano-particle objects, nano-containers, nano-reactors. The two key conceptions: nano-particles and nano-reactor have been determined. The first one characterizes dimensional parameter; the second one defines the nano-particle function [1].

It is necessary to note the one more article [2] in which the approaches to the synthesis of nano-composites on the basis of zero-, one- and two-dimensional solid-state nano-reactors formed by zeolite cavities or interlayer empty spaces of layered compounds have been considered. The work on obtaining of active nano-fibers  $\text{Bi}_2\text{Te}_3$  in matrix of porous aluminum oxide is known [3]. However, the fractal particles of nano-meter dimension [4] form in  $\text{Bi}_2\text{Te}_3$  itself as a result of crystallization in interlayers.

The fractal structures obtained in [4] are analyzed with the position of physics of fractal clusters (FC). They form in the crystal growth processes at agglutination of solid particles [5-6].

The study of  $\text{Bi}_2\text{Te}_3\text{-metal}$  surface morphology and their comparison with multi-fractals of complex signals, the consideration of interlayer fractal aggregates with observable nano-layer assemblies [7-9] require the clearance in the perception of self-organized nano-particles on the basis of cuprum, nickel and argentums between  $T_e^{(1)} - T_e^{(1)}$   $\text{Bi}_2\text{Te}_3$ .

In this connection the new experimental data on the study of (0001)  $\text{Bi}_2\text{Te}_3$  surface morphology by doped metals are required.

Taking into consideration the above mentioned it's possible to formulate the following tasks: firstly, how Van der Waals crack  $T_e^{(1)} - T_e^{(1)}$  in  $\text{Bi}_2\text{Te}_3$  can be considered as nano-reactor for metal (Cu, Ni and Ag) impurities and secondly, what are the fractality characters of forming interlayer nano-fragments.

### Investigation technique

$\text{Bi}_2\text{Te}_3$  compound is obtained by thermal synthesis at  $900\text{-}950^\circ\text{K}$  which usually is carried out in quartz ampoules where Bi, Te and impurities (Ni or Cu, Ag) are put in necessary relation. After alloy synthesis they are put in graphitized ampoules (by diameter 9 mm), melted again and then the single crystalline ingots are obtained by vertical directed crystallization at temperature gradient  $\Delta T=100\text{grad/cm}$  and solidification rate  $1\text{cm/h}$ . The impurity nano-particle morphology in such crystals after chipping along (0001)  $\text{Bi}_2\text{Te}_3$  plane is investigated. Such samples  $\text{Bi}_2\text{Te}_3\text{-Me}$  can be considered as intercalation ones from the structural point of view, because the layers of matrix-master and matrix-guest (Cu, Ni and Ag) can be emphasized. Here the increase of interlayer distance at metal atom penetration into interlayer empty spaces is character because of weak chemical bond between  $T_e^{(1)} - T_e^{(1)}$ .

The diffusion intercalation of Cu, Ni and Ag atoms is carried out at  $500^\circ\text{K}$ . For this purpose the metals are sprayed perpendicular to basis plane (0001) by thermal method on clean surface. Later the introduction (intercalation) process along (0001) layers is carried out at temperature gradient  $\Delta T=30\text{grad/cm}$ , the sprayed sample part is hot side. Note that coefficients of diffusion for all impurities are strongly anisotropic one, and for Cu, Ni and Ag along (0001) basis surface they are too big ones that promotes to their easy diffusion into  $T_e^{(1)} - T_e^{(1)}$  space during several hours. The (0001) surfaces have been investigated on the samples obtained by such method and the electron-microscopic images and X-ray-diffractometer pictures have been analyzed.

The electron-microscopic images are obtained at atom-force microscope (AFM) of NC-AFM trend. X-ray-diffractometer investigations are carried on the installation of *Philips Panalytical* trend. The preparation of atomically clean surface by the way of chip by special instruments is carried out along (0001) basis plane in the air before experiments.

AFM-images in 2D scale, nano-particle distribution functions with similar dimensions (Fourier-spectrums), nano-fractal density of distribution on (0001) surface on height (Z) (histograms) have been investigated for all doped samples besides AFM-images of (0001)  $\text{Bi}_2\text{Te}_3$  in 3D scale. However, we don't show them in the connection with limitation of number of figures.

### The experimental results and their discussion

The discussion subject is of fractal character revealing between  $T^{(1)}$ - $T^{(1)}$  layers in  $\text{Bi}_2\text{Te}_3<\text{Cu}>$ ,  $\text{Bi}_2\text{Te}_3<\text{Ni}>$  and  $\text{Bi}_2\text{Te}_3<\text{Ag}>$  nano-aggregates in the comparison of their morphology with fractal systems forming on free surface of solid bodies in unlimited volume.

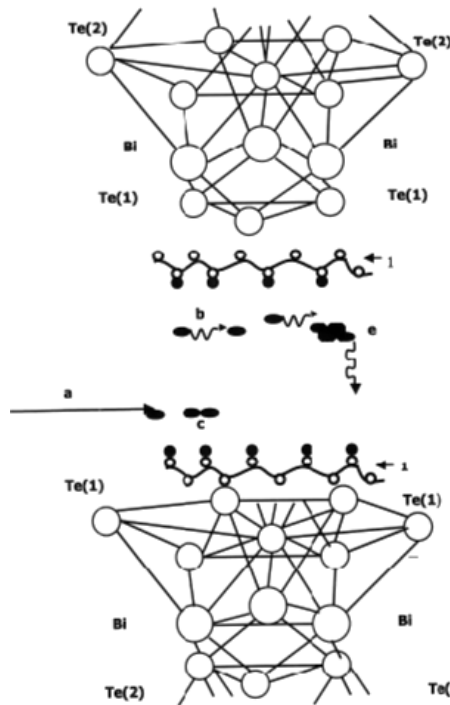


Fig.1. The scheme of atom distribution of bismuth and telluride atoms in  $\text{Bi}_2\text{Te}_3$  structure and diffusion ways at intercalation of easily-diffused impurities in interlayers:  
a is atom penetration along (0001) plane;  
b is formation of new island;  
c is particle diffusion;  
d is aggregation;  
e is island diffusion.

f is particle aggregation between  $T_e^{(1)} - T_e^{(1)}$ .

The guest atoms (Cu, Ni, Ag...) localize in bismuth telluride in Van der Waals empty spaces formed by atoms of neighbor layers of telluride quintets. Each quintet consists of five simple layers. The atoms of separate layer are similar and form the hexagonal lattice. The atoms of each following layer are posited under the triangle centers formed by the atoms of the previous layer.  $T_e^{(1)}$  atoms have on three atoms

(six Bi atoms) from each adjacent layer in the capacity of near-neighbors.  $T_e^{(1)}$  connects with three *Bi* atoms from the one side, and with three  $T_e^{(1)}$  atoms from the another one, i.e. there are two essentially different places for *Te* atoms in the lattice. The scheme of atom positions in  $\text{Bi}_2\text{Te}_3$  crystal lattice and diffusion ways (marked by the arrow (a)) and particle aggregations between telluride quintets (b, e, c) leading to nano-layer formation (1) are given on the fig.1. The distance between quintets is comparably big, i.e.  $T_e^{(1)} - T_e^{(1)}$  bond is very weak one. The vacancies after *Te*, complexes of "dislocations – impurity atom" type, boundaries of blocks and grains, micro-cracks, concentration heterogeneities and micro-segregations [7] can be the most probable places of accumulation and nano-fragment formation on the Cu, Ag, Ni basis.

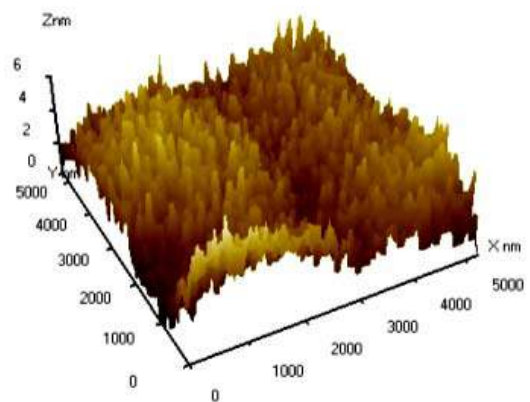


Fig.2. AFM- image of (0001) surface of bismuth telluride intercalated by Cu in 3D scale.

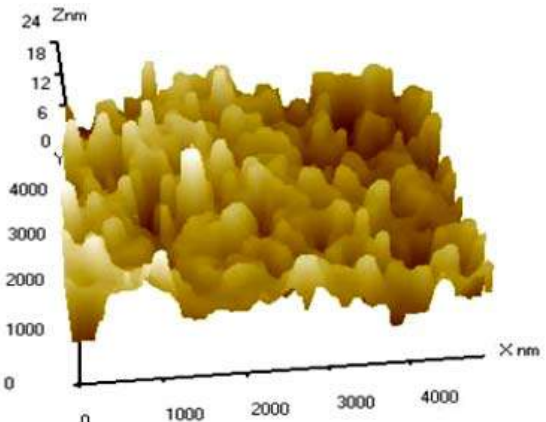


Fig.3. AFM-image of (0001) surface of self-intercalated  $\text{Bi}_2\text{Te}_3<\text{Cu}>$  (in 3D scale).

Let's give the experimental data by the example of  $\text{Bi}_2\text{Te}_3<\text{Cu}, \text{Ni}$  and  $\text{Ag}$  system. From fig. 2-3 it is seen what nano-crystalline formations appear on (0001) surface at cuprum intercalation and at synthesis of bismuth telluride towards with Cu with following crystallization. The cuprum penetrates into layers as in nano-container not interacting with super-stoichiometric components of  $\text{Bi}_2\text{Te}_3$ : tellurium or bismuth at intercalation at temperature 500°K. X-ray-diffraction peaks from cuprum nano-particles (they aren't

given here) evidence about it. X-ray-diffractograms (fig.4) of  $\text{Bi}_2\text{Te}_3\text{-Cu}$  non-intercalated samples (obtained in the crystal growth process) show the peaks mainly from nano-particles CuTe, Cu and  $\text{Cu}_{0.647}\text{Te}_{0.353}$ . Here  $T_e^{(1)} - T_e^{(1)}$   $\text{Bi}_2\text{Te}_3$  plays not only nano-reactor role (as it was mentioned in [1-2]), in which Ni, CuTe and  $\text{Cu}_{0.647}\text{Te}_{0.353}$  form, but the role of nano-container for cuprum (fig.4).

The morphology of (0001)  $\text{Bi}_2\text{Te}_3$  surface in three-dimensional scale (3D) at Ni intercalation is presented on the fig.5; here the fractal nano-structures mainly consist of Ni.

The supposed diffusion ways of particles and their aggregation with following formation of fractal aggregates (fig.1) are probably connected with filling impurity process of places round dislocation pits and vacancies after Te on (0001)  $\text{Bi}_2\text{Te}_3$  surface. The beginning of nano-cell formation

takes place in impurity diffusion processes along basis surface (0001) and with nano-fractal growth from surface on Te vacancies on the same telluride quintets. The gradually growing “towers”-benches (FC) form as a result of nano-fragment dimension increase from the surface. The surfaces on (0001) basis plane because of interacting and contacting between each other that is visually reflected on their topography. The coagulation process achieves its peak at which the parallel “mountain hills” form unique nano-fractal surface which we observe on the fig.6 for  $\text{Bi}_2\text{Te}_3\text{-Ni}$  system. Here the boundary separating the fractal surface (left one) with right part (which is similar and close one to single fractals) is clearly seen.

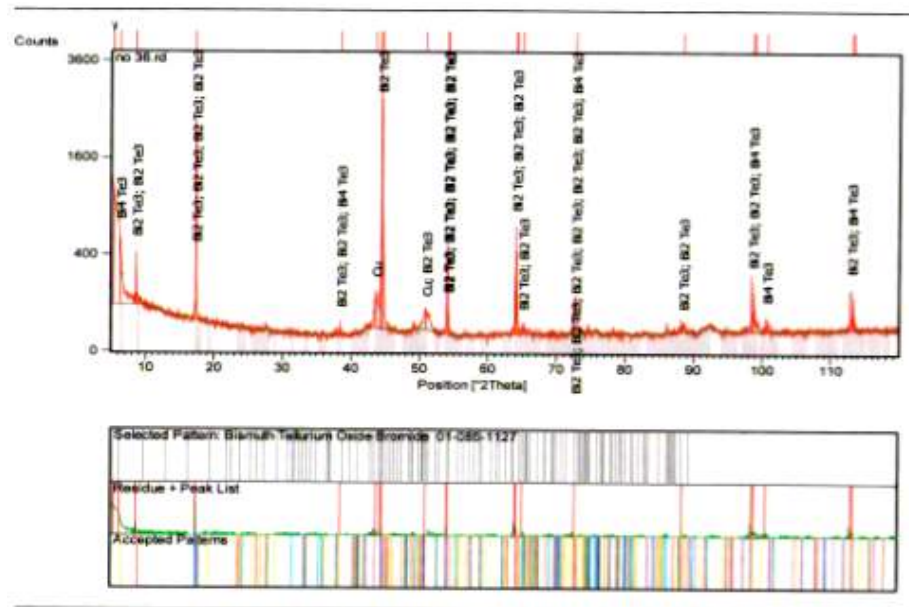


Fig. 4. X-ray-diffractometer photo of  $\text{Bi}_2\text{Te}_3$  doped by Cu.

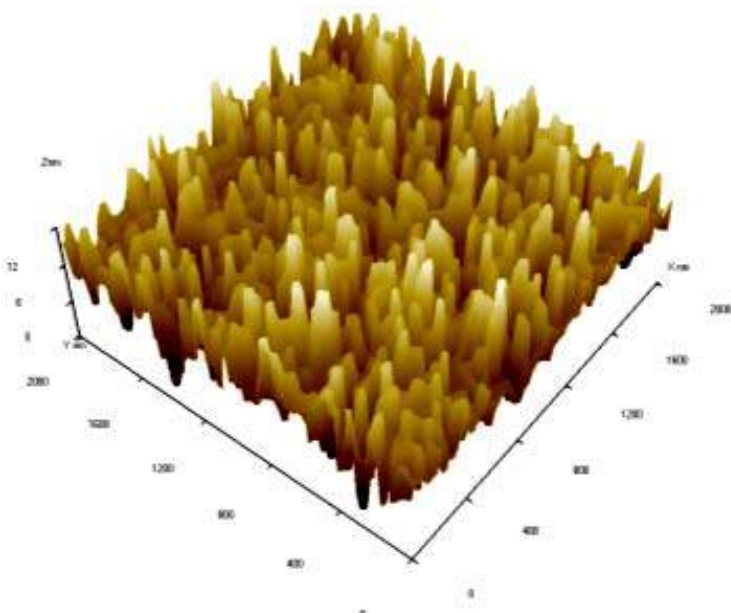


Fig. 5. AFM-image of (0001) surface  $\text{Bi}_2\text{Te}_3\text{-Cu}$  (in 3D scale).

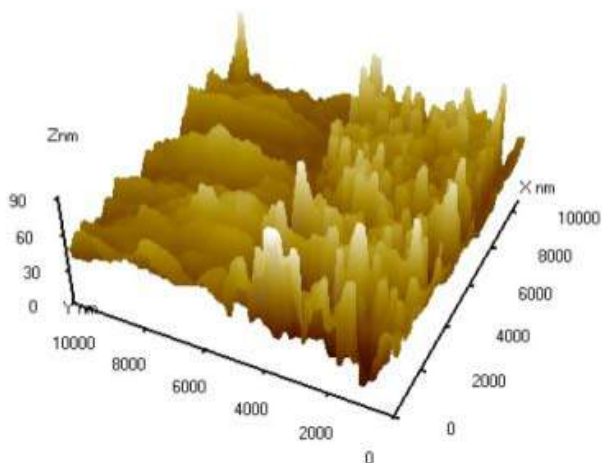


Fig. 6. AFM-image of fractal surfaces in  $\text{Bi}_2\text{Te}_3\text{-Ni}$  system.

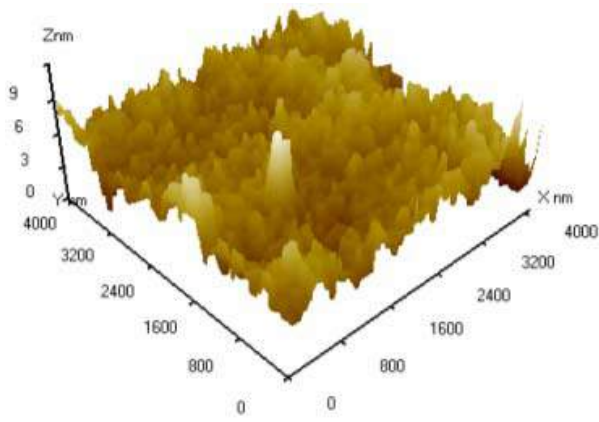


Fig. 7. (0001) surface in solid solution ( $\text{Bi}_2\text{Se}_3$  4mol% -  $\text{Bi}_2\text{Te}_3$  96mol%) doped by argentums (AFM-photo in 3D scale).

The unique fractal surfaces between  $T_e^{(1)} - T_e^{(1)}$  in  $\text{Bi}_2\text{Te}_3$  are obtained for all three impurities: Cu, Ag and Ni. The analogous fractal pictures obtained with the help of consistent occasional Foss additions algorithm are given in [6].

Almost all filling stages of Van der Waals band are connected with the process of rapid introduction of easily diffused impurities (Ag, Cu, Ni) in  $\text{Bi}_2\text{Te}_3$  along basis plane as a result of diffusion directions (direction (a) on the fig.1).

The model of diffusion-limited aggregation (DLA) is often used for revealing of real structure formation mechanisms. Using some elements of DLA [4-6] we accept the model scheme connecting formation processes of intralayer solid-state fractal structures: penetration into layer between  $T_e^{(1)} - T_e^{(1)}$  of easily-diffused atoms) Cu, Ni and Ag), diffusion on basis plane (0001) and DLA process.

We have considered the intralayer fractal aggregates (and their fractal measures) and compared them with forming FC on free surface, growing on the model of two-dimensional aggregation limited by diffusion [6,8]. This means that FC grows from the germ on telluride vacancies. Making occasional hunts Cu, Ag and Ni atoms move on basis surface (0001) because of gradient diffusion. Contacting with germ of initial cluster the moving impurity atoms get close to it. Further, the another atom making occasional hunts and

contacting with cluster increases its dimensions begins to move from new point in the space between  $T_e^{(1)} - T_e^{(1)}$ .

The dimension of interlayer space  $T_e^{(1)} - T_e^{(1)}$  in  $\text{Bi}_2\text{Te}_3 \sim 0.3$  nm, the height of nano-particles is in the limits 10-20 nm. Here it is possible the converse pressing-expansion of  $T_e^{(1)} - T_e^{(1)}$  layers like "bellows". The distance  $T_e^{(1)} - T_e^{(1)}$  can be regulated adjusting the investigated nano-reactor on the given volume by the way of filling (penetration) by impurities. The nano-formations on (0001)  $\text{Bi}_2\text{Te}_3$  surface also reveal the characters about multi-fractal structure of interlayer fragments. Their growth dynamics accepts the quantitative and qualitative description with the help of known physics conception of solid-state multi-fractal structures in the case of their obtaining in the unlimited volume [6,9].

For establishment of obtained structure fractality we need: to check the self-similarity, define the boundaries of self-similarity, define the fractal dimensionality (D). Here the main attention is paid to the one from the system classes with fractal structure. The fractal dimensionality of such nano-objects forming in three-dimensional space at association of solid particles (on aggregation model: particle-, cluster, Brownian motion) is  $D=2.46 \pm 0.05$  [5]. The qualitative characteristics of the fact how formed nano-aggregates have filled the space between  $T_e^{(1)} - T_e^{(1)}$  of layered  $\text{Bi}_2\text{Te}_3$ . The nano-objects are formed in this space and in solid solution ( $\text{Bi}_2\text{Te}_3 - \text{Bi}_2\text{Se}_3$ ) $\text{-Ag}$  accompanying by the association of close dimension particles (for example:  $\text{Ag}_2\text{Te}$  and  $\text{Ag}_2\text{Se}$ ) (see fig.7).

It is necessary to use also the multi-fractal theory [8-9] for description properties of self-similarity and complex scaling observable in obtained nano-structures. In the given case as it is seen from the fig.6 the investigated region is formed from two parts. Moreover, each of them has its own self-similarity property, and this factually means the multi-fractality: the multi-fractal is the union of fractal ensembles of different dimensionalities. The nano-objects presented on the fig.2 and 5 are more or less close to single fractal formations (i.e. D with some error presents itself the constant value). As it is known [8] the spectrum of multi-fractal processes can't be described as unique D indicator. Probably, the multi-fractals here form from the set of collected and single fractals pressed to each other (their can be analyzed on the basis of FC conception grown up from surface (0001) [5-6].

The obtained nano-objects on geometric dimension character have nano-dimensions on all three directions: their height doesn't exceed 15-20 nm, width and length varies in the limits less than 100 nm; i.e. the given nano-objects on classification [2] can be related to nano-particles with unordered distribution. However, particles by  $\sim 5\text{-}10$  nm (clusters) sizes are observed in (0001) surface morphology.

These nano-fractals and surfaces formed by them can be considered as the one from main factors defining the morphology of interlayer space between  $T_e^{(1)} - T_e^{(1)}$ .

## Conclusions

The analysis of (0001)  $\text{Bi}_2\text{Te}_3\text{-Cu,Ni}$  and  $\text{Ag}$  surface morphology shows that nano-particles (in the form of nano-

fractal formations) can form between  $T_e^{(1)} - T_e^{(1)}$  layers with participation of different surface defects.

The reason of rapid growth of nano-fractal “towers” probably is that Cu (Ni, Ag) go to the initial nano-islands, draining from not only impurities of small dimensions accumulated in vacancies, but from atoms diffusing along plane (substrate), “feeding” and changing the heights of fractal formations.

The interlayer impurity nano-fragments are characterized by interaction between its elements.

What is the dimensionality of investigated structure: if we consider them as atom accumulation separately then each particle (cluster, FC) is one dimensional one; their location on the (0001) surface between  $T_e^{(1)} - T_e^{(1)}$  is two-dimensional one; however, taking into consideration their fractals the dimensionality is between 2 and 3, i.e. it is fractional one.

- 
- [1] A.L.Buchachenko. Nanokhimiya-pryamoy put k visokim tekhnologiyam novogo veka, Uspekhi khimii, RAN, 72 (5) 2003, s.419-437.
  - [2] Yu.D. Tretyakov, A.V. Lukashin, A.A. Eliseev. Sintez funktsionalnikh nanokompozitov na osnove tverdofaznikh nanoreaktorov. Uspekhi khimii 73 (9), 2004, s. 974-998.
  - [3] O. Rabin, P.R. Herz, S.B. Cronin, L .Lin, A.I. Akinwande, M.S. Dresselhaus. Mater. Res.Soc. Symp.Proc. 637, D.4.7.1, 2001.
  - [4] F.K. Aleskerov, S.Sh. Kakhramanov, E.M. Derun, M.G. Pishkin, G. Kavei. Nekotorie osobennosti formirovaniya nanoobektov v mejsloevom prostranstve kristallov tipa  $\text{Bi}_2\text{Te}_3$ , J. Fizika, NAN AR, 2007, tom XII, №4, s.41-45.
  - [5] B.M. Smirnov. Fizika fraktalnikh klasterov, Moskva, «Nauka», 1991, s.134.
  - [6] Jens Feder. Fractals, Department of Physics University of Oslo Norway, 1988 Plenum Press, New York, p.250
  - [7] I.V. Gasenkova, T.E. Svechnikova. Issledovanie strukturi monokristallov tverdikh rastvorov na osnove tellurida vismuta. Dokladi VIII mejgosudarstvennogo seminara (2002) – Termoelektriki i ikh primeneniya, s. 145-150.
  - [8] A.N. Pavlov, V.S. Anichenko. Multifraktalniy analiz slojnikh signalov. Uspekhi fizicheskikh nauk, t.177, № 8, 2007, s. 859-876.
  - [9] V.I. Roldugin. Fraktalnie strukturi v dispersnikh sistemakh. Uspekhi khimii RAN, 72 (10) 2003, s. 831-859.

**F.K. Ələsgərov, S.Ş. Qəhrəmanov, M.Ə. Ramazanov**

### **Bi<sub>2</sub>Te<sub>3</sub>-UN LAYLAR ARALIĞINDAKI METAL NANOZƏRRƏCİKLƏRİ**

Bi<sub>2</sub>Te<sub>3</sub>- laylar  $T_e^{(1)} - T_e^{(1)}$  arasında yaranan nanoaqreqatlar yeni tipi fractal nanoobyektlərdir. Onlar metalların  $T_e^{(1)} - T_e^{(1)}$  aralığında diffuziya hərəkəti zamanı formalasır; belə nanosistemlərin yaranma mexanizmləri isə sərbəst təbəqələrdə əmələ gələn adi fractal strukturları ilə eynidir.

Nanofraqmentlərin fraktallık analizi elektron mikroskopik (AEM) və rentgendifraktometrik şəkilləri əsasında aparılır.

**Ф.К. Алескеров, С.Ш. Каҳраманов, М.А. Рамазанов**

### **МЕЖСЛОЕВЫЕ НАНОЧАСТИЦЫ МЕТАЛЛОВ В ТЕЛЛУРИДЕ ВИСМУТА**

Межслоевые наноагрегаты, формирующиеся между слоями  $T_e^{(1)} - T_e^{(1)}$  в Bi<sub>2</sub>Te<sub>3</sub> составляют новый класс фрактальных нанообъектов. Их агрегация происходит при слиянии диффундирующих атомов по тем же механизмам, что и в известных твердотельных фрактальных структурах, сформированных на свободных гранях кристаллов в неограниченном объеме.

Анализ признаков фрактальности нанофрагментов проведен на основе АСМ-изображений и рентгенодifraktometрических снимков в слоистых системах Bi<sub>2</sub>Te<sub>3</sub><металл>.

*Received: 10.04.08*

## FORMATION OF PVA-CAPPED CdSe NANOCRYSTALS UNDER ULTRASONIC WAVES

**YASHAR AZIZIAN KALANDARAGH<sup>1,2</sup>, M.B. MURADOV<sup>1</sup>, R.K. MAMEDOV<sup>1</sup>,  
A. KHODAYARI<sup>2</sup> G.M. EYVAZOVA<sup>1</sup>**

<sup>1</sup>*Baku State University, Z. Khalilov Str., 23, Baku, Azerbaijan*

<sup>2</sup>*Mohaghegh Ardabili University, P.O. Box 179, Ardabil, Iran*

Poly vinyl alcohol (PVA)-capped CdSe nanocrystals were prepared using a sonochemistry method. XRD pattern are consistent with that for cubic CdSe. The calculated result from XRD characterization shows that the sizes of particles are less than 10nm. SEM of as-prepared samples shows uniform agglomerated particle distribution. The agglomerates size is found to be less than 300nm based on observed SEM images which aggregated in the form of small nanoparticles. The elemental analysis shows that the prepared samples are exactly stoichiometric.

### Introduction

Crystals with dimensions in nanometer range show characteristics that are considerably different from the characteristics of bulk materials. For example, an effective increase in band gap is observed in nanocrystalline CdSe due to quantum confinement effect. Large surface to volume ratio of semiconductor nanoparticles makes them possess characteristics that differ from the bulk semiconductors. Furthermore these characteristics depend principally on their size and shape [1-4]. Considerable interests have been devoted during recent years in CdSe nanocrystal synthesis because of their size quantization effect and wide applications in nanoelectronic devices. However, the suitability of these nanocrystals is limited to their synthetic procedure, size distribution and surface effects. A variety of methods have been described to synthesize CdSe bulk and nanocrystals in thin film form that includes physical vapor deposition, sputtering, spray pyrolysis, electrodeposition, etc.[5,6] In the present work, CdSe nanocrystals were prepared by sonochemistry method.

### 1. Experimental section

#### 1.1. Materials

Cadmium acetate dihydrate ( $\text{C}_4\text{H}_6\text{CdO}_4 \cdot 2\text{H}_2\text{O}$ , extra pure), sodium sulfite ( $\text{Na}_2\text{SO}_3$ ), elemental selenium powder, sodium hydroxide ( $\text{NaOH}$ , extra pure) and polyvinyl alcohol powder (PVA) were obtained from Merck and employed without future purification. Double distilled water and absolute ethanol were used for washing the particles.

#### 1.2. Instruments

The X-ray powder diffraction (XRD) pattern of product was carried out on Philips X Pert X-ray diffractometer with  $\text{Cu K}\alpha$  radiation ( $\lambda = 0.154056 \text{ nm}$ ) at a scanning rate of  $0.02^\circ \text{s}^{-1}$  in the  $2\theta$  rang from  $20^\circ$  to  $60^\circ$ . The purity and elemental analysis of the product were obtained by EDAX on LEO 1430 VP instrument. Surface morphology and distribution of particles were performed via LEO 1430 VP scanning electron microscope, using an accelerating voltage of 18 kV. The sample used for SEM observations was prepared by transferring the particles, which at first was dispersed in the ethanol to the SEM stage. After allowing the evaporation of ethanol from the stage, the particles on the stage were coated with a thin layer of gold.

### 1.3. Preparation of PVA-capped CdSe nanocrystals

PVA and chemically pure reagents were used for the preparation of CdSe nanocrystals. Sodium selenosulfate ( $\text{Na}_2\text{SSeO}_3$ ) solutions were prepared via dissolution of 0.2 gr of elemental selenium powder in 50ml of 1.1 aqueous solution of sodium ( $\text{Na}_2\text{SO}_3$ ), by magnetically stirring for 2 hour at 80 C applying reflux column system. All the selenium powder was dissolved and the transparent solution was allowed to be cooled to room temperature. The reacting mixtures for the synthesis of CdSe nanocrystals were prepared from 0.2 M cadmium acetate and prepared sodium selenosulfate solutions in 10 mass % PVA solutions in distilled water. The pH of this solution brought to 9 by addition of NaOH. The mixed slowly and the color of mixture gradually changed from milky to orange. This solution was transferred to a 100 ml borosilicate rounded bottom flask and mixed well and irradiated for 1 h at room temperature in open air, using Dr. Heilscher high intensity ultrasound processor UP200H Germany (0.3 cm diameter Ti horn,  $200 \text{ W/cm}^2$ , 23 kHz). The titanium tip of the horn was immersed directly in the reaction solution. During the sonication of reaction mixture, the temperature increased to about 70°C and remained constant at the end of sonication.

After sonication, the solution was centrifuged (at revolution rate of 4000 rpm) and a plenty of orange precipitates could be observed. The precipitates were washed with double distilled water and absolute ethanol and centrifuged for several times to remove the week bounded species and PVA matrix and finally dissolved in absolute ethanol and then were dispersed on ordinary microscope glass slide and dried at room temperature for one day.

### 2. Results and discussion

The result of the powder XRD pattern of the sample is depicted in Fig. 1. It is compatible with the diffraction pattern of CdSe in cubic structure (JCPDS files No.19-0191). The broadness of peaks indicates the formation of nanosized product. The most common method of determining the particle size is from the width  $\beta$  (FWHM) of the prominent X-ray diffraction (XRD) peaks using Scherrer's formula

$$L = \frac{0.94\lambda}{\beta \cos\theta}$$

Here  $L$  is the coherent length,  $\lambda$  is the wavelength of X-ray radiation and  $\theta$  is the angle of diffraction. In the case of

spherical crystallites, the relation between  $L$  and  $D$ , the diameter of crystallite, is given by  $L = (3/4) D$ .[7,8].

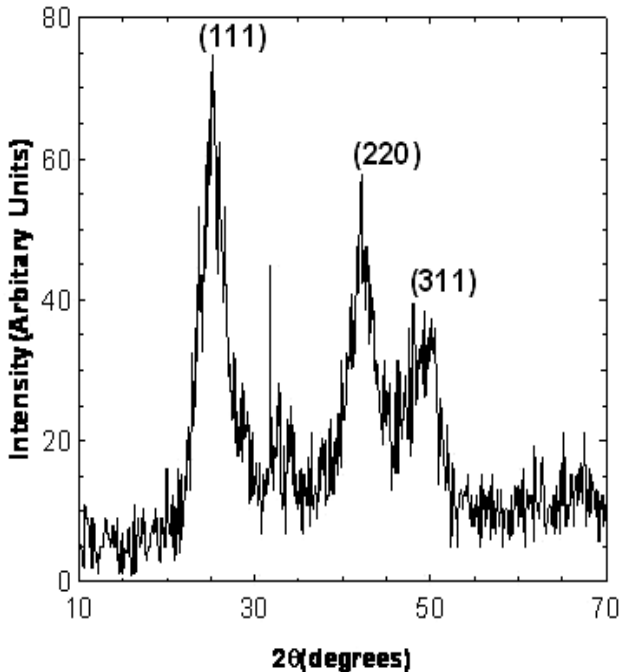


Fig. 1. XRD pattern of as-prepared CdSe nanocrystals by sonochemistry method

Although this technique does not give any proper idea about size distribution, we have estimated the average particle size of the nanocrystallite for as prepared nanoparticles using the above formula, considering three prominent peaks at  $25.23^\circ$ ,  $42.10^\circ$  and  $50.2^\circ$ . The average of  $L$  obtained from XRD pattern for these picks are less than 20 nm. The surface morphology and the distribution of the product were characterized by Scanning electron microscopy (SEM), which its images are illustrated in Fig. 2a-c at magnifications of 5k, 15k and 30k respectively.

It is obvious from Fig. 3 that produced CdSe consists of spherical nanocrystallites of about 300 nm; aggregated in the form of polydisperse agglomerates with the size in the range of 150-300 nm. Also the particle sizes are calculated by effective mass approximation model [9, 10].

It gives that the size of particle is very small and confirm the obtained results from XRD. The difference between observed results from SEM and calculated results from XRD arise from this fact that in fact the particles size is very small (less than 10 nm) and the calculated XRD results are true. The produced nanoparticles were characterized by energy dispersive X-ray analysis (EDAX) for the evaluation of its composition and purity. The EDAX spectrum for the product is shown in Fig. 3. It is evident from the peaks of the figure that the product is completely pure and they correspond to Cd and Se with an average atomic percentage ratio of about 50:50. The elemental analysis confirms the presence of corresponding elements in non-stoichiometric percentage.

The role of sonication and formation of nanoparticles is so important. In this experiment, the presence of PVA is very important in the synthesis of CdSe nanoparticles, since by the help of ultrasonic waves.

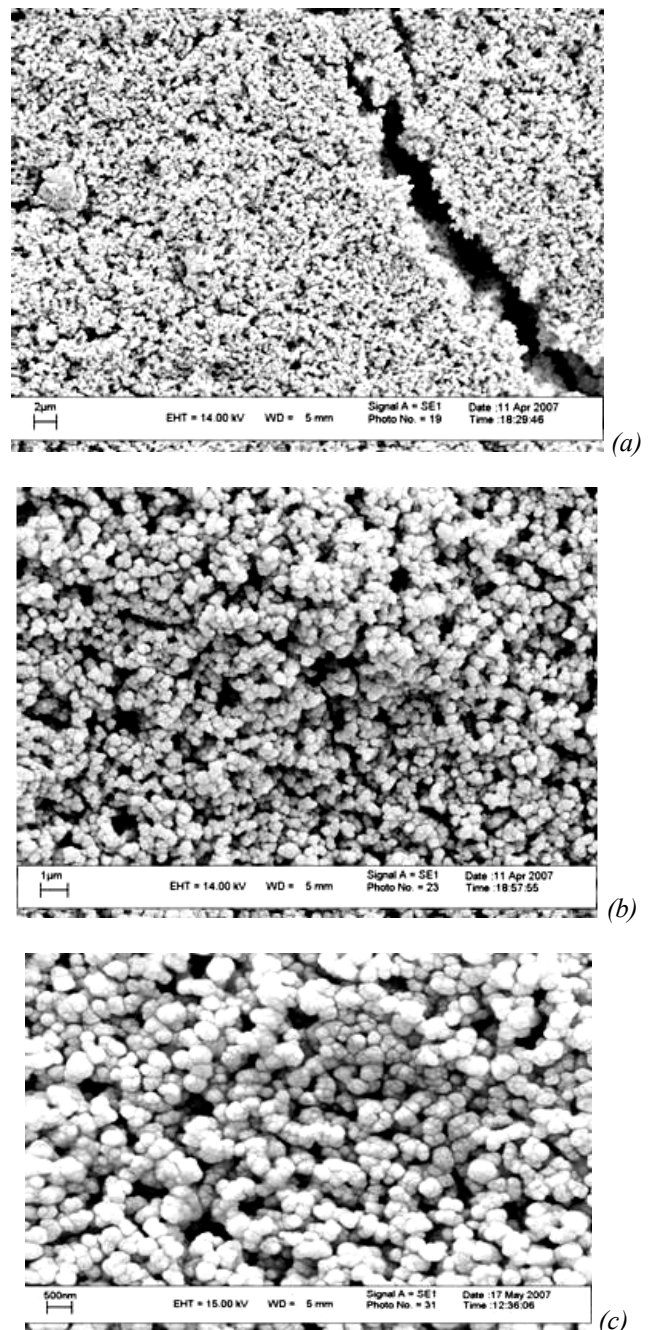


Fig. 2. SEM image of CdSe nanocrystals, magnification (a) - 5k; (b) - 15k; (c) - 30k.

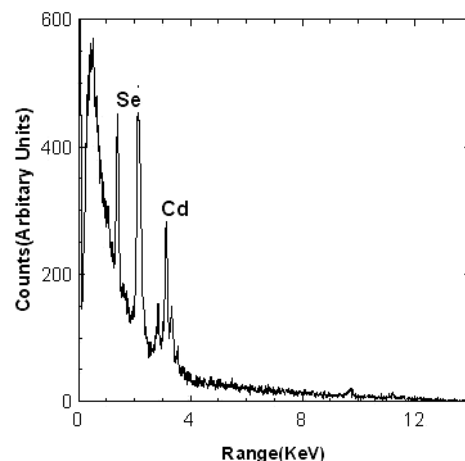


Fig. 3. EDAX spectrum of as-prepared CdSe nanocrystals by sonochemistry method

**Conclusion**

A novel and simple method for preparation of CdSe nanoparticles using ultrasonic waves has been described. The product are nanocrystallites, in cubic structure, with an

average diameter of less than 10 nm, highly pure and having higher band gap of about 4.7 eV compared to its bulk value, demonstrating a big blue shift due to CdSe nanostructure nature.

- [1] *P Alivisatos, J. Phys. Chem.* 100 ,1996,13226.
- [2] *Henglein, Chem. Rev* 89,1989,1861.
- [3] *B. Murray, C. R. Kagan, M.G. Bawendi, Ann. Rev. Mat. Sci.*30, 2000, 545.
- [4] *V.L. Colvin, M.C. schlamp, A. P. Alivisatos, Nature* 370, 1994, 354.
- [5] *G. Hodes, A. Albu-Yaron, A. Decker, P. Motisuke, Phys. Rev. B* 36, 1987, 4215.
- [6] *Y. Golan, L. Margulis, I. Rubenstein, G. Hodes, Langmuir* 8, 1992, 749.
- [7] *X. Mathew, J. Phys. D:Appl. Phys* 33, 2000, 1565.
- [8] *A. Guinier, X-ray Diffraction, Freeman, Sanfrancisco, CA,* 1963.
- [9] *L.E. Brus, J. Chem. Phys.* 80, 1984, 4403.
- [10] *L.E. Brus, J. Phys. Chem.* 90, 1986, 2555.

**Yaşar Əzizian Kələndərəq, M.B. Muradov, R.Q. Məmmədov, A. Xudayari, Q.M. Eyvazova**

**PVS ÖRTÜKLÜ CdSe NANOZƏRRƏCİKLƏRİNİN ULTRASƏS  
DALĞALARININ KÖMƏYİ İLƏ ALINMASI**

Ultrasəs dalğalarının köməyi ilə polivinil spirtli (PVS) örtüklü CdSe nanozərrəcikləri alınmışdır. Struktur tədqiqatlarına əsasən, alınmış CdSe nanozərrəcikləri kubik guruluşa malikdir. Rentgen tədqiqatlarından nanokristalların ölçüləri təyin edilmişdir (10 nm-dən kiçik). Elektron mikroskopik tədqiqatlarının nəticələri göstərdi ki, bu zərrəciklər orta ölçüsü 300nm olan bircins aqlomerat əmələ gətirir. Element analizinin nəticələrinə əsasən alınmış nanokristallar stexiometrik tərkibə malikdirlər.

**Яшар Азизиан Каландараг, М.Б. Мурадов, Р.Г. Мамедов, А. Худаяри, Г.М. Эйвазова**

**ФОРМИРОВАНИЕ НАНОКРИСТАЛЛОВ CdSe В ПВС ОБОЛОЧКЕ  
С ПОМОЩЬЮ УЛЬТРАЗВУКОВОЙ ВОЛНЫ**

Методом ультразвука были получены наночастицы CdSe в оболочке поливинилового спирта (ПВС). По результатам структурных исследований установлено, что наночастицы CdSe имеют кубическую структуру. По данным рентгенографических исследований были рассчитаны размеры нанокристаллов, которые были меньше 10 нм. Результаты исследования СЭМ показали, что полученные частицы образуют однородные агломераты со средним размером 300 нм. Элементарный анализ показал, что полученные образцы имели стехиометрический состав.

*Received: 30.03.08*

## MATCHING OF CRITERIA THE DISCERNMENT OF THE FUNCTIONAL CHARACTERISTICS OF INDEXES OF RELIABILITY OF PLANTS EES

**E.M. FARHADZADEH, A.Z. MURADALIYEV, Y.Z. FARZALIYEV**

*Azerbaijan Scientific-Research and Design-Prospecting Institute of Energetic  
Zardabi ave., 94*

References on variation of reliability on the curves received at analysis of statistical data can appear erratic if not to consider a random in character of assessments of indexes of reliability. The comparison method of criteria of a discernment of the functional characteristics indexes of reliability reduced at ordinal and nominal dials of variation of argument.

While in service the equipment and systems of plants EES there is a necessity for a reliability analysis of their activity. The reliability analysis implies an assessment and matching of some indexes of reliability (IR), describing those or other properties. As a result, of analysis the certain references on build-down of working costs formed. The greatest propagation was received with data on «weak links» plant, about conditions and character of originating of failures, a type of failures and so forth. These data in many respects determine volume of plan repair work, measures on perfecting system of maintenance, perfecting of methods verification availability index.

The solution so important for build-down of working costs of problems, in an essential degree is at a loss a small amount of information about availability index of the equipment and systems of plants EES. The averaged IR and their empirical characteristics (EC) often do not mirror a singularity of particular plant, and individual IR and matching them EC, application of special methods and the approaches considering a random in character of assessments of IR require and the statistical hypotheses orientated on check. Under EC IR we shall agree to fathom empirical regularity of IR in function of some varieties of indications (VI). Instances EC are regularity variation of IR on calendar years, duration of exploitation, a season and day, depending on the class-room of a voltage, the dispatcher numbers of the equipment, systems and electric sets, configuration items, etc. Real regularity of variation of IR in function VI we shall agree to name the functional characteristics (FC).

The urgency of a problem of the account of a random in character assessments of IR causes steadfast notice of technicians. Are developed series of criteria for matching assessments of the same type IR and their characteristics for continuous random quantities [1]. At a reliability analysis, not less characteristics of IR which scale of measurement of argument concerns to the classroom ordinal or nominal [2] often are used. For these scales of measurement, the criteria considering a random in character of watched regularities require the perfection since insufficiently full mirror as modes of an assessment of the fundamental and additional IR, and the discrete character of variation of argument. Therefore, there are reasons to believe, that the number will increase them in due course. Thus, there is a problem of matching of criteria for the purpose characteristics of their reliability (probability of a correct solution).

It is known, that in theory checks of statistical hypothesizes the preference is returned criterion, for which at the fixed value of an error of first kind, an error of second kind the least. As it noted in [1], comparison of statistical

criterions constitutes rather a challenge of modern mathematical statistics.

The most simple and illustrative mode is graphical map of characteristics of intercoupling of errors first  $[\alpha(x)]$  and second  $[\beta(x)]$  stems in the form of function  $\beta(x)=f[\alpha(x)]$ , or in the form of intercoupling of power of criterion  $W(x)=1-\beta(x)$  and  $\alpha(x)$ . However, a seeming ease of this mode is deceptive. For a case history of originating difficulties, we shall survey sequence of a presence of dependence  $\beta(x)=f[\alpha(x)]$ . She provides following determinations and evaluations:

1. Shaping of suppositions (hypotheses) concerning character of variation of examined dependence. As agency of a random in character of assessments IR is considered, normally surveyed two hypotheses. Considered, that actually a development all VI equiprobable (hypothesis  $H_1$ ). For example, assemblies of the cutout have equal reliability, and the watched divergence of assessments VI coupled only to a small amount of information, random.

The second (alternative) hypothesis ( $H_2$ ) also is natural - the watched regularity of variation of IR mirrors a real quantitative ratio of significance VI.

2. Account of distribution functions  $F(x_i / H_1)_s$  and  $F(x_i / H_2)_s$  where  $x_i$  – statistician of  $i$ -th criterion  $i=1, s$ ;  $s$  – number of compared criteria. If the distribution function of the discrete random quantity is known, formulas of account, as a rule, are known  $F(x_i / H_1)$  and  $F(x_i / H_2)$ . For example, if the model of experiment matches to a binomial low distribution, formulas of account  $F(x_i / H_1)$  and  $F(x_i / H_2)$  will differ only, accordingly, with usage for account  $F(x_i / H_1)$  hypothetical probability, and for account  $F(x_i / H_2)$  - empiric probability.

If the distribution function of a random quantity is unknown, that occurs for a greater unit of IR, allocations  $F(x_i / H_1)$  and  $F(x_i / H_2)$  evaluated by a method of simulation modeling. An instance of such characteristics are regularity of variation of an average of failures of cutouts of various class-rooms of a voltage, variation of an emergency shutdown coefficient depending on duration of exploitation and others;

3. Account of allocations  $\alpha(x_i)$  and  $\beta(x_i)$ . The solution of this problem simple enough would seem

$$\alpha(x_i / H_1) = 1 - F(x_i / H_1) \quad (1)$$

$$\beta(x_i / H_2) = F(x_i / H_2) \quad (2)$$

However, such inference is fair, if assessments of expectation of a statistician  $x_i$  for  $H_1$  and  $H_2$  satisfy to a following condition:

$$M^*(x_i / H_1) < M^*(x_i / H_2) \quad (3)$$

Otherwise, i.e. when

$$M^*(x_i / H_1) > M^*(x_i / H_2) \quad (4)$$

following equalities are fair

$$\alpha(x_i / H_2) = 1 - F(x_i / H_2) \quad (5)$$

$$\beta(x_i / H_1) = F(x_i / H_1) \quad (6)$$

If neglect a parity of means statistician  $x_i$  serious errors in an adoption of a decision are possible. The account of a parity  $M(x_i / H_1)$  и  $M(x_i / H_2)$  it is especially important at automatic application of criteria in program models. The graphical case history of a short of an erratic solution reduced on fig.1.

As follows from fig.1, not account parities  $M^*(x / H_1)$  and  $M^*(x / H_2)$  leads to sharp variation of critical value of quintiles of allocations  $\alpha(x/H_2)$  and  $\beta(x/H_1)$ . If at physically correct comprehension of errors the first and second stem, critical value of quintiles at  $\alpha_k=\beta_k=0,1$  are accordingly peer  $\bar{X}^{(1)}$  and  $\bar{X}^{(2)}$ , that at their erratic comprehension ( $M^*(x / H_1) > M^*(x / H_2)$ ), these quintiles are accordingly peer  $\underline{X}^{(1)}$  and  $\underline{X}^{(2)}$ , that  $\bar{X}^{(1)} <> \underline{X}^{(1)}$  and  $\bar{X}^{(2)} >> \underline{X}^{(2)}$ . If  $\bar{X}^{(1)} < \bar{X}^{(2)}$ , that  $\underline{X}^{(1)} > \underline{X}^{(2)}$ ;

4. Construction of dependence  $\beta(x)=f[\alpha(x_i)]$ . To build this dependence it is necessary to consider following singularities:

4.1. Levels of discrete samplings of allocations  $F(x_i / H_1)$  and  $F(x_i / H_2)$  can completely and partially differ. Here there is in view of not the partial overlapping of spacing of possible value of argument of allocations and not a complete divergence of these spacing. Difference of discrete samplings watched on the interval overlapping of possible value. It is established, that a necessary condition of existence of generic points of a discrete sampling is proportionality  $x_m$  to value  $\varepsilon = 1/n_{\Sigma}$  where  $n_{\Sigma}$  - total number of failures

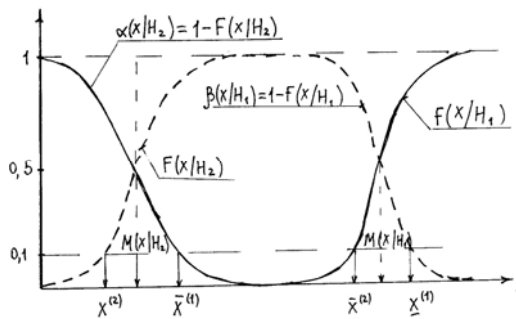


Fig. 1. A graphical case history of aftereffects of disregard a parity  $M^*(x / H_1)$  and  $M^*(x / H_2)$ .

4.2. Between dependences  $\beta(x)=f[\alpha(x)]$ , builted for conditions (3) and (4), there is a divergence. In the first event, we have dependence of probability erratic disallowance hypothesis  $H_1$  in function of probability erratic disallowance hypothesis  $H_2$ , i.e.  $\beta(x/H_2)=f[\alpha(x/H_1)]$ , and in the second event  $\beta(x/H_1)=f[\alpha(x/H_2)]$ . In discover the reflecting noted in item.3 serious errors in an adoption of a decision.

Therefore, it is necessary to compare not with value of error of second kinds at fixed error figures of the first stem, and an error at adoption of hypothesis  $H_2$  for the fixed error figure at disallowance hypothesis  $H_1$ .

Graphical case history of difference of curves  $\beta(x/H_2)=f[\alpha(x/H_1)]$  and  $\beta(x/H_1)=f[\alpha(x/H_2)]$  it reduced on fig.2. These curves are builted for criterion of matching of an assessment of chances of failure  $Q^*$  with hypothetical probability  $Q_0$ , where  $Q^*=n_i/n_{\Sigma}=3/60=0.05$ , and  $n_{\Sigma} = \sum_{i=1}^{m_r} n_i$

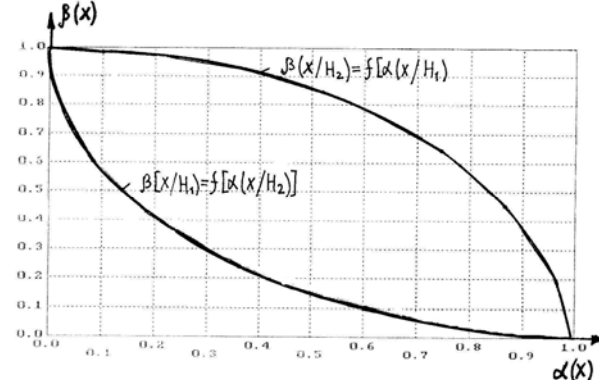


Fig. 2. A graphical case history of difference curves of intercoupling of errors of the first and second stem.

To simplify the subsequent account, to consider (3) and (4), we shall agree probability erratic disallowance hypotheses  $H_2$  to designate through  $Sh(x/H_2)$  and probability erratic disallowance hypotheses  $H_1$  to designate through  $Sh(x/H_1)$ .

The subsequent treating of singularities of matching of criteria of discernment distribution functions of variation of IR at nominal and ordinal dials of argument we shall continue on a particular instance.

5. To have a possibility to evaluate reliability of a solution, EC has been received by a method of statistical modeling, by:

a) software prototyping  $n_{\Sigma}$  random numbers  $\xi$  with an even distribution in the interval  $[0,1]$ ;

b) compliance test of these ( $n_{\Sigma}$ ) random numbers to the uniform law Kolmogorov's criterion;

c) arrangement  $n_{\Sigma}$  random numbers in  $m_r$  peer spacing by comparison  $\xi_v$  with the upper boundary values  $m_r$  spacing by formula

$$i/m_r < \xi_v \leq (i+1)/m_r \quad c \quad i=1, (m_r+1) ?????$$

d) assessments of probability of a development set VI by formula  $Q_i^* = n_i / n_{\Sigma}$ .

The first criterion is based on the supposition of correspondence of probability of a development of each of  $i=1, m_r$  VI to binomial low. Critical value of errors of the first and second stem for each spacing were sampled in view of theorem Touke according to which  $\alpha_{K,i} = \alpha_K / m_r$  and

$\beta_{K,i} = \beta_K / m_r \quad c \quad i=1, m_r ?????$ . Let's designate it conditionally through  $K_B$ .

The second criterion based on an assessment of allocation of the greatest divergences of simulated implementation of allocations  $F(i)$  и  $F^*(i)$ , where  $F(i)=i/m_r$ ;

$F^*(i) = \sum_{i=1}^{m_r} n_i / n_{\Sigma} ; \quad n_{\Sigma} = \sum_{i=1}^{m_r} n_i$ . We shall designate it conditionally through  $K_{\delta}$ .

In table 1 value of argument  $X$  and conforming discontinuous distributions are reduced  $\alpha(x_1/H_1)$ ,  $\beta(x_1/H_2)$ ,  $\alpha(x_2/H_1)$  and  $\beta(x_2/H_2)$ , where  $x_2=x_m \cdot n_{\Sigma}$ . As follows from this table, to the same  $x$  there match various value  $\alpha(x_1/H_1)$  and  $\alpha(x_2/H_1)$ , that brings ambiguity of comparison of criteria and comparison bears that  $\beta(x_1/H_2)$  and  $\beta(x_2/H_2)$  at fixed  $\alpha(x/H_1)$  it is impossible, and consequently, and it is erratic.

6. To reduce  $\alpha(x_1/H_1)$  and  $\alpha(x_2/H_1)$  to the same argument, we shall compare argument  $X$  with quotients of a significance of power of the criteria computed by formula:

$$A(x) = [1 - \beta(x/H_2)]/\alpha(x/H_1) = W(x/H_2)/\alpha(x/H_1) \quad (7)$$

at  $M^*(x/H_1) < M^*(x/H_2)$

$$B(x) = \beta(x/H_1)/[1 - \alpha(x/H_2)] = W(x/H_1)/\alpha(x/H_2) \quad (8)$$

at  $M^*(x/H_1) > M^*(x/H_2)$ .

Table 1  
Numerical values of allocations  $\alpha(x/H_1)$  and  $\beta(x_2/H_2)$

$x_i$	$\alpha(x_{1,i}/H_1)$	$\beta(x_{2,i}/H_2)$	$\alpha(x_{2,i}/H_1)$	$\beta(x_{2,i}/H_2)$
2	0,8861	0,0015	0,9810	0,0030
3	0,7471	0,0063	8322	0,0659
4	0,5672	0,0202	0,5275	0,3336
5	0,3899	0,0512	0,2178	0,6613
6	0,2312	0,1081	0,0579	0,8721
7	0,1241	0,1958	0,0090	0,9590
8	0,0596	0,3120	-	0,9860
9	0,0258	0,4464	-	0,9940
10	0,0100	0,5834	-	0,9980
11	0,0036	0,7079	-	0,9990
12	0,0011	0,8097	-	-
13	0,0003	0,8848	-	-

Outcomes of accounts  $A(x_1)$  and  $A(x_2)$  are reduced in table 2. As follows from table 2, at the fixed value of argument  $X$  quotient of a significance  $A(x_i)$  for criterion  $K_B$  it is more, than value  $A(x_2)$  for criterion  $K_{\delta}$ .

Table 2  
Outcomes of accounts of empirical value of quotients  $A(x_1)$  and  $B(x_2)$

$x_i$	$A(x_{1,i})$	$A(x_{2,i})$
2	1,13	1,02
3	1,13	1,12
4	1,73	1,26
5	2,47	1,56
6	3,86	2,21
7	6,48	4,56
8	11,54	-
9	21,46	-
10	41,66	-

It is necessary to mark, that comparison of criteria should conducted not for the same arguments  $x$ , and for critical value  $x_K=X$  [ $\alpha(x/H_1) < \alpha_K$ ], i.e. to argument with the greatest value  $\alpha(x/H_1)$ , satisfying to a condition  $\alpha(x/H_1) < \alpha_K$ . For example, according to table 1 for criterion  $K_B$  at  $\alpha_K=0.05$  value  $x_{1,k}=9$ , and for criterion  $K_{\delta}$  - pearly 8.

7. Comparison of criteria can carried out and a little differently. In a fig. 3 curves are reduced  $Sh(x/H_2)=f[Sh(x/H_1)]$ . For conforming critical value of probability  $Sh(x/H_1)$  value are determined  $Sh(x/H_2)$ . In the received

statement of conditions of comparison of criteria, than  $Sh(x/H_2)$  for matching  $Sh(x/H_1)$  it is less, that the criterion is more preferable. According to a fig 3 it is criterion  $K_B$ .

8. Despite of a seeming finality the tasks in view separate, multiply the checked out facts were not matched with noted in item 6 and 7 outcomes of comparison of criteria. To them concerned:

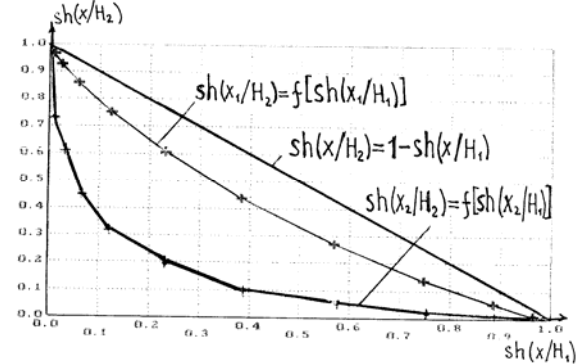


Fig. 3. The Graphical case history of matching of criteria.

8.1. If  $F(x/H_1)=F(x/H_2)$ , i.e.  $H_1=H_2$ , that irrespective of type FC function  $Sh(x/H_2)=f[Sh(x/H_1)]$  looks like  $Sh(x/H_2)=1 - Sh(x/H_1)$ . If  $H_1 \neq H_2$ , that  $Sh(x/H_2) \neq 1 - Sh(x/H_1)$ ;

8.2. The empirical value of the greatest divergence between EC and FC is less, the incurvation (bulge) of curves is less  $Sh(x/H_2)=f[Sh(x/H_1)]$  and the more error figure  $Sh(x/H_2)$ ;

8.3. At small difference EC and FC, including practically insignificant, a solution of matching EC and FC will be: «the information has not enough for an adoption of a decision »;

8.4. With magnifying of number of experiences  $n_{\Sigma}$  and correspondences  $F^*(i)$  to even distribution, value  $Sh(x/H_2)$  increases.

9. These data allow to conclude, that if EC is received by statistical modeling on some allocation  $F(i)$  with  $i=1, m_r$ , that value  $Sh(x/H_2)$  characterizes probability of an erratic deflection of hypothesis  $H_2$  owing to a random in character of assessments of the IR computed for each of  $m_r$  VI. In this case it is easy to explain, why with decrease of a divergence between EC and FC value  $Sh(x/H_2)$  at the fixed number of "experiences" increases (the less divergence, the more than data it is necessary for a discernment of this divergence) and why with magnifying of a divergence between EC and FC  $Sh(x/H_2)$  diminished

10. If to receive, that at equiprobable development VI value  $Sh(x/H_2) = \overline{Sh}(x/H_2)$ , that value

$$\Delta Sh(x/H_2) = |Sh(x/H_{2S}) - \overline{Sh}(x/H_2)| \quad (9)$$

it will be proportional to an error in a discernment of difference EC from the uniform law. At the fixed value  $Sh(x_K/H_1)$  the preference is returned criterion with greater value  $Sh(x/H_2)$ , and with allowance for item.6 the preference is returned criterion, for which greatest divergence of quotients  $A(x)$  or  $B(x)$  and units of the fixed value  $Sh(x_K/H_1)$  the least on matching with other criteria.

Systematizing the above-stated, the method and algorithm of matching  $S$  of criteria is represented the following amalgamated sequence of evaluations:

1. Allocations pay off  $F(x/H_1)$  and  $F(x/H_2)$ ;
2. Subject to the conditions (3) and (4) allocations are formed  $Sh(x/H_1)$  and  $Sh(x/H_2)$ ;
3. Real critical value of probability erratic disallowance hypotheses  $H_1$  by formula are determined

$$Sh_d(x/H_1) = \max\{Sh(x/H_1) < \alpha_K\} \quad (10)$$

4. It is determined  $Sh(x/H_2)$ , matching  $Sh_d(x/H_2)$ ;
5. The probability erratic disallowance hypotheses  $H_2$ , caused by algorithm of criterion by formula is evaluated

$$\Delta Sh(x/H_2) = |1 - Sh_d(x/H_1) - Sh(x/H_2)|$$

6. The preference returned criterion, for which  $\Delta Sh(x/H_2)$  the least.

#### **Inference.**

1. The account of an error of second kind in conditions when aftereffects from erratic solutions are indiscernible, so important, as well as an error of first kind. The disregard to physical nature of both errors leads in practical accounts to incorrect solutions;
2. Known references with reference to criteria of a discernment of the functional characteristics of indexes of reliability at ordinal and nominal dials of argument are unacceptable for matching criteria;
3. Erratic solutions at usage of these references originate owing to:

Insufficient sharpness of the gear of the account of physical nature of errors of the first and second stem. Such

"gear" the parity of means of argument of allocations can minister  $F(x/H_1)$  and  $F(x/H_2)$ ;

Difference of levels of a discrete sampling of arguments allocations  $\alpha(x/H_1)$  and  $\beta(x/H_2)$ . Characteristics  $\beta(x)=f(\alpha(x))$  should be under construction for the same value  $x$ ;

Comparisons of error of second kinds of criteria at the fixed value of an error of first kind. It is necessary to compare with an error in disallowance hypotheses  $H_2$  at the fixed value erratic disallowance hypotheses  $H_1$ ;

Differences erratic disallowance hypothesis  $H_1$  for equal levels of a discrete sampling of statistician of compared criteria. Overcoming of this nonconformity is reached by comparison of criteria on regularities of variation of a relative significance of power of criteria under formulas (7) and (8)

Irregular interpreting matching  $Sh(x/H_1)$  probabilities  $Sh(x/H_2)$ , only as probabilities erratic to deny hypothesis  $H_2$ . Actually  $Sh(x/H_2)$  characterizes probability erratic disallowance hypotheses  $H_2$  owing to roundedness of statistical data for a discernment of the functional junctions;

4. The method, algorithm and programs model of matching of criteria of a discernment of the functional characteristics of indexes of reliability of plants EES is developed. Probability of the supervision of reliability of a solution were ensured with a solution technique of "inverse problem" when empirical the characteristics of indexes of reliability were simulated on the sampled regularity of variation VI.

5. Matching of the criterion based on binomial model of probability of development VI and criterion, the greatest deflection of empirical and hypothetical characteristics based on value bears to doubtless advantage of the second criterion.

[1] I.A. Ryabinin. Bas of the theory and account of reliability ship electro energy systems; "Shipbuilding", 1971, 453 p.

[2] V.P. Trofimov. Logical organization of statistical models. M.: The Finance and statistician, 1985, 191 p.

**E.M. Fərhadzadə, A.Z. Muradəliyev, Y.Z. Fərzəliyev**

#### **EES-in OBYEKTLƏRİNİN ETİBARLIQ GÖSTƏRİCİLƏRİNİN FUNKSİONAL XARAKTERİSTİKALARININ TANIMMASI KRİTERİYALARININ MÜQAYİSƏSİ**

Əgər etibarlıq göstəricilərinin qiymətləndirilməsinin təsadüfi xarakterli olması nəzərə alınmazsa, statistik verilənlərin araşdırılması zamanı alınan əyrilər üzrə etibarlılığın dəyişməsini göstərən tövsiyələr səhv ola bilərlər. Arqumentin sıra və nominal şkalalarında etibarlıq göstəricilərinin funksional xarakteristikalarının tanınması kriteriyalarının müqayisəsi üsulu göstərilir.

**Э.М. Фархадзаде, А.З. Мурадалиев, Ю.З. Фарзалиев**

#### **СРАВНЕНИЕ КРИТЕРИЕВ РАСПОЗНАВАНИЯ ФУНКЦИОНАЛЬНЫХ ХАРАКТЕРИСТИК ПОКАЗАТЕЛЕЙ НАДЕЖНОСТИ ОБЪЕКТОВ ЭЭС**

Рекомендации по изменению надежности по кривым, полученным при анализе статистических данных, могут оказаться ошибочными, если не учесть случайный характер оценок показателей надежности. Приводится метод сравнения критерииев распознавания функциональных характеристик показателей надежности при порядковой и номинальной шкалах изменения аргумента.

*Received: 07.03.08*

## DEFINITION OF RESULTING ANGLE OF THE DEVIATION AFTER THE PASSAGE OF NEUTRONS THROUGH THE CRYSTAL

**S.G. ABDULVAHABOVA, D. MASTI**

*Baku State University, Z. Khalilov Str., 23, Baku, Azerbaijan*

The present paper is dedicated to the consideration of passage of neutrons in the crystal. The expression for intensity distribution is obtained by the method of the multiple scattering theories. The received results are applied to calculation angle of the deviation of neutrons by nucleus of the crystal. Here is shown that at the large angle of the deviation, the intensity of distribution decreases with reduction of angle much more slowly, than till Gaussian law. The received expression for the angle of the deviation of allows defining of the impulse of the neutron.

After the second act of scattering (on other nucleon) the particle moves in a direction, are defined by polar angles ( $\vartheta_2, \varphi_2$ ) concerning a direction of ( $\vartheta_1, \varphi_1$ ) occurring once scattering bunch or angles ( $\vartheta, \varphi$ ) concerning falling bunch ,i.e:

$$\cos \vartheta_2 = \cos \vartheta_1 \cos \vartheta + \sin \vartheta_1 \sin \vartheta \cos(\varphi_1 - \varphi). \quad (4)$$

To find probability of that after two consecutive, independent impacts the deviation of a particle will lay in a solid angle  $d\Omega = \sin \vartheta d\vartheta d\varphi$ , it is necessary to integrate product on  $W_1(\vartheta_1, \varphi_1) W_1(\vartheta_2, \varphi_2)$  all  $\vartheta_1, \varphi_1$  at the fixed values  $\vartheta$  and  $\varphi$ . Decomposing on  $P_l(\cos \vartheta_2)$  attached Legendre's polynomial:

$$P_l^m(\cos \vartheta_1) \exp(im\varphi_1) \text{ and}$$

$$P_l^m(\cos \vartheta) \exp(im\varphi),$$

For probability it is found:

$$W_2(\vartheta, \varphi) d\Omega = \frac{1}{4\pi} \sum_l (2l+1)(g_l)^2 P_l(\cos \vartheta) d\Omega \quad (5)$$

Similarly, for probability of a deviation in a solid angle  $d\Omega = \sin \vartheta d\vartheta d\varphi$  after  $n$  collisions it is had:

$$W_n(\vartheta, \varphi) d\Omega = \frac{1}{4\pi} \sum_l (2l+1)(g_l)^n P_l(\cos \vartheta) d\Omega \quad (6)$$

Let's designate through  $W(n)$  probability of that passing through substance the neutron will test on the average  $n$  collisions. Then the probability of that a neutron will deviate on a corner lying between  $\vartheta$  And  $\vartheta + \delta\vartheta$ , is equal:

$$I(\vartheta) \sin \vartheta d\vartheta = \frac{1}{2} \sum_l (2l+1) \left[ \sum_n W(n) (g_l)^n \right] P_l(\cos \vartheta) \sin \vartheta d\vartheta \quad (7)$$

$$\nu = Nt \int \sigma(\vartheta) d\Omega.$$

### 1. Introduction

At the analysis of angular distribution of the thermal neutrons disseminated by a layer of substance, there is a problem of finding resulting angle of the deviation after consecutive collisions with nucleus of substance. Many authors considered this problem approximately [1-3]. In works [1-2] unitary scattering is considered and it was not required any approach. In work [3] passage charged through substance is investigated and the theory for small angles and only for screen Coulomb's fields is resulted. On the basis of the theory of multiple Watson scattering [4], we deduced a basic formula for distribution of intensity and we defined angle of the deviation after passage of the neutron waves through the crystal.

### 2. Formula for definition of the angle of deviation

At the analysis of angular distribution of coherent neutron scattering, there is a problem to finding the resulting angle  $\vartheta$  of the deviation after  $n$  consecutive collisions of a neutron by nucleons of a nucleus of substance. The probability of that in one act of collision a deviation of a particle will lay in a solid, angle  $d\Omega = \sin \vartheta d\vartheta d\varphi$  is equal:

$$W_1(\vartheta, \varphi) d\Omega = \frac{\sigma(\vartheta)}{\sigma} d\Omega \quad (1)$$

where  $\sigma(\vartheta)d\Omega$  and  $\sigma$  are differential and full cross-section, accordingly. We expand (1) over Legendre's polynom:

$$W_1(\vartheta, \varphi) d\Omega = \frac{1}{4\pi} \sum_l (2l+1) g_l P_l(\cos \vartheta) d\Omega \quad (2)$$

where:

$$g_l = \frac{1}{\sigma} \int P_l(\cos \vartheta) \sigma(\vartheta) d\Omega \quad (3)$$

The average of collisions  $v_{(8)}$  passage through a film the thickness  $t$ , containing  $N$ , nucleus in unit of volume, will be written down as:

## DEFINITION OF RESULTING ANGLE OF THE DEVIATION AFTER THE PASSAGE OF NEUTRONS THROUGH THE CRYSTAL

$$\sum_{n=0}^{\infty} W(n) (g_l)^n \approx \exp[-\nu(1-g_l)] \quad (10)$$

Considering last expressions, for distribution of intensity at multiple scattering we receive:

or  $\nu \gg 1$  for  $W(n)$  it is possible to apply Poisson's distribution:

$$W(n) = \frac{e^{-\nu} \nu^n}{n!} \quad (9)$$

Thus, we get:

$$I(\vartheta) = \frac{1}{2} \sum_l (2l+1) \exp \left\{ -2\pi N t [ \sigma(\theta) [1 - P_l(\cos \theta)] \sin \theta d\theta \right\} P_l(\cos \vartheta). \quad (11)$$

Let, further the  $q(\theta)$  attitude of cross-section  $\sigma(\theta)$  scattering of a neutron on nucleus of a crystal to section on a free nucleus  $\sigma_0$ , i.e:

$$q(\theta) = \frac{\sigma(\theta)}{\sigma_0} \quad (12)$$

Designating  $y = \sin \frac{\theta}{2}$  expression (11) will become:

$$I(\vartheta) = \frac{1}{2} \sum_l l(l+1) \int_0^1 q(\theta) \frac{dy}{y} - \sum_{k=2}^l (-1)^k \frac{(l+k)!}{(l-1)!(k!)^2} \int_0^1 q(\theta) y^{2k-3} dy \quad (13)$$

$$P_l(\cos \vartheta) \approx J_0[(l+1/2)\vartheta] = J\left(\frac{\vartheta}{\theta_0}\right) \quad (16)$$

It is possible to replace summation on  $l$  in (13) integration. With this purpose we use Euler-Maclaurin's formula:

$$\sum_l f(n+1/2) = \int_0^\infty f(x) dx + \frac{1}{24} f'(0) + \dots \quad (17)$$

After enough bulky calculations, in the first Born's approach we receive:

$$J(\vartheta) \approx \int_0^\infty \left( 1 + \frac{2\theta_0}{\beta} (1-\beta) \right) \left( \ln \frac{\theta_0^2}{4} - \ln \frac{\theta^2}{4} \right) J\left(\frac{\vartheta}{\theta_0}\right) d\theta = \exp\left(-\frac{\vartheta^2}{\theta_0^2}\right). \quad (18)$$

where:

$$\beta = \frac{\nu}{c}, \bar{\vartheta}^2 = \theta_0^2 \left( 1 + \frac{2\theta_0}{\beta} \right) \ln \frac{\theta_0^2}{4} \quad (19)$$

At greater angles  $\vartheta / \theta_0 \sqrt{\ln \frac{\theta_0^2}{4}} \geq 4$  function

$J(\vartheta)$  decreases with reduction  $\vartheta$  much more slowly, than on Gaussian' law, and following members in (17), arising in the second and higher Born's approximation, become essential. Expression (19) allows defining an impulse of a neutron from data about an average square a scattering of angle  $\bar{\vartheta}^2$ .

### 4. Conclusion

The theory of multiple scattering has served in work as a

Function  $q(y)$  possesses following properties:

$$q(0) = 0, \quad q(y) = 1 \quad \text{for} \quad y > y_0, \quad (14)$$

Whence at scattering on angle  $\theta$ , greater of some angle  $\theta_0$ , influence of other nucleus a little. If in integral  $\int_0^1 q(y) y^{2k-3} dy$ ,  $k \geq 2$  to approximate  $q(y)$  expression:

$$q(y) = 1 - \exp\left(-\frac{y}{y_0}\right) \quad (15)$$

and to put:

starting point of calculation. (18) corresponds flat wave to pulse approach in which scattering on separate particles is considered independently, thus we completely ignored influence of other particles. In more perfect variant by consideration of scattering on a separate particle, the account of influence of the others is reduced to introduction of distortion of wave functions of a disseminated particle. As scattering the ideal harmonious crystal has been considered. For thermal neutrons because of small depth of their penetration into a wall of a crystal it is necessary to consider carefully influence of structure of the surface limiting disseminating environment on behavior of the neutron wave received. In the first Boron's approach expression for the angle of scattering allows to define a parameter of refraction of a neutron wave on a crystal and this to serve as object for the further researches.

- [1] E.J. Williams. Phys. Rev. 1988, 58, p. 292.  
[2] S.A. Goudsmit, J.L. Saunderson. Phys. Rev. 1990,  
57, p. 24.  
[3] H. Snyder, W. Scott. Phys. Rev. 1989, 76, p. 220.  
[4] K.M. Watson. Phys. Rev., 1967, 105, p. 1388.

**S.Q. Əbdülvahabova, D.Masti**

**NEYTRONLARIN KRISTALDAN KEÇMƏSİ ZAMANI SON DÖNMƏ BUCAĞININ TƏYİNİ**

İş neytronların kristallardan keçməsinin tədqiqinə həsr edilmişdir. Çoxdəfəli səpilmə nəzəriyyəsi əsasında intensivliyin paylanma funksiyası üçün ifadə alınmışdır. Alınmış ifadə neytronların kristaldan keçərkən kristalın nüvələrindən səpilməsinin son dönəmə bucağının hesablanmasına tətbiq edilmişdir. Müəyyən edilmişdir ki, böyük bucaq altında dönəmə zamanı intensivlik bucağın azalması ilə Qauss qanuna nəzərən az azalır. Dönəmə bucağı üçün alınmış ifadə zərrəciyiin impulsunu təyin etməyə imkan verir.

**C.K. Abdulkzagabova, D. Masti**

**ОПРЕДЕЛЕНИЕ РЕЗУЛЬТИРУЮЩЕГО УГЛА ОТКЛОНЕНИЯ ПОСЛЕ ПРОХОЖДЕНИЯ НЕЙТРОНА  
ЧЕРЕЗ КРИСТАЛЛ**

Настоящая работа посвящена рассмотрению прохождения нейтронов через кристалл. На основе многократного рассеяния было получено выражение для функции распределения интенсивности. Полученные результаты применяются к вычислению угла отклонения частицы на ядрах кристалла. Показано, что при больших углах отклонения интенсивность распределения уменьшается с уменьшением угла значительно медленнее, чем по гауссовому закону. Полученное выражение для угла отклонения позволяет определить импульс нейтрана.

*Received: 14.03.08*

**RADİASİYANIN TƏSİRİ İLƏ QURĞUŞUN SULFİD ƏSASINDA ALINMIŞ VƏ GÜCLÜ KOMPENSƏ OLUNMUŞ BƏRK MƏHLULLARIN ELEKTRİK VƏ FOTOELEKTRİK XASSƏLƏRİNİN TƏDQİQİ**

**H.Ə. HƏSƏNOV**

*MTN-in H. Əliyev adına Akademiyası*

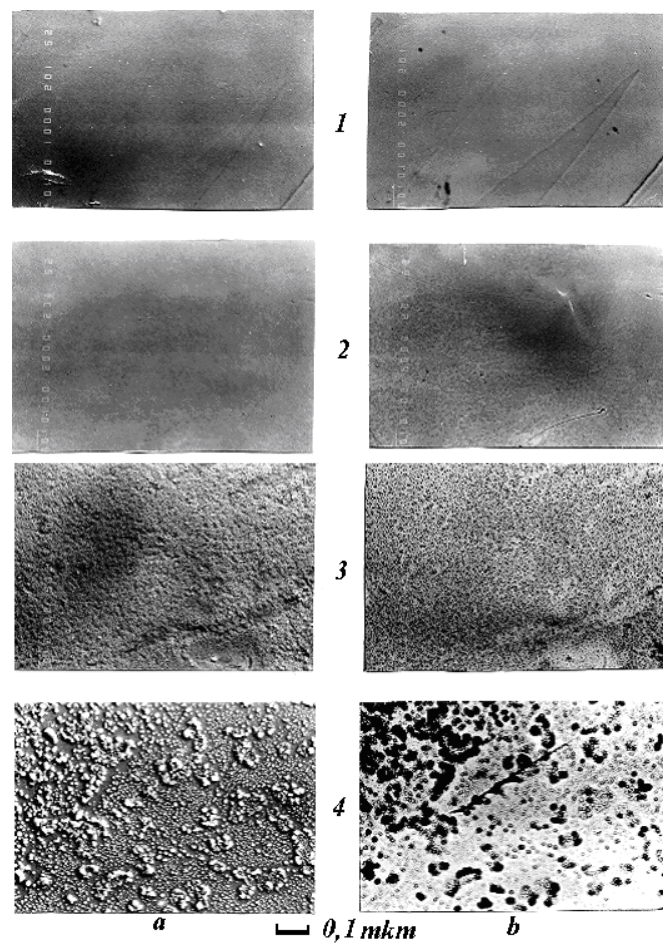
Təqdim edilən məqalə gurğusun sulfidin polikristallik epitaksial təbəqələrinin və onun əsasında radiasiyanın təsiri altında alınan bərk məhlulların strukturunun və fiziki xüsusiyyətlərinin aşdırılmasına həsr edilmişdir. Rentgen-struktur, oje-spektral və mikrostruktur aşdırımların nəticələri şərh edilmişdir. Xüsusi müqavimət, Holl əmsalı və yükdaşıyıcıların hərəkətliliyinin temperatur asılılıqları aşdırılmışdır.

Irimiqyaslı zonalar modullaşması və güclü kompensə effektinin eyni zamanda reallaşdırıldığı modelə misal olaraq radiasiya təsirinə məruz qalmış kompensə olunmuş gurğusun sulfid təbəqələrini göstərmək olar. Belə obyektlərdə, tərkibi fluktuasiya edən bircins bərk məhlullardan fərqli olaraq, zonaların effektiv relyefi materialın yüksək enerjili elektron və ionlarla şüalanılması sayəsində formalşır, kompensasiya prosesləri isə kompensədici aşqar, məxsusi və radiasiya defektlerinin birgə təsiri ilə müyyəyən edilir. Təqdim olunan məqalədə belə təbəqələrin alınma texnologiyalarının əsasları, elektrik və fotoelektrik xassələri nəzərdən keçiriləcəkdir.

Son illərdə darzonali yarımkəcicilər əsasında fotodiод strukturu hazırlamaq üçün ənənəvi metodlarla yanaşı, radiasiya texnologiyası metodundan da geniş istifadə edilir. Radiasiya texnologiyaları metodu ion şüalanması və implantasiyasının effektiv aşqarlama üsulu olması faktına əsaslanır [1]. Şüalanmaya məruz qalmış gurğusun halkogenidləri və onların əsasında formalşdırılmış bərk məhlulların materialı elektrik xassələrinə güclü təsir edən amorflaşma tərtibi və nöqtəvi defektlər, aşqar növündən asılılığı, stexiometriyadan meyletmələr kimi xüsusiyyətlərə malik olur. Radiasiyanın gurğusun halkogenidlərinin təsiri 2-4 sayılı işlərdə ətraflı təsvir olunmuşdur. Elektron və ionların gurğusun sulfid kristalına və təbəqəsinə təsiri 4 və 5 sayılı işlərdə aşdırılmışdır. Gürğusun halkogenidlərinin polikristallik təbəqələrinin fotohəssaslıq xassələrinin ionlaşdırıcı şüalanmanın təsiri nəticəsində dəyişilməsi 6 sayılı xülasədə verilmişdir.

Akseptor natrium aşqarı vurulmuş ilkin gurğusun sulfid təbəqələri (111) orientasiyalı  $\text{BaF}_2$  altlığında molekulyar-şüa epitaksiyası metodu ilə yetişdirilmişlər. *p*-tip keciciliyə malik olan təbəqələrdə deşiklərin konsentrasiyası 77K temperaturda  $3 \cdot 10^{17} \div 3 \cdot 10^{18} \text{ sm}^{-3}$  olmuşdur. Rentgen tədqiqatları formalşdırılmış strukturların monokristallik olmasını sübut edir. Nümunə metal və ya halkogen qoşulması olmayan hamar güzgü səthinə malikdir (Şək.1).  $\text{PbS(Na)}$  təbəqələrinin qalınlıqları elektronlarla şüalandırıldığda  $1 \div 2 \text{ mkm}$ , bor ionları ilə şüalandırıldığda isə  $0,1 \div 0,2 \text{ mkm}$  olmuşdur. 5 sayılı işə əsasən, gurğusun halkogenidlərində bor donor xassələrinin daşıyıcısıdır. Otaq temperaturunda elektronlarla və bor ionları ilə şüalandırılma seli müvafiq olaraq,  $\Phi_e = 10^{16} \div 10^{18} \text{ sm}^{-2}$ ;  $\Phi_B = 5 \cdot 10^{13} \div 5 \cdot 10^{16} \text{ sm}^{-2}$  olmuşdur. Elektronların enerjisi 4MeV, bor ionlarının enerjisi isə 50keV olmuşdur. Elektron şüalanması havada elektron selinin kiçik sıxlığında, borun implantasiyası isə vakuumda yerinə yetirilmişdir. Şüalandırma zamanı nümunələrin temperaturu  $40 \div 50^\circ\text{S}$ -dən böyük olmayışdır. Elektron şüalanmasında monokristallik  $\text{PbS(Na)}$  təbəqələrinin eroziyası elektron selinin  $\Phi \geq 1 \cdot 10^{17} \text{ sm}^{-2}$ -dən böyük qiymətlərində başlanır (Şək.1). Nümunələrin postimplantasiya

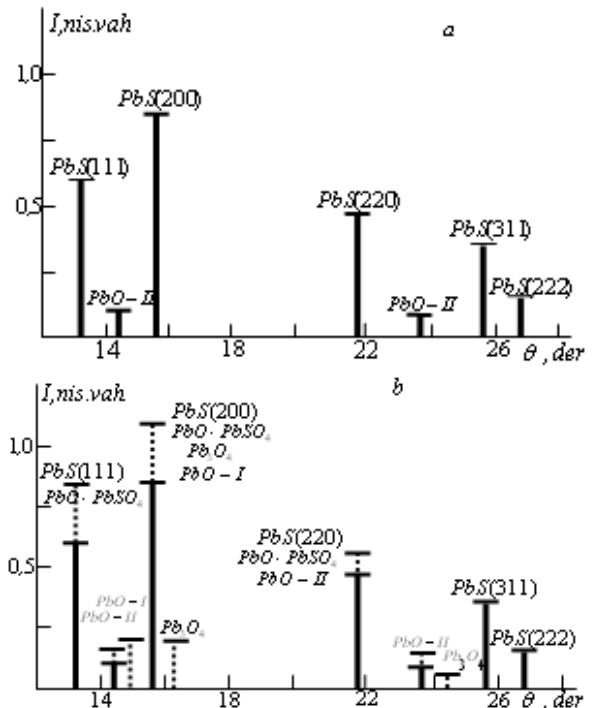
dəmlənməsi vakuum şəraitində  $200 \div 300^\circ\text{S}$  temperaturlarda 2 saat müddətində aparılmışdır.



*Şək. 1* Başlanğıc halda və 2 MeV enerjili elektronlarla şüalandırıldıqdan sonra  $\text{PbS(Na)}$  epitaksial təbəqələrinin mikrofotosu.  $\Phi_e$ : 1- 0; 2-  $5 \cdot 10^{15} \text{ sm}^{-2}$ ; 3-  $1 \cdot 10^{17} \text{ sm}^{-2}$ ; 4-  $1 \cdot 10^{17} \text{ sm}^{-2}$  + qalınlığı  $0,2 \text{ mkm}$  olan səth təbəqəsinin kimyəvi üsulla ləğv edilməsi. *a*- ikinci elektronlar rejimində, *b*- tərsinə-səpilmis elektronlar rejimində müşahidələr. Miqyas bölgüsü –  $0,1 \text{ mkm}$ .

Gürğusun sulfidin səthaltı qatının rentgenostruktur (DRON-2), ikinci ion mass-spektroskopiyası (Sameca IMS4F), oje-elektron spektroskopiyası (PHI-660) (Şək.3) metodlarının köməyiylə dəqiq təhlili təbəqənin tərkibində  $\text{PbO-II}$  (tetraqonal modifikasiya),  $\text{PbO-I}$  (romboedrik modifikasiya),  $\text{PbO-PbSO}_4$ ,  $\text{Pb}_3\text{O}_4$  oksidlərinin olmasını aşkar etmişdir. Gürğusun sulfidin müstəvilərəsasi məsafə oksid fazalardakı müstəvilərəsasi məsafəyə yaxın qiymətə malik olduğundan [3], metodik

nöqtəyi-nəzərdən, polikristallik PbS təbəqələrində aparılmış rentgen tədqiqatları daha informativ hesab edilə bilər. Bu məqsədə yetişdirilmiş polikristallik PbS nümunələrinin mis mənbəyin şüalanmasında çəkilmiş tipik rentgen difraktoqramları 2,a saylı şəkildə göstərilmişdir. İlkin vəziyyətdə kristallitlər (111), (100), (110) və (311) orientasiyalarına malikdirlər. Təbəqə səthinin havadakı oksigenlə qarşılıqlı təsiri nəticəsində PbO-II fazasında kiçik intensivlikli reflekslər müşahidə olunur. Elektron şüalanmasından sonra bəzi reflekslərdə genişlənme, intensivliyin artması və yeni difraksiya piklərinin yaranması müşahidə olunur. Difraktoqramların təhlili göstərir ki, difraksiya mənzərəsinin dəyişilməsi mürəkkəb oksid fazaları naborunun yaranması ilə əlaqədardır. Yeri golmışkən, PbS (111) və PbS (311) təbəqələrində reflekslərin intensivliyi dəyişmir (şək.2b). Verilmiş bucaqlar intervalında qurğuşun sulfiddən əksolunma 0 olduğundan, alınmış nəticələr qurğuşun sulfidin səthində onun strukturuna təsir etməyən oksid fazalarının yaranmasını sübut edir. Müxtəlif xarici təsirlər zamanı bir neçə oksid fazasının yaranması qurğuşun sulfid üçün xarakterik olub, 6 sayılı işdə təsvir olunmuşdur. Elektron şüalanması zamanı oksidləşmənin əsas xüsusiyyəti diffuziya proseslərinin yüksək temperaturla deyil, şüalanmanın təsiri altında sürətlənməsidir. O cümlədən, ionlaşdırıcı şüalanma sahəsində aşqar və defektlərin miqrasiya sürətinin artması bərk fazada kimyəvi reaksiyaların sürətini artıraraq, səthin sorbsiya qabiliyyətini çıxaldır. Modifikasiya olunmuş qatın qalınlığı mono və polikristal təbəqələr üçün eyni olub,  $5 \cdot 10^{16} \text{ sm}^{-2}$  dozasında  $80 \div 110 \text{ nm}$ ,  $1 \cdot 10^{17} \text{ sm}^{-2}$  dozasında isə  $120 \div 200 \text{ nm}$  olmuşdur.



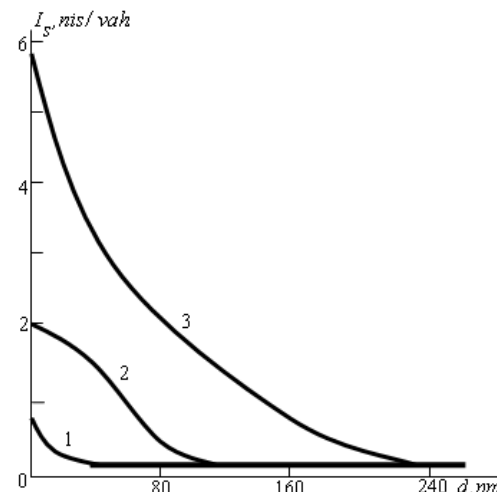
Şək.2. Polikristallik PbS təbəqələrinin elektron şüalanmasından öncə (a) və sonra (b) difraktoqram sxemləri. Şüalanmadan sonra reflekslərin dəyişilməsi ştrix-xətlərlə göstərilmişdir.

Vakuumda,  $200^\circ\text{S}$ -də aparılmış postradiasiya dəmləməsi modifikasiya olunmuş oksid təbəqəsinin xassələrini dəyişdirir. Oksigenin oje-xətlərinin intensivliyi və onun qurğuşun sulfidə nüfuzetmə dərinliyi azalır. Konsentrasiya profillərinin təhlili göstərdi ki, vakuum dəmləməsində modifikasiya olunmuş təbəqənin qalınlığı  $1,5 \div 2$  dəfə azalır. Oksid fazalarındakı

difraksiya reflekslərinin bir qisminin intensivliyi azalır, digər qismi isə yox olur. Eksperimental nəticələr vakuum dəmləməsinin oksigenin səthaltı qatdan çıxarılmasına və oksid fazaların azaldılmasına kömək etdiyini sübut edir. Bununla belə, dəmləmələr zamanı modifikasiya olunmuş təbəqə qalmaqdır.

Səthaltı qatın PbS(Na,e) təbəqələrinin elektrik və fotoelektrik xassələrinə təsirinin qarşısını almaq məqsədilə bu qatlar kimyəvi üsulla ləğv edilmişlər. Səthin kimyəvi aşilanmadan sonra çəkilmiş mikrofotoları 1 sayılı şəkildə göstərilmişdir. İkinci elektron rejimində səthdə ölçüləri  $0,01 \div 0,1 \text{ mkm}$  olan izolə edilmiş «adacıqlar» müşahidə olunmuşdur.

Kimyəvi tərkibinə görə bu «adacıqlar» oksid fazalarının ləğv edilməmiş qalıqları ola bilər. Hər halda tərsinə-səpilmüş elektronlar rejimində onlar daha tünd kontrasta malikdirlər (orta atom nömrəsi azaldıqca faza tündləşir). Izolə edilmiş yüksəkkomlu «adaciq»lar yüklerin lateral daşınması prosesinə təsir etmək iqtidarında olmadığından, kimyəvi aşilanmadan sonra modifikasiya olunmuş təbəqənin təsirinin nəzərə alınmaması barədə fikir yürütütmək mümkündür.



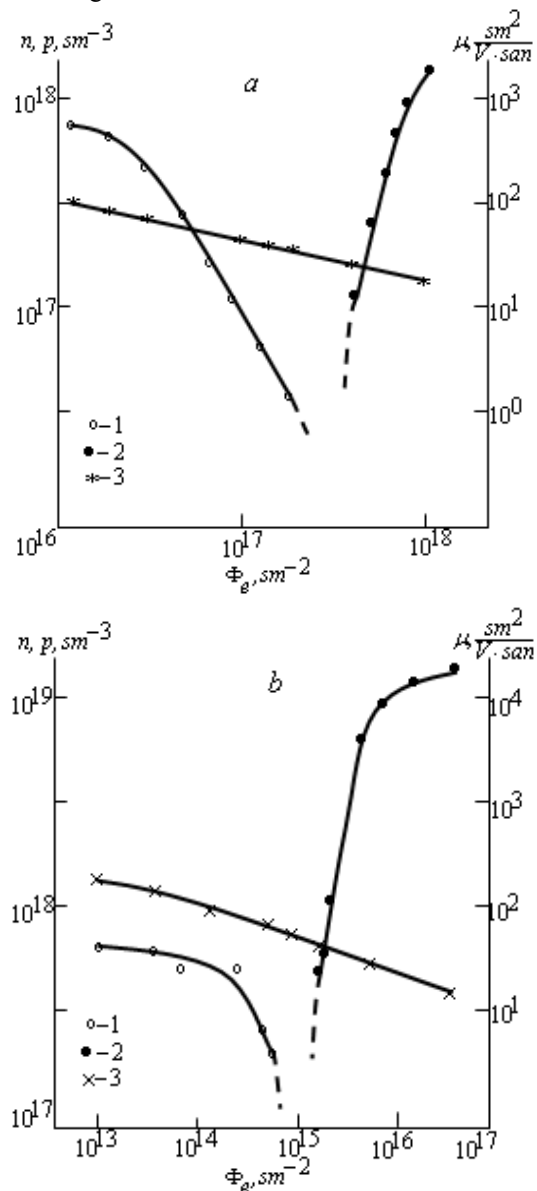
Şək.3 Qurğuşun sulfid epiteksial təbəqəsinin səthaltı qatında oksigenin oje-pikləri intensivliyinin paylanması profili. Fə: 1- 0; 2- $5 \cdot 10^{16} \text{ sm}^{-2}$ ; 3- $1 \cdot 10^{17} \text{ sm}^{-2}$ .

300K temperaturda yükdaşıyıcıların konsentrasiyası və yüvrülükünün elektron şüalanması və bor ionlarının implantasiyası dozasından asılılığı 4 sayılı şəkildə göstərilmişdir. Alınmış əyrilər 2, 3 sayılı işlərdə ilkin p-tip keçiriciliyə malik olan qurğuşun halkogenidlərində alınmış analoji eksperimental nəticələrlə yaxşı uzlaşır və darzonali qurğuşun halkogenidlərinin elektrik xassələrinin radiosiyasının təsiri altında dəyişilməsi haqqında mövcud olan təsəvvürlər çərçivəsinə yerləşir. Növündən asılı olmayaq, radiosiyasının dozası artıraq, tədqiq olunan nümunələrdə deşik konsentrasiyasının azalması, keçiricilik tipinin inversiyası və elektron konsentrasiyasının artımı müşahidə olunur. Inversiya yüksəkenerjili elektronlarla şüalanmanın  $(3 \div 4) \cdot 10^{17} \text{ sm}^{-2}$ , bor ionlarının implantasiyasında isə  $(8 \div 9) \cdot 10^{14} \text{ sm}^{-2}$  dozalarında müşahidə olunur. Elektron konsentrasiyasının borun implantasiya olunduğu nümunələrdə şüalanmanın böyük dozalarında müşahidə edilən doyması, elektron şüalanmasının hətta yüksək dozalarında da müşahidə olunmur. 1 sayılı işdə göstərilmişdir ki, bu hadisə PbS(Na,e) təbəqələrində olan natriumun müxtəlif miqdarlarında defekt yaranması prosesinin xüsusiyyətləri ilə əlaqədardır.

Daşıyıcılar konsentrasiyasının dozadan asılılığını ümumi təsvirini yaratmaq üçün qurğusun halkogenidlərinin şüalandırılması zamanı nöqtəvi defektlərin onların elektrik xassələrinə təsirini nəzərə alan Haynrix-Palmetşofer modelindən istifadə etmək olar [4]. Bu modelə əsasən qurğusunla əlaqəli olan Frenkel cütü valent zonasına bir deşik, kükürdlə əlaqəli olan Frenkel cütü isə keçiricilik zonasına əlavə iki elektron verir. Şüalanma zamanı yaranan izafə elektronlar konsentrasiyası

$$n = 2n_s - n_{Pb} \quad (1)$$

düsturuna əsasən təyin olunur. Burada,  $n_s$ ,  $n_{Pb}$  - müvafiq olaraq kükürd və qurğusundan çıxarılan atomların sayıdır. Müyyən olunmuşdur ki, şüalanma zamanı defektlərin əsas növü halkogen vakansiyalarıdır. Elektron keçiriciliyinin artması ( $n > 0$ ) kükürdüñ alt qəfəsində defekt yaranmasının böyük kəsiyi və qurğusunun alt qəfəsində güclü rekombinasiya proseslərinin getməsi ilə izah oluna bilər.

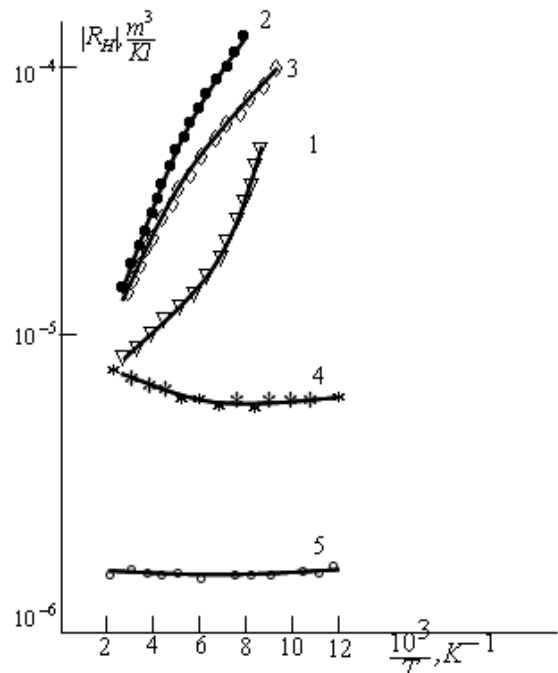


Şək. 4.  $p\text{-PbS(Na)}$  təbəqəsində 300K temperaturda yüksəkdaşıyıcıların elektron şüalanması (a) və bor ionlarının implantasiyası (b) zamanı konsentrasiya (1,2) və yüvrülüyü (3) doza asılılıqları. 1 və 2 işarələri keçiricilik tipinin inversiyadan önce və sonra olan qiymətlərini göstərir.

4 sayılı şəkildə verilmiş doza asılılıqları göstərir ki, tədqiq olunan  $\text{PbS(Na,e^-)}$  və  $\text{PbS(Na,B^+)}$  təbəqələrində, yüvrülüğün qiymətini azaltmadan, elektron şüalanması və bor implantasiyası vasitəsilə konsentrasiyanı məqsədəyönlü şəkildə tənzim etmək mümkündür. Radiasiya texnologiyalarının tətbiqi infraqırmızı diapazonda işləyən fotodiодlər üçün zəruri olan keçiriciliyin  $p$ -tipdən  $n$ -tipə dəyişməsi prosesini həyata keçirməyə imkan verir.

Radiasiya metodları güclü kompensə olunmuş qurğusun halkogenidləri üçün daha perspektivlidir. 77K temperaturda və  $\Phi_e=3\cdot10^{17}\text{ sm}^{-2}$  flüensdə  $\text{PbS(Na,e^-)}$  təbəqələrində yukdaşıyıcıların konsentrasiyası  $10^{15}\div10^{16}\text{ sm}^{-3}$  olmuşdur.

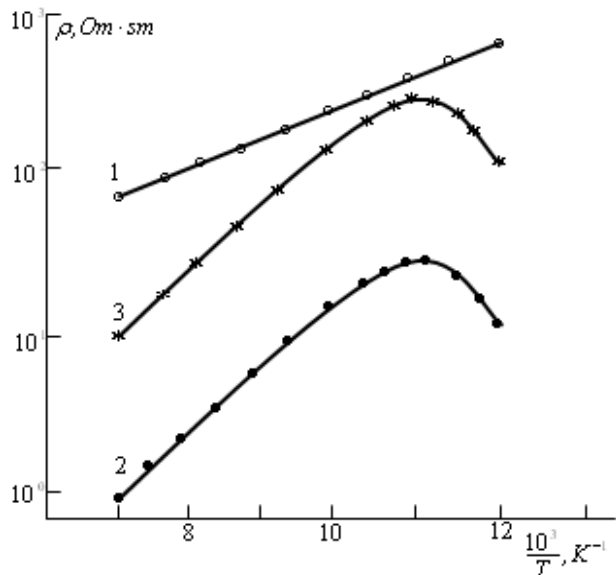
$\text{PbS(Na,B^+)}$  təbəqələrində 77K temperaturda inversiya zamanı deşiklərin minimal konsentrasiyası  $10^{14}\text{ sm}^{-3}$  olmuşdur. Təqdim olunmuş texnoloji üsul digər qurğusun halkogenidləri və onların əsasında formalasdırılmış bərk məhlullar, həmçinin implantasiya olunmuş ionlar üçün də ümumi fiziki mənzərəyə malikdir.  $\text{PbS(Na)}$  təbəqələrini hidrojen ionları ilə implantasiya etdikdə ( $\Phi_H=(1\div5)\cdot10^{15}\text{ sm}^{-2}$ ,  $E_H=50\text{ keV}$ ), elektron şüalanmasına məruz qalmış ( $\Phi_e\approx10^{17}\text{ sm}^{-2}$ ,  $E_e=(2\div4)\text{ MeV}$ )  $(\text{PbS})_{1-x}(\text{La}_2\text{S}_3)_x\text{:Pb}_{1-x}\text{Sm}_x\text{S(Na)}$  təbəqələrində də güclü kompensə olunmuş nümunələr yaradılmasının analoji nəticələri alınır. İlkin halda deşiklərin konsentrasiyası  $10^{17}\div10^{18}\text{ sm}^{-3}$  olan nümunələrdə güclü kompensasiya olmur.



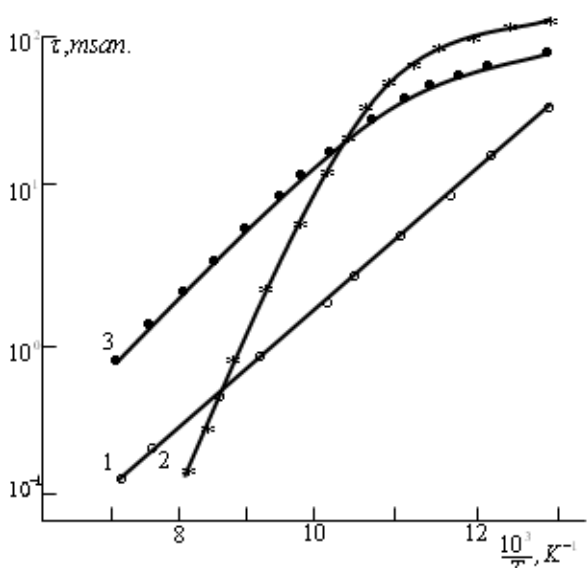
Şək. 5.  $\text{PbS(Na)}$  təbəqələrində yüksək 2MeV enerjili electronlarla şüalanmadan sonra Holl əmsalının temperatur asılılığı.  $\Phi_e$ : 1 -  $3\cdot10^{17}\text{ sm}^{-2}$ ; 2, 3 -  $5\cdot10^{17}\text{ sm}^{-2}$ ; 4 -  $7\cdot10^{17}\text{ sm}^{-2}$ , 5 -  $8.5\cdot10^{17}\text{ sm}^{-2}$  nümunəsində 300°S temperaturda termik dəmləmə aparılmışdır.

5 sayılı şəkildən göründüyü kimi, güclü kompensə olunmuş təbəqələrdə Holl əmsali aktivləşmiş xarakterə malikdir. Bütün nümunələrdə ( $\text{PbS(Na, B^+)}$  istisna olmaqla) aktivləşmə enerjisi  $E_{ak}=15\div90\text{ MeV}$  təşkil etmişdir. Radiasiya texnologiyalarının köməyilə alınmış güclü kompensə olunmuş nümunələrin ən mühüm xüsusiyyəti temperaturu 250°S-dən yüksək olan termik təsirlər zamanı qeyri-sabit olmasıdır. 300°S

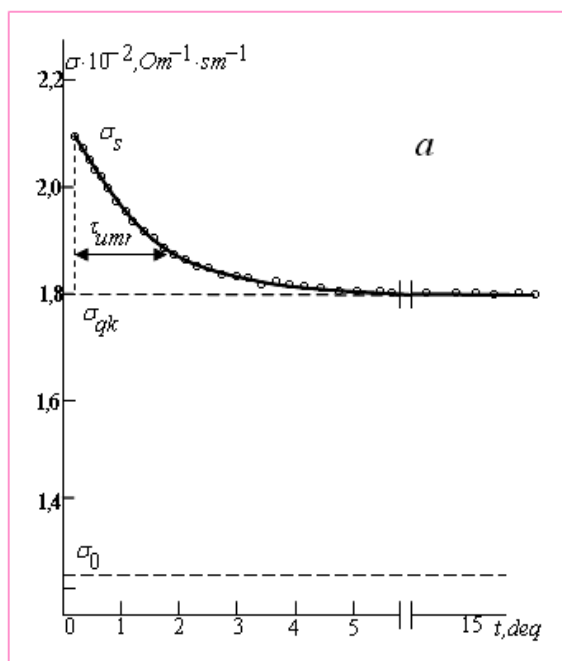
temperaturda, 1÷2 saat müddətində aparılmış postradiasiya dəmləməsi nəticəsində güclü kompensasiya halının qismən itkisi baş verir. Buna səbəb qurğunun halkogenidlərində donor təsirinə malik olan radiasiya defektlərinin dəmlənməsi materialda deşik konsentrasiyasının artmasıdır. Lakin bizim tədqiqatlar göstərir ki, 250°S-dən yüksək olan termik təsirlər zamanı meydana çıxan arzuolunmaz nəticələri aradan qaldırmaq mümkündür. Bunun üçün şüalanma və implantasiyanı əvvəlcədən daha invers etməklə,  $n$ -tip keçiriciliyə malik olan material almalı, postradiasiya dəmləməsi vasitəsilə onu  $p$ -tip keçiriciliyə malik olan güclü kompensə olunmuş hala keçirmək lazımdır. Əlavə tədqiqatlar göstərdi ki, vakuumda 250°S-dən alçaq temperaturlarda 10 saat müddətində aparılmış termoemaldan sonra şüalanmaya məruz qalmış nümunələr sabitdirilər və onların elektrik və fotoelektrik parametrləri hissələndən sonra dəyişikliyi uğramamışlar.



Şək.6. Radiasiya təsirinə uğramış kompensə olunmuş təbəqələrdə qaranlıq xüsusi müqavimətinin temperatur asılılığı:  
1- PbS(Na, B<sup>+</sup>); 2- Pb<sub>0,995</sub>La<sub>0,005</sub>S(Na,e<sup>-</sup>), 3- PbS(Na,H<sup>+</sup>).



Şək.7. Radiasiya təsirinə uğramış kompensə olunmuş təbəqələrdə fotokeçiriciliyin relaksasiya müddətinin temperatur asılılığı: 1- PbS(Na, B<sup>+</sup>); 2- Pb<sub>0,995</sub>La<sub>0,005</sub>S(Na,e<sup>-</sup>), 3- PbS(Na,H<sup>+</sup>).



Şək.8. Tek işıqlanmadan sonra 77K temperaturda şüalanmaya məruz qalmış və kompensə olunmuş PbS(Na,B<sup>+</sup>) təbəqələrində fotokeçiriciliyin relaksasiya əyriləri.

5 və 6 sayılı şəkillərdə şüalandırılmış nümunələrin fotokeçiriciliyinin qaranlıq xüsusi müqaviməti və relaksasiya müddətinin temperatur asılıqları göstərilmişdir. Relaksasiya müddəti, nümunə növbələşən impuls siqnalları ilə işıqlandırıllarkən, fotokeçiriciliyin relaksasiya əyrilərinin təhlilindən təyin olunur. Şəkildən görünür ki, 80K-dən yüksək temperaturlarda fotokeçiriciliyin xüsusi müqaviməti və relaksasiya müddətinin temperatur asılıqları aktivləşmiş xarakterə malikdir. 80K-dən aşağı temperaturlarda bəzi nümunələrdə asılılığın eksponensial xarakterdən kənara çıxmaları istilik fununun təsiri ilə əlaqədardır.  $E_{ap}=15\div90\text{MeV}$ ,  $E_{ap}=45\div140\text{ MeV}$   $PbS\langle Na, B^+ \rangle$  istisna olmaqla) olmuşdur. Holl effekti, elektrik keçiriciliyi və fotoelektrik keçiriciliyinin ölçmələrindən alınmış aktivləşmə enerjilerinin müqayisəsindən alınan  $E_{aR} > E_{aR} > E_{ap}$  ikiqat bərabərsizliyi keçiricilik zonasının döşəməsi və valent zonasının tavarı irimiqyaslı relyefə malik olan güclü kompensə olunmuş yarımkəçiricilər üçün xarakterikdir. Şüalandırılmış nümunənin 77K temperaturda maksimal relaksasiya müddəti saniyənin onda bir hissələrinə bərabər olub, şüalandırılmamış nümunələrin analoji parametrdən 2÷3 tərtib böyükdür. Alınmış  $\tau$ ,  $E_{a\tau}$ ,  $E_{aR}$ ,  $E_{ap}$  kəmiyyətləri qurğunun sulfid və qurğunun tellurid əsasında yara-

dilmiş bərk məhlulların güclü kompensə olunmuş kvazibir-cins təbəqələrinin analoji parametrlərinə uyğundur.  $PbS\langle Na \rangle$  təbəqələrində, elektron və ya ionlarla şüalandırıldığda, nizamsızlaşmış oblastların meydana çıxmazı nəticəsin-də dar və enlizonalı yarımkəciriçi bərk məhlulların kvazibir-cins təbəqələrindəki fluktuasiyalarla müqayisə oluna bilən zonalar modullaşması yaranır [6].  $PbS\langle Na, B^+ \rangle$  təbəqələri

haqqında xüsusi danişmaq lazımdır. Istsna hallarda bu təbə-qələrdə (Şək.8)  $E_{aR}$ ,  $E_{a\rho}$  enerjilərinin qiyməti  $90 \div 180 \text{ MeV}$ ,  $E_{a\tau}$ -nın qiyməti isə  $150 \div 270 \text{ MeV}$  diapazonunda olmuşdur. Bu faktı böyük kütləli bor ionları ilə şüalandırılma zamanı zonalar relyefinin daha böyük radiasiya zədələnməsinə məruz qalması ilə izah etmək olar [6].

- 
- [1] S.P. Zimin, D.S. Zimin, Yu.V. Ryabkin, A.N. Bragin Electron irradiation influence on porous silicon electric parameters. Materials of the Intern. Conf. «Porous Semiconductors. Science and Technology». Madrid, Spain, 2000. p.242-243.
  - [2] S.P. Zimin, M.N. Preobrazhensky, D.S. Zimin, R.F. Zaykina, G.A. Borzova, V.V. Naumov. Growth and properties of PbTe films on porous silicon. Infrared Phys. and Technol. 2002, v.40, p.337-342.
  - [3] R.F. Zaykina, Yu.A. Zaykin, K.V. Potatyi i dr. O dozovoy zavisimosti kontsentratsii nositeley zaryada v sulfide svintsa, obluchennom elektronami. JTF, 2001, t.71, vip.3, s.67-74.
  - [4] L. Palmetschofer. Ion implantation in IV-VI semiconductors. Appl. Phys. A. 1984, v.43, p.139-153.
  - [5] V.N. Vidrik, V.I. Zubkova, M.Yu. Putilovskaya i dr. Vliyaniya implantatsionnogo legirovaniya na strukturnie xarakteristiki plenok tellurida svintsa. Poverkhnosti. -1988, vip.2, s.104-109.
  - [6] I.H. Wilson, N.J. Zheng, U. Knipping. Scanning tunneling microscopy of an ion-bombarded PbS (001) surface. Appl. Phys. Lett., 1988, v.53, p.2039-2041.

#### H. A. Hasanov

#### STUDY OF ELECTRICAL AND PHOTOELECTRIC PROPERTIES OF STRONGLY COMPENSATED SOLID SOLUTIONS OBTAINED ON THE BASE OF LEAD SULPHIDE UNDER THE INFLUENCE OF RADIATION

The presented paper is devoted to investigation of structure and physical properties of polycrystalline epitaxial films of lead sulphide and the solid solutions obtained on its base under the influence of radiation. Results of X-ray diffraction, Auger spectral and microstructure analyses are described. Temperature dependences of a resistivity, coefficient of Hall and mobility of charge carriers are analyzed.

#### Г.А. Гасанов

#### ИЗУЧЕНИЕ ЭЛЕКТРИЧЕСКИХ И ФОТОЭЛЕКТРИЧЕСКИХ СВОЙСТВ СИЛЬНО КОМПЕНСИРОВАННЫХ ТВЕРДЫХ РАСТВОРОВ, ПОЛУЧЕННЫХ НА ОСНОВЕ СУЛЬФИДА СВИНЦА ПОД ВОЗДЕЙСТВИЕМ РАДИАЦИИ

Представленная работа посвящена исследованию структуры и физических свойств поликристаллических epitaksiyalnyx пленок сульфида свинца и твердых растворов, полученных на его основе под воздействием радиации. Изложены результаты рентгеноструктурного, оже-спектрального и микроструктурного анализов. Проанализированы температурные зависимости удельного сопротивления, коэффициента Холла и подвижности носителей заряда.

Received: 05.03.08

## INVESTIGATION OF DIELECTRIC PROPERTIES OF STRONGLY-ABSORBING LIQUIDS AND THEIR SOLUTIONS

**S.T. AZIZOV, Sh.K. AGAMURADOVA, Ch.O. KADJAR**

*G.M. Abdullayev Institute of Physics of National Academy of Sciences,  
Baku, Azerbaijan, AZ-1143 H. Javid ave., 33*

The investigation results of dielectric properties of solutions of some amides and nitromethane in dioane in SHF range are given in the work and the existence of two dispersion relaxation regions of Debye type in these polar liquids and solutions, from which the low-frequency one is defined by decay processes of molecular processes of dipole molecules, is established. The non-reflecting absorption effect of electromagnetic radiation is observed in these solutions.

### **Introduction.**

The investigations of dielectric solution properties of polar liquids in the region of their wave dispersion allow obtaining the information about their molecular structure. Besides, as it is shown in works [1,2], these investigations give possibility to study the demonstration of non-reflecting absorption effect of electromagnetic radiation which reveals in dilute solutions of polar molecules.

The study of microwave radiation reflection in acetone-benzol and water-dioane solutions shows the case of effect on definite width and concentration of these solutions of non-reflecting absorption [1, 2, 3]. The existence of similar effect forms the application perspective of dielectric materials as the basis for absorption thin layer of microwave radiation. All this makes the investigation of absorption reflection effect of microwave radiation in two-layered system reasonable, because polar solutions have the high dielectric constant and short time of dipole relaxation in nonpolar solvent. The individual polar liquids (acetone, water alcohols, acetonitrile, amides and others) and their solutions in nonpolar solvents (dioane, benzol) are used in the capacity of investigation objects. In the given article the investigations of dielectric properties and molecular structures of amides and nitromethane and their solutions in nonpolar dioane are given.

### **Investigation method.**

The polar amides suppose the presence of amine group having the big value of equilibrium dielectric constant  $\epsilon_0$ ; for example: for formamide it is equal to 110 units and has enough short relaxation time lying in the limits  $1,5 \cdot 10^{-11}$  sec.

It has been established by us that the amide dielectric properties in the range of centi- and millimeter radio waves and their solutions in nonpolar dioane are well described in terms of two relaxation processes. These processes are defined by decay processes of hydrogen-connected associates of amide molecules and relaxation of free dipole molecules [4, 5]. Besides, the existence the polar component of non-reflecting absorption effect of incident electromagnetic radiation in polar amides has been revealed

by investigations of microwave reflection characteristics from regulated layer width of diluted solutions of polar amides in nonpolar dioane [4, 5].

The properties of these solutions aren't investigated in microwave region. That's why parallel study of dielectric properties and reflection characteristics of these solutions has the definite theoretical and practical interest.

The investigations are carried out at temperature 20°C and  $\lambda=1,5\text{cm}$  and  $\lambda=8,15\text{mm}$  wave lengths with the use of panoramic measurer of standing wave on voltage R2-66, RR-67 and indicator device Y2R-67 with which the measuring wave-guide cells, short-circuited on the end, are connected. The last ones are thermostated and have the devices for regulation of solution reflecting layer width. The nitromethane, formamide, dymethylformamide, *N*-methylformamide, *NN*-dymethylacetamide and dioane by HCA trend are used in the capacity of components of investigated solutions. The method based on measurements of coefficients of standing wave  $\eta$  and width  $l$  of substance reflecting layer at which amplitudes of reflected wave achieve their minimal values is used for definition of dielectric constant  $\epsilon'$  and dielectric loss  $\epsilon''$  of individual polar liquids and their solutions in dioane. The results of these measurements are presented in table 1.

### **Result discussion.**

The estimation of intermolecular short-range forces with the use of correlation parameter  $q = \mu_l^2 / \mu_g^2$  where  $\mu_l$  and  $\mu_g$  are values of molecule dipole moments defined in liquid and gas phases is carried out for preliminary discussion about molecular nature of nitrogen-containing polar liquids and their solutions in nonpolar solvent correspondingly. The values of dipole moments of investigated substances, obtained on data of works [6,7] in gas phase are used in the capacity of  $\mu_g$ . The reference data of low-frequency measurements of equilibrium dielectric constant  $\epsilon_0$  [8] are used for finding  $\mu_l$ . The calculation of  $\mu_l$  is carried out on Onzonger-Kirkwood-Frelih equation obtained from polarization static theory [9]

$$\mu_l = [(\epsilon_0 - \epsilon_\infty)(2\epsilon_0 + \epsilon_\infty)] / [\epsilon_0(\epsilon_\infty + 2)^2] \cdot [9KT / 4\pi N_A] \quad (1)$$

where  $T$  is absolute temperature,  $N_A$  is Avogadro constant,  $k$  is Boltzman constant.

The value of high-frequency limit of dielectric constant  $\epsilon_\infty$  including in (1) is defined from Klauzius-Mosotti equation

$$[(\varepsilon_\infty - 1)/(\varepsilon_\infty + 1)] = 1,05 \left[ (n^2 - 1)/(n^2 + 2) \right] \quad (2)$$

where  $n$  is optical substance refraction index, coefficient 1,05 takes into consideration the contribution of atom polarization in  $\varepsilon_\infty$  [9].

The character of dispersion and absorption dependences of formamide, dymethylformamide, *N*-methylformamide and NN-dymethylacetamide in microwave regions essentially differs from analogous dependences for nitromethane. The  $\varepsilon'$  and  $\varepsilon''$  changes with frequency show that relaxation processes in them can't be described in limits of unique time of dipole relaxation, and also symmetric or asymmetric distribution of relaxation times on example of nitromethane-dioane solutions at temperature 20°C (see fig.1).

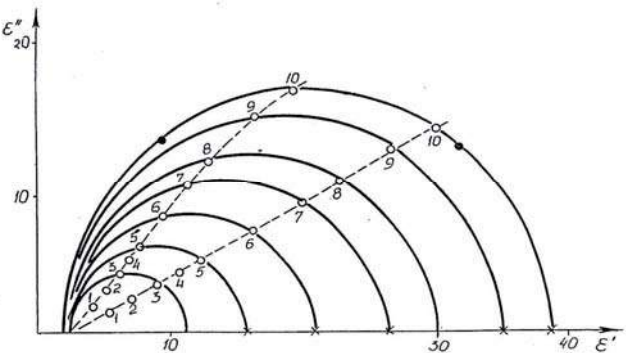


Fig.1. Debye – Kouel diagrams of nitromethane-dioane solutions at temperature 20°C and volume concentrations of nitromethane 10(1); 20(2); 30(3); 40(4); 50(5); 60(6); 70(7); 80(8); 90(9); 100(10) % on data of work [5].

Table 1.

Dielectric constant  $\varepsilon'$  and dielectric loss  $\varepsilon''$  of nitromethane, *N*-methylformamide and NN-dymethylacetamide solutions in dioane at temperature 20°C and  $\lambda=1,5\text{cm}$  and  $\lambda=8,15\text{mm}$  wave lengths. Volume concentrations  $\phi$  of polar component are in %.

φ % volume	Nitromethane-dioane				NN-dymethylacetamide-dioane				<i>N</i> -methylformamide-dioane	
	$\lambda=1,5\text{cm}$		$\lambda=8,15\text{mm}$		$\lambda=1,5\text{cm}$		$\lambda=8,15\text{mm}$		$\lambda=1,5\text{cm}$	
	$\varepsilon'$	$\varepsilon''$	$\varepsilon'$	$\varepsilon''$	$\varepsilon'$	$\varepsilon''$	$\varepsilon'$	$\varepsilon''$	$\varepsilon'$	$\varepsilon''$
100	30,2	15,1	19,2	18,1	14,1	14,9	5,8	8,01	29,7	52,9
80	26,9	13,6	16,3	16,1	12,2	11,5	5,21	5,61	16,7	29,5
60	22,7	11,3	12,8	12,8	9,92	8,24	4,53	3,85	10,2	14,0
50	19,8	9,7	11,2	11,2	8,7	6,55	4,24	3,19	8,33	9,86
40	16,3	7,5	9,41	8,59	7,45	5,1	3,92	2,49	6,9	6,84
30	12,5	5,35	7,7	6,27	6,29	3,65	3,54	1,82	5,81	4,63
20	8,92	3,45	6,04	4,25	4,98	2,4	3,2	1,19	4,68	2,37
10	5,5	1,7	4,25	1,92	3,44	1,1	2,8	0,75	3,26	0,87
0	2,28		2,28		2,28		2,28		2,28	
φ%	Formamide-dioane				Dymethylformamide-dioane					
	$\lambda=1,5\text{cm}$		$\lambda=8,15\text{mm}$		$\lambda=1,5\text{cm}$		$\lambda=8,15\text{mm}$			
	$\varepsilon'$	$\varepsilon''$	$\varepsilon'$	$\varepsilon''$	$\varepsilon'$	$\varepsilon''$	$\varepsilon'$	$\varepsilon''$		
0	2,28	-	2,28	-	2,28	-	2,28	-		
1	2,42	0,18	2,36	0,10	2,36	0,07	2,33	0,05		
2	2,56	0,34	2,41	0,16	2,45	0,17	2,37	0,12		
3	2,70	0,50	2,48	0,28	2,55	0,36	2,42	0,17		
5	2,98	0,86	2,58	0,40	2,74	0,46	2,52	0,30		
8	3,42	1,40	2,74	0,64	3,07	0,78	2,66	0,47		
10	3,73	1,80	2,85	0,75	3,30	0,98	2,75	0,60		
15	4,50	2,56	3,10	1,08	4,00	1,50	2,95	0,92		
20	5,22	3,35	3,37	1,48	4,62	2,00	3,21	1,30		
25	5,92	4,05	3,64	1,80	5,15	2,60	3,43	1,66		
30	6,60	4,82	3,92	2,20	5,76	3,22	3,70	2,20		
40	7,90	6,35	4,53	3,14	6,70	4,20	4,15	3,02		
50	9,35	7,68	5,10	3,95	7,65	5,28	4,60	4,00		
60	10,8	8,95	5,65	5,05	8,60	6,60	5,10	5,11		
80	13,2	11,20	6,20	6,61	10,4	9,75	6,23	7,12		
100	15,8	13,20	6,25	8,16	12,2	13,75	8,12	9,73		

The analysis of experimental data shows that dielectric properties of formamide, dymethylformamide, *N*-methylformamide and NN-dymethylacetamide are well described in terms of two independent

relaxation processes. In these cases the real frequency dependences  $\varepsilon'$  and  $\varepsilon''$  of substance are expressed by equations of the following form:

$$\begin{aligned} [(\varepsilon' - \varepsilon_\infty) / (\varepsilon_0 - \varepsilon_\infty)] &= [C_1 / (I\omega\tau_1^2) + C / (I\omega\tau_2^2)] \\ [\varepsilon'' / (\varepsilon_0 - \varepsilon_\infty)] &= [\omega\tau_1 C_1 / (I + \omega\tau_1^2) + \omega\tau_2 C / (I + \omega\tau_2^2)] \end{aligned} \quad (4)$$

where  $\tau_1$ ,  $\tau_2$ ,  $C_1$  and  $C_2$  are relaxation times and relative depositions of two dispersions correspondingly [4]. In general case the calculation  $\tau_1$ ,  $\tau_2$ ,  $C_1$  and  $C_2$  on equations (4) requires the application of calculation special methods. The parameter calculation results of two dispersion regions with application of calculation technique described in [5].

In accordance with data of low-frequency measurements  $\varepsilon_0$  one can consider that low-frequency dispersion region of

amides is defined by decay processes of hydrogen-connected chains. Moreover, the value which is inverse one to relaxation time of this dispersion characterizes the probability of hydrogen bond breakdown. The relaxation of monomeric molecules on chain ends defines the existence of second high-frequency dispersion region on microwaves.

Table 2.

$\phi\%$ volume	Nitrometane-dioane		<i>N</i> -methylformamide-dioane			<i>NN</i> -dymethylacetamide-dioane			
	$\tau \cdot 10^{-12}$	$\alpha$	$\tau_1 \cdot 10^{-12}$	$C$	$\varepsilon_{\infty 2}$	$\tau_1 \cdot 10^{-12}$	$\tau_2 \cdot 10^{-12}$	$C_1$	$\varepsilon_{\infty 2}$
100	4,40	0,01	24,2	0,96	12,3	13,1	9,98	0,86	5,50
80	4,63	0,03	24,2	0,96	7,0	12,2	7,83	0,84	5,06
60	4,80	0,04	23,2	0,94	5,3	11,5	6,26	0,81	4,50
40	4,69	0,03	20,7	0,90	4,3	10,4	5,91	0,74	3,80
20	4,48	0,02	17,9	0,86	3,4	9,80	4,50	0,64	3,10

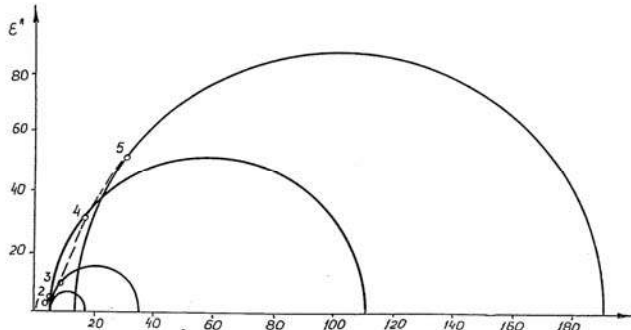


Fig.2. Debye – Kouel diagrams of *N*-methylformamide-dioane solutions at temperature 20°C and volume concentrations of *N*-methylformamide 20(1); 30(2); 50(3); 80(4); 100(5) % on data of work [5].

The decrease of  $\tau$  value of main dispersion region of *NN*-dymethylacetamide in the comparison with *N*-methylformamide is defined by locking actions of methyl groups decreasing the possibility of formation of molecular associates formed because of hydrogen bonds. It is character that relaxation times and relative depositions of second dispersions are close between each other in spite of differences in behavior of main dispersion regions of amides. Dielectric behavior of *N*-methylformamide and *NN*-dymethylacetamide solutions in dioane in studied concentration interval is so close to behavior of pure polar components (fig.2) as in the case of pure polar amides, the obtained results aren't in limits of symmetric or asymmetric distribution of relaxation times. The mechanism of two relaxation processes which probably keeps its significance at amide dilution by nonpolar solvent, gives the best approximation. In *N*-methylformamide solutions the relaxation time  $\tau_1$  defining the low-frequency dispersion region in formamide and its solutions decreases on value with increase of dioane content (table 2).

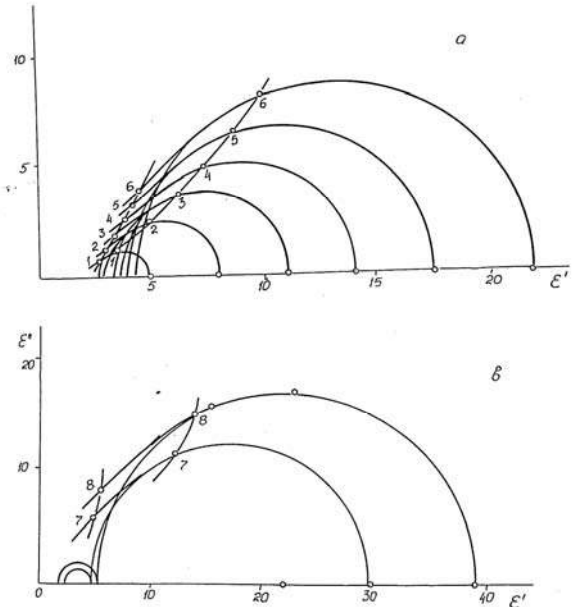


Fig.3. Debye – Kouel diagrams of *N*-dymethylacetamide-dioane solutions at temperature 20°C and volume concentrations of *NN*-dymethylacetamide 20(2); 30(3); 40(4); 50(5); 60(6); 80(7); 100(8) % on data of work [5].

This result shows that the decay of chain complexes of formamide molecules formed with help of hydrogen bonds takes place at *N*-methylformamide dissolution, this leads to decrease of associate life time and also to life time of average size of such associates of *N*-methylformamide molecules and molecules on chain ends. This is experimentally confirmed by the fact that the relative deposition  $C_1$  of low-frequency region decreases with dilution of *N*-methylacetamide by dioane. The similar result is observed in *NN*-dymethylacetamide-dioane solutions, the decrease of relaxation time value  $\tau_1$  of solutions with increase of nonpolar

dioane in them is accompanied by increase of part of second dispersion regions; Moreover  $\tau_2$  value stays practically independent on dioane concentration (see table 2, fig.3).

**Conclusion.**

The obtained experimental data  $\epsilon'$  and  $\epsilon''$  solutions of different concentrations are used for finding of resonance

concentrations of solution polar components at which it is expected the revealing of predictable effect of non-reflecting absorption of electromagnetic radiation of given wave length and at known sizes of wave-guide directing system by graph-analytic method.

- 
- [1] E. Salve, E.R.Kasimov, S.T.Azizov, Ch.O.Qajar. «Resonance reflektionless absorptions of electromagnetic waves in solutions», Turkish journal of Physics, 1998, n. 5, p. 389 – 393.
  - [2] E.R. Kasimov, M.A. Aleph, Ch.O. Qajar, Fizika, 1995, v. 1, p. 37 – 44.
  - [3] R.M.Kasimov, M.A.Kalaphy, E.R.Kasimov, Ch.O.Qajar, E.J. Salaev. JTR, 1996, v. 6, №5, p. 167-171.
  - [4] E.R.Kasimov, S.T.Azizov, Ch.O.Qajar R.M. Kasimov. «Dielectric properties and molecular structure of solutions formamiddioxn and dimethyl-formamiddioxn », Fizika, 1998, t.4, №1, p. 30-33.
  - [5] E.R.Kasimov, S.T.Azizov, Ch.O.Qajar R.M. Kasimov. «Dielektricheskiye svoystva i molekulyarnye stroyeniya N – metilformamida, NN – dimetilacetamida i nitrometana», Fizika, 1999, №3, s. 30 – 44. (in Russian).
  - [6] R.M. Kasimov. Metrologiya, №7, 1987, s.45-51. (in Russian)
  - [7] O.A. Osipov, V.I. Minkin. Spravochnik po dipolnim momentam. Moskva. Vissaya shkola. 1965.(in Russian).
  - [8] Ya.Yu. Akhadov. Dielektricheskiye svoystva binarnikh rastvorov. M., Nauka, 1977,c. 400. (in Russian).
  - [9] M.P. Shakharonov. Metodi issledovaniya dvijeniya molekul stroyeniya jidkostey. Moskva, MGU, 1963. (in Russian).

**S.T. Əzizov, Sh.K. Ağamuradova, Ç.O. Qacar**

**YÜKSƏKUDUŞLU MAYELƏRİN VƏ ONLARIN MƏHLULLARININ  
DİELEKTRİK XASSƏLƏRİNİN TƏDQİQİ**

Bəzi amidlərin və nitrometanın dioksanda olan məhlullarında ƏYT diapozonunda dielektrik xassələrinin tədqiqatının nəticələri göstərilib və bu polyar mayelərdə və onların məhlullarında iki dispersiyalı Debay tipli relaksasiya sahələri müəyyən olunmuşdur ki, bunlardan da aşağızlkli dipol molekul komplekslərinin molekullarının dağılma prosesi ilə təyin edilmişdir. Bu məhlullarda elektromaqnit şüaların əksolunmadan udulması effekti müşahidə edilmişdir.

**С.Т. Азизов, Ш.К. Агамурадова, Ч.О. Каджар**

**ИССЛЕДОВАНИЕ ДИЭЛЕКТРИЧЕСКИХ СВОЙСТВ  
СИЛЬНОПОГЛОЩАЮЩИХ ЖИДКОСТЕЙ И ИХ РАСТВОРОВ**

В статье приведены исследования диэлектрических свойств растворов некоторых амидов и нитрометана в диоксане в диапазоне СВЧ и установлено существование в этих полярных жидкостях и растворах двух дисперсионных областей релаксации дебаевского типа, из которых низкочастотная определена процессами распада молекулярных комплексов дипольных молекул. В этих растворах наблюдался эффект безотражательного поглощения электромагнитного излучения.

*Received: 19.12.07*

## POLİMER – PİROKERAMİKA KOMPOZİTLƏRİN VƏ ONLARIN KOMPONENTLƏRİNİN ELEKTROFİZİKİ XASSƏLƏRİ ARASINDA ƏLAQƏ

**H.Q. HƏSƏNOV, E.Ə. KƏRİMÖV**

*Milli Aerokosmik Agentliyi Elmi Tədqiqat Aerokosmik İnformatika İnstitutu*

**M.Ə. QURBANOV, S.N. MUSAYEVA**

*Azərbaycan MEA H.M. Abdullayev adına Fizika İnstitutu,*

*Bakı, AZ-1143, H. Cavid pr., 33*

Polimer-pirokeramika kompozitlərin reorientasiya polyarizasiyasının ( $P_r$ ), dielektrik nüfuzluğunun  $\left(\frac{\varepsilon_{33}^T}{\varepsilon_0}\right)$ , pyezomodulunun  $d_{31}$ , piroelektrik əmsalının ( $\gamma$ ) piroelektrik fazanın  $\text{PbTiO}_3$  komponentinin konsentrasiyasından asılılıqları tədqiq edilmişdir. Müəyyən edilmişdir ki, kompozitlərin və onların komponentlərinin konsentrasiya asılılıqları fərqlidir. Göstərilmişdir ki, bu effekt əsasən kompozitdə pirohissəciklərin səthinin təsiri nəticəsində polimer fazasının ifrat molekulyar quruluşunun  $\text{PbTiO}_3$ -ün konsentrasiyasından asılı olaraq dəyişməsi və onda gedən elektron-ion və polyarizasiya prosesləri ilə əlaqədardır.

Hal-hazırda seqnetoaktiv bərk məhlullar (SABM) əsasında yaradılmış piroelektrik çeviriciləri texnikada geniş tətbiq olunur. Bir fazalı klassik piroelektrik materialların texnologiyasının təkmilləşdirilməsi son həddə yaxınlaşdırıcı və tətbiqləri ilə əlaqədar olaraq cox tələbləri ödəmədikləri üçün pyezo-, piroelektrik materialların yeni növü – coxfazalı kompozit materiallar yaradılır. Polimer – SABM əsasındaki kompozitlər yüksək effektivliyə malik piroelektrik materiallar olğunu üçün onların elektrofiziki və piroelektrik xassələrinin kompozitin tərkibindən, fazaların strukturundan, kristallofiziki və kimyəvi parametrlərindən asılılığının tədqiq edilməsi aktual məsələlərdəndir. Polimer – SABM kompozitdə piroelektrik effektinin formalşmasına fazalarası sərhəddə polyarizasiya prosesində toplanmış yük daşıyıcılarının böyük əhəmiyyətə malik olması müəyyən olunmuşdur [1-4]. Ona görə yüksək piroelektrik xassələrə malik kompozitlərin yaradılmasında aktual məsələlərdən biri də fazaların struktur heterogenliyinin və fazalararası fiziki (sərhəddə polimer matrisanını ifrat molekulyar quruluşunun piroelektrik hissəciklərin təsiri şəraitində formalşması), kimyəvi (pirohissəciklə polimer makromolekullar arasında donor-akseptor tipli rabitələrin yanlanması) effektlərin kompozitdə polyarizasiya prosesində sərhəddə elektrik yük daşıyıcılarının stabillaşməsində və piroelektrik effektinin formalşmasında rolunun öyrənilməsidir. Göstərilən problemin həlli üçün polimer – SABM kompozitlərin və onların komponentlərinin elektrofiziki xassələri arasındakı əlaqənin təyin edilməsi mühüm amillərdən biridir.

İşin əsas məqsədi polimer –  $\text{PbTiO}_3\text{-PbZrO}_3\text{-PbNb}_{2/3}\text{Zn}_{1/3}\text{O}_3\text{-PbNb}_{2/3}\text{Mg}_{1/3}\text{O}_3$  və polimer –  $\text{PbTiO}_3\text{-PbZrO}_3\text{-PbNb}_{2/3}\text{Zn}_{1/3}\text{O}_3\text{-PbW}_{1/2}\text{Mg}_{1/2}\text{O}_3$  kompozitlərin reorientasiya polyarizasiyası ( $P_r$ ), dielektrik nüfuzu  $\left(\frac{\varepsilon_{33}^T}{\varepsilon_0}\right)$ , pyezomodulu  $d_{31}$ , piroelektrik əmsali ( $\gamma$ ) ilə piroelektrik fazanın uyğun parametrləri arasındaki əlaqənin təyin edilməsidir.

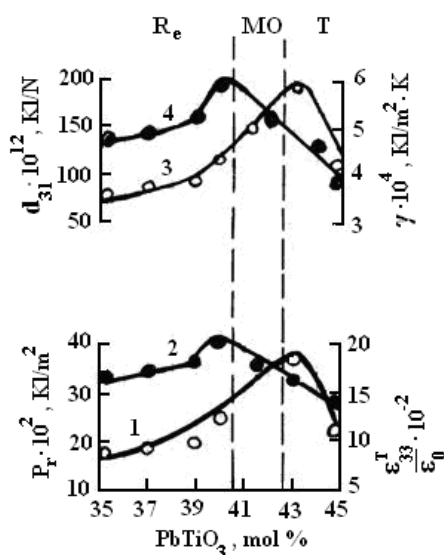
### Eksperimentin metodikası

Polimer faza kimi polyar polimer polivinildenftorid (PVDF) götürülmüşdür. Piroelektrik faza kimi birinci  $\text{PbTiO}_3\text{-PbZrO}_3\text{-PbNb}_{2/3}\text{Zn}_{1/3}\text{O}_3\text{-PbNb}_{2/3}\text{Mg}_{1/3}\text{O}_3$  və poli-

mer -  $\text{PbTiO}_3\text{-PbZrO}_3\text{-PbNb}_{2/3}\text{Zn}_{1/3}\text{O}_3\text{-PbW}_{1/2}\text{Mg}_{1/2}\text{O}_3$  və ikinci tərkibli çoxkomponentli SABM – dan istifadə edilmişdir. Piroelektrik kompozitlər polimer və pirokeramika tozlarının homogen qarışığından isti preslənmə metodu ilə alınmışdır. Pirofazanın kompozitdə həcmi tərkibi 50% - dir. Pirokeramika hissəciklərin ölçüləri 63÷100 mkm seçilmişdir. Kompozitlərin reorientasiya polyarizasiyası termostimullaşmış depolyarizasiya (TSD) metodu ilə təyin edilmişdir. Bu metodla həm də kompozitin piroelektrik əmsali təyin edilmişdir [5]. Pyezoelektrik modul  $d_{31}$  statik metod ilə ölçülümdür [6].

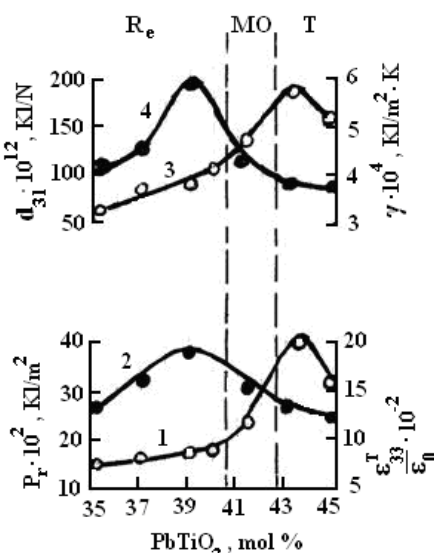
### Eksperiment

Hər iki tərkibin makroskopik xarakteristikalarının ( $\varepsilon, P_r, d_{31}, \gamma_p$ )  $\text{PbTiO}_3$  komponentinin konsentrasiyasından (mol%) asılı olaraq dəyişməsi uyğun olaraq şəkil 1 və şəkil 2-də verilmişdir.



Şək. 1. Pirofazanın elektrofiziki parametrlərinin  $\frac{\varepsilon_{33}^T}{\varepsilon_0}$  (1),

$P_r$ (2),  $d_{31}$ (3),  $\gamma$ (4)  $\text{PbTiO}_3$ -ün konsentrasiyasından asılılıqları. 1-ci tərkib üçün [7,8].



Şək. 2. Pirofazanın elektrofiziki parametrlərinin  $\frac{\epsilon^T}{\epsilon_0}$  (1),

$P_r$  (2),  $d_{31}$  (3),  $\gamma$  (4) PbTiO<sub>3</sub>-ün konsentrasiyasından asılılıqları. 2-ci tərkib üçün [7,8].

Polimer-pirokeramika kompozitlərdə pirofaza kimi götürülen tərkiblərin hər birində PbTiO<sub>3</sub>-in molekulyar faizlərlə konsentrasiyasını dəyişib polimer matrisaya salsaq və alınmış kompozit xarakteristikalarını təyin etsək, onda pirokeramik fazanın makroskopik parametrləri ilə kompozitin uyğun parametrləri arasında əlaqəni tapa bilərik. Məsələnin bu cür həlli nöinki kompozitlə pirokeramik fazanın parametrləri arasındaki əlaqəni tapmağa, həm də pirokeramikanın strukturunun pirokompozitin xassələrinə təsirini təyin etməyə imkan verir, çünki götürülən  $Pb(Zr_{1-x}Ti_x)O_3 - \sum_n PbB_{1-\alpha}B''_\alpha O_3$

sistemində PbTiO<sub>3</sub> komponentinin konsentrasiyasını dəyişməklə, sistem romboedrik strukturdan ( $R_e$ ) morfotrop oblastı (heterogen struktur  $R_e+T$ ) keçərək tetraqonalala ( $T$ ) çevrilir. Romboedrik – tetraqonal keçidi PbTiO<sub>3</sub> mürəkkəb oksidin konsentrasiyasının 40,5 – 42,5 mol. % - nə uyğundur.

Polimer fazanın kompozit xassələrinin formalaşmasında rolu daha mürəkkəbdür. Fazalararası sərhəddə gedən müxtəlif təbiətli qarşılıqlı təsirlər, fazalararası kimyovi rəbitlərin yaranması, kristallaşma prosesində polimer fazanın ifrat molekulyar quruluşunun pirokeramik hissəciklərin səthinin aktivliyindən asılı olaraq formalaması kompozitin piroelektrik xassələrinə bilavasitə təsir edən istilik-fiziki parametrlərini kəmiyyətcə təyin edən əsas amillərdir. Pirokompozit bir fazasındaki (polimer) elektron-ion, polaryazasiya prosesləri digər fazadakı (pirokeramika) analogi proseslərin inkişafına təsiri son nəticədə piroelektrik kompozitin qalıq reorientasiya polaryazasiyasını və piroəmsalını təyin edir. Pirofaza kimi götürülən 1-ci və 2-ci tərkibli seqnetoaktiv bərk məhlullarda PbTiO<sub>3</sub> komponentinin konsentrasiyasını dəyişməklə polimer fazada kompozit piroelektrik xassələrinə təsir edə bilən proseslərin intensivliyini müəyyən qədər idarə etmək olar. Bu tərkibləri bir-birindən fərqləndirən, pirokompozitlərin fizikasını və texnikasını işləmək baxımından əhəmiyyətli edən faktorlar aşağıdakılardır:

- 1-ci (şək. 1) və 2-ci (şək. 2) tərkiblərin dielektrik nüfuzluğunun  $\frac{\epsilon^T}{\epsilon_0}$  maksimumları tetraqonal oblastda yerləşir,

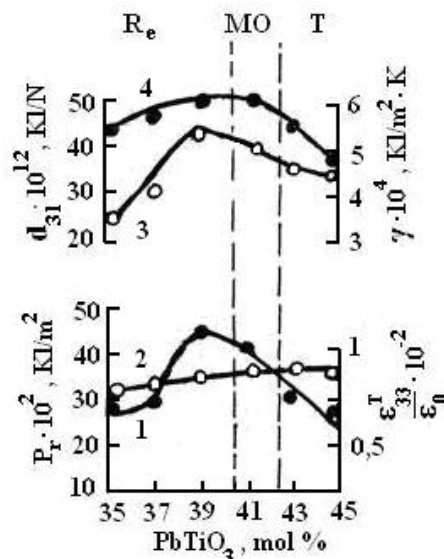
lakin 2-ci tərkibin  $\frac{\epsilon^T}{\epsilon_0}$  maksimumu tetraqonal oblastın nisbətən daha dərinliklərinə tərəf sürüşür;

- tərkiblərin reorientasiya polaryazasiyası PbTiO<sub>3</sub>-ün konsentrasiyasından asılıdır və romboedrik oblastda maksimal qiymətə çatır, sonra isə morfotrop və tetraqonal oblastlarda kəskin azalır;

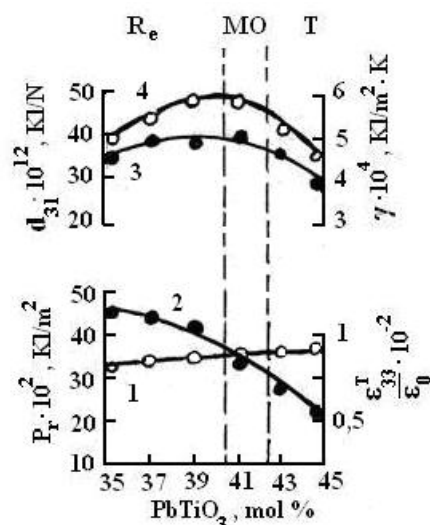
- öyrənilən tərkiblərin piroelektrik əmsallarının konsentrasiya asılılıqları fərqlənir (şək. 1 və 2);

- hər iki tərkibə daxil olan kationların elektromənfiliyindən asılı olaraq onların seqnetosərtliyi və ya domen strukturun istiliyi qarşı dayanıqlığı dəyişir;

- 1-ci tərkibə Nb, Zn, Mg, 2-ci tərkibə isə Nb, Zn, W, Mg kationları daxildirlər və 2-ci tərkibdə elektromənfiliyi kiçik olan kationların sayı çoxdur.



Şək. 3. Pirokompozitlərin elektrofiziki parametrlərinin  $P_r$  (1),  $\frac{\epsilon^T}{\epsilon_0}$  (2),  $d_{31}$  (3),  $\gamma$  (4) PbTiO<sub>3</sub>-ün konsentrasiyasından asılılıqları.



Şək. 4. Pirokompozitlərin elektrofiziki parametrlərinin  $\frac{\epsilon^T}{\epsilon_0}$  (1),  $P_r$  (2),  $d_{31}$  (3),  $\gamma$  (4) PbTiO<sub>3</sub>-ün konsentrasiyasından asılılıqları.

Şək. 3 və 4-də piroelektrik kompozitlər üçün tərkibdən asılı olaraq elektrofiziki xarakteristikaların dəyişməsi verilmişdir. Cox aydın görünür ki, pirofaza kimi işlədiñen piroelektrik keramikaların elektrofiziki xarakteristikalarının tərkibdən asılılıqları ilə onlar əsasında alınmış pirokompozitlərin uyğun xarakteristikaları arasında oxşarlıq çox azdır. Pirofazanın tərkibdən asılı olaraq  $\frac{\varepsilon^T}{\varepsilon_0}, \gamma, P_r, \frac{\gamma}{\varepsilon^T}$  parametrləri

ləri üçün alınmış dəqiq maksimumlar pirokompozitlərin uyğun xarakteristikaları üçün alınmir (şək. 3 və 4). Hər tərkibin xarakteristikaları  $\gamma$ -nin maksimal qiymətinə uyğun konsentrasiya üçün ( $PbTiO_3$ , mol %) hesablanmışdır. Şək. 1, 2 və şək. 3, 4-ün müqayisəsi göstərir ki, pirokompozitlər üçün additivlik prinsipi ödənmir. Kompozitin makroskopik parametrləri  $\left( \frac{\gamma_p}{\varepsilon_{33}^T}, \frac{\gamma_p}{d_{31}}, \frac{\gamma_p}{\varepsilon_{33}^T C_V D} \right)$  ancaq pirokeramik fazanın parametrləri ilə təyin olunmur. Bu onu göstərir ki, kompozitlərdə piroelektrik effektinin formalaşması daha mürəkkəb proseslərin nəticəsidir və polimer fazanın mühüm rolunu əks etdirir. Lakin polimer matrisanın rolunu təyin edərkən onu heç zaman piroelektrik fazadan tədric formada aparmaq olmaz. Digər tərəfdən məlumdur ki [7-10],  $\gamma$  materialların piroaktivliyinin ölçüsüdür və  $\gamma = \frac{\Delta P}{\Delta T}$  kimi təyin olunur.

Burada  $P$  - polarizasiyadır. Bu kəmiyyət monokristalda spontan polarizasiyaya  $P_s$ , pirokeramikada və pirokompozitdə qalıq reorientasiya polarizasiyasına bərabərdir. Bu fundamental faktorlardan istifadə edərək  $\gamma$ -nın artırılması üçün tələb olunan şərtlər haqqında fikir söyləmək olar. Heç şübhəsiz ki, bu şərtlər kompozitin komponentlərinin strukturunu ( $R_e, T$ ,

$R_e + T$ , sferolitlik, polyarlıq, amorfluq), kristallokimyəvi və kristallofiziki parametrləri (elektromənfilik və  $B''-O$  rabiələrin kovalentliyinin dərəcəsi, perovskit özəyin bircins spontan deformasiyası  $180^\circ$ -li domenlərdən fərqli domenlərin öz səmtinin dəyişməsi qabiliyyəti, domenlərin ölçüləri və yürüklüyü), elektro- və istilik-fiziki xarakteristikaları ( $P_r, \varepsilon, \operatorname{tg}\delta, \gamma, d_{ij}, c_V, D$ ) ilə əlaqəli olmalıdır. Pirokompozitlərin fiziki strukturunu yüksək heterogenlidir, çoxfazalı sistemdir və fazalararası keçid təbəqəyə malikdir. Fazalararası keçid təbəqənin olması və fazaların (üzvi – polimer və qeyri-üzvi - pirokeramika) xarakteristikalarının bir-birindən kəskin fərqlənməsi kompozitdə elektrotermopolaryarizasiya zamanı kifayət qədər mürəkkəb elektron-ion və polaryarizasiya proseslərinin yaranmasını təmin edir. Belə ki, polimer-pirokeramika sərhəddində elektron, ion və polaryarizasiya prosesləri əsasən pirohissəciyin təsiri altında formalılmış polimer matrisanın ifrat molekulyar quruluşundan asılıdır.

### Nəticə.

Polyar polimerdən və çoxkomponentli SABM-dan [ $PbZrO_3 - PbTiO_3 - PbNb_{\frac{1}{3}}Zn_{\frac{1}{3}}O_3 - PbB''_{1-\beta}B'''_{\beta}O_3$ ;  $B''_{1-\beta}B'''_{\beta}$  ( $Nb_{\frac{1}{3}}Mn_{\frac{1}{3}}$ ;  $Nb_{\frac{1}{3}}Co_{\frac{1}{3}}$ ;  $Nb_{\frac{1}{3}}Zn_{\frac{1}{3}}$ ;  $Nb_{\frac{1}{3}}Ni_{\frac{1}{3}}$ ;  $Nb_{\frac{1}{3}}Mg_{\frac{1}{3}}$ ]) ibarət kompozitlərin xarakteristikaları – komponentlərin strukturu və elektrofiziki parametrləri arasındaki asılılıqlar əsasında piroelektrik materialların yaradılmasının fiziki-texnoloji xüsusiyyətləri müəyyən edilmişdir.

- 
- [1] M.K. Kerimov, M.A. Kurbanov, E.A. Kerimov and et all. Fizika tverdogo tela, 2005, t. 47, p. 686-690.
  - [2] M.K. Kerimov, E.A. Kerimov, A.E. Panich and et all. Fizika tverdogo tela, 2007, t. 49, p. 877-880.
  - [3] M.A. Kurbanov, M.K. Kerimov, S.N. Musaeva, E.A. Kerimov. VMS, 2006, ser.B, t.48, №10, p. 1892-1897.
  - [4] M.A. Kurbanov, S.N. Musaeva, E.A. Kerimov. VMS, 2004, ser.B, t.46, №12, p. 2100-2103.
  - [5] Yu.A. Qoroxovatskiy. Osnovi termodepolyarizatsionnogo analiza. Moskva: Nauka.1981. 175 p.
  - [6] Q.A. Lusheykin. Polimernie pyezoelektri. Moskva: Ximiya.1990. 176 p.
  - [7] A.Ya. Dantsiger Segnetoelektricheskie tverdie rastvori mnogokomponentnih system slojnih oksidov i visoko-effektivnie pyezokeramicheskie materiali na ix osnove: Dis. ... dokt. f.-m.n. Rostov na Donu: 1985, 480 p.
  - [8] E.G. Fesenko, A.Ya. Dantsiger, O.N. Razumovskaya. Novie pyezokeramicheskie materiali. Rostov na Donu: RGU, 1983, 145 p.
  - [9] Dj. Barfut, Dj. Teylor. Polyarnie dielektriki i ix primenenie. Moskva: Mir,1981. 527 p.
  - [10] M.A. Kurbanov. Elektretniy, pyezo-, piroelektricheskiy, varistorniy i pozistorniy effekti v polimernix kompozitsionnih dielektrikax: Dis. ... dokt. f.-m.n. Baku: 1985, 473 p.

**Х.Г. Гасанов, Е.А. Керимов, М.А. Курбанов, С.Н. Мусаева**

## **ВЗАИМОСВЯЗЬ МЕЖДУ ЭЛЕКТРОФИЗИЧЕСКИМИ СВОЙСТВАМИ КОМПОЗИТОВ ПОЛИМЕР-ПИРОКЕРАМИКА И ИХ КОМПОНЕНТОВ**

Исследованы зависимости реориентационной поляризации ( $P_r$ ), диэлектрической проницаемости  $\left( \frac{\varepsilon_{33}^T}{\varepsilon_0} \right)$ , пьезомодуля  $d_{31}$ , пироэлектрического коэффициента  $\gamma$  композитов полимер-пирокерамика от концентрации компонента  $PbTiO_3$  пироэлектрической фазы. Определено, что концентрационные зависимости композитов и их компонентов отличаются. Показано, что этот эффект, в основном, связан с изменением надмолекулярной структуры полимерной фазы под действием поверхности пирочастиц композита в зависимости от концентрации  $PbTiO_3$  и электронно-ионными, поляризационными процессами, происходящими в ней.

**Kh.G. Gasanov, E.A. Kerimov, M.A. Kurbanov, S.N. Musaeva**

**INTERRELATION BETWEEN ELECTROPHYSICAL PROPERTIES OF POLYMER - PYROKERAMICS COMPOSITES AND THEIR COMPONENTS**

The dependences of a reorientation polarization ( $P_r$ ) a dielectric permittivity  $\left(\frac{\varepsilon_{33}^T}{\varepsilon_0}\right)$ , a piezomodulus  $d_{31}$ , a pyroelectric coefficient  $\gamma$  of polymer - pyroceramics composites from concentration of the  $\text{PbTiO}_3$  component of a pyroelectric phase are investigated. It is determined, that the concentration dependences of composites and their components differ. It is shown, that this effect, basically, is connected to change of a super molecular structure of a polymer phase under action of a pyroparticles surface of a composite depending on the  $\text{PbTiO}_3$  concentration and an electron-ion, polarizing processes occurring in her.

*Received: 10.03.08*

## STARK STATE STRUCTURE $^4I_{9/2}$ OF Nd<sup>3+</sup> ION IN $\gamma$ -La<sub>2</sub>S<sub>3</sub> CRYSTAL AT SELECTIVE LASER EXCITATION

**G.I. ABUTALIBOV, D.I. GUSEYNOV, A.A. MAMEDOV**

*G.M. Abdullayev Institute of Physics of National Academy of Sciences,  
AZ-1143, Baku, H. Javid ave., 33*

The luminescence spectra of Nd<sup>3+</sup> ions in  $\gamma$ -La<sub>2</sub>S<sub>3</sub> crystal have been investigated with the application of selective resonance laser excitation at helium temperature and diagram of Stark splittings of main state is constructed.

Nowadays crystals with disordered structure, activated by rare-earth ions, are the ones from the prevailing active mediums for solid-state lasers. The spectral bands of activator in these mediums are characterized by considerable heterogeneous widening. The physical nature of such widening is that different activator centers are in disordered matrix in inequivalent positions and static crystal fields influence on them.

$\gamma$ -La<sub>2-2x</sub>Nd<sub>x</sub>S<sub>3</sub> crystal is related to disordered structures of Th<sub>3</sub>P<sub>4</sub> type. Each Th atom in structure of thorium phosphide is surrounded by eight P atoms, being from it on equal distances and forming "twisted normal eight-top wood" of ThP<sub>8</sub> symmetry ( $\bar{4} - S_4$ ). Six Th atoms surround P atoms, forming strained (twisted) octahedron [PTh<sub>6</sub>] of  $3-C_3$  symmetry. The lanthanide atoms take positions of thorium atoms in Ln<sub>2</sub>X<sub>3</sub> chalcogenides, and atoms of sulfur, selenium and tellurium take positions of P atoms. The coordination polyhedron of Th(Ln) atom can be presented as it would be formed by two penetrating tetrahedrons. The one third of cation knots in elementary cell in  $\gamma$ -La<sub>2-2x</sub>Nd<sub>x</sub>S<sub>3</sub> crystal is vacant one (the cell consists of four formula units) and these vacancies have irregular distribution on crystal volume. Thus, irregularly distributed vacancies distort the crystal field, influencing on ions, being near them. There is no such division even at very low temperatures and their spectra are characterized by wide bands, presenting themselves the superpositions of variety of lines unlike simple many-centered crystals in optical centers of which the clearly resolved peaks are belonged to each center. The contours of absorption and luminescence bands of activator ions in disordered crystals are heterogeneously widened at any temperature. This circumstance is revealed in absorption and luminescence bands of neodymium ions in  $\gamma$ -La<sub>2</sub>S<sub>3</sub> crystals, recorded at  $T=4,2$ K. The spectral lines are nonelementary ones that makes the scheme construction of Stark splitting difficult.

The absorption and luminescence spectra  $\gamma$ -La<sub>2-2x</sub>Nd<sub>x</sub>S<sub>3</sub> had been studied earlier in [1,2]. The authors of [1] relate  $\gamma$ -La<sub>2-2x</sub>Nd<sub>x</sub>S<sub>3</sub> crystal to type of mixed ones with the one activator quazicenter. The conception of activator quazicenter, which later isn't justify itself at spectrum investigation, has been proposed at study of luminescence property of big series of disordered laser crystals with Nd<sup>3+</sup> ions in [3]. The some conceivable static construction which generalizes the properties of variety of elementary centers, differing by structure, but having nearest Stark splitting of energy states is understood as quazicenter. It is clear that construction of Stark splitting without taking into consideration the heterogeneous widening of absorption and

luminescence band (at stationary excitation) in the conception limits of quazicenter is wrong. That's why the investigation necessity of spectrum thin structure of neodymium ions in  $\gamma$ -La<sub>2</sub>S<sub>3</sub> crystal arises. These investigations have been carried out with the application of method of selective resonance laser excitation and spectroscopy of time resolution.

The selective luminescence spectra and diagram of Stark splittings of Nd<sup>3+</sup> ions in  $\gamma$ -La<sub>2</sub>S<sub>3</sub> crystal are presented on the fig.1.

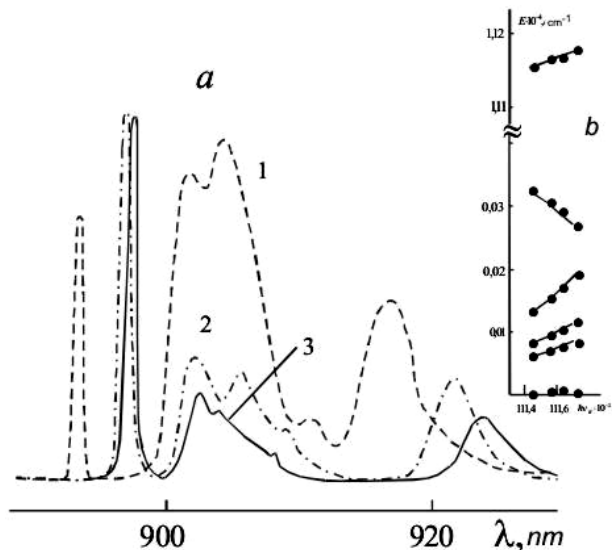


Fig.1. The selective luminescence spectra (a) taken in 25 mcs time after finishing of light exciting impulse action at helium temperature:  
 $1-\lambda_{exc}=895,4 \text{ nm}; 2-\lambda_{exc}=896,4 \text{ nm}; 3-\lambda_{exc}=897,4 \text{ nm};$   
 and diagram of Stark splittings (b) of Nd<sup>3+</sup> ions in  $\gamma$ -La<sub>2</sub>S<sub>3</sub> ions.

The weak structure of  $^4F_{3/2} \rightarrow ^4I_{9/2}$  transition reveals in luminescence spectra at excitation of absorption band, corresponding to  $^4I_{9/2} \rightarrow ^4F_{3/2}$  transition in short-wave side. That's why it is established to excite the short-wave side of absorption band (from wave length 893 nm up to 897,4 nm with step 1 nm). The thin structure in best form (fig.1a, spectrum-3) reveals at light excitation of wave length  $\lambda_w=897,4 \text{ nm}$  in luminescence spectra (fig.1,a) taken at helium temperature. The thin structure also reveals in luminescence spectrum at shift 1nm to short-wave side, i.e. at light excitation with wave length  $\lambda_w=896,4 \text{ nm}$  (fig.1a, spectrum-2), but moreover maximums of luminescence bands shift to spectrum different sides. The bands with

## STARK STATE STRUCTURE $^4I_{9/2}$ OF Nd<sup>3+</sup> ION IN $\gamma$ -La<sub>2</sub>S<sub>3</sub> CRYSTAL AT SELECTIVE LASER EXCITATION

corresponding transitions between Stark components  $^4F_{3/2}$  and  $^4I_{9/2}$  multiplets heterogeneously widen in luminescence spectrums at further shift 1 nm to short-wave side of absorption spectrum at light excitation with wave length  $\lambda_w=895,4$  nm (fig.1a, spectrum-1). Thus, luminescence spectrum analysis obtained at selective resonance laser excitation shows that they essentially differ from spectrums at nonselective excitation and strongly depend on excitation wave length.

Taking into consideration the value of transition energy  $^4I_{9/2} \rightarrow ^4F_{3/2}$  as index of ligand field force, the scheme of

Stark splittings of  $^4I_{9/2}$  multiplet in different optical centers in matrix (fig.1,b) is constructed in the dependence on this parameter. The definition of level energies is carried out on maximum positions in luminescence spectrums beginning from low Stark component of main state  $^4I_{9/2}$ .

The given diagram shows the connection between energies of different Stark levels of  $^4F_{3/2}$  and  $^4I_{9/2}$ , their correlated changes and quantitative values of Stark splittings of  $^4I_{9/2}$  multiplet in different centers.

- 
- [1] A.A. Kaminskiy, S.E. Sarkisov, *Ngok Chan i dr.* Neorganicheskie materiali, t.16, №8, 1980. s.1333-1345.

- [2] J.R. Henderson, M.J. Muramoto. Chem. Phys., 1970, v.52, n.5, p.2311-2314.  
[3] A.A. Kaminskiy. JTEF, 1970, t.58, vip.2, s.407-419.

**Н.И. Абуталибов, С.И. Гусейнов, А.А. Мамедов**

## **$\gamma$ -La<sub>2</sub>S<sub>3</sub> KRİSTALLARINDA SELEKTİV LAZER HƏYƏCANLAŞMASINDA Nd<sup>3+</sup> İONLARININ $^4I_{9/2}$ HALININ STARK STRUKTURU**

Helium temperaturunda rezonans lazer həyəcanlaşma metodunu tətbiq etməklə  $\gamma$ -La<sub>2</sub>S<sub>3</sub> kristallarında Nd<sup>3+</sup> ionlarının luminesenssiya spektrləri tədqiq edilmiş və əsas halın stark parşalanmasının diaqramı qurulmuşdur.

**Г.И. Абуталыбов, Д.И. Гусейнов, А.А. Мамедов**

## **ШТАРКОВСКАЯ СТРУКТУРА СОСТОЯНИЯ $^4I_{9/2}$ ИОНА Nd<sup>3+</sup> В КРИСТАЛЛЕ $\gamma$ -La<sub>2</sub>S<sub>3</sub> ПРИ СЕЛЕКТИВНОМ ЛАЗЕРНОМ ВОЗБУЖДЕНИИ**

При гелиевой температуре, с применением метода селективного резонансного лазерного возбуждения исследованы спектры люминесценции ионов Nd<sup>3+</sup> в кристалле  $\gamma$ -La<sub>2</sub>S<sub>3</sub> и построена диаграмма шарковских расщеплений основного состояния.

Received: 06.03.08

## DIELECTRIC CONSTANT OF RESTORED SrTiO<sub>3</sub>

**A.A. AGASIYEV, M.M. PANAHOV, M.Z. MAMEDOV, V.J. MAMEDOVA, H.O. GAFAROVA**

*Baku State University*

*AZ-1148, Baku, Z. Halilov str., 23*

The metal-nonmetal transition in restored SrTiO<sub>3</sub> has been considered. SrTiO<sub>3</sub> films have dielectric constant ~300 at room temperature. It is shown that system endures transition into state of generated polaron gas at electron concentration higher ~10<sup>17</sup> cm<sup>-3</sup>.

If any band in substance is partly filled at absolute zero then such substance will be metal: the resistance of ideal crystal strives for zero, and it strives for final limit with temperature decrease. If all bands are filled or empty then crystal is nonmetal and its resistance strives for infinity at temperature decrease.

The substance with two-valent element which crystallizes in face-centered or volume-centered cubic lattice should be nonmetal, if overlapping of valent band and conduction band doesn't take place as it is observed in two-valent bands. If we imagine that lattice constants essentially increase then width of both bands will be decreased and overlapping will disappear at some moment, moreover the substance will be nonmetal. The increase of lattice constant only on several percents can be achieved because of heat expansion. The essentially wider change range of interatomic distances can be achieved in substances, having noncrystalline structure.

The metal-nonmetal transition is observed in doped or restored SrTiO<sub>3</sub> and in substances like it. Renetikor has investigated the thin layers of SrTiO<sub>3</sub> produced by cathode sputtering in mixture Ar and O<sub>2</sub> [1]. He has revealed that the crystalline particle dimensions and oxygen pressure influence mainly on properties of obtained films.

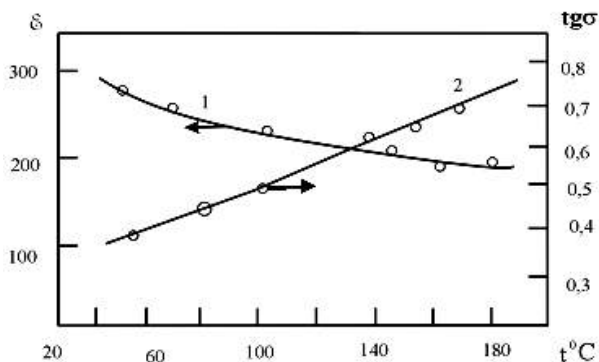


*Fig.1. The temperature dependences of dielectric constant (1) and dielectric loss tangent (2) of SrTiO<sub>3</sub> films on the frequency 1 kHz.*

SrTiO<sub>3</sub> films are obtained by us by method of magnetron sputtering in pure argon. These films are restored and have metallic conductivity. The condensates have high resistance and electric strength up to 10<sup>8</sup> V/sm at addition into argon 5% O<sub>2</sub>. The dielectric constant of such films at room temperature is equal to 300 (fig.1) that is ~65% from the value for massive SrTiO<sub>3</sub> [2]. If  $n$  is concentration of free carriers,

$R_b = \frac{\hbar^2 \epsilon}{m^* \cdot e^2}$  is Borov's radius, where  $\epsilon$  is dielectric constant,  $m^*$  is carrier effective mass, then the expression for

atom number in volume unit at which metal-nonmetal transition takes place, will be  $n^{1/3} R_b \sim 0.25$ .

This result well agrees with experimental data for donor concentrations at which transition in doped semiconductors takes place [3,4]. Consequently, it is supposed the bursting change of carrier concentration  $n$  when a ( $s$  is lattice constant) goes through values corresponding to transition.

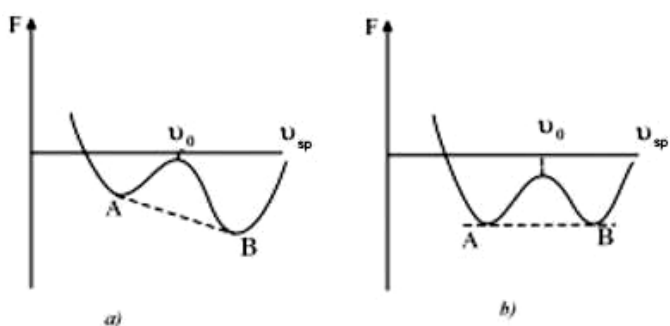


*Fig.2. The dependence of free energy on specific volume for nonmetal*

- a) at pressure which is equal to zero;
- b) at pressure at which the phase transition takes place;  $v_0$  is value of specific volume at which the metal-nonmetal transition appears.

The crystal lattice parameter can be measured only because of pressure change at  $T=0$  at definition of crystal behavior near transition point and it is possible that energy of metal-nonmetal transition is high where two minimums on the curve of free energy dependence on volume (fig.2.a) correspond to two phases. The transition takes place at pressure when both minimums will be on one horizontal (fig.2.b). The metal-nonmetal transition for cubic metal will take place if any parameter influencing on the width of forbidden band (for example, lattice constant) changes continuously. Coulomb gravitation of electrons and holes, the energy of which is equal to  $e^2 / \epsilon r$  will lead to formation of couples with bond energy

$$E \sim \frac{e^4 m^*}{2\hbar^2 \epsilon^2} \quad (1)$$

and transition in such system will be accompanied by concentration jump [5]. The state, in which the small overlapping of two bands exists, i.e. the state, which could be correspond to semimetal unless the formation of electron-hole couples called excitonic isolator. The analogous situation can appear in the semiconductor with final width of forbidden band  $\Delta E$ , if  $\Delta E$  will be less than exciton bond energy and in this case the excitons will form spontaneously.

### DIELECTRIC CONSTANT OF RESTORED SrTiO<sub>3</sub>

The metal-nonmetal transition is observed in restored SrTiO<sub>3</sub> and if we use formula (1) then it is unclear how to use the value of dielectric constant: as static one ( $\epsilon$ ) or high-frequency one ( $\epsilon_\infty$ ). If polaron of small radius doesn't form, then it is followed to use the some combination from  $\epsilon$  and  $\epsilon_\infty$  which is expressed by Sympson formula [6,7]:

$$\epsilon_{eff.} = \frac{1}{\epsilon} + \frac{5}{16} \left( \frac{1}{\epsilon_\infty} - \frac{1}{\epsilon} \right) \quad (2)$$

The effective permeability will be approximately equal to  $2,5\epsilon_\infty$  in the case of materials with high static dielectric constant.

At consideration of strongly localized states, the radius  $r_0$  is defined firstly by disorder as for example round vacancy and not strongly depends on polarization of any distortion of environment. Moreover polaron energy will be

$$E_p = \frac{m^* \epsilon^4}{20 \epsilon_p^2 \hbar^2} \quad (3)$$

where  $m^*$  is effective mass. The polaron effective mass will be equal to  $r_p = \frac{5\hbar^2 \epsilon_p}{m^* e^2}$  that is less than given value ( $m^* = m$ ,  $\epsilon_p = 10$  and  $r_p = 25\text{\AA}$ ).

If  $r_p$  value is comparable with distance between ions in solid state or less than it then polaron is called polaron of small radius. This can take place in the case if effective mass  $m^*$  in unbroken lattice is essentially bigger than  $m$ , that's why it is possible to use the approximation of strong one and consider the bands as narrow ones (fig.3). Naturally, that radius of polarization pit should exceed the ion or atom radius on which the electron is. Then ion radius is the rough approximation to  $r_p$ . The polaron has potential energy

$e^2 / \epsilon R$  on  $R$  distance from charged center, if  $R > r_p$  where  $\epsilon$  is static dielectric constant and interaction in substances  $\epsilon \approx 100$  will be weak one and two cases of polaron of small radius differ.

If radius  $\hbar^2 \epsilon / m_p e^2$  is big one in comparison with  $R$  (the distance of nearest-neighbor metal ion from center) then polaron can be described by hydrogen-like wave functions and energy, necessary for its elimination from center is equal to  $e^4 m_p / 2\hbar^2 \epsilon_p^2$  at  $\epsilon > 100$ , as for example in SrTiO<sub>3</sub>.

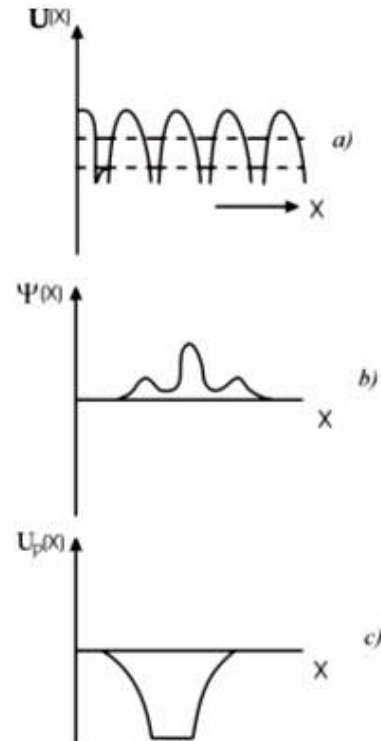


Fig. 3. a) electron potential energy in ideal lattice;  
b) polaron wave function of big or intermediate radius;  
c) polarization pit.

If polarons of small radius form and interaction energy of electron with donor has the form  $-e^2/\epsilon r$  then there are no foundations to expect the appearance of metal-nonmetal transition. If, however, Borov's radius  $\hbar^2 \epsilon / m e^2$  is bigger than  $R$ , then it is possible to imagine the hydrogen-like orbitals of polarons of small radius. Such system will endure the transition into state of generated polaron gas when condition is achieved

$$n^{1/3} \left( \frac{\hbar^2 \epsilon}{m_p e^2} \right) \sim 0,25$$

This case is carried out in SrTiO<sub>3</sub> and series of other materials which have metallic conduction at concentration higher  $\sim 10^{17} \text{ cm}^{-3}$  [8].

- 
- [1] W.B. Pennebauer SrTiO<sub>3</sub> films grown in argon and oxygen mixture / IBMJ. Reberch and Developm. Eng. vol.13, 1964, p.686-689.
  - [2] A.A. Agasiev. Formirovanie I elektrofizicheskie svyozstva plynok slojnikh metalloksidov. Diss. Na soiskanie stepeni dokt. Fizmat. Nauk, Baku, 1995.
  - [3] N.F. Mott, R.V. Gerni. Elektronnie protsessi v ionnikh kristallakh. IL. M. 1950.
  - [4] N.F. Mott. A. Davis., Phil.mag, 17, (1968), ctp.1269.
  - [5] R. Noks. Teoriya eksitativ. M. Nauka, 1966.
  - [6] J.H. Simpson. Phys.Stat Solids, 40, (1970), ctp.207.
  - [7] N.F. Mott. A. Davis. Elektronnie protsessi v nekristallicheskikh veshestvakh. Izd-vo "Mir", Moskva, 1982.
  - [8] N.Konofaos<sup>ax</sup>, E.K.Evangelon<sup>ax</sup>. Electrical characterization of SrTiO<sub>3</sub>/Si interfaces. Zhongchun Wang<sup>b</sup>, V Kugler<sup>b</sup>, U.Helmereson<sup>b</sup>. Journal of Non-Crustalline Solids 303(2002), 185-189.

**A.A. AGASIYEV, M.M. PANAHOV, M.Z. MAMEDOV, V.J. MAMEDOVA, H.O. GAFAROVA**

**A.A. Ağasıyev, M.M. Pənahov, M.Z. Məmmədov, V.C. Məmmədova, H.O. Qafarova**

## **ВƏRPA OLUNMUŞ SrTiO<sub>3</sub> TƏBƏQƏSİNİN DİELEKTRİK NÜFUZLUĞU**

Вərpa olunmuş SrTiO<sub>3</sub> təbəqəsində metal-qeyri metal keçidinə baxılmışdır. Alınmış SrTiO<sub>3</sub> təbəqəsinin otaq temperaturunda dielektrik nüfuzluğu ~300 olmuşdur. Müəyyən edilmişdir ki, elektronların konsentrasiyası  $\sim 10^{17}$  cm<sup>-3</sup> tərkibindən çoxlu olduqda sistem çırlanması polyaron qaz halına keçir.

**А.А. Агасиев, М.М. Панахов, М.З. Мамедов, В.Дж. Мамедова, Х.О. Гафарова**

## **ДИЭЛЕКТРИЧЕСКАЯ ПРОНИЦАЕМОСТЬ ВОССТАНОВЛЕННОГО SrTiO<sub>3</sub>**

Рассмотрен переход метал-неметалл в восстановленном SrTiO<sub>3</sub>. Пленки SrTiO<sub>3</sub> имели диэлектрическую проницаемость ~300 при комнатной температуре. Показано, что система претерпевает переход в состояние вырожденного поляронного газа при концентрации электронов выше  $\sim 10^{17}$  см<sup>-3</sup>.

*Received: 16.03.08*

## THE ROLE OF ZINC ATOMS IN MODIFICATION STABILIZATION IN Cu<sub>2</sub>Se

**Yu.G. ASADOV, Yu. I. ALIYEV, F.G. MAGERRAMOVA, A.G. BABAYEV**

*G.M. Abdullayev Institute of Physics of National Academy of Sciences,  
AZ-1143, Baku, H. Javid ave., 33*

The single crystals of Cu<sub>2</sub>Se, Cu<sub>1.80</sub>Zn<sub>0.20</sub>Se and Cu<sub>1.75</sub>Zn<sub>0.05</sub>Se composition have been synthesized and grown up. The structural phase transformations in single crystals of the given compositions are investigated by high-temperature rentgeno-diffractometer method and it is shown that the orthorhombic modification at 407 K transforms into FCC modification in Cu<sub>2</sub>Se. High-temperature FCC modification stabilizes at room temperature and low-temperature orthorhombic modification stabilizes at high-temperature in Cu<sub>1.80</sub>Zn<sub>0.20</sub>Se crystal where definite part of Cu atoms is exchanged by Zn atoms. The polymorphous transformation are absent in two-phase crystals Cu<sub>1.80</sub>Zn<sub>0.20</sub>Se in temperature interval from room one up to melting point.

Cu<sub>2</sub>Se compound exists in 38.22 weight % Se [1] region in state diagram of cuprum-selenium system, melting point is  $T_{mp} = 1390\text{K}$ , molecular weight is 206.04 and density  $\rho = 6.749 \text{ g/cm}^3$ .

In work [2] it is shown that low-temperature orthorhombic modification with lattice parameters  $a=4.119 \text{ \AA}$ ,  $b=7.028 \text{ \AA}$ ,  $c=20.390 \text{ \AA}$ ,  $Z=12$  at 407 K transforms into high-temperature FCC modification with lattice parameters  $a=5.837 \text{ \AA}$ ,  $Z=4$  and space group Fm3m. In work [3] the large single crystals are obtained by method of structural transformation after ocouple cycle of transformations and it is noted that the stresses and cracks accumulate in single crystal as a result of which it becomes the polycrystal if transformation cycle would be continued later. It is also shown that Cu<sub>2</sub>Se  $\rightarrow$  Cu<sub>2-x</sub>Se ( $x=0.20$ ) takes place in the dependence on transformation order, i.e. some cuprum atoms leave the lattice and crystal has FCC structure with  $a=5.72 \text{ \AA}$  parameter and space group  $F\bar{4}3m$ ,  $Z=4$  at room temperature. This compound is stable in temperature interval from room one up to melting point.

In the given paper the role of zinc atoms in modification stabilization and structural aspects of polymorphous transformations in Cu<sub>2</sub>Se is considered.

Table 1

Atom percentages of components being part of Cu<sub>2</sub>Se, Cu<sub>1.80</sub>Zn<sub>0.20</sub>Se, Cu<sub>1.75</sub>Zn<sub>0.05</sub>Se compositions.

Composition	Cu, at. %	Zn, at. %	Se, at. %
Cu <sub>2</sub> Se	61.677	-	38.323
Cu <sub>1.80</sub> Zn <sub>0.20</sub> Se	55.458	6.162	38.380
Cu <sub>1.75</sub> Zn <sub>0.05</sub> Se	57.488	1.690	40.822

The method of direct synthesis, i.e. chemical interaction of initial components is used for obtaining of homogeneous samples of given compositions. The ampoules from high-quality quartz with internal diameter 1 cm and length 10 cm are applied for synthesized compositions in the capacity of reactor. The ampoules are filled by initial components Cu, Zn and Se in quantities which are necessary for each composition: Cu<sub>2</sub>Se, Cu<sub>1.80</sub>Zn<sub>0.20</sub>Se and Cu<sub>1.75</sub>Zn<sub>0.05</sub>Se, are evacuated up to pressure 1.3 MPa, and later are sealed. The used initial components for syntheses have the following purifications: cuprum has electrolytic one, zinc and selenium are crystalline «04» one. The quantities of initial components which are necessary for synthesizing for each composition (by mass 5 g) separately are given in table 1.

All ampoules with corresponding compositions are put in furnace simultaneously so that they would be in furnace stable band for achieving of similar synthesis conditions.

Further furnace temperature is increased up to selenium melting point ( $T_{mp}=493\text{K}$ ) and is kept at this temperature during 3 hours for which the total reaction selenium-cuprum and selenium-zinc takes place. Further furnace temperature is increased with rate 50K/hour up to temperature which is close to Cu<sub>2</sub>Se melting point ( $T_{mp}=1390\text{K}$ ). The furnace with rate 50K/hour is cooled up to 350K (below the temperature of polymorphous transformations) after two-hour keeping at this temperature and the annealing is carried out for total composition homogenization at this temperature during 200 hours.

The roentgen-phase analysis is carried out for individuality establishment of obtained compositions and also for definition of phase compositions. The samples in powder forms are produced from ingots of each synthesized material for definition of phase relations of composition. The powder of each composition is filled in glass capillary with internal diameter  $\sim 0.8 \text{ mm}$  and the pressed powder in wire form appears from capillar one end at pressing-out by wire with diameter  $\sim 0.7 \text{ mm}$  from another end. The powdergrams in RCD-57.3 camera on CuK<sub>α</sub> radiation are taken from such sample at similar conditions. The powdergram calculations are given in the tables 2, 3 and 4. In these tables the interplanar spacings calculated from diffraction data and also interplanar spacings with corresponding indexes  $hkl$  calculated on computer on structural data are given.

As it is seen from table 2, Cu<sub>2</sub>Se powdergrams are indicated in low-temperature orthorhombic structure with lattice parameters  $a=4.118 \text{ \AA}$ ,  $b=7.028 \text{ \AA}$ ,  $c=20.360 \text{ \AA}$ ,  $Z=12$ .

All registered 24 diffraction reflections from Cu<sub>1.80</sub>Zn<sub>0.20</sub>Se are explicitly indicated on the base of orthorhombic structure as Cu<sub>2</sub>Se, but in this case the reflections from high-temperature FCC modification with (111), (220), (311) и (222) indexes collide on the reflections from planes (002), (00 10), (042) and (044) correspondingly (table 3).

As it is seen from the table 4 the powdergram of Cu<sub>1.75</sub>Zn<sub>0.05</sub>Se composition is explicitly indicated on the basis of FCC lattice with parameter  $a=5.7412 \text{ \AA}$  which corresponds to lattice parameter Cu<sub>2-x</sub>Se ( $x=0.20$ ).

The synthesized samples of Cu<sub>2</sub>Se, Cu<sub>1.80</sub>Zn<sub>0.20</sub>Se and Cu<sub>1.75</sub>Zn<sub>0.05</sub>Se are put in ampoules from high-quality quartz tubes of length 10 cm and internal diameter 1 cm after roentgen-phase analysis carrying out. The ampoules evacuated up to pressure 1.3 MPa with corresponding compositions are moved inside furnace having three temperature zones with the help of special mechanism. The temperature on 50K higher than the compound melting point

is kept in upper furnace zone, the temperature on 50K below is kept in the second zone. The crystal germ creates from the side of least temperature when the temperature of ampoule

sharp end exceeds the compound melting point. The ampoule moves with rate 0,2 cm/h is suitable for growth of created germ.

Table 2

The calculation of Cu<sub>2</sub>Se powdergram.  
CuK<sub>α</sub> is radiation ( $\lambda_{\alpha}=1.5418 \text{ \AA}$ ), Ni is filter, regime: 35 kV, 8 mA, experiment continues 12 hours.

$\theta$	$I/I_0$	$d_{exp}, \text{\AA}$	$d_{calc}, \text{\AA}$	$hkl$	Lattice parameters
			Orthorhombic		
6°42'	30	6.614	6.6475	011	$a=4.119 \text{ \AA}$
12°32'	20	3.553	3.3535	110	$b=7.028 \text{ \AA}$
12°51'	10	3.466	3.4648	021	$c=20.390 \text{ \AA}$
13°27'	70	3.316	3.3237	022	$Z=12$
18°18'	10	2.455	2.4551	116	$V=590.2565 \text{ \AA}^3$
19°43'	20	2.285	2.2843	032	$\rho=6.749 \text{ g/cm}^3$
20°06'	90	2.241	2.2358	125	
20°57'	10	2.156	2.1557	019	
21°59'	10	2.060	2.0590	200	
22°14'	100	2.038	2.0381	0 0 10	
23°49'	10	1.909	1.9090	204	
26°06'	60	1.753	1.7580	040	
30°45'	10	1.507	1.5083	233	
35°27'	20	1.330	1.3295	055	
40°33'	50	1.185	1.1845	330	
43°00'	10	1.131	1.1323	0 0 18	
45°24'	10	1.083	1.0819	340	
48°30'	10	1.030	1.0295	400	
51°33'	10	0.984	0.9834	422	

Table 3

The results of X-ray investigation of Cu<sub>1.80</sub>Zn<sub>0.20</sub>Se.  
CuK<sub>α</sub> is radiation ( $\lambda_{\alpha}=1.5418 \text{ \AA}$ ), Ni is filter, regime: 35 kV, 8 mA, experiment continues 12 hours.

$\theta$	$I/I_0$	$d_{exp}, \text{\AA}$	$d_{calc}, \text{\AA}$	$hkl$	$d_{calc}, \text{\AA}$	$hkl$	Lattice parameters
			Orthorhombic		FCC		
6°39'	30	6.6571	6.6522	001			
11°39'	70	3.8182	3.8175	102			
12°32'	20	3.5525	3.5536	110			Orthorhombic
13°06'	10	3.4005	3.3990	006			$a=4.1169 \text{ \AA}$
13°24'	70	3.3271	3.3261	022	3.3255	111	$b=7.0288 \text{ \AA}$
18°18'	10	2.4551	2.4563	116			$c=20.3932 \text{ \AA}$
19°54'	20	2.2647	2.2660	009			$Z=12$
20°10'	90	2.2358	2.2367	125			$\rho=6.9675 \text{ g/sm}^3$
21°00'	10	2.1509	2.1569	019			
21°51'	60	2.0712	2.0714	118			FCC
22°14'	100	2.0378	2.0381	0.0.10	2.0365	220	$a=5.7599 \text{ \AA}$
23°49'	10	1.9091	1.9051	029			$Z=4$
24°58'	10	1.8263	1.8275	1.0.10			$V=191.0930 \text{ \AA}^3$
26°01'	60	1.7572	1.7592	040			$\rho=7.1722 \text{ g/cm}^3$
26°24'	36	1.7327	1.7336	042	1.7367	311	
26°56'	8	1.7019	1.7031	043			
27°37'	5	1.6629	1.6630	044	1.6627	222	
30°48'	10	1.5057	1.5060	047			
31°55'	80	1.4584	1.4567	0.0.14			
35°26'	20	1.3296	1.3303	055			
40°36'	50	1.1845	1.1845	330			
42°54'	10	1.1325	1.1330	0.0.18			
45°24'	10	1.0827	1.0821	340			
48°35'	10	1.0279	1.0279	401			
51°24'	10	0.9867	0.9867	421			

Table 4

The results of X-ray investigation of Cu<sub>1.75</sub>Zn<sub>0.05</sub>Se. CuK<sub>α</sub> is radiation ( $\lambda_{\alpha}=1.5418 \text{ \AA}$ ), Ni is filter, regime: 35 kV, 8 mA, experiment continues 12 hours.

$\theta$	$I/I_0$	$d_{exp}, \text{\AA}$	$d_{calc}, \text{\AA}$	$hkl$	Lattice parameters
			FCC		
13°27'	100	3.3147	3.3147	111	
15°35'	10	2.8706	2.8706	200	
22°19'	95	2.0298	2.0298	220	
26°27'	25	1.7310	1.7310	311	$a=5.7412 \text{ \AA}$
27°43'	20	1.6573	1.6573	222	$Z=4$
32°29'	35	1.4353	1.4353	400	$V=189.2379 \text{ \AA}^3$
35°49'	20	1.3171	1.3171	331	$\rho=6.7869 \text{ g/cm}^3$
41°08'	50	1.1719	1.1719	422	
44°14'	15	1.1049	1.1049	511, 333	
49°26'	10	1.0149	1.0149	440	
52°36'	30	0.9704	0.9704	531	
58°07'	25	0.9078	0.9078	620	
61°42'	15	0.8755	0.8755	533	
68°29'	10	0.8287	0.8287	444	

The ampoule, containing the crystals of high-temperature FCC modification at further shift achieves the third furnace zone where transformation of FCC modification into low-temperature orthorhombic modification takes place. In this furnace zone the ampoule with crystals is annealed during 50 hours. The single crystals obtained by such way are the objects of high-temperature-roentgen-diffractometer investigations. The experiments are carried out on diffractometer DRON-3M (CuK<sub>α</sub> is radiation,  $\lambda_{\alpha}=1.5418 \text{ \AA}$ , Ni is filter) with high-temperature attachment URVT-2000 providing the vacuum  $10^{-2} \text{ Pa}$ , the record angular resolution is  $\approx 0.1^\circ$ , error of angle of reflection definition doesn't exceed  $\Delta\theta=\pm 0.02^\circ$ .

**1. Cu<sub>2</sub>Se.** The obtained single crystals Cu<sub>2</sub>Se easily shear in [011] direction. The six clear diffraction peaks with (011), (022), (027), (040), (055) and (0.0.18) indexes are fixed from such crystals at room temperature in angle interval  $10^\circ \leq 2\theta \leq 90^\circ$ . Not changing this crystal orientation, the furnace is switched on and records are taken at 323, 373, 405 and 413K temperatures. The temperature before each record is supported constant during 30 minutes.

The record taken at 423K is related to high-temperature FCC modification. Moreover all diffraction reflections belonging to low-temperature orthorhombic modification disappear and diffraction reflections with (111), (222) and (333) indexes belonging to high-temperature FCC modification with lattice parameter  $a=5.8356 \text{ \AA}$  are fixed in previous angle interval.

The counter is fixed on maximum of one from diffraction reflections of low-temperature modifications  $2\theta=40^\circ 12'$  (027) which disappears after transformation and appears at inverse transformation for detail definition of equilibrium temperature between modifications. Heating the low-temperature modification from 393K with rate 2 K/h it is defined that equilibrium temperature between modifications  $T_0=407\pm 1 \text{ K}$ .

The parameters of elementary orthorhombic cell are calculated at temperatures 298, 323, 373, 405K and parameters of FCC modification are calculated at temperatures 423, 473, 523, 573K. The results are given in tables 5,6 and graphically on the fig.1.

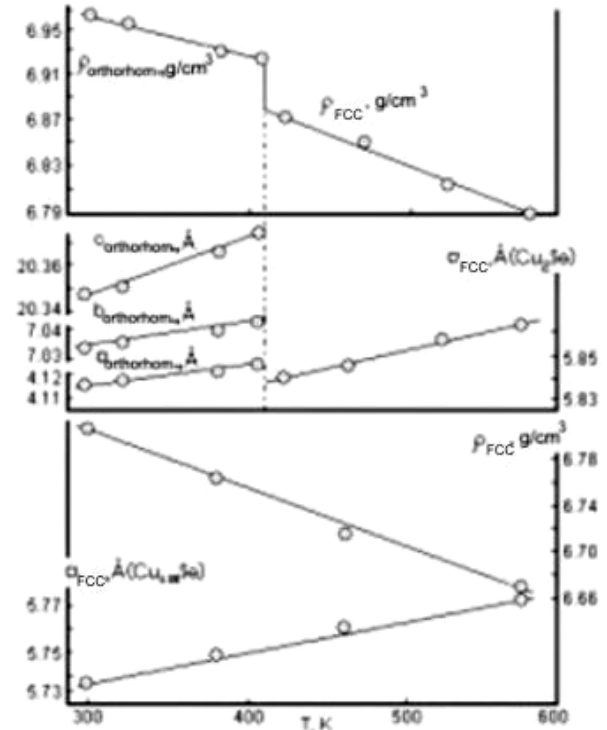


Fig.1. The temperature dependences of lattice parameters and densities of low-temperature orthorhombic and high-temperature FCC modifications Cu<sub>2</sub>Se and lattice parameter and Cu<sub>1.80</sub>Se crystal density.

The density dependence of orthorhombic and FCC modifications on temperature shows that density at equilibrium temperature of modifications  $T_0=407 \text{ K}$  is changed by jump on  $0.062 \text{ g/cm}^3$ . It is necessary to note that concentration change takes place in the dependence on transformation order, i.e. the transition Cu<sub>2</sub>Se into Cu<sub>2-x</sub>Se ( $x=0.20$ ) with cuprum extraction on Cu<sub>2-x</sub>Se block boundaries. This non-stoichiometric composition also has FCC lattice with parameter  $a=5.740 \text{ \AA}$ . This compound is stable in temperature interval from room one up to melting point.

Table 5

The temperature dependence of crystal lattice periods of orthorhombic phase Cu<sub>2</sub>Se.

$T_{exp}$ , K	Orthorhombic				$V$ , Å <sup>3</sup>	$\rho$ , g/cm <sup>3</sup>
	$a$ , Å	$b$ , Å	$c$ , Å	$Z$		
298	4.1168	7.0320	20.3472	12	589.038	6.968
323	4.1180	7.0336	20.3508	12	589.4480	6.963
373	4.1212	7.0384	20.3670	12	590.7785	6.947
405	4.1248	7.0416	20.3796	12	591.9293	6.934

Table 6

The temperature dependence of crystal lattice periods and thermal expansion of FCC phase Cu<sub>2</sub>Se.

$T_{exp}$ , K	$a$ , Å	$Z$	$V$ , Å <sup>3</sup>	$\rho$ , g/cm <sup>3</sup>	$T_{exo}$ , K	$\alpha_{[100]} \times 10^{-6} \text{K}^{-1}$
423	5.8391	4	199.0846	6.872	423-473	17.47
473	5.8442	4	199.6067	6.854	423-523	27.74
523	5.8553	4	200.7463	6.815	423-573	26.37
573	5.8622	4	201.4568	6.791		

The thermal expansion on main crystallographic directions of orthorhombic and FCC modifications Cu<sub>2</sub>Se is given in tables 6 and 7, and FCC modifications Cu<sub>2-x</sub>Se is given in table 8.

Table 7

Thermal expansion of orthorhombic phase Cu<sub>2</sub>Se.

$T_{exp}$ , K	Thermal expansion coefficients $\times 10^{-6} \text{K}^{-1}$			
	$\alpha_{[100]}$	$\alpha_{[010]}$	$\alpha_{[001]}$	$\bar{\alpha} = \frac{\alpha_{[100]} + \alpha_{[010]} + \alpha_{[001]}}{3}$
298-323	11.66	9.10	7.08	9.28
298-373	14.25	12.14	12.97	13.12
298-405	18.16	12.76	14.88	15.27

Table 8

Temperature dependence of crystal lattice periods and thermal expansion of FCC phases Cu<sub>1.80</sub>Se.

$T_{exp}$ , K	$a$ , Å	$Z$	$V$ , Å <sup>3</sup>	$\rho$ , g/cm <sup>3</sup>	$T_{exp}$ , K	$\alpha_{[100]} \times 10^{-6} \text{K}^{-1}$
298	5.7356	4	188.625	6.804	298	-
383	5.7480	4	189.911	6.760	298-383	25.74
473	5.7610	4	191.910	6.714	298-473	32.57
573	5.7746	4	192.559	6.667	298-573	24.82

**2. Cu<sub>1.80</sub>Zn<sub>0.20</sub>Se.** Cu<sub>1.80</sub>Zn<sub>0.20</sub>Se single crystals also easily shear on plane (011). The plate samples with sizes 4×4×1 mm which are suitable for diffractometer investigation are separated from crystalline ingot for temperature investigation. The six diffraction reflections fixed from such

samples at room temperatures in angle intervals  $30^\circ \leq 2\theta \leq 70^\circ$  are indicated in the same way as powder diffractogram Cu<sub>1.80</sub>Zn<sub>0.20</sub>Se on the basis of parameters of orthorhombic and FCC modifications which stabilize at room temperature (table 9).

Table 9

The crystal lattice periods of existing phases Cu<sub>1.80</sub>Zn<sub>0.20</sub>Se at 290-870K.

$T_{exp}$ , K	Syngony	$a$ , Å	$b$ , Å	$c$ , Å	$Z$	Sp.gr.	$V$ , Å <sup>3</sup>	$\rho$ , g/cm <sup>3</sup>
290	Orthorhombic	4.1274	7.0327	20.3618	14	-	591.0372	6.957
	FCC	5.7560	-	-		Fm3m	190.7051	7.187
370	Orthorhombic	4.1310	7.0491	20.4085	12	-	591.2921	6.919
	FCC	5.7651	-	-	4	Fm3m	191.6110	7.153
470	Orthorhombic	4.1486	7.0535	20.4390	12	-	598.0831	6.875
	FCC	5.7724	-	-	4	Fm3m	192.3398	7.126
570	Orthorhombic	4.1559	7.0700	20.4705	12	-	601.4686	6.836
	FCC	5.7818	-	-	4	Fm3m	193.2810	7.091
670	Orthorhombic	4.1667	7.0877	20.5055	12	-	605.5750	6.790
	FCC	5.7931	-	-	4	Fm3m	194.4165	7.050
770	Orthorhombic	4.1885	7.0892	20.5168	12	-	609.277	6.749
	FCC	5.8019	-	-	4	Fm3m	195.3038	7.018
870	Orthorhombic	4.1959	7.1015	20.5352	12	-	611.8911	6.720
	FCC	5.8110	-	-	4	Fm3m	196.2242	6.985

## THE ROLE OF ZINC ATOMS IN MODIFICATION STABILIZATION IN Cu<sub>2</sub>Se

The control diffraction recordings are carried out saving crystal orientation in temperature interval 290-900K in each 100K. The temperature before each record is kept constant during 30 minutes. It is necessary to note that the essential changes of intensity values aren't observed in the given temperature intervals.

The parameters of elementary cell of orthorhombic modifications are calculated from reflections with (009), (0010), (1.0.10), (042), (043), (044) indexes which are given in table 10, and FCC parameter of modification is calculated from reflections with (220), (311) and (222) indexes, its results are also given in table 10.

Table 10

Thermal expansion of elementary cell parameters of orthorhombic phase Cu<sub>1.80</sub>Zn<sub>0.20</sub>Se in temperature interval 290-870K.

$T_{exp}$ , K	Thermal expansion coefficients $\times 10^{-6} \text{ K}^{-1}$			
	$\alpha_{[100]}$	$\alpha_{[010]}$	$\alpha_{[001]}$	$\bar{\alpha} = \frac{\alpha_{[100]} + \alpha_{[010]} + \alpha_{[001]}}{3}$
290-370	10.90	29.15	28.67	22.91
290-470	28.54	16.56	21.12	22.07
290-570	24.66	18.94	19.07	20.89
290-670	25.22	20.58	18.57	21.46
290-770	31.64	16.14	15.86	21.21
290-870	29.35	16.87	14.68	20.30
290-370	20.63			
290-470	11.00			
290-570	17.25			
290-670	18.10			
290-770	17.55			
290-870	16.44			

The temperature dependences of elementary cell parameters of orthorhombic and FCC modifications are graphically given on the fig.2.

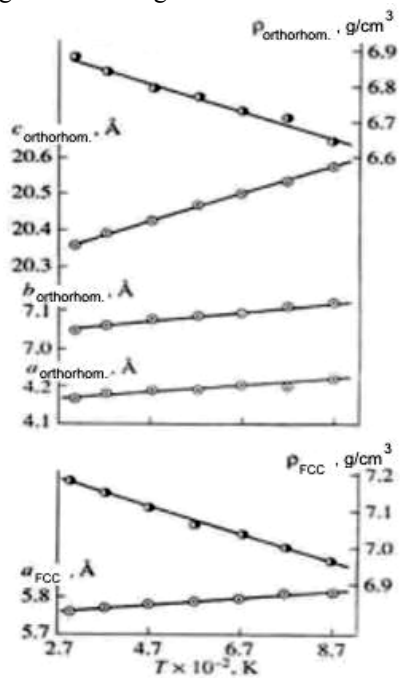


Fig.2. The temperature dependences of elementary cell parameters of orthorhombic and FCC phase Cu<sub>1.80</sub>Zn<sub>0.20</sub>Se.

As it is seen from fig.2 the values of elementary cell parameters of orthorhombic and FCC modifications in temperature function increase linearly. The linear increase of lattice parameters of both modifications shows that both modifications stably exist in considered temperature interval, i.e. low-temperature orthorhombic modification metastably exists at high temperatures, and high-temperature FCC modification exist at room temperature.

The calculated values of  $\rho$  (g/cm<sup>3</sup>) orthorhombic and FCC modifications given in table 9 are also graphically shown on the fig.2. As it is seen from the figure the density of both modifications is linearly decreases and FCC modification density is bigger than density of orthorhombic one, i.e.  $\Delta\rho = \rho_{\text{FCC}} - \rho_{\text{orthorhom.}} = 0.25 \text{ g/cm}^3$ .

The crystal thermal expansion of orthorhombic and FCC modifications are given in table 10.

**3. Cu<sub>1.75</sub>Zn<sub>0.05</sub>Se.** The plane samples with sizes 5×4×2 mm (of undefined crystallographic orientation) are taken for temperature-diffractometer investigations. The reflections from (111), (200), (220), (311) and (400) planes which are enough for calculation of elementary cell parameter are fixed at room temperature in angle interval  $20^\circ \leq 2\theta \leq 70^\circ$ . The investigation is carried out in temperature interval 290-670K.

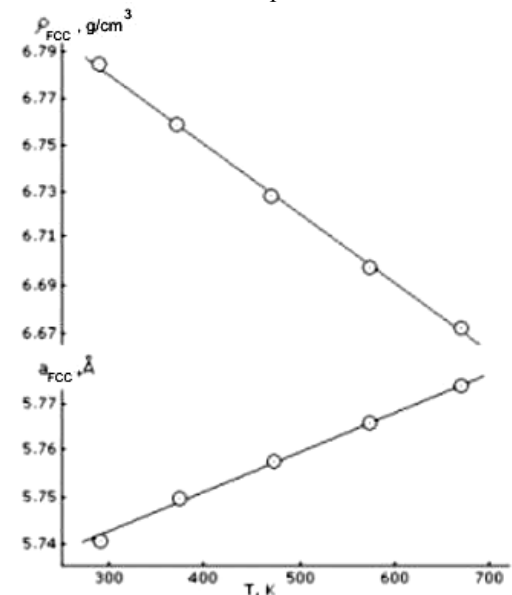


Fig.3. The temperature dependence of elementary cell parameters of FCC phase Cu<sub>1.75</sub>Zn<sub>0.05</sub>Se.

The results of these investigations and also thermal expansion are given in the table 11. As it is seen on the

fig.3a elementary cell parameter in temperature function linearly increases, and density linearly decreases.

Table 11

The temperature dependence of crystal lattice periods and thermal expansion of FCC phase  $\text{Cu}_{1.75}\text{Zn}_{0.05}\text{Se}$ .

$T_{exp}$ , K	FCC		Sp. gr.	$V, \text{\AA}^3$	$\rho, \text{g/cm}^3$	$T_{exp}$ , K	$\alpha_{[100]} \times 10^{-6} \text{K}^{-1}$
	$a, \text{\AA}$	Z					
290	5.7412	4	Fm3m	189.2379	6.787	290-370	17.42
370	5.7492	4	Fm3m	190.0300	6.759	290-470	16.06
470	5.7578	4	Fm3m	190.8841	6.728	290-570	15.68
570	5.7664	4	Fm3m	191.7407	6.698	290-670	14.90
670	5.7737	4	Fm3m	192.4698	6.673		

Finally note that  $\text{Cu}_2\text{Se}$  lattice carcass belongs to  $\text{Se}^{2-}$  atoms (ion radius is 1.93 Å), Cu atoms are statistically situated between them. There are defects with empty cuprum knots in crystal lattice. The cuprum atoms can easily move from one crystal region to another one. The atom oscillation in lattice increases with temperature increase and lattice becomes unstable one at given temperature. As a result the structural transformations take place.

Usually cuprum atoms in cuprum chalcogenides in lattices of stoichiometric compounds participate in two different valent states, i.e.  $\text{Cu}^+(0.98)$  and  $\text{Cu}^{++}(0.80)$ . This is the main existence reason of non-stoichiometric compounds  $\text{Cu}_{2-x}\text{Se}$ ,  $\text{Cu}_{2-x}\text{Te}$  и  $\text{Cu}_{2-x}\text{S}$  where  $0 \leq x \leq 25$  and excess of structural transformations. The obtained crystals

$\text{Cu}_{1.80}\text{Zn}_{0.20}\text{Se}$  at room temperature in  $\text{Cu}_{2-x}\text{Se}$  at isomorphous exchange of definite cuprum atom quantity by  $\text{Zn}^+(0.83)$  atoms become two-phase ones, i.e. high-temperature FCC modification stabilizes at room temperature and low-temperature orthorhombic modification stabilizes at high temperature.  $\text{Cu}_{1.75}\text{Zn}_{0.05}\text{Se}$  crystals at all considered temperatures are one-phase and have FCC structure.  $\text{Zn}^{++}$  atoms in  $\text{Cu}_{1.80}\text{Zn}_{0.20}\text{Se}$  and  $\text{Cu}_{1.75}\text{Zn}_{0.05}\text{Se}$  crystal structures take  $\text{Cu}^{++}$  places in tetrahedral empty spaces. The mobility of  $\text{Zn}^{++}$  atoms in  $\text{Cu}_{1.80}\text{Zn}_{0.20}\text{Se}$  and  $\text{Cu}_{1.75}\text{Zn}_{0.05}\text{Se}$  lattices and Zn-Se and Zn-Cu bonds differ from mobility of Cu atoms in  $\text{Cu}_{2-x}\text{Se}$ , and also from Cu-Se and Cu-Cu bonds which are the reason of modification stabilization in  $\text{Cu}_{1.80}\text{Zn}_{0.20}\text{Se}$  and  $\text{Cu}_{1.75}\text{Zn}_{0.05}\text{Se}$ .

- 
- [1] M. Khansen, K. Anderko. Struktura dvoynikh splavov. 1962, tom 1. (in Russian)  
 [2] Yu G. Asadov, G.A. Jabrailova, V.I. Nasirov. Izv. AN SSSR, Neorganicheskie materiali. 1972, t.8, №6, s.1144. (in Russian)  
 [3] Yu G. Asadov, G.B. Gasimov, G.A. Jabrailova. Izv. AN SSSR, Neorganicheskie materiali. 1972, №12, s.2208.

**Y.Q. Әсәдов, Ү.И. Алиев, Ф.Q. Мәхәррәмова, Ә.Q. Бабаев**

## Cu<sub>2</sub>Se BİRLƏŞMƏLƏRİNDEKİ MODİFİKASIYALARIN STABİLLƏŞMƏSİNDE Zn ATOMLARININ ROLU

$\text{Cu}_2\text{Se}$ ,  $\text{Cu}_{1.80}\text{Zn}_{0.20}\text{Se}$  və  $\text{Cu}_{1.75}\text{Zn}_{0.05}\text{Se}$  birləşmələri sintez edilmiş və monokristalları göyərdilmişdir. Yüksəktemperatur rentgenendifraktoimetrik metodla qeyd olunan monokristallarda struktur faza keçidləri tədqiq edilmiş və göstərilmişdir ki,  $\text{Cu}_2\text{Se}$ -də ortorombik modifikasiya 407K temperaturda ÜMK modifikasiyaya keçir, Cu atomlarının müəyyən hissəsi Zn atomları ilə əvəz olunmuş  $\text{Cu}_{1.80}\text{Zn}_{0.20}\text{Se}$  birləşməsində isə yüksəktemperatur ÜMK modifikasiyasi otaq temperaturunda ortorombik modifikasiya ilə stabillaşır. İkifazalı  $\text{Cu}_{1.80}\text{Zn}_{0.20}\text{Se}$  kristalında otaq temperaturundan ərimə temperaturuna qədər intervalda polimorf çevrilmə baş verir.

**Ю.Г. Асадов, Ю.И. Алиев, Ф.Г. Магеррамова, А.Г. Бабаев**

## РОЛЬ АТОМОВ ЦИНКА В СТАБИЛИЗАЦИИ МОДИФИКАЦИЙ В Cu<sub>2</sub>Se

Синтезированы и выращены монокристаллы состава  $\text{Cu}_2\text{Se}$ ,  $\text{Cu}_{1.80}\text{Zn}_{0.20}\text{Se}$  и  $\text{Cu}_{1.75}\text{Zn}_{0.05}\text{Se}$ . Высокотемпературным рентгенодифрактометрическим методом исследовались структурные фазовые превращения в монокристаллах указанных составов и показано, что в  $\text{Cu}_2\text{Se}$  орторомбическая модификация при 407К превращается в ГЦК модификацию. В кристалле  $\text{Cu}_{1.80}\text{Zn}_{0.20}\text{Se}$ , где определенная часть атомов Cu заменена атомами Zn, высокотемпературная ГЦК модификация стабилизируется при комнатной температуре, а низкотемпературная орторомбическая модификация стабилизируется при высокой температуре. В двухфазных кристаллах  $\text{Cu}_{1.80}\text{Zn}_{0.20}\text{Se}$  в интервале от комнатной температуры до температуры плавления полиморфные превращения отсутствуют.

Received: 17.03.08

## WAVE DIFFRACTION ON PLANE BELT WITH RESISTIVE BOUNDARY CONDITIONS

**T.M. AHMEDOV**

*Institute of Mathematics and Mechanics of Azerbaijan NAS  
AZ-1141, Baku, Azerbaijan, F.Agayev str., 9*

The multiple articles [1-3] are dedicated to task solution of wave diffraction on plane belt with ideal boundary conditions (BC). BC of Dirihle and Neyman types correspond to ideal BC. Such BC appear when it is supposed that belt has ideal electric or magnetic conductivity [1,4]. However, in practice the plane metallic belt has the finite conductivity. In this case the boundary is described by BC of impedance type [4]. From mathematics point of view, BC of third kind corresponds to this boundary [5]. In the given paper we'll solve the task of E-polarized wave diffraction on the belt with resistive BC which is the special case of impedance BC. The more general approach which as special case will include the task solution with ideal BC will be suggested for solution of this task.

### 1. Problem definition.

Let's the plane wave falls on plane belt of  $2a$  dimension situated in XOZ plane in the center of coordinate system XYO from  $y>0$  side.

$$V^i(x, y) = e^{-ik(x\cos\theta + y\sin\theta)} = e^{-ik(x\alpha_0 + y\sqrt{1-\alpha_0^2})} \quad (1)$$

Here  $\alpha_0 = \cos\theta$ ,  $\theta$  is wave incidence angle,  $k = \frac{2\pi}{\lambda}$  is wave number.

The complete field is presented in the form of sum of incident and scattered fields, i.e.

$$e_z(x, y) = V^i(x, y) + e_z^s(x, y) \quad (2)$$

The complete field should correspond to following conditions:

- everywhere out of belt surface to Helmholtz equation

$$\left( \frac{\partial^2}{\partial x^2} + \frac{\partial^2}{\partial y^2} + k^2 \right) e_z(x, y) = 0 \quad (3)$$

- on belt surface to resistive BC of [4] type

$$\frac{\partial e_z(x, \pm 0)}{\partial y} \pm \frac{ik}{\eta} e_z(x, \pm 0) = 0 \quad (4)$$

where  $\eta$  parameter characterizes the belt resistivity.

-to Meyksner condition on edges [1,6]

-Scattered field  $e_z^s(x, y)$  should correspond to condition of Zommerfeld radiation on infinity which has the form [1]

$$\lim_{r \rightarrow \infty} \sqrt{r} \left( \frac{\partial}{\partial r} + ik \right) e_z^s(x, y) = 0, \quad (5)$$

### 2. Task solution.

Let's write the conception of following type [1,5] for scattered field  $e_z^s(x, y)$  on the base of potential theory

$$e_z^s(x, y) = \int_{-a}^a f_1(x') G(x - x', y) dx' = -\frac{i}{4} \int_{-a}^a f_1(x') H_0^{(1)}(k \sqrt{(x - x')^2 + y^2}) dx', \quad (6)$$

here  $G(x - x', y)$  is Grin's bivariate function of free product; a  $H_0^{(1)}(x)$  is Hunkel function of zeroth order. The unknown function  $f_1(x')$  is potential density of simple layer corresponds to density function of surface current and is defined as component jump of complete field on belt surface ( $y=\pm 0$ ), i.e.

$$f_1(x) = \frac{\partial e_z(x, +0)}{\partial y} - \frac{\partial e_z(x, -0)}{\partial y}, \quad |x| < a \quad (7)$$

It is seen that perception for scattered field (6)

corresponds to Helmholtz equation and condition of radiation on infinity (5).

Let's obey the complete field  $e_z(x, y)$  to boundary condition (4) at  $y=\pm 0$  for definition of unknown current density. Taking into consideration (7), we obtain:

$$f_1(x) + \frac{ik}{\eta} \{e_z(x, +0) + e_z(x, -0)\} = 0, \quad |x| < a \quad (8)$$

Further we obtain the integral equation (IE) of following type with taking into consideration of (2) and (6) perceptions for definition of  $f_1(x)$  function:

$$-\frac{\eta}{k} f_1(x) = 2iV^i(x, 0) + \frac{1}{2} \int_{-a}^a f_1(x') H_0^{(1)}(k|x - x'|) dx', \quad |x| < a \quad (9)$$

The equation (9) is Fredholm's IE of second kind. Let's rewrite the given IE in images of Fourier function  $f_1(x)$ .

With this aim we continue this function by the zero out of  $|x| \geq a$ . Then we can write:

$$\begin{aligned} F_1(\alpha) &= \int_{-a}^a f_1(x') e^{-ik\alpha x'} dx', \\ f_1(x) &= \frac{k}{2\pi} \int_{-\infty}^{\infty} F_1(\alpha) e^{ik\alpha x} d\alpha \end{aligned} \quad (10)$$

where  $F_1(\alpha)$  function is image of Fourier function  $f_1(x)$ .

Then take into consideration that spectral perception [1,7] takes place for Hankel function  $H_0^{(1)}(x)$ .

$$H_0^{(1)}(k\sqrt{(x-x')^2 + y^2}) = \frac{1}{\pi} \int_{-\infty}^{\infty} e^{ik(\alpha(x-x')+|y|\sqrt{1-\alpha^2})} \frac{1}{\sqrt{1-\alpha^2}} d\alpha, \quad (11)$$

where that function branch  $\sqrt{1-\alpha^2}$  for which  $\operatorname{Im}\sqrt{1-\alpha^2} \geq 0$  at  $|\alpha| \rightarrow \infty$  along real line. This is followed from radiation condition (5).

Substituting (10) and (11) in IE (9) for Fourier image we obtain IE of following type:

$$-\frac{\eta}{\varepsilon} \tilde{f}_1(\xi) = 2iV^i(a\xi, 0) + \frac{1}{2\pi} \int_{-\infty}^{\infty} F_1(\alpha) e^{i\varepsilon\xi\alpha} \frac{1}{\sqrt{1-\alpha^2}} d\alpha, \quad |\xi| < 1 \quad (12)$$

Here the non-dimensional quantities are introduced.

$$x' = a\xi', \quad \varepsilon = ka, \quad x = a\xi, \quad \tilde{f}_1(\xi) = af_1(a\xi) \equiv af_1(x) \quad (13)$$

Further multiplying IE (12) both sides on  $e^{i\varepsilon\beta\xi}$  function and integrating on variable  $\xi$  in limits [-1,1], we obtain IE of following type:

$$-\eta F_1(\beta) = 4i \frac{\sin \varepsilon(\beta + \alpha_0)}{\beta + \alpha_0} + \frac{1}{\pi} \int_{-\infty}^{\infty} \frac{\sin \varepsilon(\alpha - \beta)}{\alpha - \beta} \frac{F_1(\alpha)}{\sqrt{1-\alpha^2}} d\alpha \quad (14)$$

$$\int_{-\infty}^{\infty} \frac{1}{\beta} J_{n+1/2}(\varepsilon\beta) J_{m+1/2}(\varepsilon\beta) d\beta = \frac{2}{2m+1} \delta_{mn}, \quad (18)$$

$$\frac{1}{\pi} \int_{-\infty}^{\infty} \frac{J_{m+1/2}(\varepsilon\beta)}{\sqrt{\beta}} \frac{\sin \varepsilon(\alpha - \beta)}{\alpha - \beta} d\beta = \frac{J_{m+1/2}(\varepsilon\alpha)}{\sqrt{\alpha}}, \quad (19)$$

Then we obtain infinite system of linear algebraic equations (ISLAE) of second kind of following type for obtaining unknown  $f_n^1$ :

$$-\eta f_m^1 = \gamma_m^E + \sum_{n=0}^{\infty} \tilde{C}_{mn}^E f_n^1, \quad m = 0, 1, 2, \dots \quad (20)$$

Here the designations are introduced:

$$\gamma_m^E = -\sqrt{2\pi\varepsilon}(2m+1)(-i)^{m+1} \frac{J_{m+1/2}(\varepsilon\alpha_0)}{\sqrt{\alpha_0}}, \quad (21)$$

$$\tilde{C}_{mn}^E = \frac{2m+1}{2} (-i)^{n-m} C_{mn}^E,$$

$$C_{mn}^E = \{1 + (-1)^{n+m}\} \int_0^{\infty} \frac{J_{n+1/2}(\varepsilon\alpha) J_{m+1/2}(\varepsilon\alpha)}{\alpha \sqrt{1-\alpha^2}} d\alpha, \quad (22)$$

It is seen that estimations take place:

$$\sum_{m=-\infty}^{\infty} |\gamma_m^E|^2 \leq \infty, \quad \sum_{n=-\infty}^{\infty} \sum_{m=-\infty}^{\infty} |C_{mn}^E|^2 \leq \infty, \quad (23)$$

This means that ISLAE is Fredholm equation of second kind and its approximate solution with any given accuracy can be obtained on the base of reduction method.

### 3. Integral calculation in matrix elements.

The calculation of matrix elements  $\tilde{C}_{mn}^E$ , which are presented by integrals on compositions of Bessel functions, is

$$\tilde{f}(\xi) = (1 - \xi^2)^{\nu} \sum_{n=0}^{\infty} f_n^1 C_n^{\nu+1/2}(\xi), \quad (16)$$

where  $\tilde{f}_n^{\nu}$  are unknown coefficients, and  $C_n^{\nu+1/2}(\xi)$  are Gegenbauer polynomials.

We can obtain the following perception on the base of perception (16) for image of Fourier function  $\tilde{f}_1(\xi)$ :

$$F_1(\alpha) = \frac{2\pi}{\Gamma(\nu+1/2)} \sum_{n=0}^{\infty} (-i)^n f_n^1 \beta_n^{\nu} \frac{J_{n+\nu+1/2}(\varepsilon\alpha)}{(2\varepsilon\alpha)^{\nu+1/2}}, \quad (17)$$

$$\text{here } \beta_n^{\nu} = \frac{\Gamma(n+2\nu+1)}{\Gamma(n+1)} \sim n^{2\nu}.$$

Let's substitute the perception for Fourier image (17) in IE (14) and take into consideration that the following relations [1,7,9] take place for values of  $\nu=1/2$  parameter.

## WAVE DIFFRACTION ON PLANE BELT WITH RESISTIVE BOUNDARY CONDITIONS

the main moment at ISLAE solution (20). The subintegral function becomes quick oscillating one that makes calculation process difficult at increase of  $\varepsilon$  parameter values. The following algorithm is suggested for solution of this problem. Let's express the matrix elements in the form:

$$C_{mn}^E = \{1 + (-1)^{n+m}\} I_{mn}^E(1/2, 1/2), \quad (24)$$

$$I_{mn}^E(\lambda, \mu) = I_{mn}^{E,1}(\lambda, \mu) - i I_{mn}^{E,2}(\lambda, \mu) \quad (25)$$

$$I_{mn}^E(\lambda, \mu) = \int_0^\infty J_{m+\lambda}(\varepsilon\alpha) J_{n+\mu}(\varepsilon\alpha) \frac{d\alpha}{\alpha^{\lambda+\mu} \sqrt{1-\alpha^2}}, \quad (26)$$

$$I_{mn}^{E,1} = \int_0^1 J_{m+\lambda}(\varepsilon\alpha) J_{n+\mu}(\varepsilon\alpha) \frac{d\alpha}{\alpha^{\lambda+\mu} \sqrt{1-\alpha^2}},$$

$$I_{mn}^{E,2} = \int_1^\infty J_{m+\lambda}(\varepsilon\alpha) J_{n+\mu}(\varepsilon\alpha) \frac{d\alpha}{\alpha^{\lambda+\mu} \sqrt{1-\alpha^2}} \quad (27)$$

Here  $\lambda$  and  $\mu$  parameters which accept values from [0,1] interval, are introduced for community. Later let's use two following perceptions [7,9] for product of Bessel functions.

$$J_{m+\lambda}(\varepsilon\alpha) J_{n+\mu}(\varepsilon\alpha) = \frac{1}{\sqrt{\pi}} \sum_{k=0}^\infty d_{kmn}^{\lambda\mu} (\varepsilon\alpha)^{2k+m+n+\lambda+\mu}, \quad (28)$$

$$I_{mn}^{E,2}(\lambda, \mu) = \frac{1}{2\pi i} \int_{c-i\infty}^{c+i\infty} \frac{\pi \cot \pi(s+N)}{2 \sin \pi s} \frac{f(s)}{g(s)} ds, \quad N = \frac{m+n}{2} \quad (29)$$

Here the designations are introduced

$$d_{kmn}^{\lambda\mu} = \frac{(-1)^k}{\Gamma(k+1)} \frac{\Gamma(k + \frac{m+n+\lambda+\mu+1}{2}) \Gamma(k + \frac{m+n+\lambda+\mu+2}{2})}{\Gamma(k+m+n+\lambda+\mu+1) \Gamma(k+m+\lambda+1) \Gamma(k+n+\mu+1)}, \quad (30)$$

$$f(s) = \varepsilon^{2s+m+n+\lambda+\mu} \Gamma(s+N+\frac{1}{2}) \Gamma(s+N+\frac{\lambda+\mu}{2}+\frac{1}{2}) \Gamma(s+N+\frac{\lambda+\mu}{2}+1), \quad (31)$$

$$g(s) = \Gamma(s+1) \Gamma(s+N+1) \Gamma(s+m+\lambda+1) \Gamma(s+n+\mu+1) \Gamma(s+m+n+\lambda+\mu+1), \quad (32)$$

The  $c$  contour is parallel to imaginary axis of complex plane  $s$  and corresponds to relation:

$$-Re \frac{m+n+\lambda+\mu+1}{2} \leq c \leq 0 \quad (33)$$

Substituting (28) and (29) perceptions in (27) integrals and integrate on the base of theory of residues for desired

quantities, we obtain the new perceptions in the form of rapidly-convergent series. They have the form:

$$I_{mn}^{E,1}(\lambda, \mu) = \frac{\varepsilon^{m+n+\lambda+\mu}}{2} \sum_{k=0}^\infty d_{kmn}^{\lambda\mu} \varepsilon^{2k} \frac{\Gamma(\frac{m+n}{2} + k + \frac{1}{2})}{\Gamma(\frac{m+n}{2} + k + 1)}, \quad (34)$$

$$\begin{aligned} I_{mn}^{E,2}(\lambda, \mu) &= -\left[ -\sum_{k=0}^{N-1} \frac{1}{2\pi} \Gamma(-k+N) \Gamma(k+\frac{1}{2}) \Gamma(k+\frac{\lambda+\mu}{2}+\frac{1}{2}) \Gamma(k+\frac{\lambda+\mu}{2}+1) \varepsilon^{2k+\lambda+\mu} \right] / \\ &\quad / \{\Gamma(k+1) \Gamma(k-N+m+\lambda+1) \Gamma(k-N+n+\mu+1) \Gamma(k+N+\lambda+\mu+1)\} + \\ &\quad + \sum_{k=0}^\infty \frac{1}{2\pi} \frac{\Gamma(k+N+\frac{1}{2})}{\Gamma(k+N+1)} d_{kmn}^{\lambda\mu} \varepsilon^{2k+m+n+\lambda+\mu} \times \{2 \ln \varepsilon + \Psi(k+N+\frac{1}{2}) + \\ &\quad + \Psi(k+N+\frac{\lambda+\mu}{2}+\frac{1}{2}) + \Psi(k+N+\frac{\lambda+\mu}{2}+1) - \Psi(k+1) - \Psi(k+N+1) - \\ &\quad - \Psi(k+m+\lambda+1) - \Psi(k+n+\mu+1) - \Psi(k+m+n+\lambda+\mu+1)\}. \end{aligned} \quad (35)$$

The corresponding integrals have the following form for index values  $m=n=0$ :

$$\begin{aligned}
 I_{00}^{E,2}(\lambda, \mu) = & \sum_{k=0}^{\infty} \frac{1}{2\pi} \frac{\Gamma(k+\frac{1}{2})}{\Gamma(k+1)} d_{k00}^{\lambda\mu} \varepsilon^{2k+\lambda+\mu} \times \\
 & \times \{2 \ln \varepsilon + \Psi(k+\frac{1}{2}) + \Psi(k+\frac{\lambda+\mu}{2}+\frac{1}{2}) + \Psi(k+\frac{\lambda+\mu}{2}+1) - \\
 & - 2\Psi(k+1) - \Psi(k+\lambda+1) - \Psi(k+\mu+1) - \Psi(k+\lambda+\mu+1)\}.
 \end{aligned} \quad (36)$$

The suggested approach allows forming the high-performance computational algorithms on the base of which the calculations of scattering characteristics of plane belt are carried out.

#### 4. Physical characteristics.

The following parameters: directional diagram (DD), diameters of complete diffusion and backscattering [1,4] are considered in the capacity of physical values characterizing the belt scattering properties. Let's give the definition of these values.

DD characterizes the scattered field behavior in long-distance band which will be written in cylindrical coordinate system in the following form:

$$e_z^s(r, \varphi) \approx A(kr)\phi_E^1(\varphi), \quad kr = k\sqrt{(x^2+y^2)} \rightarrow \infty \quad (37)$$

$$A(kr) = \sqrt{\frac{2}{\pi kr}} e^{i(kr-\pi/4)},$$

$$\phi_E^1(\varphi) = \frac{\sqrt{2\pi}}{4} \sum_{n=0}^{\infty} (-i)^{n+1} f_n^1 \frac{J_{n+1/2}(\varepsilon \cos \varphi)}{\sqrt{\varepsilon \cos \varphi}} \quad (38)$$

The diameters of complete diffusion  $\sigma_s^E$  and backscattering  $\sigma^E$  are defined by the following [1,4]:

$$\frac{\sigma_s^E}{4a} = -\frac{1}{\varepsilon} \operatorname{Re} \phi_E^1(\theta), \quad \frac{\sigma^E}{\lambda} = \frac{2}{\pi} |\phi_E^1(\varphi)|^2 \quad (39)$$

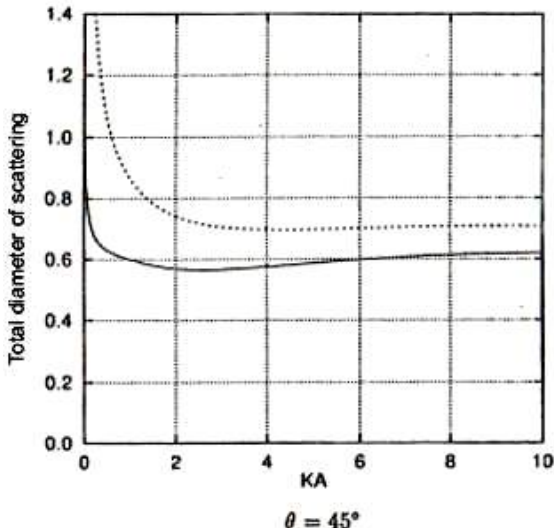


Fig. 1.

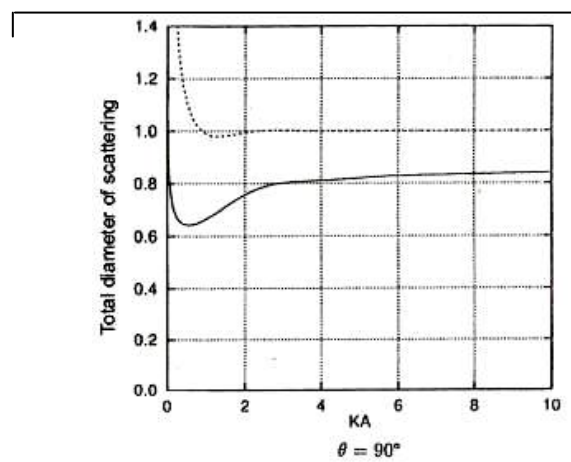


Fig. 2.

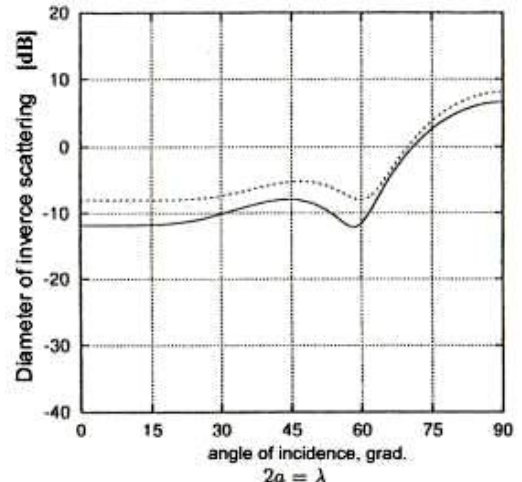


Fig. 3.

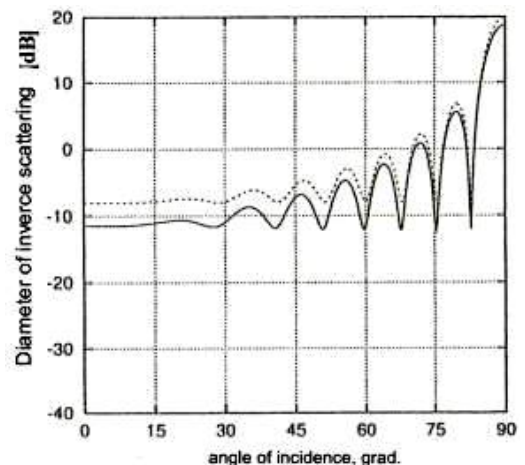


Fig. 4.

The calculation results of diameters of complete diffusion and backscattering on the base of developed efficient computational algorithms are presented on fig.1-6. The frequency dependences of complete diffusion diameter for cases of normal and off-normal incidences are shown on the fig.1,2. The dotted curves correspond to resistive belt, and total ones correspond to electrical ideally-conducting belt.

The dependences of scattering reverse diameter on incidence angle for different values of wave belt dimension are presented on fig. 3,4. As above mentioned, the dash curves correspond to resistive belt and total ones correspond to ideal-conducting belt.

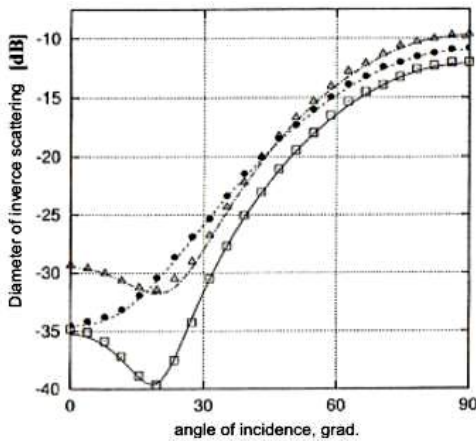


Fig. 5.

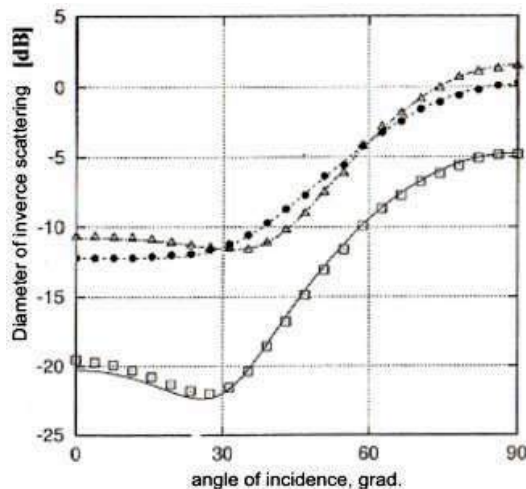


Fig. 6.

The calculation results of backscattering diameter for different resistivity values obtained on the base of our approach and work [4], are compared on the figures 5,6. The wave dimension is equal to  $2a=0.5\lambda$ . The resistivity value  $\eta = -i4$  correspond to dashed lines and  $\eta = 4$  value correspond to total ones. As it is seen from these figures, the coincidence of our results with results [4] (points, rectangles, squares) aren't in a doubt.

- 
- [1] Kh. Khenl, A. Maye, K. Vestpfal. Teoriya difraktsii. Moskva: Mir. 1964, -428s.
  - [2] E.I. Nefedov, A.T. Fialkovskiy. Asimptoticheskaya teoriya difraktsii elektromagnitnykh voln na konechnikh strukturakh. M.: Nauka. 1972, -247s.
  - [3] L.N. Litvinenko, S.L. Prosvirnin. Spektralnie operatori rasseyaniya v zadachakh difraktsii voln na ploskikh ekranakh. Kiev: Nauk. Dumka, 1984, -240s.
  - [4] T.V. Senior and J. Volakis. Approximate Boundary Conditions in Electromagnetics. The Institution of Electrical Engineers, London, United Kingdom, 1995.
  - [5] R.M. Mors, G. Feshbach. Metodi teoreticheskoy fiziki. T.1.M. – IL. 1958, -930s.
  - [6] R. Mittra, S. Li. Analiticheskie metodi teorii volnovodov. M.-Mir, 1974, -327s.
  - [7] A.P. Prudnikov, Yu.A. Brichkov, O.I. Marichev. Integrali i ryadi (spetsialnie funktsii). M.: Nauka, 1983, -752s.
  - [8] I.M. Braver, P.Sh. Fridberg and I.M.Yakovlev. The behavior of the electromagnetic field near the edge of a resistive half-plane. IEEE Trans. Antennas and Propagat., Vol.AP-36, pp.1760-1768. 1988
  - [9] D.N. Vatson. Teoriya Besselevikh funktsiy. T.1. M.: IL , 1949, -1000s.

### Т.М. Әхмәдов

### РЕЗИСТИВ СƏРХƏD ŞƏRTLƏRİ İLƏ MÜSTƏVİ LENT ÜZƏRİNDƏ DALĞALARIN DİFRAKSİYASI

Ideal sərhəd şərtləri ilə müstəvəi ləntdə dalğaların difraksiya məsələsinin həllinə çoxlu sayıda məqalələr [1-3] həsr olunmuşdur. Ideal SŞ-ə Dirixle və Neyman tipli SŞ uyğun gəlir. Belə SŞ-lər ideal elektrik və ya maqnit keçiriciliyinin olduğu güman edildiyi halda yaranır [1-4]. Ancaq praktiki olaraq müstəvəi metallik lənlər sonlu keçiriciliyə malikdir. Bu halda sərhədlər SŞ impedans tipinə uyğundur [4]. Riyazi nöqtəyi nəzərdən bu sərhədə qızılıncı tip SŞ uyğundur. Bu içdə biz difraksiya məsələsini müstəvəi E-polarizasiyalı dalğa üçün həll edəcəyik. Bu hal impedans SŞ-in xüsusi halıdır. Bu məsələnin həlli üçün daha ümumi yanaşma təklif olunur ki, bu da SŞ-in xüsusi halı olacaq.

### Т.М. Ахмедов

### ДИФРАКЦИЯ ВОЛН НА ПЛОСКОЙ ЛЕНТЕ С РЕЗИСТИВНЫМИ ГРАНИЧНЫМИ УСЛОВИЯМИ

Решению задач дифракции волн на плоской ленте с идеальными граничными условиями (ГУ) посвящены многочисленные статьи[1-3]. Идеальными ГУ соответствуют ГУ типа Дирихле или Неймана. Такие ГУ возникают, когда предполагается, что лента имеет идеально электрическую либо магнитную проводимость [1,4]. Однако на практике плоская металлическая лента имеет конечную проводимость. В этом случае граница описывается ГУ импедансного типа[4]. С математической точки зрения этой границе соответствует ГУ третьего рода [5]. В данной работе мы построим решение задачи дифракции плоской Е- поляризованной волны на ленте с резистивным ГУ, которая является частным случаем импедансных ГУ. Для решения этой задачи будет предложен более общий подход, который как частный случай будет содержать и решение задачи с идеальными ГУ.

Received: 04.03.08

## ELECTROMAGNETIC PROCESSES IN FREQUENCY-DEPENDENT RESISTOR SHEATH

**T.R. MEHDIYEV, N.R. BABAYEVA, A.M. GASHIMOV, A.A. HABIBZADE**

*G.M. Abdullayev Institute of Physics of National Academy of Sciences,  
AZ-1143, Baku, H. Javid, 33*

The electrical and magnetic properties of frequency-dependent resistor sheath consisting of the heterogeneous ferrite powder and polymer dielectric mixture are investigated. The charge carries transfer processes, concentration and temperature dependences of electroconductivity are researched. The character of current transport process through the heterogeneous mixture, two mechanisms of hopping and spin current presence are established. The influence of scin-effect on alternating current passing through the heterogeneous mixture is considered. The spectrums of absorption of frequency-dependent resistor sheath are investigated experimentally and theoretically.

### INTRODUCTION

The electromagnetic radiation absorption power of frequency-dependent resistor in the frequency interval from 50Hz up to 50MHz presents the big interest because the availability of these resistors in the devices and of high voltage network is essentially defined by electrophysical, heat and magnetic properties of their ferromagnetic sheathes in strong impulses or alternating (low-or high-frequency) fields. Nowadays the different constructions of ferromagnetic sheathes, in which the different mixtures containing the dielectric and ferromagnetic powders or metallic and ferromagnetic ones are used, have been developed and investigated [1-12]. In these works the ferromagnetic sheath is considered as (see [9-11]) percolation mixture and its electric and magnetic properties are studied. The theoretic works [13-14] in which two variants of dielectric constant determination for mixtures in approximation of particle sphericity in constant electric field when the mixture can be considered as homogeneous and isotropic medium with respect of average electric field are investigated, are well known. In first case, fine-dispersed mixtures in which all mixture particles are isotropic ones and difference between their dielectric constants is small one in the comparison with dielectric constant of. In the second case, the emulsions with arbitrary difference between medium dielectric constant and dispersed extrinsic phase of small concentration are considered.

The theory of absorption of electromagnetic radiation by strongly heterogeneous two-component systems is considered in work [15]. The composite presents itself the thin film of two-component mixture consisting of dielectric matrix and macroscopic magnetic particles. It is shown that the absorption of electromagnetic radiations can be changed

adding the magnetic, metallic and other foreign substances in main matrix. In the case of metallic inclusions, the absorption region shifts to the side of frequency increase that is connected with decrease of relaxation time of electronic subsystem.

Note that dipolar polarization not depending on frequency is observed in dipole dielectrics in radio-frequency region  $10^{13} - 10^{11}$  Hz. The relaxation losses are observed in the region of relaxation dispersion when dipoles haven't time in order to reorient in half-period of electric field variation. The structures and losses connected with them having maximum on the relaxation frequency of interlayer polarization at which the electric charges accumulate on the heterogeneity interfaces during long time, are observed on low frequencies in heterogeneous dielectrics in polarization spectrum.

The investigation results of electric and magnetic properties of frequency-dependent resistor ferromagnetic sheath by thickness from 2 up to 5 mm in alternating electric field carried out on the base of strongly heterogeneous mixture of dielectric (polyvinylchloride) and ferromagnetic (nickel-zinc) powders are presented in the given work.

### THE SAMPLE PREPARATION

The photos of microstructure of frequency-dependent resistor sheath obtained on electronic microscope in different increase regimes at 45% volume concentration of filler are given on fig.1.

The photos have been obtained for sheath section which is perpendicular to resistor "z" axis (see.fig.2). As analysis shows, the ferromagnetic powder component has the similar volume density upon the average along whole resistor sheath.

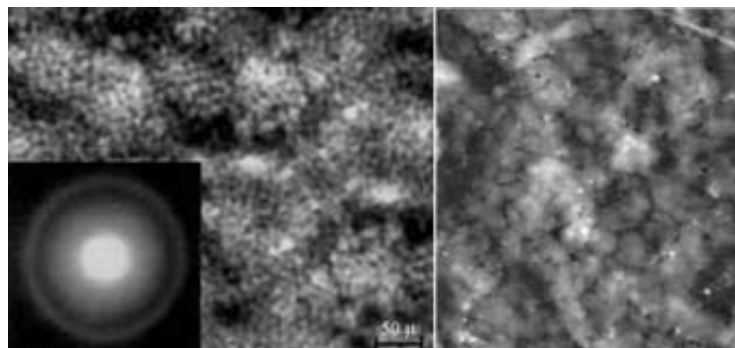


*Fig.1. The photos of sheath microstructure of frequency-dependent resistor obtained on electronic microscope in different increase regimes at 45% volume concentration of filler.*

The matrix produced on the base of polyvinylchloride, is filled by ferromagnetic powder preliminary treated for better adherence with matrix in solution of stearic acid and benzene. The solvent excess is eliminated by drying of ferromagnetic powder at temperature 23°C.

The matrix filling by filler is carried out gradually by the method of hot roll-forging up to achievement of necessary concentration. In the given experiments the concentration of ferromagnetic particles in the volume is achieved  $x=0.65$ . It is known [16], that limit concentrations of filler are defined by its properties and degree of interaction with polyvinylchloride. As it is shown in [16] the peculiarities of temperature dependences of mixture volume expansion at filler high concentrations can be explained by thermoelastic voltages appearing as a result of difference of coefficient of expansion of polymer and filler. Note that obtained filler concentrations up to temperature 100°C don't lead to the destruction of powder mixtures. Further, the created composition is reduced and pressed round current-carrying-rode of created frequency-dependent resistor in vacuum furnace under the pressure about 10<sup>-1</sup>Pa and temperature 160°C. The forms of ferromagnetic particles uniformly distributed enough on matrix volume are close to spherical ones and their dimensions don't exceed 50μ. Note [23] that the dimensional effects don't affect in samples by thickness up to 0,8 cm and at frequencies from 0,1-50MHz and

therefore the complex magnetic permeabilities of nickel-zinc ferrite filler can be defined by results of magnetic and electric measurements. By other hand, the ferromagnetic sheath of frequency-dependent resistor has the big dimensions and therefore the observation of volume resonance is quite possible.

### THE EXPERIMENT, FREQUENCY PROPERTIES OF SHEATH DIELECTRIC MATRIX OF FREQUENCY-DEPENDENT RESISTOR

The differential spectrums of frequency dependences of real and imaginary parts of dielectric constant and also dielectric loss tangent are investigated on automatic measuring device realizing the method of susceptance variation. The measurements are carried out in frequency interval from 1Hz up to 100MHz. The relative error of measurements is no more than 2%. The experiment control and experimental data processing are carried out by computer connected to measurement module. The differential spectrums are obtained by direct differentiation of experimental dependences.

The differential frequency spectrums of real and imaginary parts of dielectric constant and also dielectric loss tangent of dielectric matrix, which are given on the fig.2, have been obtained for calibration of experimental device.

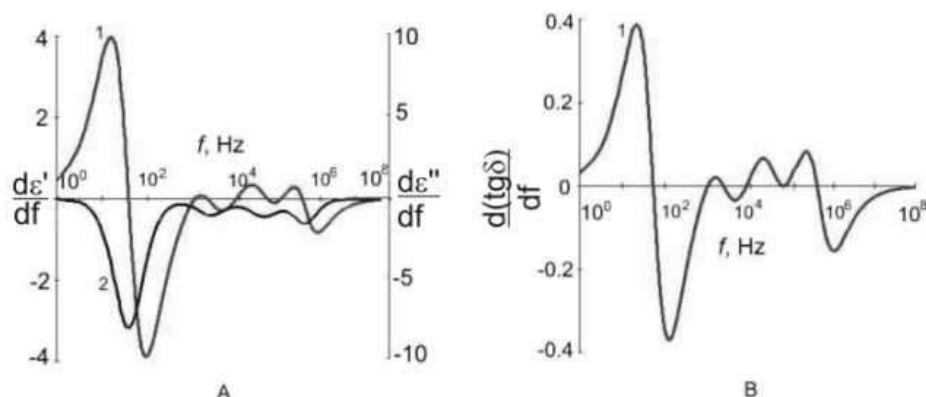


Fig. 2. Differential frequency spectrums a -  $\epsilon'$ ,  $\epsilon''$  and b -  $(tg \delta)'$  of dielectric constant of PVCh matrix. Here 1 is imaginary part of dielectric constant, 2 is real part of one.

The polyvinylchloride is related to linear polar polymer with big value of dielectric constant and dielectric loss tangent that is caused by construction asymmetry of macromolecule elementary units because of which the dipole-relaxation polarization appears. The polar groups in polyvinyl chloride are strongly connected with main chain. The connectedness of orientation movement of side polar group in respect of the main chain changes in the dependence on dipole position. It is obvious that dipole C-Cl in polyvinyl chloride, in the composition of which the carbon of main chain includes, can shift in glassy state only at presence of some part of main chain. Naturally, that this relaxation process has some features which are character ones to orders of dipole-elastic losses, but it can be observed at the temperature that is essentially lower than the glass-transition one. Thus, this process isn't connected with heat motion of chain segments.

As would be expected the real part of dielectric constant weakly depends on external alternating field frequency higher 700Hz and its fuzzy structure corresponds to contribution of

different polar groups and radicals in spectrum of dipole-orientation polarization.

The quantity of observable structures in the spectrum in real part of polyvinylchloride permeability at 23°C shows on the fact that spectrum can be interpreted by the set of four Debye's functions, i.e.:

$$\epsilon' = \epsilon_{\infty} + \Delta\epsilon \sum_{i=1}^4 \frac{g_i}{1 + (\omega\tau_i)^2};$$

$$\epsilon'' = \Delta\epsilon \sum_{i=1}^4 \frac{g_i(\omega\tau_i)}{1 + (\omega\tau_i)^2}; \quad tg \delta = \frac{\epsilon''}{\epsilon'},$$

where  $\epsilon_{\infty}$  is dielectric constant for frequency  $\omega >> \frac{1}{\tau_0}$ , equal to 4.289;  $\tau_0$  is relaxation time of  $i$ -th process;  $\Delta\epsilon = (\epsilon_c - \epsilon_{\infty}) = 10.0$  is total dispersion width of  $i$ -th set of

relaxation time;  $\varepsilon_c$  is dielectric constant for  $\omega \ll \frac{1}{\tau_0}$ , equal to 14.289;  $g_i$  is weighting coefficient for  $i$ -th relaxation oscillator. The obtained values of weighting coefficients and relaxation times coincide with data [17] in the investigated frequency region.

The analysis of obtained spectrums shows that dielectric constant dispersion peculiarities are defined dipole-group polarization of polyvinylchloride molecules. As it was shown in work [17] even insignificant content of polar plasticizers, for example lead zirconate titanate, differing on chemical composition in polymer volume should lead to the set of relaxation times of dipole-orientation polarization in wide frequency region of external electric field. The dispersions of spectrum structures of complex dielectric constant are caused by the content of investigated polymer of polar radicals C-Cl in main chain by one hand, by another one, they are caused by the content of molecule polar groups in plasticizers. Note that plasticizers decrease the polymer toughness because of decrease of intermolecular interaction energy and change the relaxation times of processes of dipole-orientation polarization of polar groups and radicals. The using of

powder of nickel zinc ferrite in the capacity of filler for polyvinylchloride is caused by the following reasons. Firstly, the nickel zing ferrites widely use in electronic devices for the frequency turning. That allows us to solve the problem of the construction of frequency-dependent ferromagnetic sheath with given magnetic properties. Secondly, as well known, zing compounds are stabilizers for polyvinylchloride and these mixtures widely use in window glass production. The relatively big dielectric constant, which depends on frequency and material content, is character for nickel zinc ferrites. The ferrite dielectric constant decreases with frequency increase. Thus, nickel zinc ferrites have  $\varepsilon = 400$  on frequency 1kHz, but  $\varepsilon = 15$  on frequency 10MHz. By other hand it is well known that alternating valence ions the concentration increase of which leads to increase of material dielectric constant, strongly influence on ferrite polarized properties. The differential spectrums of dielectric constant and functions of dielectric loss  $\text{tg}\delta$  in the dependence on frequency of alternating electric field and filler concentration are shown on fig.3. Here curve 1 corresponds to filler volume concentration (on 1 cm<sup>3</sup>) equal to 0.25, curve 2 corresponds to one equal to 0.45, and 3 corresponds to one equal to 0.65.

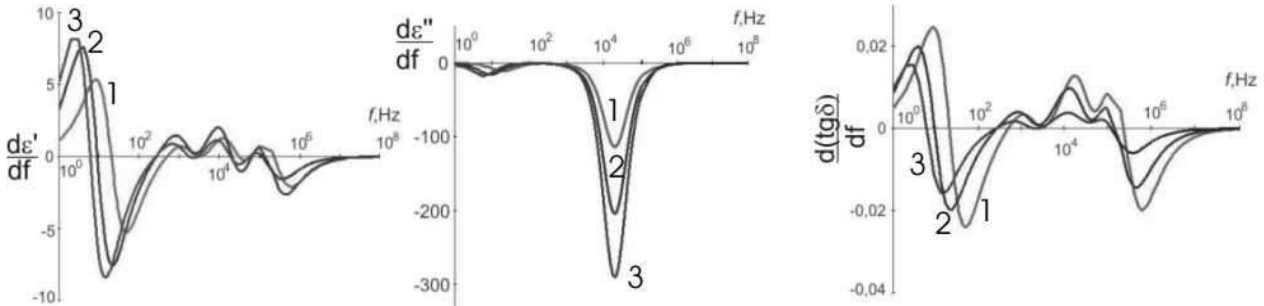


*Fig.3. The differential spectrums of dielectric constant (a,b) and functions of dielectric loss  $\text{tg}\delta$  (c) in dependence on frequency of alternating electric field and filler concentration (ferrous powder). Here curve 1 corresponds to filler concentration equal to 0.25, curve 2 corresponds to one equal to 0.45, and 3 corresponds to one equal to 0.65.*

As it was mentioned above, the orientation and deformation components make the main contribution to polarization of polar polymers. The deformation polarization is steadied during the time from  $10^{-14}$  up to  $10^{-12}$  sec. The induced dipoles appear so quickly that their shift reveals at any frequencies of alternating field, i.e. this process practically doesn't depend on frequency  $\omega$ . The dipole orientation doesn't take place immediately, but for enough long time. Thus, dielectric loss corresponding to the quantity of heat emitting at current going in dielectric volume unit shows on the fact that the sluggishness of orientation polarization is energy dissipation reason. Thus, the dependence of dielectric constant of polar polymers on alternating field frequency is defined by orientation dipole polarization, i.e. by the dipole moment value and group polarity, their number, position, temperature accordingly. As it is shown in the work [17], the observable shift of complex dielectric constant spectrums and dielectric loss of investigated mixture to the region of more low frequencies at increase of filler concentration in matrix is explained by the interaction of ferromagnetic powder particles with matrix polar radicals (-C-Cl). At lack of above mentioned interaction, the positions of maximums of dielectric loss function shouldn't be practically changed. The big value of

ferrite filler dielectric constant on low frequencies should lead to strong domain polarization and the interactions of matrix polar radicals with filler particles will lead to dielectric constant dispersion spectrums, correspondingly. By other hand, the essential decrease of dielectric constant on high frequencies (after 10MHz) decreases the domain polarization and dielectric constant dispersion of resistor sheath decreases in high-frequency spectrum region correspondingly. Confirming the above mentioned, the obtained experimental results show (fig.3) on dispersion of first maximum observable on fig.2 at 37Hz and practical lack of dispersion of rest spectrum maximums. This means that observable spectrum changes reflect the interaction of matrix polar radicals (-C-Cl) with filler particles.

#### THE SHEATH ELECTRIC CONDUCTIVITY

As it was above mentioned, the sheath of frequency-dependent resistor sheath presents itself the heterogeneous mixture, conglomerate of small ferromagnetic particles enough uniformly distributed in the volume, connected mechanically with dielectric and electrically isolated from each other at small concentrations.

Such heterogeneous structure is similar to structure of magnetodielectrics under the conditions that electric

conductivity of dielectric is insignificantly small, has the small electric loss and constant of magnetic permeability. The task solving of influence of material heterogeneity on frequency dependence of its electric polarization is connected with taking into consideration the processes of movable charges in the model of composite conductivity. The diffusion "smears" the charge in volume changing the field distribution in the system and the diffusion is stronger, the size of heterogeneities is smaller than Debye's radius. The charge distribution will be equilibrium at small frequencies independently of the value of alternating electric field every time moment. The diffusion plays the progressively less important role with concentration increase, the charge presses to the surface. The concentration gradient of moveable charges hasn't time to appear on the frequencies essentially exceeding the dispersion frequency and diffusion current becomes inessential one. Thus, physical meaning of conductivity increase with increase of frequency of alternating electric field lies in the limitation of the establishment velocity of polarization equilibrium state. From above mentioned, we can conclude that low-frequency region is connected with sample polarization as a whole, but high-frequency region is connected with polarization of separate conducting inclusions.

The using of nickel zinc ferrite powder makes task difficult because the mechanism of semiconductor electric conductivity of transition elements (Fe, Ni and etc) isn't explained in the framework of band theory, because the eigenfunctions of 3-d electrons of neighbor atoms or ions in the lattice don't cover because of weak interaction. The electric conduction mechanism in these compounds is caused by processes of electron exchange between ions of alternating valence ("hopping mechanism"), i.e. it is necessary that ions of the one and the same element with different charges are in equivalent places of crystalline lattice. It is known that the compounds of transition element oxides with spinel structure, for example magnet, have such lattice. The unit cell of spinel ferrite has space group (O7h – F3dm) and presents itself the cube formed by 8 MeO<sub>2</sub>O<sub>3</sub> molecules and consisting of 32 of O<sup>2-</sup> anions. Here Me is Ni<sup>2+</sup>, Co<sup>2+</sup>, Fe<sup>2+</sup>, Mn<sup>2+</sup>, Mg<sup>2+</sup>, Li<sup>+</sup> and Cu<sup>2+</sup>.

The oxygen anions form the close face-centered cube packing consisting in 64 tetrahedral (A) and 32 octahedral (B) empty spaces partly populated by Fe<sup>3+</sup> and Me<sup>2+</sup> cations. There are direct spinels (non-magnetic) and reverse ones (ferrimagnetic) in the dependence on the fact what kind of ions and in what order A and B take empty spaces. In reverse spinels the half of Fe<sup>3+</sup> ion number is in tetrahedral interspaces, but Me<sup>2+</sup> ions and the second half of Fe<sup>3+</sup> ion number are in octahedral ones. Moreover,  $M_A$  magnetization of octahedral sublattice is bigger than  $M_B$  magnetization of tetrahedral one that leads to ferrimagnetism formation. The nickel zinc ferrites are reverse spinels and present themselves the displacement solid solutions formed by two simple ferrites the one of which NiFe<sub>2</sub>O<sub>4</sub> is ferromagnetic, but another ZnFe<sub>2</sub>O<sub>4</sub> doesn't have the magnetic properties. The zinc cations in spinel structure always take tetrahedral points of lattice that cause the antiparallel spin orientation of Fe<sup>3+</sup> iron cations being in the one octahedral sublattice. The composition of solid solution with taking into consideration the cation distribution on oxygen interstices is characterized by formula:  $(Zn_x^{2+} Fe_{1-x}^{3+})[Ni_{1-x}^{2+} Fe_{1+x}^{3+}]O_4$ . The static

distribution on octahedral empty spaces of Ni<sup>2+</sup> and Fe<sup>3+</sup> ions and high compound electric conductivity are explained by the fact that Fe<sup>2+</sup> ions are easily displaced by bivalent Ni<sup>2+</sup> and Zn<sup>2+</sup> ions. As the cations with different valences take crystallographically and energy-wise equivalent positions in lattice, then reactions of electron exchange should carry out with inessential ( $\Delta E$ ) activation energy which is about 0,05eV. The zinc inclusion into crystalline lattice is accompanied by iron transition on octahedral positions. The magnetization of tetrahedral (A) sublattice and compensation factor of cation magnetic moments being in different sublattices (A and B) decrease correspondingly. As a result, the increase of concentration of non-magnetic moment leads to increase of solid solution magnetization (and  $B_s$  consequently), weakens the exchange interaction of A-O-B type that leads to monotonous decrease of Curie temperature ( $T_c$ ) at increase of mole fraction of ZnFe<sub>2</sub>O<sub>4</sub> in ferrospinel composition. In  $x > 0,5$  region the ion magnetic moments in tetrahedral sublattice don't have possibility to orientate the cation moments being in B-sublattice antiparallel to themselves, that leads to fast drop of saturation induction, decrease of crystalline anisotropy, increase of initial ferrite permeability. The point in composition triangle with orientation coordinates 50%Fe<sub>2</sub>O<sub>3</sub>, 15%NiO and 35%ZnO to which the solid solution Ni<sub>1-x</sub>Zn<sub>x</sub>Fe<sub>2</sub>O<sub>4</sub> corresponds where  $x \approx 0,7$ , corresponds to maximal value of permeability.

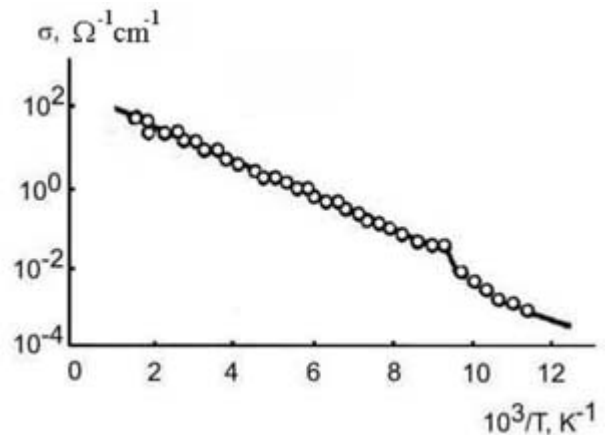
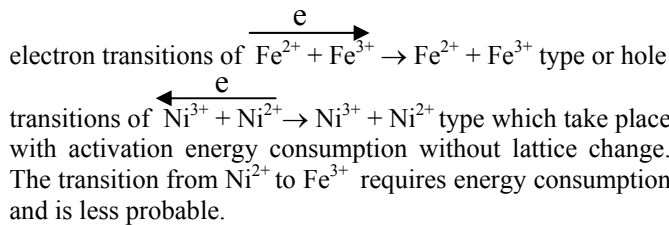


Fig.4. The temperature dependence of  $(Zn_{0.6}^{2+} Fe_{0.4}^{3+})[Ni_{0.4}^{2+} Fe_{1.6}^{3+}]O_4$  ferrite electroconductivity.

The temperature dependence of ferrite  $(Zn_{0.6}^{2+} Fe_{0.4}^{3+})[Ni_{0.4}^{2+} Fe_{1.6}^{3+}]O_4$  electroconductivity is given on the fig.4. Note that the break which is analogous to revealed one in magnetite is observed on temperature dependence near 120K. The strong decrease of magnetite electroconductivity nowadays is interpreted by following way. The electrons under the influence of exchange field formed by Fe<sup>2+</sup> and Fe<sup>3+</sup> cations being in octahedrons localize on these cations orientating by their spins antiparallel to magnetic moments of iron cations at temperature decrease up to some critical value. This process forms the magnetic short range ordering in temperature interval up to critical one, but it forms the magnetic long range ordering at achievement of critical temperature. Thus, the magnetic phase transition of induced type takes place at critical temperature.

As appears from the above [18,19] the electroconductivity of nickel zinc ferrite is explained by



The electrons taking part in exchange can be considered as charge carriers the concentration of which doesn't depend on temperature. However, it is shown that probability of transition between ions of alternating valence increases with temperature increase and temperature dependence of ferrite specific resistance is expressed with enough accuracy by the following relation  $\rho = \rho_\infty \cdot \exp\left(\frac{E_a}{kT}\right)$ , where  $k$  is Boltzmann constant,  $T$  is temperature,  $E_a$  is activation energy. The last one proves the investigation results of electroconductivity temperature dependence shown on the fig.4. The ferrite conductivity linearly increases and activation energy decreases with increase of concentration of iron bivalent ions. It follows from this that the height of energy barriers which overcome the electrons at the transition between neighbor ions decreases at approach of alternating valence ions. For example, the electroconductivity activation energy of nickel zinc ferrites decreases from 0,5 up to 0,1eV. (The magnetite has the most concentration of  $\text{Fe}^{2+}$  ions the specific resistance of which is equal to  $5 \cdot 10^{-5} \text{ Om} \cdot \text{m}$ ).

It is known [20] that value of limit particle radius at which the homogeneous magnetization is kept, can be defined from the following expression:

$$R_c \approx \frac{0.95}{J_s} (10A)^{\frac{1}{2}} \left( Q - \frac{2K}{J_s^2} - \frac{H}{J_s} \right)^{-\frac{1}{2}}$$

where  $J_s$  is saturation magnetization;  $A$  is parameter of exchange energy;  $K$  is anisotropy constant;  $Q$  is demagnetizing factor;  $H$  is field strength. Note that particle with radius satisfying to given equation at all field values  $H > -\frac{2K}{J_s}$  stays one-domain. The condition of absolute one-domain lattice for simple OCC and FCC lattices has the following form:

$$R < R_c \approx \frac{0.95}{J_s} \left( \frac{10cB}{a_0 Q_R} \right)^{\frac{1}{2}}$$

where  $c = 1/2, 1$  and  $2$  are for OCC and FCC lattices correspondingly;  $B = z^2 A$  is parameter of exchange energy;  $z$  is number of uncompensated spins per atom;  $A$  is exchange integral;  $a_0$  is parameter of crystalline lattice;  $Q_R$  is demagnetizing factor of one-domain ellipsoid along short axis.

It is significant that one-domain particle with critical radius has maximal coercitive force. At further radius decrease the particle keeps the homogeneous magnetization, because the atomic moments are taken by exchange forces, however, the probability of Brownian motion of summary magnetic moment vector increases in particle system. The probability of such process is proportional to  $\exp(E/k_B T)$ , where  $E$  depends on anisotropy constant and particle volume and has the meaning of energy barrier at overcoming of

which the heat fluctuations can cause the magnetic moment rotation. Thus, particle system with radii less than critical ones behaves itself similar to ensemble of paramagnetic atoms having the big magnetic moment. The estimation of relaxation time is the value by  $10^6$  order for particles having diameter of 30nm order at  $T=300\text{K}$ . Evidently, that value of energy barrier and consequently relaxation time depend on external magnetic field strength. The total impurity magnetization is defined by the following expression:

$$J = J_s V_0 \int_0^\infty \left( \operatorname{cth} \frac{J_s W H}{k_B T} - \frac{k_B T}{J_s W H} \right) f(W) dW$$

where  $f(W)$  is the dimension distribution function

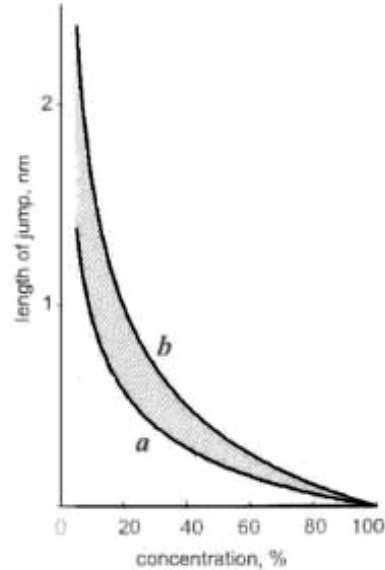


Fig.5. The dependences of jump lengths on concentration of ferrite component in mixture.

The dependence of jump lengths on concentration of ferrite component in mixture is given on the fig.5. As analysis shows all experimental data on jump lengths take place in hatched region limited by "a" and "b" curves corresponding to minimal and maximal distances between two particles at the given concentration and uniform distribution on ferrite particle volume. The jump length of

charge carriers is estimated by  $l(T) = \frac{3}{8} a \left( \frac{B}{T} \right)^{\frac{1}{4}}$  expression

in which "B" value is obtained from experimental data on electroconductivity of whole mixture. The dependence of jump length distribution on temperature obtained from experiments evidences about presence at least two mechanisms of hopping, the first of which is connected with jump mechanism in ferrite impurity component, and second one is connected with jump mechanism in ferrite-dielectric-ferrite structure.

The experimental results of investigations of temperature dependences of electric conductivity of ferrite-polymer dielectric-ferrite structure in temperature interval 70-120K shows on domination of hopping mechanism [22] with alternating jump length on localized states for three concentrations of ferrite components: 1 is 25%; 2 is 45%; 3 is

65%. The observable temperature dependence of jump mechanism is character for amorphous mediums. That's why localized states are connected not with impurities but with structural defects of dielectric matrix and presence of interfaces of dielectric matrix-ferrite particle. Such interesting interpretation is quite real one, because the density of localized states has the big values changing in the limits from  $10^{21}$  up to  $10^{22} \text{ eV}^{-1} \text{ cm}^{-3}$  in the dependence on ferrite component concentration.

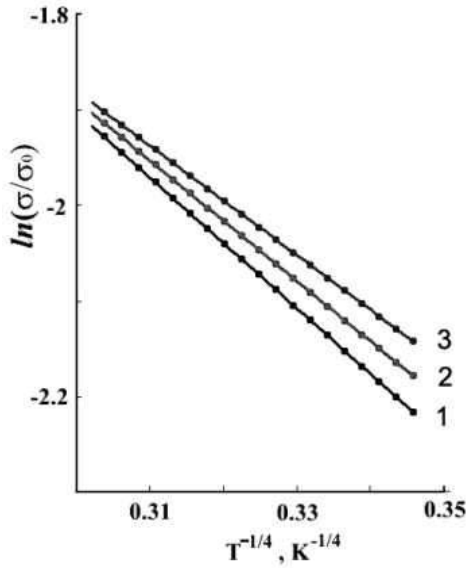


Fig.6. The temperature dependence of electroconductivity of ferrite-polymer dielectric mixture in interval from 70 up to 120K. Here 1 is 25%; 2 is 45%; 3 is 65% of concentration of ferrite component in the mixture.

As it is shown on the fig.7, the character of electric conductivity change with temperature has  $T^{1/2}$  dependence in the temperature interval from 120 up to 300K that is probably the consequence of essential influence of phonon processes on transfer of charge carriers. It is shown in [25] that the density distribution of states in neighborhood of Fermi level doesn't depend on interaction nature on small distances. Thus, the appearance of coulomb crack in density distribution of states in neighborhood of Fermi level, which observe near metal-dielectric transition where state radius and dielectric constant are abnormal big ones, because tend to infinity near transition point, is the reason of appearance of following

$$\text{dependence } \sigma \sim \exp \left[ \left( -\frac{B_1}{T} \right)^{\frac{1}{2}} \right], \quad B_1 = \frac{2.8e^2}{ke}, \quad \text{where } a \text{ is}$$

state radius.

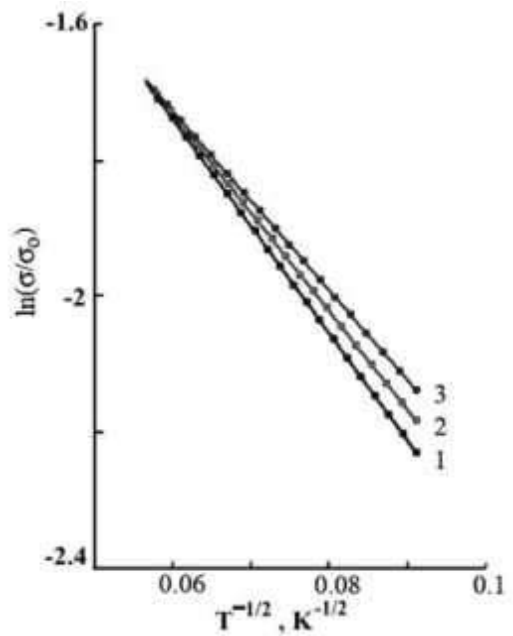


Fig.7. Temperature dependence of electroconductivity of ferrite-polymer dielectric mixture in the region from 120 up to 300K. Here 1 is 25%; 2 is 45%; 3 is 65% concentration of ferrite component in mixture.

Moreover, the thickness of layer of non-magnetic polymer dielectric between ferrite particles corresponds to condition of tunnel current appearance in the given structure. The appearing tunnel current has two components corresponding to two possible orientations of electron spins. Tunneling electrons take only vacancies with similar spin polarization. It follows from this that ferrite-polymer-ferrite structure will have the less resistance at similar spin orientation of two ferromagnetics, but at opposite orientation it will have the biggest one. If we take into consideration that all ferrite grains have similar parameters and dimensions and their spin volume distribution has chaotic character then the summary tunnel current must be equal to zero. The model of spin-dependent electron transfer through ferromagnetic-dielectric-ferromagnetic structure supposed in work [21], shows on essential role of parameters of tunnel barrier and ferromagnetic and on the oscillations appearing of the magnetoresistance at the dielectric thickness change or shift external voltage change as a result of wave function interference change.

According to this model the value of tunnel current can be estimated using Tsu-Isaki equation [22] by the following form:

$$I = \frac{2\pi e}{\hbar^3} m_{f\sigma}^* \iint T(E_z, E_{||}) (f_1 - f_3) dE_z dE_{||}$$

$$T = \frac{k_{col} m_{em}^*}{k_{em} m_{col}^* |t_{ii}|^2}; \quad t_{ii} = \left( \prod_i t_i \right); \quad t_i = \begin{pmatrix} e^{ik_i z_i} + e^{-ik_i z_i} \\ \frac{ik_i}{m_i^*} e^{ik_i z_i} - \frac{ik_i}{m_i} e^{-ik_i z_i} \end{pmatrix}^{-1} \begin{pmatrix} e^{ik_{i+1} z_i} + e^{-ik_{i+1} z_i} \\ \frac{ik_{i+1}}{m_{i+1}^*} e^{ik_{i+1} z_i} - \frac{ik_{i+1}}{m_{i+1}} e^{-ik_{i+1} z_i} \end{pmatrix};$$

$$k_{col} = \frac{\sqrt{2m_{col}^* \left( E_z \pm \frac{h_0}{2} + eV \right)}}{\hbar}; \quad k_{em} = \frac{\sqrt{2m_{em}^* \left( E_z \pm \frac{h_0}{2} \right)}}{\hbar};$$

$$k_i = \frac{\sqrt{2m_d^* (E_z - U_0 + \frac{I}{n}eV - eV_s \delta(z - z_1)(z - z_2) + e\varphi_i \frac{n^2}{i(n-i+1)} - \left( I - \frac{m_d^*}{m_{cm}^*} \right) E_{||})}}{\hbar};$$

$i = 1, 2 \dots n$

Here  $I$  is tunnel current;  $f_1$  and  $f_3$  are Fermi-Dirac distribution functions in emitter and collector regions correspondingly;

$T$  is wave transmission coefficient;  $k_i$  and  $m_i^*$  are wave vector and effective mass of  $i$ -th barrier region correspondingly;

$z_i$  is division coordinate of  $i$ -th and  $(i+1)$ -th barrier regions;

$m_{em}^*, m_{col}^*, m_d^*$  are effective masses in emitter, collector and dielectric;

$E_z, E_{||}$  are longitudinal and transversal components of electron energy;

$V$  is voltage applied to ferrite-polymer dielectric-ferrite structure;

$t_{ii}$  is element of matrix transmission;

$a$  is barrier thickness;

$U_0$  is height of potential barrier;

$V_s$  is potential of wave scattering;  $\varphi_i$  is image force potential in  $i$ -th region;

$\hbar$  is Plank constant;

$h_0$  is molecular field inside dielectric.

The transversal component of electron energy is constant, i.e.  $k_{||} = const$  at electron tunneling through potential barrier.

The following parameters have been accepted for calculations in the capacity of examples: height of potential barrier is 2.0 eV; width of potential barrier is 1-2 nm; effective masses of electrons having spin-up, spin-down and being in barrier are  $1.27m_0$ ,  $1.36m_0$  and  $0.4m_0$ , correspondingly; molecular field is 1.9 eV; potential of wave scattering is 0-0.2 eV.

The presence of frequency dependence of current passing through mixture of ferrite and dielectric, i.e. the skin-effect, are also taken into consideration at calculation. Thus, the value of current density on  $r$  distance on wire axis is defined by the  $j_0 \frac{M_0(kr)}{M_0(ka)}$  value, where  $M_0(kr)$  is modified Bessel function at passing of alternating electric current on cylindrical semiconductor. If we consider the mixture of ferrite and polymer dielectric used in our work as percolation system and use the [11] work results, then we notice that character of current passing is defined by scale of mixed conductivity at skin effect.

The current distribution in the structure will have two-dimensional character at skin-effect depth less than scale of mixed conductivity, but current will have three-dimensional one at skin-effect depth bigger than scale of mixed conductivity. The conductivity in the region of small frequencies is mainly defined by conductivity of "good"

conductor. As it follows from experiments and it was mentioned in [11] earlier the conductivity change and position one of boundary of mixed conductivity in small frequency region doesn't practically take place [24]:

$$\sigma(\omega) \approx \omega \left[ \ln \left( \frac{\omega_{ph}}{\omega} \right) \right]^4, \quad \text{где } \omega_{ph} \text{ is phonon}$$

frequency. It is equal to  $10^{12}$  sec.<sup>-1</sup> approximately.

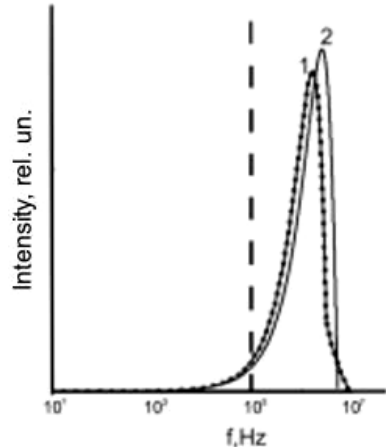


Fig.8. Experimental (1) and theoretical (2) of absorption spectrums of frequency-dependent resistor sheath in region from 10 up to  $10^7$  Hz.

The experimental and theoretical absorption spectrums of frequency-dependent resistor sheath in frequency region from 10 up to  $10^7$  Hz are shown on the fig.8. The changes of experimental absorption spectrum aren't practically observed up to 1000 B voltages, 10A current.

The presence of maximum on the curves absorption spectrum (Fig. 8) is caused by frequency dependence of ferrite permeability, frequency dependence of resistor inductance, and transition from three-dimensional character to two-dimensional one of current passing, and also by difference of spin-up spin current and spin-down one.

## CONCLUSION

The operation of frequency-dependent resistor sheath presenting itself the heterogeneous mixture Zn-Ni of ferrite powder with polar polymer dielectric-polyvinylchloride and physical properties of sheath components have been considered in detail. The ferromagnetic powder component has the similar volume density on whole resistor sheath in average. The properties of polymer matrix with ferrite filler have been studied.

The mechanisms of charge transport in both separate components and along whole ferrite-polymer dielectric ferrite

structure have been considered. The presence of two types of hopping mechanisms of charge transfer in the given structure has been established experimentally. The theoretical analysis of current passing in alternating field, in which the uniform distribution of current density on section of frequency-

dependent resistor as a result of skin-effect, the presence of spin-up spin current and spin-down one and also frequency dependence of ferrite permeability have been taken into consideration, are presented.

- 
- [1] *N.R. Babayeva*. Problems of Power Engineering, №4, 2005, pp. 40-47.
  - [2] *A.M. Gashimov, T.R. Mehdiyev, N.R. Babayeva*. Frequency-dependent resistor. International conference «Physics-2005», Baku, June, 7-9, 2005, pp.613-617.
  - [3] *A.M. Gashimov, T.R. Mehdiyev, N.R. Babayeva*. The limitation possibilities of high-frequency overvoltages at the use of frequency-dependent resistor. International conference energy of Moldova-2005, Kishinev, September, 21-24, 2005, pp.265-269.
  - [4] *A.M. Gashimov, T.R. Mehdiyev, N.R. Babayeva*. Effect of magnetic multi-layer to resistive properties of frequency-dependent resistor. TPE-2006, 3<sup>rd</sup> International conference on Technical and Physical Problems in Power Engineering, Ankara, Turkey 29-31 may 2006, pp. 604-606.
  - [5] *N.R. Babayeva*. Problems of Power Engineering, №3-4, 2006, pp.32-37.
  - [6] *A.M. Hashimov, T.R. Mehdiyev, N.R. Babayeva*. Fizika, №4, vol. XII, 2006, pp.28-32.
  - [7] *A.M. Gashimov, T.R. Mehdiyev, N.R. Babayeva*. On appropriateness of use of frequency-dependent resistor at limitation of high-frequency Overvoltages. Modern Electric Power Systems'06, Wroclaw, Poland, September 6-8, 2006, pp.379-382.
  - [8] *E.V. Dmitriyev, A.M. Gashimov, T.R. Mehdiyev, N.R. Babayeva*. The heat parameters and mode of operation of frequency-dependent resistor. Scientific conference dedicated to memory of Vershinin U.N. «Electrophysics of materials and installations». Novosibirsk, January,9-12, 2007, pp.55-60.
  - [9] *N.R. Babayeva, A.M. Gashimov, E.V. Dmitriyev, T.R. Mehdiyev*. Fizika, № 1-2, vol. XIII, 2007, pp.102-107.
  - [10] *N.R. Babayeva, A.M. Gashimov, T.R. Mehdiyev*. Fizika, №4, vol. XIII, 2007, pp.230-235.
  - [11] *V.G. Kuznecov, T.R. Mehdiyev, N.R. Babayeva*. To calculation of characteristics of frequency-dependent resistor. Technical electrodynamics, Kiev, 2007, pp.88-91.
  - [12] *E.V. Dmitriyev, A.M. Gashimov, N.R. Babayeva*. Power Engineering (Notes of high education organizations and power engineering cooperations of UIS), Minsk, 2007, № 4, pp. 29-38.
  - [13] *L.D. Landau, E.M. Lifshic*. Electrodynamics of continua. Science, 1982, 629p.
  - [14] *A.L. Efros, B.I. Shklovskii*. Phys. Stat. Sol.(b), 1976, v.76, p.475.
  - [15] *S.O. Gladkov*. JTPH, 1999, vol.69, №.7, pp. 89-94.
  - [16] *V.M. Ulyanov, E.P. Ribkin, A.D. Gudkovich, G.A. Pishin*. Polyvinylchloride, M.: Chemistry, 1992, p.288.
  - [17] *O.S. Gefle, S.M. Lebedev, U.P. Poholkov*. The frequency spectrums of complex dielectric constant of compositional dielectrics on the base of polyvinylchloride. Notes of Tomsk Politechnical University, 2007, vol.310, №1, pp. 87-91.
  - [18] *E. J. W. Verwey, P. W. Hayman and F.C. Romein*. J. Chem. Phys. 15, 181, 1947.
  - [19] *E.J.Verwey*. Semiconducting Materials, London, Butterworths Sci, Publ., 1951.
  - [20] *E.I. Kondorskii*. Notes of Azerbaijan SSR, physics series, 1952, vol.16, p.398.
  - [21] *S.A. Ignatenko, A.L. Daniluk, B.E. Borisenko*. JTPH, 2005, vol.75, №6, pp.8-12.
  - [22] *D. Ferry, S. Goodnik*. Transport in Nanostructures, Cambridge, 1997, p.512.
  - [23] *N. Mott, E.Devis*. The electron processes in non-crystalline substances. "World" publisher, Moscow, 1974, p.472.
  - [24] *B.I. Shklovski, A.L. Efros*. Flow theory and conductivity of strongly heterogeneous mediums. UFN, 1975, vol.117, №3, pp. 401-435.
  - [25] *B.I. Shklovski, A.L. Efros*. The modern state of hopping theory of electroconductivity. UFN, 1983, vol.141, №4, p.711.

**T.R. Mehdiyev, N.R. Babayeva, A.M. Həşimov, Ə.Ə. Həbibzadə**

### TEZLİKDƏN ASILI REZİSTOR ÖRTÜYUNDƏ ELEKTROMAQNİT PROSESLƏRİ

Məqalədə ferrit tozu və polimer dielektrik qeyri-bircins qatışından ibarət tezlikdən asılı rezistor örtüyünün elektrik və məqnit xüsusiyyətlərinin tədqiqinin nəticələri təqdim olunmuşdur. Yükdaşıyıcıların keçid prosesləri, elektrikkeçiriciliyinin konsentrasiya və temperatur asılılıqları araşdırılmışdır. Qeyri-bircins qatışından cərəyanın ötürülməsi proseslərinin xarakteri, sıçrayış keçiriciliyinin azı iki mexanizminin və spin cərəyanının olması müəyyən edilmişdir. Qeyri-bircins qatışından keçən dəyişən cərəyan axınına skin-effektin təsirinə baxılmışdır. Tezlikdən asılı rezistor örtüyü ilə yüksəkətezlilikli küylərin udulma spektrləri eksperimental və nəzəri olaraq araşdırılmışdır.

**T.P. Məhtiyev, N.R. Babaeva, A.M. Gashimov, A.A. Xəbibzadə**

### ЭЛЕКТРОМАГНИТНЫЕ ПРОЦЕССЫ В ОБОЛОЧКЕ ЧАСТОТНОЗАВИСИМОГО РЕЗИСТОРА

В настоящей работе представлены результаты исследований электрических и магнитных свойств оболочки частотнозависимого резистора, состоящей из неоднородной смеси ферритового порошка и полимерного диэлектрика. Исследованы процессы переноса носителей заряда, концентрационные, температурные зависимости электропроводности. Установлен характер процессов транспорта тока через неоднородную смесь, наличие, по крайней мере, двух механизмов прыжковой проводимости, наличие спинового тока. Рассмотрено влияние скин-эффекта на протекание переменного тока через неоднородную смесь. Экспериментально и теоретически исследованы спектры поглощения высокочастотных помех оболочкой частотнозависимого резистора.

*Received: 16.03.08*

**(CD<sub>3</sub>)<sub>2</sub>CDOH MOLEKULUNUN TRANS-KONFORMERİNİN “QADAGAN OLUNMUŞ” KECİDLƏRİ. “MƏRKƏZƏQAÇMA” KECİDLƏRİ VƏ “ZƏİF” KEÇİDLƏR**

**S.B. KAZIMOVA, M.E. ƏLİYEV, A.S. HƏSƏNOVA**  
*Azərbaycan MEA H.M. Abdullayev adına Fizika Institutu,  
 AZ-1143, H. Cavid pr., 33*

(CD<sub>3</sub>)<sub>2</sub>CDOH molekulunun trans-konformerinin fırlanması spektri tədqiq edilmiş, əsas rəqs halında 56 “qadağan olunmuş”- 44 “zəif” və 12 “mərkəzəqaçma” kecidi identifikasiya edilmişdir. Fırlanması spektrinin nəzəri təfsiri Watsonın A-reduksiyalı fırlanması hamiltonianı ilə aparılmışdır. Molekulun fırlanması və mərkəzəqaçma sabitləri əhəmiyyətli dərəcədə dəqiqləşdirilmişdir.

Son zamanlar mikrodalğa spektroskopiyasının sürətli inkişafı və yeni tədqiqat üsullarının, o cümlədən ikiqat rezonanslar üsulunun spektrometrlərdə tətbiq edilməsi sayəsində molekulların fırlanması spektrlərində “qadağan olunmuş” kecidlərin (“mərkəzəqaçma” kecidlərinin, həmçinin intensivlikləri mümkün kecidlərin intensivliklərindən bir neçə tərtib aşağı olan “zəif” kecidlərin) müşahidə olunması və tədqiq ediləməsi mümkün olmuşdur.

Ümumiyyətlə, spektriskopiyada “qadağan olunmuş” kecidlər termini mütləq mənə daşımır [1,2].

Məlum olduğu kimi, adiabatik yaxınlaşmada molekularda elektron, rəqs və fırlanması hərəkətləri arasındaki qarşılıqlı təsir nəzərə alınmir və bu da molekulun rəqsini fırlanması hərəkətinin “sərt” fırfırı və harmonik ossilyator modeli əsasında tədqiq olunmasına imkan verir [2]. “Qadağan olunmuş” kecidlər dedikdə, bu cür yaxınlaşmada qadağan olunan kecidlər nəzərdə tutulur. Başqa sözlə deyilsə, “qadağan olunmuş” kecidlər elektron-rəqs-fırlanması hərəkətləri arasındaki qarşılıqlı təsir və mərkəzəqaçma həyəcanlaşmasının təsiri nəticəsində yaranan kecidlərdir.

Bu cür kecidlərin nəzəri olaraq hesablanması üçün rəqsini fırlanması hamiltonianı aşağıdakı kimi götürülür [3]:

$$H = H_{20} + H_{02} + H_{12} + H_{30} + H_{21} + \dots \quad (1)$$

burada:

$$H_{20} + H_{02} = \frac{1}{2} \sum_k \omega_k (p_k^2 + q_k^2) + \sum_\alpha B_\alpha J_\alpha^2 \quad (2)$$

$$H_{12} = \sum_{\alpha\beta} B_k^{\alpha\beta} q_k J_\alpha J_\beta, B_k^{\alpha\beta} = \left( \frac{\partial B_{\alpha\beta}}{\partial q_k} \right)_e \quad (3)$$

$$H_{30} = \frac{1}{6} \sum_{ijk} K_{ijk} q_i q_j q_k \quad (4)$$

$$K_{ijk} = \left( \frac{\partial^3 V_\alpha}{\partial q_i \partial q_j \partial q_k} \right)_e \quad (5)$$

$$H_{21} = -2 \sum_{jk} \sqrt{\frac{\omega_j}{\omega_k}} q_k p_j \sum_\alpha B_\alpha \xi_{kj}^\alpha J_\alpha \quad (6)$$

$\xi_{kj}^\alpha$  – koriolis qarşılıqlı-təsir sabitləridir.  $\mu_\alpha$ -nın sıraya ayrılmamasını aşağıdakı şəkildə göstərmək olar:

$$\mu_\alpha = \mu_{00}^\alpha + \mu_{10}^\alpha + \mu_{20}^\alpha + \dots \quad (7)$$

Verilmiş ifadədə:

$$\begin{aligned} \mu_{00}^\alpha &= \mu_\alpha^l, \mu_{10}^\alpha = \sum_k \left( \frac{\partial \mu_\alpha}{\partial q_k} \right)_e q_k, \\ \mu_{20}^\alpha &= \frac{1}{2} \sum_{jh} \left( \frac{\partial^2 \mu_\alpha}{\partial q_j \partial q_k} \right)_e q_j q_k. \end{aligned} \quad (8)$$

H<sub>12</sub> fırlanması zamanı molekulun təhrifini ifadə etdiyinə görə H<sub>12</sub> ( $\mu_{10}$  və  $\mu_{00}$  ilə) hesabına baş verən kecidlər “mərkəzəqaçma” kecidləridir. H<sub>30</sub> ( $\mu_{10}$  və  $\mu_{20}$  ilə) hesabına baş verən kecidlər isə anharmonik kecidlərdir. Birinci yaxınlaşmada H<sub>21</sub> təmiz fırlanması kecidləri üçün seçmə qaydalarının pozulmasına səbəb olmur. Unitar çevirmə nəticəsində H operatoru  $\Psi_0$  dalğa funksiyasının ( $\Psi_0$ -H<sub>0</sub> operatorunun məxsusi funksiyasıdır) bazisində diaqonal şəklə gətirilir:

$$\tilde{H} = \exp(iS) \exp(-iS) = H + i[S, H] - \frac{1}{2}[S, [S, H]] + \dots \quad (9)$$

burada:

$$[S, H] = SH - HS$$

Bu isə, öz növbəsində  $\langle i | \mu_A | l \rangle$ -nin  $\Psi$  dalğa funksiyasının bazisində hesablanması

$$\tilde{\mu}_A = \exp(iS) \mu_A \exp(-iS) = \mu_A + i[S, \mu_A] - \frac{1}{2}[S, [S, \mu_A]] + \dots \quad (10)$$

operatorunun  $\Psi$  bazisində hesablanması gətirir.

Cədvəl 1

(CD<sub>3</sub>)<sub>2</sub>CDOH molekulunun “qadagan olunmuş” kecidləri.

Keçid							<i>V<sub>təc</sub></i>	<i>V<sub>hes</sub></i>	$\Delta v = V_{təc} - V_{hes}$
3	1	3	-	2	1	2	25933,36	25933,26	0,14
3	2	1	-	2	2	0	33356,62	33356,57	0,05
4	3	2	-	3	1	3	65595,73	65595,87	-0,13
4	2	2	-	3	0	3	62188,00	62187,81	0,19
5	5	0	-	5	3	3	31371,99	31371,87	0,12
5	4	1	-	4	4	0	54236,85	54236,65	0,19
6	1	6	-	5	1	5	49539,58	49539,37	0,21
6	1	6	-	5	1	4	26767,00	26766,99	0,01
7	0	7	-	6	0	6	57369,89	57369,85	0,04
7	6	1	-	6	6	1	74500,06	74499,89	0,17
8	2	6	-	7	2	5	75495,58	75495,77	-0,19
9	9	0	-	9	7	3	55180,26	55180,49	-0,23
9	7	3	-	9	3	6	72913,95	72914,16	-0,21
9	3	6	-	9	3	7	32509,05	32509,19	-0,14
9	4	5	-	8	6	2	69150,64	69150,83	-0,19
9	4	6	-	9	2	7	32577,68	32577,81	-0,12
10	5	6	-	10	3	7	32236,08	32235,92	0,16
10	3	8	-	9	3	6	58586,24	58586,36	-0,12
10	5	6	-	9	7	2	54477,98	54477,91	0,07
11	4	7	-	10	8	3	32914,05	32914,06	-0,01
11	5	6	-	11	5	7	31082,28	31082,13	0,15
11	8	3	-	10	10	0	57841,67	57841,81	-0,14
11	11	1	-	11	9	2	69135,68	69135,76	-0,08
11	3	9	-	11	1	10	48230,24	48230,23	0,01
12	10	3	-	12	8	4	52454,45	52454,48	-0,03
12	8	4	-	11	10	1	74946,42	74946,41	0,01
12	8	5	-	12	6	6	29769,33	29769,43	-0,10
13	9	4	-	13	7	7	64496,72	64496,52	0,19
13	4	9	-	12	6	6	58355,47	58355,55	-0,08
13	11	3	-	13	9	4	61518,62	61518,48	0,14
13	10	3	-	13	8	6	60203,21	60202,98	0,23
13	9	5	-	12	11	2	72231,14	72230,96	0,18
15	9	7	-	15	7	8	36069,27	36069,14	0,13
15	3	12	-	15	3	13	63389,14	63389,35	-0,22
16	12	5	-	16	10	6	55655,37	55655,18	0,19
17	12	5	-	17	10	8	73910,04	73910,15	-0,11
18	14	5	-	18	12	6	75642,06	75641,99	0,06
19	6	14	-	19	4	15	73171,55	73171,52	0,02
19	6	13	-	18	10	9	28974,31	28974,74	-0,14
20	11	10	-	20	9	11	49704,35	49704,42	-0,07
21	8	13	-	20	12	9	58824,72	58824,61	0,11
23	0	23	-	22	2	21	72926,30	72926,38	-0,08
24	1	24	-	23	1	22	75645,73	75645,71	0,02
24	9	16	-	23	11	12	34268,16	34268,28	-0,12
24	5	20	-	23	7	17	28881,45	28881,41	0,03
24	13	11	-	24	13	12	50101,86	50101,96	-0,11
25	10	15	-	24	14	11	73167,90	73167,91	-0,01
26	9	18	-	25	11	14	17884,35	17884,15	0,20
27	14	13	-	27	14	14	61964,25	61964,48	-0,23
28	16	13	-	28	14	14	61605,18	61604,97	0,21
28	17	11	-	28	17	12	29022,03	29021,81	0,22
29	6	23	-	28	8	20	48477,34	48477,41	-0,07
29	7	23	-	28	9	20	48477,34	48477,41	-0,07
29	18	12	-	29	16	13	57834,93	57834,91	0,02
30	16	15	-	30	14	16	72789,12	72789,27	-0,16
31	15	16	-	31	15	17	78347,59	78347,71	-0,13

İkiqat çevrilmə nəticəsində  $\mu_A$  üçün aşağıdakı ifadə alınır:

$$\begin{aligned}\tilde{\mu}_A &= \sum_{\alpha} \lambda_{A\alpha} \mu_{\alpha}^e + i \sum_{\alpha} ([S_{12}, \mu_{10}^{\alpha}] \lambda_{A\alpha} + [S_R, \lambda_{A\alpha}] \mu_{\alpha}^e + \\ &+ \sum_{\alpha} \lambda_{A\alpha} (\mu_{20}^{\alpha} + i[S_{30}, \mu_{10}^{\alpha}]) + \dots\end{aligned}\quad (11)$$

(11) ifadəsində birinci hədd “sərt” polyar molekulun təmiz firlanma spektrini, ikinci hədd mərkəzəqaçma həyəcanlaşması hesabına meydana çıxan “qadağan olunmuş” keçidləri ( $\Delta k \leq 4$  ilə), üçüncü hədd mexaniki ( $[S_{30}, \mu_{10}^{\alpha}]$ ) və elektrooptik anharmonizm hesabına yaranan “qadağan olunmuş” keçidləri ( $\Delta k \leq 1$  ilə) ifadə edir. Əgər (10) ifadəsində sira davam etdirilsədi,  $\Delta k > 4$ -ə uyğun olan keçidləri ifadə edən yeni həddlər meydana çıxmış olardı. Beləliklə, rəqs-firlanma qarşılıqlı təsirinin və anharmonizmin nəzərə alınması ilə molekulların firlanma spektrləri keyfiyyətə dəyişir. Belə ki, qeyri-polyar molekulların “qadağan olunmuş” spektrləri, meydana çıxır və polyar molekulların firlanma spektrlərinə isə yeni keçidlər əlavə olunur.

“Zəif” və “qadağan olunmuş” keçidlərin tədqiq edilməsi həm nəzəri cəhətdən (molekulun quruluşu haqda məlumat alınması və s.), həm də praktik nöqtəyi nəzərdən (ulduzlararası fəzanın və planet atmosferlərinin, həmçinin atmosfer tullantılarının spektrlərinin identifikasiyası, molekulların əmaləgəlmə və parçalanma mexanizminin aydınlaşdırılması) mühüm əhəmiyyət kəsb edir. Bu deyilənləri nəzərə alaraq,  $(CD_3)_2CDOH$  molekulunun trans-konformerinin timsalında mövcudluğu nəzəri olaraq M.R. Əliyev [4] tərəfindən söylənilən “qadağan olunmuş” firlanma keçidlərini tədqiq etməyi qərara aldıq.

Tədqiq olunan  $(CD_3)_2CDOH$  molekulunun trans konformeri “İzotop” birliyində istehsal olılmış OP-2 markalı (99,8%) götürülmüşdür. Bu molekulun tədqiqinə bir sıra işlər həsr olunmuşdur [6-9]. Verilmiş molekulun dipol momentinin sıfırdan fərqli iki komponenti ( $\mu_b$  və  $\mu_c$ ) olduğuna görə onun üçün “b” və “c” kecidləri mümkün kecidlərdir,  $\mu_a = 0$  olduğunu üçün “a” kecidləri qadağan olunmuş kecidlərdir. Spektrometrin həssaslığının və ayırdetmə qabiliyyətinin artırılması ilə  $(CD_3)_2CDOH$  molekulunun trans-konformerinin firlanma spektrində dipol momentinin rəqsi-firlanma qarşılıqlı təsiri və mərkəzəqaçma həyəcanlaşması hesabına  $\mu_a$  komponentinin

hesabına meydana çıxan yeni “mərkəzəqaçma” kecidlərini müşahidə etmək imkanına malik olduq [5]. Həmçinin incə qurluş effektleri secmə qaydalarına zidd olan ( $\Delta k_{-1}$  və  $\Delta k_{+1}$  cüt qiymətlər alır) “mərkəzəqaçma” kecidlərinin də meydana çıxmamasına səbəb olur. Firlanma və mərkəzəqaçma sabitlərinin yüksək səviyyədə və dəqiqləşdirilmiş qiymətləri ilə Vatsonun A-reduksiyalı və yalnız kvartik mərkəzəqaçma termlərinin daxil olduğu  $H_R$  hamiltonianı ilə II<sup>r</sup> koordinat təsvirdə hesablanmış firlanma spektri tədqiq olunan diapazona kifayət qədər çox “qadağan olunmuş” kecidlərin - “zəif”  $\mu_a$  və “mərkəzəqaçma” kecidlərinin düşdүünü göstərdi. Odur ki, bu kecidlərin identifikasiya edilməsinə başlandı. “Zəif” və “mərkəzəqaçma” firlanma kecidlərinin identifikasiyasına başlamazdan əvvəl firlanma və mərkəzəqaçma sabitlərinin məlum qiymətlərinə əsasən Vatsonun A-reduksiyalı firlanma hamiltonianı ilə tədqiq olunan diapazona düşən firlanma kecidlərinin tezlikləri və onların təyinolunma xətaları hesablandı. Bu zaman tezlikləri bir-birindən çox az ( $\approx 2$  MHS) fərqlənən dublet kecidləri müşahidə olundu və mərkəzəqaçma kecidlərinin interpretasiyasına məhz bu dubletlərin identifikasiyası ilə başlandı. Tərs spektroskopik məsələnin həllinə daxil edilmiş hər yeni identifikasiya olunmuş keciddən sonra yenidən firlanma kecidlərinin tezliklərini və təyinolunma xətaları hesablanaraq növbəti dəfə tərs spektroskopik məsələnin həlli üçün təyinolunma xətası minimal olan kecidlərin tezlikləri seçildi. Bu qayda ilə əsas rəqs halında 44 “zəif” və 12 “mərkəzəqaçma” kecidi identifikasiya edildi. Cədvəl 1-də bu kecidlərin tezlikləri verilib. Cədvəldə həmçinin bu kecidlərin ölçülülmüş və hesablanmış qiymətləri arasındaki fərq də verilmişdir.  $(CD_3)_2CDOH$  molekulunun mikrodalğa spektrində bir sıra kecidlərin parçalanması rəqsi-firlanma qarşılıqlı təsirlərə əlaqədardır. Öz aralarında dublet olan  $Q^b$  və  $Q^a$ , həmçinin  $R^b$  və  $R^a$  budaqlarına aid olan kecid seriyalarının mövcudluğu və bu seriyalara daxil olan kecidlərin identifikasiyası mövcudluğu nəzəri olaraq M.R. Əliyev tərəfindən söylənilmiş mərkəzəqaçma kecidlərinin  $(CD_3)_2CDOH$  molekulunun trans-konformerinin müşahidə olunan firlanma spektrində varlığını təcürübi olaraq təsdiq edən faktdır. Hesablamalar göstərdi ki, bu dubletlərin parçalanması  $J$  artdıraqca sıfır qədər azalır,  $J$  kvant ədədinin müəyyən qiymətində isə bu dubletlər arasında fərq 2 MHS-dən böyük olmur. 56 “qadağan olunmuş” kecidi identifikasiyası firlanma və mərkəzəqaçma sabitlərini əhəmiyyətli dərəcədə dəqiqləşdirdi. Cədvəl 2-də bu parametrlər və onların korrelyasiya matrisi verilmişdir.

Cədvəl 2.

$(CD_3)_2CDOH$  molekulunun “qadağan olunmuş” kecidləri firlanma və mərkəzəqaçma sabitləri və onların koorelyasiya matrisi.

Spektroskopik sabitlər	Koorelyasiya matrisi
A = 7035,7709 MHS (0,0012)	0,91
B = 6006,3450 MHS (0,0011)	0,90 0,96
C = 3915,4440 MHS (0,0009)	0,72 0,77 0,75
$\Delta_J = 2,8861$ kHs (0,0011)	-0,12 -0,15 -0,03 -0,29
$\Delta_{JK} = -1,8168$ kHs (0,0009)	0,11 0,20 0,18 0,42 -0,87
$\Delta_K = 2,8296$ kHs (0,0008)	-0,43 -0,66 -0,61 -0,83 0,05 -0,25
$\delta_J = -0,9402$ kHs (0,0003)	0,07 0,06 0,03 0,02 0,53 -0,54 -0,22
$\delta_K = -0,3318$ kHs (0,0003)	

- [1] G. Gertsberg. Elektronnie spektri i stroenie mnogoatomnikh molekul. «Mir», 1969.
- [2] R.H. Garstang, Atomic and Molecular Processes, Ed.D.R.Bates, N.Y., Academic Press,1962.
- [3] H.H. Nielsen, Rev.Mod.Phys.23,90 (1951).
- [4] M.R. Aliyev. Uspekhi phizicheskikh nauk. 119, № 3, (1976), 557.
- [5] Ch.O. Gadjar, S.A. Musayev, A.A. Abdullayev, M.E. Aliyev. Pribori i tekhnika eksperimenta,2005, №2, s.95-97.
- [6] Ch.O. Gadjar, S.A. Musayev, E.Yu. Salayev. Jurnal prikladnoy spektroskopii, 1983, t. 39, № 1, s. 69-74.
- [7] Ch.O. Gadjar, S.A. Musayev, E.Yu. Salayev. Optika i spektroskopiya, 1983, t. 55, № 4, s. 648-652.
- [8] Ch.O. Gadjar, S.A. Musayev, E.Ch. Saidov. Fizika, 2001, t. 7, № 2, s. 25-31
- [9] Ch.O.Qajar, S.A.Musayev, S.B.Kazimova, M.E.Aliyev, E.Ch. Saidov. Fizika, 2008, c. XIV, N 1, s. 38-42.

**S.B. Kazimova, M.E. Aliyev, A.S. Hasanova**

**“FORBIDDEN” ROTATIONAL TRANSITIONS OF TRANS-KONFORMER (CD<sub>3</sub>)<sub>2</sub>CDOH MOLECULE.  
CENTRIFUQAL ROTATIOHAL TRANSITIONS AND WEAK ROTATIOHAL TRANSITIONS**

The microwave rotational spectrum of transconformer (CD<sub>3</sub>)<sub>2</sub>CDOH molecule has been analyzed. 56 “forbidden” transitions: 44 “weak” transition and 12 “centrifugal” ones in main oscillation state have been identified. The theoretical description of a rotational spectrum is carried out by the A -reduction Watson Hamiltonian in II' axial representation. The spectroscopic parameters of above specified molecules has been recalculated with bigger accuracy.

**С. Б. Кязимова, М. Е. Алиев, А.С. Гасанова**

**«ЗАПРЕЩЕННЫЕ» ПЕРЕХОДЫ ТРАНС-КОНФОРМЕРА МОЛЕКУЛЫ (CD<sub>3</sub>)<sub>2</sub>CDOH.  
«ЦЕНТРОБЕЖНЫЕ» И «СЛАБЫЕ» ПЕРЕХОДЫ**

Исследован микроволновый вращательный спектр молекулы (CD<sub>3</sub>)<sub>2</sub>CDOH. Идентифицировано 56 «запрещенных»- 44 «слабых» переходов и 12 «центробежных» переходов в основном колебательном состоянии. Теоретическая обработка спектра осуществлялась вращательным гамильтонианом Ватсона А- редукции в II' осевом представлении. Существенно уточнены спектроскопические параметры.

*Received: 16.04.08*